From weak to ultrastrong coupling in light-matter interactions

Diego Fernández De La Pradilla Viso

UAM
Universidad Autónoma
de Madrid

Universidad Autónoma de Madrid | Escuela de Doctorado

From Weak to Ultrastrong Coupling in Light-Matter Interactions

Author

Diego Fernández de la Pradilla Viso

Supervisors

Esteban Moreno Soriano

Johannes Feist

Programa de Doctorado en
Física de la Materia Condensada, Nanociencia y Biofísica

Departamento de
Física Teórica de la Materia Condensada

Facultad de Ciencias
Universidad Autónoma de Madrid

Madrid, 2025

Memoria presentada para optar al grado de Doctor en Ciencias Físicas

Universidad Autónoma de Madrid

Departamento de Física Teórica de la Materia Condensada
Condensed Matter Physics Center (IFIMAC)

Directores:
Dr. Esteban Moreno Soriano
Dr. Johannes Feist

Tribunal:
Dr. Antonio Isaac Fernández Domínguez
Dra. Sol Carretero Palacios
Dr. Alejandro Manjavacas Arévalo
Dr. Timur Shegai
Dr. Mauro Antezza
Dra. Susana Fernández Huelga (suplente)
Dr. Miguel Bello Gamboa (suplente)

Madrid, abril de 2025

Grant us, O saints of heaven, an all-encompassing and sufficiently approximate vision.

Amanece, que no es poco, José Luis Cuerda.

Jörg-Lukas I want to be a physicst, Daddy.

Möbius (*staring at his youngest son alarmed*) Physicist?

Jörg-Lukas Yes, Daddy.

Möbius You must not do that, Jörg-Lukas. Absolutely not. Get it out of your head. I – I forbid you to do it.

Jörg-Lukas (*is confused*) But you became a physicst, Daddy –

Möbius I should have never become one, Jörg-Lukas. Never. I wouldn't be in the asylum right now.

Die Physiker, Friedrich Dürrenmatt.

Agradecimientos

Bueno, pues aquí estamos. La tesis, escrita. Los "papers", algunos, ya publicados. Y yo, satisfecho. Satisfecho porque, después de mucho trabajo, vislumbro el final de una etapa de mi vida. Porque aunque la vida es un flujo continuo de experiencias, es muy humano agruparlas en paquetes discretos (¿cuánticos?); nos ayuda a darles sentido. En cierta manera, esta memoria es precisamente el lazo final que cierra los últimos cinco años. Los agradecimientos que siguen son un homenaje humilde y simpre insuficiente a todas aquellas personas que han formado parte de este largo camino, y con las que espero contar también para lo que depare el futuro.

Como no puede ser de otra manera, comienzo con mis supervisores de tesis, Esteban y Johannes. Sonrío mientras escribo al recordar que me acerqué a Esteban al acabar tercero de carrera para hacer un proyectillo de verano. Había decidido preguntarle a él porque nunca me había gustado tanto la física como durante sus clases de Mecánica y Ondas I del año anterior. Fue Esteban quien me presentó a Johannes, y así les fui conociendo durante el verano y el curso siguiente en el TFG. Da qué pensar... sin ese cambio del turno de tarde al de mañana no habría conocido a Esteban ni a Johannes, seguramente no habría hecho el TFG con ellos, y me habría perdido a dos personas extraordinarias a quienes debo mucho de lo que he madurado y aprendido en este tiempo. Gracias, a ambos, por vuestra paciencia, por vuestro "feedback" incansable, profundo y detallado, y por vuestras palabras de consuelo en los momentos más oscuros y de felicitación en los más luminosos. Siento que, venga lo que venga a continuación, estaré preparado en gran medida gracias a vosotros.

Quiero parar también a reconocer el inmejorable ambiente del departamento. Sin excepción, todo el mundo con quien he interactuado ha contribuido a hacer de mi paso por el módulo 5 una experiencia acogedora y cálida. De mis comienzos, no puedo evitar acordarme de Clàudia, Mónica y Rui, que fueron los primeros en integrarme en el grupo de Johannes. Entre los muchos "soldados de a pie" con quienes el día a día se hace más llevadero, quiero mencionar especialmente a Alejandro Vivas, Maksim, Franje,

Ruth, Anael, Miguel Ángel, Carlitos, Caspar, Alejandro Caballero, Anna-Luisa, Gorm, Juanjo, Mimi, Jorge y Manu. Cada uno de vosotros sabe por qué está en esta lista, y con eso es suficiente. Otras personas que han ido y venido, pero que de una forma u otra se quedan para siempre, son Jacopo, Petros, Frieder y Jake. Además, quiero dedicar un par de líneas a Diego Martín, Antonio, Guilherme, FJ, Paloma, Francesca y Patricia, por las oportunidades que me han brindado en distintos momentos. A todos los anteriores, y a los que no he incluido por falta de espacio o descuido, gracias por hacerme sentir uno más del departamento y del IFIMAC, cada uno a vuestra manera.

Una de las actividades más enriquecedoras del doctorado ha sido la oportunidad de enseñar física introductoria en laboratorios y aulas. En concreto, me siento afortunado de haber conocido a Carlota Gil, una alumna cuyo espíritu brillante y apasionado trajo al primer plano de mi memoria recuerdos del estudiante cándido que era cuando empecé la carrera. Fue un placer discutir contigo el *Theoretical Minimum*, y lo sigue siendo cuando me pones al día de tus últimas aventuras por el mundo de las ideas.

I can't go any further without a taking slight detour to Montréal, where I had the outstanding chance to work under the supervision of Sean Molesky, and with his students Paul and Justin. With their warmth and welcoming Canadian attitude, they made it not just an experience to remember, but to forever cherish, not least because they introduced me to the best Poutin one can find in Montréal.

Según mi cuenta personal, toca volver a España y hablar de deporte. Desde que tiré a canasta por primera vez siendo un crío, el baloncesto ha formado parte integral de mi vida, y no ha sido distinto durante el doctorado. Las pachanguitas del "IFIMAC sports" han sido el mejor desestresante. Ha sido un placer compartir la pista con Carlos Sabín, Pablo Ares, Juan Luengo, entre otros, y, más recientemente, con Miguel Verde. ¡Menudos jugones! ¡Vamos, Memphysics! Fuera de la universidad, he tenido la suerte y el gusto de entrenar junto con Luis a varios equipos maravillosos, con los que he pasado momentos que atesoraré para siempre. Aunque estéis en una edad difícil y muchas tenéis casos de "pavo" que van de lo moderado a lo fuerte, os llevo a todas en el corazón.

Ya que estamos hablando de gente que ha dejado su marca en mi persona y mi carácter, no puedo pasar por alto a todos los amigos que me rodean y acompañan en este camino. Por un lado, Luis y Ali (tú ya sabes que eres mejor amig@), Aldán, Juan y Vila, no hay mejores compañeros de viaje en el mundo. Por otro, Miguel, Víctor, Víctor, Andrés y Merino. Ya son muchos años juntos, pero me encanta que sigamos contándonos las mismas batallitas del Ramiro

como si acabásemos de vivirlas. Termino con Paula “Portu” y Adri que, junto con Ali, son las “yogurinas” que más presentes siguen en mi vida.

Para acabar, quiero mencionar a las familias; empiezo por la adquirida. Gracias, Luis, Sonia y José Luis, por dejarme formar parte de vuestra vida, por compartir vuestra felicidad y por traer al mundo a Cris. Gracias, Cris, compañera en las alegrías y los pesares, en lo cotidiano y lo extraordinario, en la incertidumbre y la certeza; compañera, en definitiva, en la vida. La mejor pinche para mi chef, y la mejor chef para este pinche. La única capaz de aguantar mi versión gruñona mientras le doy un masaje en los “pieses”. A mi artista y bibliotecaria de cabecera, gracias por estar ahí, y por enseñarme los detalles del MARC21 y del Dublin Core.

Gracias, Sara y Emma, hermanitas mías, que a veces sois ángeles y a veces demonios, pero siempre vosotras mismas. Seguid así. Gracias, Alma y Roberto, porque sois los mejores padres que podría imaginar. Gracias por vuestro amor, por vuestro apoyo incondicional, y por ayudarme a convertirme en la persona que soy hoy. No sabéis cuánto me alegra el corazón reconocerme en vosotros.

Abstract

English

Keywords *light-matter interactions, macroscopic quantum electrodynamics, open quantum systems, ultrastrong coupling regime, quantum emitter*

The study of the interactions between light and matter forms, today, an exceptionally broad field that connects many specialized areas of research. In this thesis, we analyze various aspects of light-matter interactions. Specifically, the situations considered here can be regarded as instances of a common scenario involving three main components: emitters, photons and macroscopic media. By emitters, we refer to small material systems, such as atoms or molecules. The photons, in turn, are the particles that carry the electromagnetic field, that is, the light. Finally, media are extended material systems. In the low-energy regime (up to a few eV), this tripartite division allows us to ascribe a definite role to each element. The media condition the behavior of the electromagnetic field, which, in turn, modifies the dynamics of the emitters. Additionally, in certain relevant regimes, the media and emitters also interact directly and meaningfully through the electrostatic Coulomb potential. The work presented in this thesis explores a potpourri of light-matter-related phenomena within the confines of such a vastly rich scenario. The results of our research are contained in chapters 3 to 5, which are preceded by chapters 1 and 2, where we set the stage and introduce the necessary theoretical tools. To avoid overwhelmingly technical discussions, we have given chapters 3 to 5 a streamlined tone, and moves the details to several appendices at the end.

In chapter 3, we strip the electromagnetic field and the media of their peculiarities, reducing them to a rather generic environment in which an emitter resides. Accordingly, we focus our attention on an arbitrary emitter that interacts weakly with its environment. The question of the chapter is, then, how to describe the dynamics of the emitter. Historically, attempts at answering this question gave birth to the well-established field of open quantum systems, where different so-called master equations have been derived to predict the temporal evolution of emitters in environments. These master equations have

different properties that can render them more or less appropriate. For instance, Lindblad master equations are known to fulfill certain very desirable mathematical properties, but its parameters do not always have a straightforward connection with an underlying model of the environment. In contrast, the Bloch-Redfield master equation is, right from its derivation, linked to a concrete environment, while not generally satisfying the aforementioned mathematical properties. This much has been known for a long time, and there is actually a systematic procedure to turn the Bloch-Redfield equation into a Lindblad equation: the secular approximation. Nevertheless, it has been realized that the secular approximation can be inadequate in common situations. In this chapter, we discuss an alternative approach that retrieves a Lindblad master equation from the Bloch-Redfield equation, designed to overcome the limitations of the secular approximation.

Inspired by the shortcomings of the secularization procedure, we devise a specific system in chapter 4 that directly illustrates these limitations. From the analysis and conclusions of chapter 3, it is clear that the secularized Lindblad equation lacks any environment-induced couplings between off-resonant states, which would manifest as off-diagonal terms in the energy shift and complex networks of dissipative pathways. After some consideration, we realized that, under the right circumstances, the precise interplay of these effects could give rise to remarkable consequences explored in this chapter. To that end, we study the dynamics of an emitter, a hydrogen atom, in the vicinity of an AlN spheroidal nanoparticle that alters the properties of the electromagnetic field. The hydrogen atom is a clean analytical system that already provides us with realistic energetic spectra featuring narrowly separated energy levels corresponding to different hydrogenic fine-structure states. Such configurations are especially prone to being misrepresented by the secular approximation. As for the nanoparticle's material and shape, they ensure that its electromagnetic response along the symmetry axis is enhanced within an appropriate frequency range, tailored to target a particular atomic transition. The question is, in this chapter, what the temporal evolution of the atom looks like, and how our circumventing of the secular approximation is reflected in it. This calls for an open quantum systems' perspective such as the one developed in chapter 3. After carrying out the calculations, we confirm that the nanoparticle-field environment does, indeed, strongly affect the hydrogen atom in ways that would be completely missing from a secularized master equation. In particular, we show that the bare hydrogenic eigenstates become drastically mixed to give rise to a new atomic structure. These effects manifest in the energy spectrum, which develops avoided-crossing features, and

in the dynamics, where Rabi-like oscillations are observed. Furthermore, under the right circumstances, we show that the dissipative rates of the atomic eigenstates, expected to increase monotonically as the atom-nanoparticle separation decreases, can actually exhibit the opposite trend. The mechanism for the "Purcell-effect reversal" phenomenon is the emergence of an eigenstate that becomes more and more decoupled from the environment, as the mixing of the hydrogenic fine-structure states increases while approaching the nanoparticle.

Finally, we switch gears in chapter 5 by investigating a different regime of light-matter interactions, the ultrastrong coupling regime, while still considering the same three elements as before: an emitter, photons and a material medium. The topic addressed in this chapter is the role that the direct emitter-medium interaction can have in reaching the ultrastrong coupling regime, specifically in comparison to the medium-modified emitter-photon interaction. Recently, there has been ongoing debate in the literature around this very issue. In short, even if similar models can be used to describe either situation, the meaning of the parameters is radically different depending on the underlying mechanism that achieves ultrastrong coupling. Furthermore, the relevance of terms in the light-matter Hamiltonian such as the polarization self-energy crucially depends on this distinction. Naturally, these issues can seriously affect the modeling of experiments as well as fuel theoretical misunderstandings. In chapter 5, we devise an argument based on electromagnetic constraints showing that, the interaction strength between the emitter and the photons cannot exceed a specific bound, even when the medium modifies their interaction in an optimal way. With this result, we can explicitly show that if the emitter is small, such as an atom or molecule, the ultrastrong coupling regime can only be reached via the emitter-medium interaction through subwavelength confinement, while the emitter-photon interaction is, in fact, negligible. Because the reasoning used to reach this conclusion is somewhat abstract, we illustrate them with an analytically solvable model of the dipolar resonance of a plasmonic nanoparticle. In practice, we write the emitter-photon and emitter-nanoparticle interactions in terms of the photon-nanoparticle eigenmodes, such that we can quantitatively compare the coupling strength associated with each physical process.

Castellano

Palabras clave *interacciones luz-materia, electrodinámica cuántica macroscópica, sistemas cuánticos abiertos, régimen de acoplamiento ultrafuerte, emisor cuántico*

El estudio de las interacciones entre la luz y la materia forma, hoy en día, un campo excepcionalmente amplio que conecta numerosas áreas de investigación. En esta tesis, analizamos aspectos variados acerca de dichas interacciones. Específicamente, las situaciones consideradas aquí pueden plantearse como casos concretos de un escenario común con tres componentes principales: emisores, fotones y medios macroscópicos. Por emisores entendemos sistemas materiales pequeños, como átomos o moléculas. Los fotones, por su parte, son las partículas que describen el campo electromagnético, esto es, la luz. Finalmente, los medios son sistemas materiales extensos. En el régimen de bajas energías hasta unos pocos eV, esta división en tres fragmentos nos permite atribuirle un papel definido a cada elemento. Los medios condicionan el comportamiento del campo electromagnético que, a su vez, modifica la dinámica de los emisores. Además, en ciertos regímenes de relevancia, los medios y los emisores interactúan de forma directa y significativa entre sí, a través del potencial electrostático de Coulomb. El trabajo presentado en esta tesis explora un popurrí de fenómenos relacionados con la luz y la materia dentro de los confines de un escenario tan variado como este. Los resultados de nuestra investigación están contenidos en los capítulos 3 a 5, precedidos por los capítulos 1 y 2, donde preparamos el camino e introducimos las herramientas teóricas necesarias. Para aliviar las discusiones de detalles técnicos, damos a los capítulos 3 a 5 un tono fluido, moviendo los detalles a varios apéndices tras el cuerpo principal.

En el capítulo 3, dejamos de lado las peculiaridades del campo electromagnético y los medios, reduciéndolos a un entorno genérico en el que reside un emisor. De acuerdo con ello, centramos nuestra atención en un emisor arbitrario, que interactúa con su entorno débilmente. La pregunta del capítulo es, entonces, cómo describir la dinámica del emisor. Históricamente, el campo de los sistemas cuánticos abiertos nació de los intentos de dar respuesta a dicha cuestión. En dicho campo, diferentes ecuaciones, conocidas como ecuaciones maestras, han sido derivadas para predecir la evolución temporal de emisores en entornos. Tales ecuaciones maestras tienen distintas propiedades que pueden volverlas más o menos adecuadas. Por ejemplo, se sabe que las ecuaciones maestras de Lindblad satisfacen ciertas propiedades matemáticas muy deseables, pero sus parámetros deben ser relacionados con algún modelo subyacente del entorno. La ecuación maestra de Bloch-Redfield, por contra, está

relacionada desde su derivación con un entorno concreto, mientras que no satisface las condiciones matemáticas anteriores. Todo esto es conocido desde hace mucho tiempo, y existe un procedimiento sistemático que convierte la ecuación de Bloch-Redfield en una ecuación de Lindblad: la aproximación secular. Aun así, se ha señalado en la literatura que la aproximación secular puede resultar inadecuada en situaciones comunes. En este capítulo, discutimos un método alternativo que recupera una ecuación maestra de Lindblad a partir de la ecuación de Bloch-Redfield, diseñado para superar las limitaciones de la aproximación secular.

Inspirados por las deficiencias del proceso de secularización, diseñamos un sistema específico en el capítulo 4 para ilustrarlas directamente. A partir del análisis y las conclusiones del capítulo 3, está claro que la ecuación de Lindblad secularizada carece de ciertos acoplamientos atómicos inducidos por el entorno, que se manifiestan como términos no diagonales en el desplazamiento de energías y como redes complejas de caminos de disipación. Tras cierta consideración, nos percatamos de que, bajo las circunstancias adecuadas, el efecto combinado de estos elementos podría dar lugar a consecuencias notables, exploradas en el capítulo. Con este objetivo, estudiamos la dinámica de un emisor, un átomo de hidrógeno, en la vecindad de una nanopartícula esferoidal de AlN que altera las propiedades del campo electromagnético. El átomo de hidrógeno es un sistema analítico limpio que nos provee con espectros energéticos realistas, incluyendo niveles próximos en energías que se corresponden con distintos estados hidrogenoides de estructura fina. En tales situaciones, la aproximación secular es susceptible de fallar. En cuanto al material y la forma de la nanopartícula, sirven para ensalzar su respuesta electromagnética en el eje de simetría y en el rango de frecuencias adecuado para resaltar una transición atómica concreta. La pregunta de este capítulo es qué aspecto tiene la evolución temporal del átomo, y cómo nuestro tratamiento, alternativo a la aproximación secular, se refleja en ella, lo que requiere un tratamiento de sistemas cuánticos abiertos como el desarrollado en el capítulo 3. Tras llevar a cabo los cálculos, confirmamos que el entorno formado por la nanopartícula y el campo electromagnético afecta al átomo de hidrógeno de maneras importantes que se escaparían a una ecuación maestra secularizada. En particular, mostramos que los estados hidrogenoides se mezclan de forma drástica, dando lugar a una nueva estructura atómica. Estos efectos se manifestan en el espectro de energía, en el que aparecen “cruces evitados”, y en la dinámica, donde se observan oscilaciones de tipo Rabi. Es más, bajo las circunstancias adecuadas, comprobamos que las tasas de decaimiento de los autoestados atómicos pueden decrecer a medida que la separación entre el

átomo y la nanopartícula disminuye, en contra de la expectativa habitual. El mecanismo por el cual el efecto Purcell se revierte es la aparición de un autestado atómico cada vez más desacoplado del entorno, a medida que la mezcla de los estados hidrogenoides de estructura fina aumenta al acercar el átomo a la nanopartícula.

Finalmente, ponemos el foco en un régimen de interacción entre la luz y la materia distinto en el capítulo 5, adentrándonos en el régimen de acoplamiento ultrafuerte, aunque reteniendo los mismos tres elementos de antes: un emisor, los fotones y un medio material. La cuestión tratada en este capítulo es el papel que juega la interacción de Coulomb directa entre el emisor y el medio en alcanzar el régimen de acoplamiento ultrafuerte. Específicamente, comparamos dicha interacción de Coulomb con la interacción entre emisor y fotones en presencia del medio. En los últimos años, ha habido un debate en la literatura precisamente sobre este tema. Una presentación breve del mismo consiste en que incluso si se pueden emplear modelos similares para describir ambas situaciones, el significado de los parámetros cambia radicalmente dependiendo del mecanismo subyacente que permite alcanzar acoplamiento ultrafuerte. Además, la relevancia de términos del Hamiltoniano de luz y materia, como la autoenergía de polarización, depende crucialmente de este punto. Naturalmente, problemas así pueden afectar seriamente a la modelización de experimentos, así como generar malentendidos sobre la teoría. En el capítulo 5, construimos un argumento basado en restricciones sobre el campo electromagnético que demuestra que la fuerza de interacción entre el emisor y los fotones está fundamentalmente limitada, incluso si el medio modifica la interacción emisor-fotón de forma óptima.

Con este resultado, mostramos explícitamente que, si el emisor es pequeño, como un átomo o molécula, el régimen de acoplamiento ultrafuerte solo puede alcanzarse mediante la interacción de Coulomb entre el emisor y el medio, mientras que la interacción entre el emisor y los fotones es, de hecho, despreciable. La intuición que sostiene a esta conclusión es que, para llegar a acoplamiento ultrafuerte con uno o pocos emisores, es preciso confinar la luz a escalas muy inferiores a su longitud de onda, lo que potencia enormemente los campos electrostáticos. Dado que los argumentos empleados para llegar a esta conclusión son más bien abstractos, los ilustramos con un modelo de la resonancia dipolar de una nanopartícula plasmónica con solución analítica. En la práctica, escribimos las interacciones del emisor con los fotones y del emisor con la nanopartícula en términos de los modos normales del sistema de la nanopartícula y los fotones. Así, logramos una comparación cuantitativa directa entre la magnitud de la interacción asociada a cada proceso físico.

Notation conventions

The elements of a clear notation are as much a matter of opinion as anything else, but clarity often lies in the balance between precision and simplification. Erring in either direction tends to yield equations that are hard to decipher. In this thesis, we have tried to strike that balance by choosing, for the most part, a standard notation, or a slightly simplified version thereof. A major goal in this regard has been to strive for consistency throughout the thesis, in spite of the broad nature of the discussion. Here, we summarize our choices and provide a reference for the reader.

Subscripts and superscripts We use roman subscripts when the subscript in question is a label, e.g., indicating the system that the object belongs to (examples: the atomic Hamiltonian is H_{at}; the system's density matrix is ρ_{s}). Italic subscripts are used when the index is a variable that can take different values, such as vector components or to number the charges in a system. For consistency's sake, we have tried to reserve at most two purposes for each character, such that the broad context and concrete character are enough to identify the nature of the indexed object. Greek letters have been used primarily to specify harmonic modes, except for λ and μ. The first one also identifies the electric and magnetic fundamental operators $\mathbf{f}_\lambda$ in macroscopic quantum electrodynamics, according to the most extended notation in the literature, and both λ and μ are used in the definition of some functions in appendix A. The symbols $\perp$ and $\parallel$ indicate the transverse and longitudinal nature of fields and tensors.

Scalars, vectors and tensors We distinguish them by reserving lightface for scalars and boldface for vectors, tensors and generic matrices. The context should make clear the distinction between tensors and vectors. Their dependence on space and time is generally omitted, except if it would lead to ambiguous or inconsistent expressions. On a more particular note, $\mathbf{B}$ will be called magnetic field, as $\mathbf{H}$ is not used explicitly in the results discussed here.

Differential operators Differentiation with respect to a given spatial coordinate $\mathbf{x}$ is denoted by $\nabla_{\mathbf{x}}$. If only one spatial variable appears (or is implicit) in the expression, then we may omit the subscript. Partial derivatives with respect to time are denoted with ∂_t, and we use a dot ($\dot{a} \equiv \partial_t a$) except when the name of the quantity being differentiated has a dot of its own, such as $\partial_t \mathbf{j}$. The Laplace operator is denoted by ∇^2.

Dirac delta functions Starting from the basic $\delta(x-y)$, we denote the multidimensional $\delta^{(3)}(\mathbf{r}-\mathbf{r}')$, which is the product of a simple delta for each Cartesian coordinate: $\delta^{(3)}(\mathbf{r}-\mathbf{r}') = \prod_{i\in\{x,y,z\}} \delta(r_i - r_i')$. We also make use of the tensor-valued delta distribution $\boldsymbol{\delta}(\mathbf{r}-\mathbf{r}') = \mathbf{1}\delta^{(3)}(\mathbf{r}-\mathbf{r}')$, where $\mathbf{1}$ is the identity in real space, and its transverse and longitudinal cousins, defined in appendix A, $\boldsymbol{\delta}^{\perp}(\mathbf{r}-\mathbf{r}')$ and $\boldsymbol{\delta}^{\parallel}(\mathbf{r}-\mathbf{r}')$.

Integrals When integrating over several variables of the same kind and with the same limits, we place all the dx's after a single $\int$ symbol. In spatial (frequency) integrations, the absence of explicit limits indicates that the integration is to be taken from $-\infty$ (0) to ∞. In particular, integrals over a volume V are written as $\int_V \mathrm{d}^3 r$, respectively, or $\int \mathrm{d}^3 r$ if $V = \mathbb{R}$. Solid angle integrations are always over the full 4π range, and are made explicit with the subscript Ω: $\int_\Omega \mathrm{d}\Omega$.

Miscellaneous More specific choices are as follows: The mode-expansion coefficients of vector fields use the same symbol as the field in lightcase. Quantum operators have no hat. H.c. denotes the Hermitian conjugate of the expression to the left. Complex conjugation is indicated with an asterisk. Spherical coordinates are denoted by r (or $|\mathbf{r}|$), ϑ ($\in [0,\pi]$) and φ ($\in [0,2\pi)$). $\mathbf{I}_n$ is the $n \times n$ identity matrix. A positive (semi-)definite matrix $\mathbf{M}$ is indicated by $\mathbf{M} > 0$ ($\mathbf{M} \geq 0$). The S symbol indicates that the expression that follows is symmetrized. The symbol $\otimes$ denotes the tensor product that combines Hilbert spaces in quantum mechanics, and also the dyadic product of vectors in real space.

List of Acronyms

This is a list of the acronyms used throughout the text, in alphabetical order.

BRE	Bloch-Redfield equation
CP	Casimir-Polder
CPTP	completely positive and trace preserving
DOF	degrees of freedom
DSE	dipole self-energy
EM	electromagnetic
LME	Lindblad master equation
MQED	macroscopic quantum electrodynamics
OQS	open quantum system
PSE	polarization self-energy
PZW	Power-Zienau-Woolley
QCT	quantum canonical transformation
QED	quantum electrodynamics
QO	quantum optics
QFT	quantum field theory
RWA	rotating wave approximation
SC	strong coupling
2LA	two-level atom
3LA	three-level atom
USC	ultrastrong coupling

Contents

Chapter One | Introduction to the interaction between light and matter

> ... and then the rest is just
> classical electromagnetism.
>
> *Johannes Feist*

Chapter summary In this chapter, we first take a bird's-eye view of the key historical moments in the study of light, matter and their interactions (section 1.1). There, we briefly stop by to revisit the ensuing development of cavity quantum electrodynamics and quantum optics, reaching the frontier of well-established results. In direct continuation, we highlight in section 1.2 the current state of light-matter research and its role in the quantum technological revolution. Finally, section 1.3 frames the contents of the thesis in the light of the previously discussed ideas.

1.1 Light and matter yesterday

The present state of research in any given field cannot be properly understood without at some point appreciating the origins and development of its main ideas. We give here a brief overview of the research trends that shaped our present description of light and matter.

1.1.1 Switching the light on: quantum electrodynamics

Our current account of known physics lists *electromagnetism* as one of the four fundamental interactions in the universe. Together with gravity and the strong and weak nuclear forces, these interactions provide a complex set of rules that all particles seem to abide by. However, unlike the nuclear interactions, both gravity and electromagnetism have rather palpable effects at the human scale.

Accordingly, the history of our species has been deeply conditioned by the study and exploitation of electromagnetic (EM) phenomena. Surely, the technological revolution that led up to present-day electronics is a perfect illustration of the impact of EM phenomena on our lives. Such refined technological applications have been made possible only after a centuries-long exploration of nature. From the theoretical side, the first great culmination in the understanding of electromagnetism came in the 1860s, when the efforts of numerous great minds were succinctly summarized in a set of twenty equations by James C. Maxwell [1]. In their modern form, *Maxwell's four equations* determine the evolution of the electric and magnetic fields, affected by the presence of charged matter. In turn, the fields exert the Lorentz force on charged particles, and we have, thus, a closed set of five coupled dynamical equations whose solutions represent a wide range of seemingly disparate physical situations.

The current notation as fewer vector identities is due to Oliver Heaviside.

The remarkable simplicity and soundness of Maxwell's equations is further evidenced by their continued presence in modern theories. Indeed, not only have they withstood the two major revolutions of XX-century physics in relativity and quantum mechanics, but Maxwell's equations have actually been foundational to theoretical progress on both ends. Essentially, their invariance under Lorentz transformations lies at the heart of Albert Einstein's development of special relativity [2]. The advent of quantum physics was also steered by electromagnetic phenomena, as exemplified by Max Planck's explanation of black-body radiation [3], Einstein's theory for the photoelectric effect [4] or Niels Bohr's model for the EM spectra of excited atoms [5]. The next great theoretical achievement happened in 1927, when Paul Dirac quantized the EM field itself in terms of "an assembly of particles moving with the velocity of light and satisfying the Einstein-Bose statistics" [6]. Of course, these particles are nowadays known as *photons*. Dirac's seminal work represents the birth of quantum electrodynamics (QED), but a few more ingredients were missing to form the current version. First, Dirac's paper described an atomic system with the "standard" quantum mechanics of the time, that is, with a finite number of degrees of freedom (DOF), while the EM field was a quantized field with a continuum of DOF. Such asymmetry led Pascual Jordan to propose that the matter part should also be accounted for with "a quantum-mechanical wave theory of matter, [...] in which electrons are represented by quantized waves in the usual three-dimensional space" [7], an idea further developed by Wolfgang Pauli and Werner Heisenberg in the following years [8, 9]. Through their research, they paved the way for the modern understanding of quantum field theories (QFT), of which QED is the paradigmatic example describing a charged fermionic field that interacts with the bosonic EM field.

This fermionic field is sometimes referred to as the Dirac field, because he derived the relativistic equation for fermionic particles.

With the benefit of hindsight, it is now recognized that the QFT approach is the proper manner in which relativistic covariance can be built into the problem of light-matter interactions. However, this realization came only after dealing with the very disturbing appearance of divergences in a priori sensible calculations, such as the electron's self-energy. Indeed, in the decades that followed the first results, an atmosphere of dissatisfaction settled among the QED community, only lifted by occasional partial successes. Through huge doses of inspiration and effort, the pieces of a complex puzzle were gradually laid on the collective imagination. Such was the situation until the second half of the 1940s, when the full QED picture was finally put together with the works of Sin-Itiro Tomonaga, Julian Schwinger and Richard Feynman, who shared the 1965 Nobel Prize in Physics [10], and Freeman Dyson. As a result, the systematic process to consistently remove the divergences, and thus renormalize calculations, became an integral part of the theory. Their ideas were consolidated in the next decades with the construction of the Standard Model of particle physics, a triumph of QFT in modern physics. The interested reader should find Ref. [11] an engaging book with a much more detailed account of the complex history sketched here. Yet, behind all the technical sophistication of QED, Maxwell's equations are still recognizable as an integral part, with only a change in interpretation. Now, they relate the dynamics of evolving *quantum field operators*, rather than that of classical fields. Still, the essence of Maxwell's theory is very much present in QED; after all, it is "just classical electromagnetism" with quantum touches.

Before moving on, it would be remiss of us to not discuss any further the *non-relativistic limit* of QED. This theory is completely aligned with Dirac's first calculations in that the EM field is fully quantized, but the charged particles are described through standard quantum mechanics. Non-relativistic QED is a suitable representation of the interaction between photons and bound matter systems such as atoms, molecules or larger assemblies thereof [12–14], where the typical energy scales are low enough ($< 1\,\mathrm{KeV}$) that a non-relativistic treatment retains the relevant processes. Just like full-fledged QED had tremendous impact on the evolution of QFTs, its non-relativistic version grounded the broad branches of physics wherein this thesis lies: *cavity QED* and *quantum optics*. The seeds of both research areas were planted during the 1940s and 1950s with perhaps a more specialized and applied perspective. Even if both have been around for some time, they still represent a rich source of research questions with dynamic scientific communities to this day. In the following, we will glance at some of the most significant milestones that have brought us to the state-of-the-art results being explored today.

1.1.2 Trapping the light: cavity QED

In 1946, Edward Purcell realized that the relaxation rate of a spin system could be enhanced many orders of magnitude by coupling it to a resonant electric circuit [15]. The reasoning was that the resonator strongly modified the EM local density of states accessible to the system, thereby affecting its spontaneous decay rate. Soon after, Hendrik Casimir and Dirk Polder published a *perturbative* calculation of the energy shift of an atom due to its proximity to a perfectly conducting plane [16]. This effect is a correction to the free-space atomic energy shift [17] due to the presence of macroscopic bodies, and depends on the relative atom-body position. It can be thought of either in terms of virtual photons being exchanged between the atom and the large structure or as a result of the interaction between fluctuating dipoles. In any case, these effects exposed the fact that a material structure, generally termed *cavity*, could alter the interaction between light and material emitters (see figs. 1.1a and 1.1b). In doing so, they also foreshadowed what the motto of cavity QED would later become: the properties of matter can be designed by suitably engineering its EM environment.

After the two foundational predictions, a first wave of theoretical and experimental articles were published throughout the 1970s and 1980s [18–23]. These works described decay rate modulation in different platforms and geometries. Similarly, an in-depth study of the energy shifts took place in the 1990s [24–28]. It became clear that a new knob to manipulate matter had been mastered, which forms the foundation of techniques as relevant as atomic force microscopy [29]. However, despite the great success, these studies were limited to the realm of perturbative light-matter physics. Indeed, the light-matter interaction strength had been increased compared to atoms in free space, but it was still weak enough that they could be conceived as two separate entities interacting with each other. Nevertheless, physicists could now envision reaching the so-called strong coupling (SC) regime with the improved experimental capabilities that were being developed.

In the SC regime, the atom-cavity coupling strength g is larger than the decay rate of either component. This hierarchy allows for coherent *energy exchange* between the atom and the cavity, whereby an atom emits a photon into the cavity and reabsorbs it later on as the system undergoes Rabi oscillations. The atom-cavity system is then most naturally described in terms of *polaritons*, mixed light-matter excitations. It is no longer adequate to think of the system as two independent subsystems with minor corrections, but instead a holistic atom-cavity treatment is required. Clear signatures of SC physics were ob-

Rabi oscillations, named after Isidor Isaac Rabi, describe the behavior of a quantum system due an interaction comparable to its emission rates.

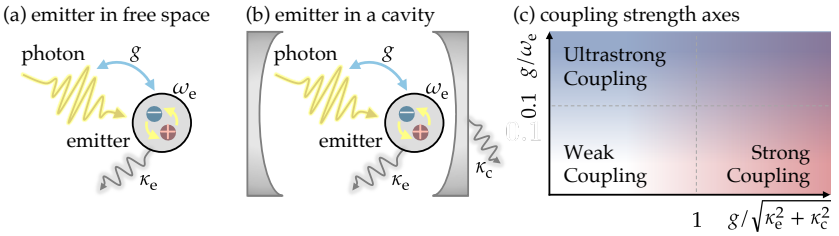

Figure 1.1: Simple illustrative sketches of the relevant parameters which determine the coupling regime: the light-matter coupling strength, g, the excitation energy scale, $\hbar\omega_e$, the emitter's free-space decay rate, κ_e and the cavity's losses κ_c. (a) Small quantum emitter weakly interacting with the EM environment. (b) Schematics of a cavity enhancing the light-matter coupling. (c) Landscape of coupling regimes depending on the ratios $\frac{g}{\sqrt{\kappa_e^2+\kappa_c^2}}$ and $\frac{g}{\omega_e}$ (USC).

served in the second half of the 1980s with the experimental configuration that became known as the micromaser, where the cavity field is inferred from the atomic state after traversing the cavity [30]. Among other effects, Rabi oscillations [31] and trapping field states [32] were measured with the micromaser. From the 1990s onwards, experiments with optical cavities, in which the properties of the atoms were deduced from the photons leaked from the cavity, also revealed SC phenomena. For instance, the spectrum of the cavity's output light developed a double peak structure marking the new polaritonic resonances when an atom was in the cavity [33–35], and Rabi oscillations were directly observed too [36]. These developments soon gave rise to all kinds of studies exploring different aspects such as real time atom counting through the instantaneous cavity spectrum [37, 38], single atom trapping in the cavity [39, 40] or on-demand single photon emission [41, 42]. Since then, the study of strongly coupled light-matter systems has birthed several subfields concerned with modifying material properties with cavities in different contexts, such as in chemistry [43], condensed matter [44], lasers [45] or even quantum information processing [46].

Strong coupling and, perhaps to a lesser extent, weak coupling are routinely featured in current works addressing light-matter interactions. However, theoretical and experimental progress has begun to write the next chapter, dealing with the ultrastrong coupling (USC) regime [47, 48]. A system is said to be *ultrastrongly* coupled when g becomes comparable to the bare excitation frequency ω_e of the individual constituents. By convention, its onset is defined as $\eta_{\text{USC}} = \frac{g}{\omega_e} \simeq 0.1$, but it should be kept in mind that USC effects appear continuously as g increases. Something to notice is that the SC and USC criteria compare the coupling with completely different system parameters.

Accordingly, even though the first SC experiments remained at $\eta_{\mathrm{USC}} \ll 0.1$, the USC regime it not simply a continuation of the coupling strength axis beyond SC, but rather a new axis altogether, as illustrated in fig. 1.1c. In simple, yet technical, terms, this regime is defined by the breakdown of the rotating wave approximation (RWA), which neglects the so-called *counter-rotating* part of the light-matter Hamiltonian. Such a contribution involves processes that do not preserve the number of excitations measured using the corresponding observables of the uncoupled systems. Naturally, then, the most direct consequence of the USC regime is that the light-matter system's joint states are combinations of the individual states, without a well-defined number of excitations. For instance, the joint ground state contains individual states with both material and photonic excitations, despite its being the lowest energy state of the coupled system. This feature is the hallmark of USC physics, and any potential application is traceable back to it somehow.

Any linear account of history is doomed to be incomplete. To be more precise, we note that some aspects of the USC regime had already been discussed since the 1960s in early studies focusing on the Bloch-Siegert shift, an effect beyond the RWA [49–51].

In the context of cavity QED, it was realized during the early 2000s that the USC regime could be reached by inserting semiconductor quantum wells as the matter component in the cavity. In these solid-state systems, the coupling between the transitions between certain states of its band structure and the electromagnetic field is naturally much stronger than in atoms or molecules, due to collective effects. Building upon previous work on intersubband transitions, a concrete theoretical proposal to reach the USC regime was published in 2005 [52], which was soon followed by experimental demonstrations [53, 54]. Those initial works gave way to an increasing stream of articles exploring different aspects of the USC regime. From the theoretical side, concrete characterizations and promising applications were proposed [55–57]. Experimentally, new platforms started to be investigated, including molecular ensembles collectively coupled to a cavity mode [58, 59], adding chemistry to the mix of fields where the USC regime may play a role [60–63]. In any case, it became apparent that creating ultrastrongly coupled light-matter systems with traditional cavity QED techniques and systems was challenging. In this context, circuit QED emerged as a natural playground for these effects. Indeed, it had been shown that the elements of a cavity QED setup had direct analogs in superconducting circuits [64–66]. Together with the naturally large relative coupling strengths, the direct mapping between cavity and circuit QED enabled a joint theoretical and experimental effort that translated into numerous studies with superconducting circuits probing physics beyond the RWA [67–71]. We finish this simplified account of cavity QED by noting that the so-called deep strong coupling regime, defined by $\eta_{\mathrm{DSC}} = \frac{g}{\omega_{\mathrm{e}}} > 1$, has also been studied and observed with superconducting circuits [72, 73], revealing its own

phenomenological signatures.

All in all, the above historical notes point out cavity QED as a highly relevant field of research in light-matter interactions, a field that has reshaped our conception of what a light-matter system can look like or how it can behave. In the process, it has delivered on its promise to manipulate matter with a suitably engineered EM environment and unveiled a vast landscape of interaction strengths with distinct features. In the last 70 years, cavity QED has grown to the point that it now significantly overlaps with many other branches of physics, such as superconducting circuits, quantum information, or nanophotonics. Some of these connections will be explored further in the next chapters of this thesis.

1.1.3 Observing the light: quantum optics

As the name indicates, quantum optics (QO) is the study of light embracing its quantum nature, taken to its ultimate consequences. Accordingly, it is a natural step from the development of QED, just like cavity QED, and is inevitably intertwined with the latter. The difference, then, lies more so on the focus than on the actual formalism or experimental implementations. The birth of QO is usually credited to the Hanbury Brown and Twiss intensity interferometer experiment in 1956 [74]. However, a semiclassical explanation by Purcell [75] was very soon available. The ability of semiclassical explanations to account for this and other phenomena cast a shadow of uncertainty over the scientific community regarding the existence and nature of photons or, equivalently, the "quantumness" of light.

The photoelectric effect, for instance, had also been given a semiclassical interpretation (see, e.g., Chapter 9 of [76]).

In this context, two key realizations led Roy Glauber to develop a full theory of quantum optical coherence and correlations in a series of works published in 1963 [77–79]. The first one was that the success of semiclassical treatments could be attributed to "the fact that optical experiments to date [had] paid very little attention to individual photons" [78]. The second involved the vastly superior phenomenological richness in the quantum states of light compared with their classical counterparts. Glauber's work expanded the classical notion of optical coherence, now absorbed in its quantum version, and then built photon correlators around it. These foundational quantities remain a centerpiece of modern QO studies to this day.

We must also acknowledge E. C. G. Sudarshan's work here [80], who independently developed QO tools related to the representation of arbitrary states of light in terms of coherent states, in line with Glauber's formal manipulations.

Remarkably, the new framework not only provided a completely quantum-mechanical description of the Hanbury Brown-Twiss effect, but it was also well-suited to account for numerous effects completely out of reach for semiclassical theories. Some of these effects include the antibunched detection of

photons [81] or the collapse and revival of Rabi oscillations in cavity QED-like scenarios [31, 82]. It was also realized that the process of spontaneous parametric downconversion, in which a photon enters a non-linear crystal and splits into two new, less energetic photons [83], was a fantastic tool to observe many genuinely quantum phenomena. Indeed, it was used to generate single-photon states in 1986 [84], to probe two-photon interference effects with the Hong-Ou-Mandel experiment in 1987 [85], to study squeezed states of light [86], and to produce polarization-entangled photon pairs [87].

The great control achieved over QO set-ups allowed it to seep into many other areas of research over the years. Some examples include the foundations of physics, with numerous photon-based tests of Bell's inequalities [87, 88], the implementation of quantum information protocols, including quantum cryptography and quantum computation [89–94], and the successful detection of gravitational waves with squeezed light [95, 96]. We finish this summarized account of QO by noting that, like cavity QED, it is an extremely fruitful field. Indeed, the distinction between the two is, in many ways, arbitrary. Current topics under their umbrella include the previously mentioned quantum information processing, quantum non-linear optics [97], sensing and metrology, among many others. All these varied and active research lines have been directly spurred by the development of QO; as Glauber succinctly put it, "[t]here is ultimately no substitute for the quantum theory in describing quanta" [77].

1.2 Light and matter today and tomorrow

We now turn our attention to the current scientific trends and debates in the field of light-matter interactions. Perhaps the most exciting lines or research are those concerned with finding either novel technological solutions or new ways to probe intrinsically quantum features of nature in unexplored regimes. At the same time, the new developments have expanded our view of the field and, on occasion, raised reasonable doubts regarding the validity and meaning of fundamental descriptions and simplified models alike. This section is structured along those lines, with a first part devoted to quantum technologies in a broad sense, and a second part dedicated to more fundamental questions. Note that the following paragraphs inevitably contain a simplified and biased view of the latest research in light and matter. Many more concrete ideas are being tested and developed in laboratories, blackboards and computers all over the world. Doing justice to this global endeavor would require a much longer exposition. Still, even this simplified perspective should show how rel-

evant the interaction between light and matter is today, and hint at what kind of role it can play tomorrow.

Quantum technologies Broadly speaking, the development of quantum mechanics has brought with it new physical possibilities in processing and extracting (quantum) information. The promises behind the term "quantum technologies" typically involve using these new possibilities to find novel technological solutions to certain problems. In this context, light and matter come into play as the physical elements that are supposed to implement any of these solutions in practice. We now take a quick glance over some future technological implications of quantum science.

The first one that we must mention here is the field of *quantum computing*. The earliest ideas of what a quantum computer should be or do have been around since the 1980s [98, 99]. Over the last few years, however, quantum computers have made headlines and attracted the public's attention like almost no technology before. The reason for such an uptick has been the recent advance in experimental capabilities, which have sparked a frenzy of theoretical and experimental activity, both in academic circles and private enterprises. There are two main approaches to quantum computing. On one hand, we have the more straightforward application of these devices to solve mathematical problems by running quantum algorithms [100]. On the other, a quantum computer can, in principle, be used to "digitally" simulate another quantum system in a controlled way [101].

In the realm of digital quantum computation, interesting quantum algorithms have been known for about 30 years [102], but these algorithms must be run on some device. As mentioned before, this is where light and matter come into the picture; after all, the fundamental information-processing units, the qubits, need a physical implementation. There are many promising candidate systems that rely on different effects and, thus, come with unique advantages and disadvantages. Some noteworthy qubit implementations in matter include cold atoms [103, 104], trapped ions [105], quantum dots [106, 107], superconducting circuits [108, 109] and hybrid systems [110]. These physical systems are generally manipulated through some combination of electric and magnetic fields, which can be used to move atoms around [111–113] or tune the qubit's properties and interactions [114]. Another strong platform are integrated photonic circuits, where single photons propagate through some engineered dielectric material and carry quantum information in, e.g., their polarization [115, 116].

Regarding the use of general-purpose quantum computers to digitally

simulate systems by running particular algorithms, we note that the picture would not be complete without mentioning the parallel research line of "analog" quantum simulators [117]. The idea is to build a setup of controllable and tunable elements that replicates some inaccessible many-body target properties. Analog quantum simulators have been available for some years now with different implementations, and have proven useful to probe condensed matter physics [118], quantum chaos [119], out-of-equilibrium dynamics [120] and many other examples. Quite recently, new analog simulation ideas have been proposed for chemistry [121] or elementary particle interactions [122, 123].

Quantum computing and simulation, in their many flavors, are far from the only technological promises brought forth by quantum mechanics. Further notable avenues are the fields of *quantum metrology* and *quantum sensing*. The ultimate goal of research in these directions is to estimate or measure unknown parameters of an interesting system, in a way that generates a precision advantage compared with classical parameter estimation protocols through quantum mechanics. Light-matter interactions play a main role in this field, as one can extract information of some material system by coupling it to quantum states of light [116, 124]. Different implementations of this core concept have been proposed as of late [125–128].

The last line that we highlight here involves the *quantum communication* protocols that benefit from the quantum properties of light to communicate information. The main examples of quantum communication are the mechanisms that use photons to produce and share a cryptographic key, usually referred to as quantum key distribution protocols. Research on this topic has been going on for some time [129], but there are still new results and improvements being published today [130, 131].

A final relevant comment is that, for most of the ideas described above, only after thorough research in "basic science" have these entered the realm of possibility. As a single example that relates to the previous section, the strong and ultrastrong light-matter coupling regimes, which emerged as part of fundamental research, are nowadays being considered as a way to implement quantum information protocols such as the ones just overviewed [132–135]. This shows that basic research does, indeed, provide extrinsic value to society. In the next part, however, we shift our focus to the more intrinsic value of basic science in pushing the limits of our knowledge.

Frontiers of physics Science can be seen as a highly complex network of knowledge and practices to acquire more of it. Certain parts of the network are commonly regarded as "fundamental" knowledge, which shape and ce-

ment the layers stacked above. Nevertheless, science is not restricted to such "vertical" imprints. In reality, there is an equally important horizontal transmission of influence, whereby established fundamental scientific knowledge powers fundamental research in a neighboring area. In these respects, the field of light-matter interactions is a prime example, as we discuss in the following.

The first main field that we will mention here is that of *macroscopic quantum superpositions*, an effort to bring quantum-mechanical effects out of the microscopic scale to which they are typically confined. This has been a long-time quest in quantum science [136, 137], but the ever-increasing progress in experimental capabilities has yielded new avenues to test these limits. One such approach is levitodynamics, in which a relatively large particle is optically levitated as a means to effectively isolate it [138–140]. The high degree of control achieved with these setups offers the possibility to test the quantum nature of the particle's motional degrees of freedom. Another idea involves the use of cavity quantum acoustodynamics, where a mechanical resonator is controlled through superconducting quantum circuits [141]. Both these avenues harness light-matter interactions to probe the limits of quantum mechanics.

Levitating objects have long captivated the imagination of scientists, particularly so for IgNobel and Nobel laureate Andre Geim, who had a penchant for magnetically levitating frogs.

The next way in which light-matter interactions have seeped in into other adjacent areas is under the term *polariton*. Polaritons represent the hybrid excitations that arise from light-matter interactions, and have populated the literature ever since the SC regime was realized. Nowadays, they are explored in countless ways to both improve our understanding of fundamental principles and test new pathways for physical processes. Among other topics, we have polaritonic chemistry [43, 142–147], with the goal of modifying reaction rates by inserting the reactants in a cavity and the ensuing light-matter hybridization. Polaritons are also used to explore lasing physics [148] and Bose-Einstein condensation [149–151].

Thus far, we have described some examples in which fundamental knowledge of light-matter interactions is horizontally transferred. Still, it can be argued that these instances correspond to "first-neighbors" interactions, as the fields are, indeed, close to each other. There is, however, a remarkable illustration of the potentially long-ranged nature of scientific horizontal transfer, namely, the relevance of light-matter interactions in the study of *gravitational waves* [95, 96]. Indeed, gravitational wave detectors work due to the interaction between EM radiation and the oscillatory motion of the cavity mirrors through radiation pressure. This kind of setting is the object of study of *cavity optomechanics* [152, 153]. Moreover, the sensitivity of the detectors was crucially enhanced by using a particular kind of light states known as squeezed

states [95, 154]. Gravitational wave research has not been the only interesting byproduct of cavity optomechanics. In fact, it has opened several other opportunities, including the preparation of non-classical states of both the cavity modes and the mirrors [155–158], the study of properties of quantum non-linear and chaotic systems [159–161], or their interplay with other components [162]. More recently, the field has expanded to study the interaction between light and molecular oscillations too [163, 164].

We finish here with an example that illustrates how fundamental research on a well-established field, such as the one of light-matter interactions, can still be very active nowadays. As was mentioned in section 1.1.2, the experimental achievement of the *ultrastrong coupling regime* took the field by storm. A specific consequence for theorists was that extremely widespread models became inadequate (see section 5.1.1 for a more detailed discussion). For instance, the ways in which dissipative phenomena were dealt with in the SC regime are no longer valid in the USC regime. Essentially, out of the USC regime, it is enough to account for the dissipation of the individual components of the system, light and matter, separately. This is no longer the case for the USC regime, and there have been several theoretical proposals to correct it [165–167]. Another theoretical debate sparked by the USC regime concerned how gauge transformations and various common subsequent approximations could yield incorrect results [168–171]. This also happened to occur at a particularly tense time, soon after the validity of the multipolar coupling picture, one of the theoretical cornerstones of light-matter interactions, had been called into question [172], even if those claims had been refuted [173, 174]. A final theoretical aspect that has been the topic of some debate is the role of the longitudinal and transverse EM fields in achieving the USC regime. Ever since some studies reported or simulated USC physics at the single-molecule level [175, 176], there have been two schools of thought regarding the correct modeling of these systems. On one hand, there are researchers who implicitly argue that the transverse EM fields are the dominating mechanism, which has some implications regarding the terms that appear in the Hamiltonian [177, 178]. On the other, some physicists have pointed out that the length scales involved in these experiments call for a purely electrostatic description in terms of longitudinal fields [179–181]. Addressing this debate will be a central issue of chapter 5.

Something common to sections 1.1 and 1.2 is that they are meant to reflect the sheer scope of the field of light-matter interactions. In section 1.1, this is achieved by putting the focus on rather general aspects of the history of quantum light-matter interactions as a whole. Next, we have provided here an overview of the current state of research in this area, covering very disparate

topics, but not mentioning many others. Thus, we have tried to emphasize the depth and breadth of the field of light-matter interactions. Such an approach was deliberately chosen to build the subtext through which the rest of the manuscript plays out. Indeed, the rest of the tesis deals with ideas that lie scattered on the frontiers of research in the interaction between light and matter. With sections 1.1 and 1.2 we have set the stage for the next chapters, and finish this introductory chapter with section 1.3, where we present the main topics that will be covered in the following.

1.3 Light and matter in this thesis

In the work that forms the basis of the next chapters, we have studied several concrete aspects of the coupling between light and matter, across different coupling regimes, and for different purposes. Such a scattered approach offers a distinct perspective on the breadth and diversity of phenomena that emerge from the same basic foundations. For that reason, the introduction has, up to this point, focused on rather general aspects of light-matter interactions, as a way to prepare the broad ground for the rest of thesis. A consequence is, however, that no one topic within this large field truly stands out, which has forced us to settle for a more superficial account of some details in the previous sections. In contrast, the following paragraphs introduce in some depth the contents that will be treated in the next chapters.

We continue the discussion with a relatively self-contained theoretical background in chapter 2. There, we review the essential aspects of QED, paying particularly close attention to its equivalent formulations and the role of physical quantities and operators in them. We continue with a theoretical extension that allows for the direct inclusion of macroscopic bodies such as cavities or nanoparticles into the problem. Next, we revisit concepts regarding atomic physics, pertinent to the rest of the thesis, with a specific focus on the hydrogen atom for both illustration and future reference. Finally, we end the chapter by framing light-matter interactions as an open quantum system, where the EM field generally acts as a reservoir with infinitely many degrees of freedom that dissipates excitations initially localized in the matter system. This whole chapter follows fairly standard derivations for the most part, but it also includes many remarks and digressions highlighting certain aspects that proved relevant to reach the conclusions of the next chapters.

After setting up the context and theoretical foundations in chapters 1 and 2, the next three chapters are devoted to the results extracted from the

research activities that have culminated in this thesis. First, chapter 3 delves into methodological aspects of the framework of open quantum systems. This formalism is perhaps best-known for the so-called master equations, each of which possesses different mathematical properties and underlying physical assumptions. From the mathematical point of view, the Lindblad master equation is the most desirable one. However, for the equation to be meaningful, it must be related to some detailed model of the system-environment interaction. To that end, the standard procedure reaches first the so-called Bloch-Redfield equation, which, unfortunately, is not a Lindblad equation. There is a common additional procedure that is guaranteed to turn the Bloch-Redfield equation into a Lindblad equation: the secular approximation. The problem is that the conditions under which this step is adequate are quite restrictive as soon as one considers somewhat realistic system models. In this chapter we devise an alternative to the secular approximation that does not sacrifice any physical effect while producing a Lindblad master equation in all cases.

In chapter 4, we take advantage of the master equation developed in the previous chapter and apply it to accurately describe the internal dynamics of a hydrogen atom placed in the vicinity of a dielectric nanoparticle. From the atom's weak coupling to the nanoparticle-modified EM vacuum, we straightforwardly recover the well-known expressions for the Purcell enhancement of the decay rates and the Casimir-Polder energy shifts induced by the nanoparticle. However, we also obtain additional terms that effectively couple different atomic states, both coherently and incoherently. These off-diagonal shifts and decay rates induce large state mixing between the original eigenstates of the hydrogen atom, with clear spectroscopic signatures such as avoided crossings between the energy levels as the atom approaches the nanoparticle. A particularly striking effect that we noticed was that, under the right circumstances, the Purcell enhancement of decay rates could actually be reversed within certain ranges of atom-nanoparticle separation. Then, the closer the atom gets to the nanoparticle, the darker some states become, in complete opposition to the naive expectation based on the EM local density of states alone.

We finally turn our attention to the USC regime in chapter 5. In this part, we address an important debate concerning the role of longitudinal and transverse EM fields in single-emitter USC. The key intuition is that the subwavelength confinement required to reach USC implies that transverse fields, i.e., propagating photons, are negligible, with the full weight of the mechanism being due to longitudinal fields, i.e., charge-charge Coulomb interactions. Concretely, we combine different notions from electromagnetic theory to reach the conclusion that the coupling between small emitters and photons is fundamen-

tally limited, regardless of the kind of structure or cavity used to herd the photons and force them to interact with the emitter. When applying this bound to the USC, we find that photons actually play no role at all in single-emitter USC, with further corollaries discussed in the chapter. We follow this general argument with an illustration of the claims solving an analytical model of a plasmonic nanoparticle and an atom, where the magnitudes of charge-photon and charge-charge interactions are easily separable.

To avoid lengthy calculations that disrupt the narrative thread of each chapter, we supplement them with appendices at the end of the manuscript that contain these details. Still, we include enough of the key ideas or steps in the chapters to avoid sacrificing rigor and vagueness in the exposition. Also, we finish each chapter with some particular conclusions regarding its specific discussion. Last, we close the thesis with some general conclusions in chapter 6 about the research results presented here and their place in the vast landscape of light-matter interactions.

Chapter Two | Theoretical prerequisites

> [Theory], like whiskey, loses its beneficial effect when taken in too large quantities.
>
> *Adapted from Edward Plunkett*

Chapter summary We devote this chapter to setting up the theoretical building blocks on which the next parts of the thesis rest. We begin with an overview of non-relativistic QED, sometimes referred to as molecular QED, in section 2.1. This part is written in a way that prioritizes the aspects of the theory that play an important and direct role on the rest of the thesis, while attempting to be relatively self-contained. Next, we continue in section 2.2 with a consistent extension of QED that accounts for the presence of large bodies through their macroscopic response functions, namely, macroscopic quantum electrodynamics (MQED). After discussing field-theoretical ideas of electrodynamics in various limits, we turn our focus into the charges that comprise atoms, molecules or, more generally, quantum emitters. In section 2.3, we study the hydrogen atom in detail, as well as the corrections to the non-relativistic model arising from relativistic effects and from its interaction with external EM fields. Last, we revisit the formalism of open quantum system (OQS) in section 2.4, which emerges naturally as a tool to deal with the EM field's complexity, insofar as the full light-matter system can be split in an interesting subsystem coupled to an environment.

2.1 QED: A theory of photons and atoms

We outline here the basic theoretical concepts underlying the interaction between light and matter, in the non-relativistic limit that is convenient to treat atoms or molecules [12, 14]. To that end, we start with Maxwell's equations

in their modern form

$$\nabla \cdot \mathbf{E} = \frac{1}{\varepsilon_0}\rho, \tag{2.1a}$$

$$\nabla \cdot \mathbf{B} = \mathbf{0}, \tag{2.1b}$$

$$\nabla \times \mathbf{E} = -\dot{\mathbf{B}} \quad \text{and} \tag{2.1c}$$

$$\nabla \times \mathbf{B} = \mu_0 \mathbf{j} + \frac{1}{c^2}\dot{\mathbf{E}}. \tag{2.1d}$$

Here, $\mathbf{E}$ and $\mathbf{B}$ are the electric and magnetic vector fields, ε_0 and μ_0 are the vacuum electric permittivity and magnetic permeability constants, $c = (\varepsilon_0 \mu_0)^{-1/2}$ is the speed of light, and $\mathbf{j}$ and ρ are vector and scalar fields that represent the electric current and charge densities that act as sources and describe the matter interacting with the EM field. We will drop the explicit space and time dependence $(\mathbf{r}, t)$ if it can be omitted without creating some kind of inconsistency and without hindering understanding. For a system of point charges q_i at positions $\mathbf{r}_i$ and with velocities $\dot{\mathbf{r}}_i$, these variables are

$$\rho(\mathbf{r}, t) = \sum_i q_i \, \delta^{(3)}[\mathbf{r} - \mathbf{r}_i(t)] \quad \text{and} \tag{2.2a}$$

$$\mathbf{j}(\mathbf{r}, t) = \sum_i q_i \dot{\mathbf{r}}_i(t) \, \delta^{(3)}[\mathbf{r} - \mathbf{r}_i(t)]. \tag{2.2b}$$

The current and charge density are, additionally, related through a continuity equation that represents local charge conservation and can be derived by combining eqs. (2.1a) and (2.1d):

$$\nabla \cdot \mathbf{j} + \dot{\rho} = 0. \tag{2.3}$$

These equations are complemented by the Lorentz force density,

$$\mathbf{f} = \rho \mathbf{E} + \mathbf{j} \times \mathbf{B}, \tag{2.4}$$

exerted by the fields on charged matter. With these five coupled differential equations, one can, in principle, account for any and all phenomena involving light and matter. This assertion, accurate as it may be, fails to provide much intuition. Thus, we develop in the following the ideas behind these equations and the quantum nature of the players involved in greater detail.

2.1.1 CANONICAL APPROACH TO QED

We begin by noting that the EM fields can be conveniently described in terms of a scalar and vector potential, ϕ and $\mathbf{A}$, respectively, such that

$$\mathbf{E} = -\dot{\mathbf{A}} - \nabla\phi \quad \text{and} \tag{2.5a}$$

$$\mathbf{B} = \nabla \times \mathbf{A}. \tag{2.5b}$$

The introduction of the potentials has certain advantages concerning the canonical formulation of QED and, as innocent as it seems, actually brings with it one major consequence. To illustrate it, let us engage in a simple counting exercise. For some given sources $\mathbf{j}$ and ρ, the EM fields naively seem to require the specification of 6 spatial components. However, eqs. (2.1a) and (2.1b) only involve spatial derivatives and, if the fields satisfy them at a given time t, eqs. (2.1c), (2.1d), (2.3) and (2.4) ensure that they will remain true. Hence, the divergence equations are to be understood as constraints that the fields must observe. This fact, together with the boundary condition that fields vanish at infinity, implies that, actually, only four specified components are needed, related to each other through first order differential equations. Incidentally, the components that have been successfully accounted for by the constraints are usually known as longitudinal, and physically correspond to the Coulomb electric field produced by charges and the absence of the magnetic monopolar sources. The canonical approach to electrodynamics with the potentials treats them, in principle, as independent degrees of freedom to which one associates a canonical momentum starting from a Lagrangian. That would leave us with a total of eight components that satisfy first order differential equations, that is, Hamilton's equations. Those are twice as many components as before. This is, however, not a problem, but rather a manifestation of one of the deepest notions in physics that has firmly shaped much of the field-theoretical progress since the 1950s: *gauge invariance*.

There are many sides to gauge invariance, but its simplest interpretation is the statement that for any given $\mathbf{E}$ and $\mathbf{B}$ satisfying eqs. (2.1a) to (2.1d), there is no unique choice of ϕ and $\mathbf{A}$ that reproduces the EM fields. Indeed, once a valid instance of potentials is found, it turns out that

$$\phi' = \phi - \dot{\chi} \quad \text{and} \tag{2.6a}$$

$$\mathbf{A}' = \mathbf{A} + \nabla\chi \tag{2.6b}$$

also give rise to the same $\mathbf{E}$ and $\mathbf{B}$, for any arbitrary gauge function χ. An immediate conclusion is that there is some redundancy in the potentials, usually

Another key realization is that, even if all gauges are equivalent, the mathematics might look particularly simple with a given choice, which renders different gauges effectively not equivalent for whoever is in charge of the calculations.

dealt with by fixing a particular gauge. The most common choice in the low energy regime is the so-called Coulomb gauge, where $\nabla \cdot \mathbf{A} = 0$ and ϕ is the electrostatic Coulomb potential.

Once the main protagonists of QED have been introduced, we are ready to discuss the details regarding their quantum nature. To do so, we follow the canonical quantization approach, and note that Maxwell's equations in eq. (2.8) are, in fact, the equations of motion of a Lagrangian, namely,

$$L = \sum_i \frac{m_i \dot{\mathbf{r}}_i^2}{2} + \int \mathrm{d}^3 r \left[\mathbf{j} \cdot \mathbf{A} - \rho\phi\right] + \frac{\varepsilon_0}{2} \int \mathrm{d}^3 r \left[\left(\dot{\mathbf{A}} + \nabla\phi\right)^2 - c^2 (\nabla \times \mathbf{A})^2\right]. \tag{2.7}$$

The introduction of the potentials renders eqs. (2.1b) and (2.1c) tautological by construction, and the equations of motion are reduced to

$$\nabla^2 \phi = -\frac{1}{\varepsilon_0}\rho - \nabla \cdot \dot{\mathbf{A}} \quad \text{and} \tag{2.8a}$$

$$\frac{1}{c^2}\ddot{\mathbf{A}} - \nabla^2 \mathbf{A} = \frac{1}{\varepsilon_0 c^2}\mathbf{j} - \nabla\left(\nabla \cdot \mathbf{A} + \frac{1}{c^2}\dot{\phi}\right). \tag{2.8b}$$

In order to canonically quantize this theory, we need to find pairs of conjugate variables. However, the gauge redundancy present in the potentials makes this otherwise straightforward procedure much more involved. A first possibility is to follow Dirac's quantization program for constrained systems. Indeed, eq. (2.7) corresponds to a constrained system because, for instance, ϕ's canonical momentum is zero. This observation, however, leads to the other possible approach: fix the gauge first to remove redundant variables and, retaining only the *true dynamical variables*, quantize the remaining unconstrained system. We choose here the second option for simplicity, implemented by working in the Coulomb gauge.

Dynamical variables in the Coulomb gauge: Transverse and longitudinal vector fields

As elaborated upon in appendix A.3, the defining condition of the Coulomb gauge, $\nabla \cdot \mathbf{A} = 0$, can be equivalently seen as projecting $\mathbf{A}$ into the space of transverse (divergence-free) vector fields. In reciprocal space, this means that the vector potential at $\mathbf{k}$ has only 2 available polarizations: the orthogonal directions to $\mathbf{k}$. Accordingly, the Coulomb vector potential $\mathbf{A}_\mathrm{C}$ is equal to the transverse vector potential $\mathbf{A}^\perp$. Note that there is no gauge ambiguity left,

as the gauge transformations in eq. (2.6b) only affect its longitudinal part $\mathbf{A}^{\parallel}$ and, as per Helmholtz's theorem, the decomposition $\mathbf{A} = \mathbf{A}^{\perp} + \mathbf{A}^{\parallel}$ is unique. In other words, $\mathbf{A}^{\perp}$ is a gauge-invariant quantity, hence we generally write it without the C subscript. As for the scalar potential, the transversality of $\mathbf{A}$ transforms eq. (2.8a) into the Poisson equation for electrostatics, whose inhomogeneous solution is:

$$\nabla^2 \phi_{\mathrm{C}} = -\frac{\rho}{\varepsilon_0} \implies \phi_{\mathrm{C}} = \int \mathrm{d}^3 r' \, \frac{\rho(\mathbf{r}')}{4\pi\varepsilon_0 |\mathbf{r}' - \mathbf{r}|} = \sum_i \frac{q_i}{4\pi\varepsilon_0 |\mathbf{r}_i - \mathbf{r}|}. \tag{2.9}$$

Therefore, ϕ_{C} is also completely determined as long as the fields go to zero when $|\mathbf{r}| \to \infty$ [182]. In fact, eq. (2.9) relates ϕ_{C} to the charges' coordinates $\mathbf{r}_i$. Accordingly, the scalar potential is, in the Coulomb gauge, not a dynamical variable at all; instead, it is a function of the other true dynamical variables.

By setting $\mathbf{A}^{\parallel}_{\mathrm{C}} = \mathbf{0}$, the (gauge-invariant) longitudinal and transverse EM fields are related to the Coulomb potentials through

$$\mathbf{E}^{\parallel} = -\nabla \phi_{\mathrm{C}}, \qquad \mathbf{E}^{\perp} = -\dot{\mathbf{A}}_{\mathrm{C}} = -\dot{\mathbf{A}}^{\perp} \quad \text{and} \tag{2.10a}$$

$$\mathbf{B}^{\parallel} = \mathbf{0}, \qquad \mathbf{B}^{\perp} = -\nabla \times \mathbf{A}_{\mathrm{C}} = -\nabla \times \mathbf{A}^{\perp}, \tag{2.10b}$$

such that the physical separation between longitudinal and transverse fields is faithfully present in the potentials as well. Another advantage of the Coulomb gauge is that, for a given ρ, only four numbers are needed to specify the state of the fields at any point, (three components for $\mathbf{A}^{\perp}$ and $\dot{\mathbf{A}}^{\perp}$, minus two restrictions $\nabla \cdot \mathbf{A}^{\perp} = \nabla \cdot \dot{\mathbf{A}}^{\perp} = 0$), and thus no redundancy is left. Therefore, $\mathbf{A}^{\perp}$ is the appropriate generalized coordinate of the field.

TIME TO QUANTIZE: MINIMAL COUPLING HAMILTONIAN IN THE COULOMB GAUGE AND COMMUTATION RELATIONS

Once convenient field coordinates have been found, we can calculate their canonical momenta and switch to the Hamiltonian formalism, where quantization is more direct. Choosing the Coulomb gauge the Lagrangian is, then,

$$\begin{aligned} L = &\sum_i \frac{m_i \dot{\mathbf{r}}_i^2}{2} - \sum_{i \neq j} \frac{q_i q_j}{8\pi\varepsilon_0 |\mathbf{r}_i - \mathbf{r}_j|} \\ &+ \frac{\varepsilon_0}{2} \int \mathrm{d}^3 r \left[\left(\dot{\mathbf{A}}^{\perp}\right)^2 - c^2 \left(\nabla \times \mathbf{A}^{\perp}\right)^2 \right] + \int \mathrm{d}^3 r \, \mathbf{j} \cdot \mathbf{A}^{\perp}, \end{aligned} \tag{2.11}$$

where the divergent, but constant, Coulomb self-energy of the point charges has been discarded. Note that, even if the Coulomb gauge has been fixed,

every quantity in eq. (2.11) is manifestly gauge invariant. Thus, in a way, taking eq. (2.11) as starting point for QED has more to do with equivalent Lagrangians, than with gauge fixing. More specifically, eq. (2.11) can be obtained from eq. (2.7) by adding a total temporal derivative of the form $\frac{\mathrm{d}}{\mathrm{d}t}\int \mathrm{d}^3 r\, \rho f$, which is known to preserve the equations of motion. If the function f is suitably chosen, the Lagrangian can be stripped from the redundancies of $\mathbf{A}^{\parallel}$ and ϕ completely, such that only the dynamical variable $\mathbf{A}^{\perp}$ and gauge-invariant $\mathbf{E}^{\parallel}$ appear. That does not mean that we have actually changed what we call $\mathbf{A}$, it only makes explicit the practical choice of $\mathbf{A}^{\perp}$ as canonical field variable. It just so happens that $\mathbf{A}^{\perp} = \mathbf{A}_{\mathrm{C}}$, and thus eq. (2.11) can also be seen as choosing the Coulomb gauge in eq. (2.7).[1] Regardless of how one prefers to think about it, we keep here the usual "Coulomb gauge Lagrangian" nomenclature for eq. (2.11) and proceed without reservations.

From the above Lagrangian, the conjugate canonical momenta of $\mathbf{r}_i$ and $\mathbf{A}^{\perp}$ are

$$\mathbf{p}_i = m_i \dot{\mathbf{r}}_i + q_i \mathbf{A}^{\perp}(\mathbf{r}_i) \quad \text{and} \tag{2.12a}$$

$$\mathbf{\Pi}^{\perp} = \varepsilon_0 \dot{\mathbf{A}}^{\perp} = -\varepsilon_0 \mathbf{E}^{\perp}, \tag{2.12b}$$

respectively, and the corresponding Hamiltonian is

$$H = \sum_i \frac{\left(\mathbf{p}_i - q_i \mathbf{A}^{\perp}(\mathbf{r}_i)\right)^2}{2m_i} + \sum_{i \neq j} \frac{q_i q_j}{8\pi\varepsilon_0 \left|\mathbf{r}_i - \mathbf{r}_j\right|} + \int \mathrm{d}^3 r \left[\frac{\left(\mathbf{\Pi}^{\perp}\right)^2}{2\varepsilon_0} + \frac{\varepsilon_0 c^2}{2} \left(\nabla \times \mathbf{A}^{\perp}\right)^2 \right]. \tag{2.13}$$

The $\mathbf{p}_i - q_i \mathbf{A}^{\perp}(\mathbf{r}_i)$ part in the kinetic part of the Hamiltonian gives it the "minimal coupling" label, because the interaction depends on the charge density only. Now, we can straightforwardly quantize the theory by promoting the positions and momenta to quantum operators satisfying the basic commutation rules

$$\left[\mathbf{r}_i, \mathbf{p}_j\right] = i\hbar \mathbf{1} \delta_{ij} \quad \text{and} \tag{2.14a}$$

$$\left[\mathbf{A}^{\perp}(\mathbf{r}), \mathbf{E}^{\perp}(\mathbf{r}')\right] = -\frac{1}{\varepsilon_0}\left[\mathbf{A}^{\perp}(\mathbf{r}), \mathbf{\Pi}^{\perp}(\mathbf{r}')\right] = -\frac{i\hbar}{\varepsilon_0} \delta^{\perp}(\mathbf{r} - \mathbf{r}'). \tag{2.14b}$$

Here, $\mathbf{1}$ is the identity operator in $\mathbb{R}^3$, and the transverse Dirac delta $\delta^{\perp}$ projects any vector field onto the space of transverse fields (see appendix A.3). It's appearance in the fields' commutation relation is essentially inherited from the

[1] See [173] for a detailed discussion on this admittedly subtle matter.

transverse nature of the physical DOF, and is most clearly understood by quantizing in reciprocal space [14]. We can manipulate eq. (2.13) further to arrive at another very common expression of the Hamiltonian:

$$H = \sum_i \frac{\mathbf{p}_i^2}{2m_i} + \sum_{i\neq j} \frac{q_i q_j}{8\pi\varepsilon_0 |\mathbf{r}_i - \mathbf{r}_j|} + \int \mathrm{d}^3 r \left[\frac{\left(\mathbf{\Pi}^\perp\right)^2}{2\varepsilon_0} + \frac{\varepsilon_0 c^2}{2} \left(\nabla \times \mathbf{A}^\perp\right)^2 \right] - \sum_i \frac{q_i}{m_i} \mathbf{p}_i \cdot \mathbf{A}^\perp(\mathbf{r}_i) + \sum_i \frac{q_i^2}{2m_i} \left(\mathbf{A}^\perp(\mathbf{r}_i)\right)^2, \tag{2.15}$$

where we have obtained an interaction term $\mathbf{p}_i \cdot \mathbf{A}^\perp(\mathbf{r}_i)$ using that $\nabla \cdot \mathbf{A}^\perp = 0$, and the so-called diamagnetic A^2 term.

The above Hamiltonian dictates the temporal evolution of the field and matter operators in the Heisenberg picture according to the familiar

$$\dot{O} = \frac{i}{\hbar}[H, O], \tag{2.16}$$

from which Maxwell's and Lorentz's equations can be retrieved. One detail worth mentioning in this regard is that Ampere's and Lorentz's equations (eqs. (2.1d) and (2.4)) become

Due to the vector product, the symmetrization actually acquires a negative sign: $S[\mathbf{a}\times\mathbf{b}] = (\mathbf{a}\times\mathbf{b} - \mathbf{b}\times\mathbf{a})/2$.

$$\nabla \times \mathbf{B} = \mu_0 S[\mathbf{j}] + \frac{1}{c^2}\dot{\mathbf{E}}$$
$$m_i \ddot{\mathbf{r}}_i = q_i \mathbf{E}(\mathbf{r}_i) + S[\dot{\mathbf{r}}_i \times \mathbf{B}(\mathbf{r}_i)].$$

Here, S is the symmetrization operator defined by $S[a,b] = (ab+ba)/2$, and it comes from the fact that $\dot{\mathbf{r}}_i$ and $\mathbf{r}_i$ do not commute.

2.1.2 EQUIVALENT FORMULATIONS OF QED

In this section, we elaborate upon a fundamental aspect of physical theories, instantiated in electrodynamics, namely, the multiplicity of representations of the same physics. To that end, we start by observing that the charges' canonical momenta $\mathbf{p}_i$ do not coincide with the kinetic momenta $\mathbf{p}_i^{(\mathrm{k})} = m_i \dot{\mathbf{r}}_i$. Instead, these momenta are misaligned by the photonic "position" DOF, that is $\mathbf{A}^\perp$, and it is exactly this misalignment wherein the interaction lies. Indeed, if we did not know any better, we could mistakenly think that the light and matter DOF remain uncoupled in eq. (2.13), since it can be rewritten as

$$H = \sum_i \frac{m_i \dot{\mathbf{r}}_i^2}{2} + \sum_{i\neq j} \frac{q_i q_j}{8\pi\varepsilon_0 |\mathbf{r}_i - \mathbf{r}_j|} + \frac{\varepsilon_0}{2} \int \mathrm{d}^3 r \left[\left(\dot{\mathbf{A}}^\perp\right)^2 + c^2 \left(\nabla \times \mathbf{A}^\perp\right)^2 \right], \tag{2.17}$$

and nothing seems to couple charges and photons. Fortunately, we know better and, from analytical mechanics, we understand that the canonical momentum is the adequate variable to describe the dynamics, rather than the kinetic one. In admitting so, however, the pristine separation between physical DOF and their corresponding canonical dynamical variables is lost. The same distinction is not present in the field, whose canonical and kinetic momenta coincide: $\mathbf{\Pi}^{\perp} = \left(\mathbf{\Pi}^{\perp}\right)^{(\mathrm{k})} = \varepsilon_0 \dot{\mathbf{A}}^{\perp}$.

This situation raises the question of the existence of other choices of canonical momenta where the physical DOF are shared differently between the dynamical variables. The answer, again known from analytical mechanics, is that such multiplicity indeed exists. Gauge transformations, for instance, can be understood in this way. Notably, the family of transformations that take us from one formulation to another is much broader than gauge transformations alone. Here, we briefly review the basic formulation of these ideas, and later on we apply them to find a particularly useful representation of the interaction between light and matter.

We begin by illustrating the multiplicity of descriptions of the same classical dynamics in the simplest possible scenario. Consider a system with a single degree of freedom X and Lagrangian $L\big(X, \dot{X}; t\big)$. It is well-known that equivalent Lagrangians can be obtained by adding the total temporal derivative of a function $F(X;t)$:

$$L'\big(X, \dot{X}; t\big) = L\big(X, \dot{X}; t\big) + \frac{\mathrm{d}}{\mathrm{d}t} F(X;t) = L\big(X, \dot{X}; t\big) + \big(\dot{X}\partial_X + \partial_t\big) F(X;t). \quad (2.18)$$

More specifically, we say that L and L' are equivalent because they yield the same equation of motion for X. The remarkable aspect is that, when moving to the Hamiltonian description required for the canonical quantization procedure, each Lagrangian will produce theory whose main elements, i.e. the canonical conjugate variables and the Hamiltonian, are different. Concretely, L and L' will give rise to unequal canonical momenta P and P', respectively, as well as different Hamiltonians H and H':

$$P\big(X, \dot{X}\big) = \partial_{\dot{X}} L, \quad (2.19a)$$

$$P'\big(X, \dot{X}\big) = \partial_{\dot{X}} L' = P\big(X, \dot{X}\big) + \partial_X F \quad \text{and} \quad (2.19b)$$

$$H'(X, P') = H(X, P) - \dot{F}(X;t), \quad (2.19c)$$

where $H^{(\prime)} = XP^{(\prime)} - L^{(\prime)}$. Then, $\{X, P, H\}$ and $\{X, P', H'\}$ constitute two alternative and equivalent representations of the dynamics through Hamilton's equations.

From the Hamiltonian descriptions, the canonical quanization approach associates a quantum operator to each canonical variable. Thus, we end up with two equivalent quantum formulations, $\mathcal{R}$ and $\mathcal{R}'$, depending on the initial Lagrangian chosen. In $\mathcal{R}$, we represent X and P with $\hat{x}$ and $\hat{p}$, operators that act on wavefunctions through multiplication by x and partial differentiation with respect to x ($-i\hbar\partial_x$), respectively. The evolution of these operators and, therefore, the observables they represent, is determined by $H(\hat{x},\hat{p})$. On the other hand, the situation in $\mathcal{R}'$ is changed. Now, X and P' are replaced by $\hat{x}$ and $\hat{p}$, and the evolution is dictated by $H'(\hat{x},\hat{p})$. What can be an interesting source of confusion is that, in either quantum formulation, P and P' are both replaced by $\hat{p}$. In other words, different canonical momenta (that is, specific combinations of the physical variables X and $\dot{X}$) are replaced by the same exact mathematical operator in their corresponding quantum formulation. Still, the operator $\hat{p}$ evolves differently in $\mathcal{R}$ and $\mathcal{R}'$, a fact that accommodates its different meaning in either formulation. Finally, we note that P and P' are represented in $\mathcal{R}'$ and $\mathcal{R}$ as $\hat{p} - \partial_x F(\hat{x};t)$ and $\hat{p} + \partial_x F(\hat{x};t)$, respectively. See table 2.1 below for a summarized account of these results.

In the following, we discuss the role of unitary transformations in implementing changes of representation at the quantum level directly, and their relation to the canonical transformations of classical mechanics. Then, we will perform a change of representation in QED, from the version described in the previous sections to the so-called multipolar coupling picture.

Table 2.1: Summary of the map between physical quantities and the operators associated to them in quantum formulations $\mathcal{R}$ and $\mathcal{R}'$.

Physical quantity	**Operator in $\mathcal{R}$**	**Operator in $\mathcal{R}'$**
X	$\hat{x}$	$\hat{x}$
P	$\hat{p}$	$\hat{p} - \partial_x F(\hat{x};t)$
P'	$\hat{p} + \partial_x F(\hat{x};t)$	$\hat{p}$

UNITARY TRANSFORMATIONS

It is well-known that unitary transformations play several key roles in quantum mechanics. For example, the temporal evolution equation, eq. (2.16), can be succinctly represented through the unitary operator

$$U(t,t_0) = \exp\left\{-\frac{iH(t-t_0)}{\hbar}\right\} \implies O(t) = U(t,t_0)O(t_0)U^\dagger(t,t_0). \tag{2.20}$$

The time-evolution operator can be generalized for time-dependent Hamiltonians with a so-called time-ordered exponential.

At this point, we want to focus on their other main role: changing the representation of the underlying physics. As we saw above, the same quantum operator can represent different dynamical variables, and it depends on the initial choice of canonical variables. It turns out that unitary transformations can be used to implement coordinate transformations such as the one that illustrates the discussion above. Not only are they more convenient, as they spare us from going back to the classical theory, finding the new momenta, and quantizing again, but they also naturally incorporate a larger class of transformations. Indeed, they allow us to generalize these ideas to purely quantum degrees of freedom with no classical analog as well.

Let us start with the same degree of freedom X from before in the $\mathscr{R}$ formulation. Then, the unitary transformation

$$T = \exp\left\{\frac{i}{\hbar}F(\hat{x};t)\right\} \tag{2.21}$$

implements the transformation from $\mathscr{R}$ to $\mathscr{R}'$, where $F(\hat{x};t)$ is Hermitian and corresponds to the same function whose total time derivative connected the equivalent Lagrangians before. The action of this transformation on operators at the quantum level is expressed through

$$T\hat{x}T^\dagger = \hat{x} \quad \text{and} \quad T\hat{p}T^\dagger = \hat{p} - \partial_x F(\hat{x};t), \tag{2.22a}$$

where the momentum transformation follows from eq. (A.46). Stated more explicitly, given a physical observable O with associated operator $\hat{o}$ in $\mathscr{R}$, the expression $T\hat{o}T^\dagger$ tells us which operator corresponds to the observable O in the formulation $\mathscr{R}'$. In that sense, eq. (2.22a) tells us that P is represented by $T\hat{p}T^\dagger = \hat{p} - \partial_x F(\hat{x};t)$ in $\mathscr{R}'$, as we saw before in table 2.1. The only exception to this rule is the Hamiltonian, which acquires an additional term if the transformation depends on time explicitly:

$$\begin{aligned} TH(\hat{x},\hat{p})T^\dagger + i\hbar\dot{T}T^\dagger &= H\big(\hat{x}, T\hat{p}T^\dagger\big) - \dot{F}(\hat{x};t) \\ &= H(\hat{x},\hat{p} - \partial_x F(\hat{x};t)) - \dot{F}(\hat{x};t) = H'(\hat{x},\hat{p}). \end{aligned} \tag{2.22b}$$

Here $\dot{T} = \partial_t T$, that is, only the explicit time-dependence is accounted for with this derivative, and not the one coming from the evolution of the dynamical variables themselves. Last, the quantum states of the system are also transformed:

$$|\psi\rangle \to T|\psi\rangle, \tag{2.22c}$$

ensuring the preservation of the theory's meaning. In this regard, we must

note that there are two equivalent views of these arguments, akin to active and passive transformations in geometry. The one discussed here is passive in the sense that the physical quantity is invariant, while the operator that represents it is modified.

In the active view, one would apply $T^\dagger$ instead of T and take the operator $T\hat{\mathbf{p}}_i T^\dagger$ to represent the new canonical momentum, rather than keep $\hat{\mathbf{p}}$ as the operator that represents the canonical momentum.

In the scenario of interest here, non-relativistic QED, general unitary transformations to change the quantum formulation are given by [14]

$$T = \exp\left\{\frac{i}{\hbar}F(\dots,\hat{\mathbf{r}}_i,\hat{\mathbf{p}}_i,\dots;\hat{\mathbf{A}}^\perp,\hat{\mathbf{\Pi}}^\perp;t)\right\}. \tag{2.23}$$

We emphasize once more that $\hat{\mathbf{p}}_i$ is just the quantum mathematical representation of a particular combination of physical variables satisfying certain relations (its Poisson bracket with $\mathbf{r}_i$ is $-\mathbb{1}$), such that we can choose it as canonical momentum, and the same goes for the other operators. To make this distinction more apparent, we have added the $\hat{}$ symbol on the operators. Of course, in our current formulation of electrodynamics, the map between physical quantity and quantum operators are "trivial", e.g., the canonical positions of the charges corresponds precisely to their physical locations, and the field operators match the canonical field variables. With such a transformation, the operators and states in $\mathcal{R}$ are transformed into new operators and states in $\mathcal{R}'$, according to $T\hat{o}T^\dagger$, $THT^\dagger + i\hbar\dot{T}T^\dagger$ and $T|\psi\rangle$, as before.

A very common and useful particular case of the general unitary transformations in eq. (2.23) is given by their restriction to depend solely on positions and, possibly, on time. This kind of transformation is the quantum implementation of the well-known invariance of the classical Euler-Lagrange equations of motion after the addition of the total temporal derivative of a function of the coordinates and time in the Lagrangian formalism. In fact, it corresponds precisely to the initial example with one degree of freedom X. In QED, transformations that only depend on $\mathbf{r}_i$ and $\mathbf{A}^\perp$ would yield non-trivial transformations in the canonical momenta, i.e.,

$$T\hat{\mathbf{r}}_i T^\dagger = \hat{\mathbf{r}}_i, \qquad T\hat{\mathbf{A}}^\perp T^\dagger = \hat{\mathbf{A}}^\perp \quad \text{and} \tag{2.24a}$$

$$T\hat{\mathbf{p}}_i T^\dagger = \hat{\mathbf{p}}_i + T\left[\hat{\mathbf{p}}_i, T^\dagger\right] \neq \hat{\mathbf{p}}_i, \qquad T\hat{\mathbf{\Pi}}^\perp T^\dagger = \hat{\mathbf{\Pi}}^\perp + T\left[\hat{\mathbf{\Pi}}, T^\dagger\right] \neq \hat{\mathbf{\Pi}}. \tag{2.24b}$$

If we now restrict the transformations further to those where the Hermitian function F in the exponential can be brought to the form

$$F(\dots,\hat{\mathbf{r}}_i,\dots;\hat{\mathbf{A}}^\perp;t) = \sum_j q_j \chi(\hat{\mathbf{r}}_j;\hat{\mathbf{A}}^\perp;t), \tag{2.25}$$

we obtain a subset of transformations that are equivalent to gauge transforma-

tions. Indeed, χ corresponds to the gauge function, and the gauge-dependent parts of the potentials are

$$\mathbf{A}^{\parallel} = -\nabla\chi \quad \text{and} \tag{2.26a}$$

$$\phi = \phi_C + \dot{\chi}. \tag{2.26b}$$

Note, however, that the canonical field position is still $\mathbf{A}^{\perp}$, and its quantum representation is unmodified. In this approach to the Hamiltonian formalism where we have already isolated the adequate DOF, the change of gauge is only apparent in the field's momentum.

Canonical vs. Unitary

After the previous discussion on unitary transformations and the associated change in quantum representation, one may be left wondering what happened to the canonical transformations of classical mechanics. Indeed, canonical transformations, i.e., those that preserve the Poisson bracket, are a powerful tool in classical mechanics. Additionally, the fundamental algebraic relations in quantum mechanics are to a large extent built by analogy with those in analytical mechanics. Is there such a thing as a quantum canonical transformation (QCT)? As it turns out, not only do they exist, but they were a critical and instrumental element of the early days of quantum mechanics [183–188]. Nevertheless, apart from some relatively simple cases, the general theory of QCTs has not received as much attention since the foundations of quantum theory were established, with only occasional contributions to the literature. Here, we only highlight some relevant aspects for the remainder of the thesis.

The definition of a QCT is straightforwardly generalized from their classical counterpart. If (q,p) represents a canonically conjugate pair of variables with $[q,p] = i\hbar$, then a QCT changes (q,p) into $(Q(q,p),P(q,p))$, while respecting the commutation relation $[q,p] = [Q,P] = i\hbar$. As was proved by Jordan [185], all QCT can be implemented uniquely (up to a multiplicative factor) by an operator T such that

The proof is constructive in that it finds T, given the generating function of a canonical transformation.

$$Q = TqT^{-1} \quad \text{and} \quad P = TpT^{-1}. \tag{2.27}$$

Note that unitary operators trivially implement QCTs. However, not all QCTs can be implemented by a unitary transformation and, in this sense, QCTs are even broader than unitary transformations [189]. The last important remark is that, sometimes, it is not easy to work out the precise expression of T for a given QCT. If there is a classical canonical transformation, it can be sim-

pler to apply the transformation in the classical theory and then quantize by promoting the resulting variables to operators. We finish this brief exploration of QCT by analyzing three simple examples that will be useful in chapter 5.

EXAMPLE 1: RESCALING. The transformation that rescales position and momentum according to $Q = kq$ and $P = k^{-1}p$, for some non-zero constant k, is evidently canonical. It can be shown that its quantum version is implemented by the unitary transformation

$$T = \exp\left\{\frac{i \log k}{\hbar} S[qp]\right\}. \tag{2.28}$$

EXAMPLE 2: POSITION AND MOMENTUM SWAP. Another interesting canonical transformation is the one that swaps position and momentum: $Q = -p$ and $P = q$. Here, p and q have the same dimensions, which can be achieved through rescalings like the one of the first example. This transformation is equivalent to a $\pi/2$ rotation in phase space, whose generator is $p^2 + q^2$. Then, the transformation is

$$T = \exp\left\{\frac{i}{\hbar}\frac{\pi}{2}\frac{p^2 + q^2}{2}\right\}, \tag{2.29a}$$

which is most easily proved by defining the ladder operators

$$a^{(\dagger)} = \frac{1}{\sqrt{2\hbar}}(q \pm ip) \tag{2.29b}$$

and realizing that $Ta^{(\dagger)}T^\dagger = \mp i a^{(\dagger)}$. Of course, if the system is a harmonic oscillator, then the generator of T coincides with the generator of the time-evolution operator. A well-known consequence is the circular motion of coherent states, the right eigenvectors of a, in phase space. We finish the example by noting that a rotation angle different from $\pi/2$ would generally mix positions and momenta, rather than merely swap them. Nowadays, this kind of transformation is more commonly described in terms of a and $a^\dagger$. In that context, these are known as Bogoliubov transformations.

EXAMPLE 3: GENERAL COORDINATE TRANSFORMATIONS. If we start with a set of coordinates q_i with their canonical momenta p_i ($\left[q_i, p_j\right] = i\hbar\delta_{ij}$) and find functions of them $Q_k(\dots, q_i, \dots)$ and $P_k(\dots, p_i, \dots)$ such that $[Q_k, P_l] = i\hbar\delta_{lm}$, we have effectively done a canonical coordinate transformation, also known as point transformations. Due to their indubitable relevance to physics, this kind of transformation has been discussed in some detail dating back to 1926, when Jordan found a general form for T for point transformations [185]. In

short, point transformations in Hamiltonian mechanics can be written as

$$Q_k = Q_k(\dots, q_i, \dots) \quad \text{and} \quad P_k = \sum_l \frac{\partial q_l}{\partial Q_k} p_l. \tag{2.30}$$

Then, the associated T turns out to be

$$T = \exp\left\{\frac{i}{\hbar}(\dots|R_i p_i|R_{i+1} p_{i+1}|\dots)\right\}, \tag{2.31}$$

up to a multiplicative factor. Here,

$$R_k = Q_k - q_k = R_k(\dots, q_i, \dots), \tag{2.32}$$

and the notation in the exponent indicates a particular position-momentum ordering, namely, all position (momentum) operators are to be pushed to the left (right) upon series expansion. For example

$$\exp\{(q_1 p_1|q_2 p_2|\dots|q_N p_N)\} = \sum_{n_1, n_2, \dots, n_N} \frac{(q_1^{n_1} q_2^{n_2} \dots q_N^{n_N})(p_1^{n_1} p_2^{n_2} \dots p_N^{n_N})}{n_1! n_2! \dots n_N!}. \tag{2.33}$$

This general solution is straightforwardly applicable to the case where Q_k are linear functions of q_i.

The above examples illustrate the difficulties associated with the use of general QCTs. In this thesis, only simple transformations are required, where the above considerations can be ignored by directly manipulating the coordinates and momenta before quantizing. Nevertheless, QCTs remain an interesting topic and deserve at least the above succinct discussion.

Multipolar coupling Hamiltonian

We finish the overview of non-relativistic QED by transforming the minimal coupling Coulomb gauge Hamiltonian into an equivalent form that is often more convenient: the multipolar coupling Hamiltonian. The reason behind such nomenclature is that the matter-field interaction is written in terms of polarization and magnetization fields, as we will see shortly, and thus allows for a systematic and straightforward perturbative expansion in multipolar terms: electric and magnetic dipoles, electric and magnetic quadrupoles and so on. The corresponding unitary transformation is given by [14, 190, 191]

$$T = \exp\left\{-\frac{i}{\hbar}\int \mathrm{d}^3 r\, \mathbf{P}\cdot\mathbf{A}^\perp\right\} = \exp\left\{-\frac{i}{\hbar}\int \mathrm{d}^3 r\, \mathbf{P}^\perp\cdot\mathbf{A}^\perp\right\} \tag{2.34}$$

and is known as the Power-Zienau-Woolley (PZW) transformation, where the equality is due to the fact that

$$\int \mathrm{d}^3 r\, \mathbf{X}^{\parallel} \cdot \mathbf{Y}^{\perp} = 0 \tag{2.35}$$

for any given pair of vector fields $\mathbf{X}$ and $\mathbf{Y}$. Here, $\mathbf{P}$ is the polarization density of the charges, and satisfies

$$\nabla \cdot \mathbf{P} = -\rho. \tag{2.36}$$

An interesting remark is that, because $\nabla \cdot \mathbf{P}^{\perp} = 0$, eq. (2.36) only specifies the longitudinal part of the polarization $\mathbf{P}^{\parallel}$. In and of itself, this is not surprising. However, what is interesting about the PZW transformation is that only the unspecified $\mathbf{P}^{\perp}$ really appears in eq. (2.34). Thus, there are infinitely many versions of the PZW transformation, uniquely characterized by the choice of $\mathbf{P}^{\perp}$. This freedom has, in fact, been used to propose convenient options [192, 193]. Nevertheless, the most common choice in the literature is the so-called Power form:

$$\mathbf{P}(\mathbf{r}) = \sum_i q_i (\mathbf{r}_i - \mathbf{r}_{\mathrm{O}}) \int_0^1 \mathrm{d}\sigma\, \delta^{(3)}[\mathbf{r} - \mathbf{r}_{\mathrm{O}} - \sigma(\mathbf{r}_i - \mathbf{r}_{\mathrm{O}})] \tag{2.37}$$

which has a direct physical interpretation in terms of infinitesimal dipoles going from $\mathbf{r}_{\mathrm{O}}$ to each point charge through a straight path. However, this polarization brings some questions with it as we shall see below.

For the sake of brevity, we only reproduce here the results of the transformation and relegate the detailed derivations to appendix D. Still, an interesting observation that is worth making here is that the PZW transformation is, in essence, a displacement operator of the canonical momenta of both the transverse EM field and the charges. The Hamiltonian in eq. (2.13) becomes, after the PZW transformation with eq. (2.37) [14],

$$\begin{aligned} H' = &\sum_i \frac{\left(\mathbf{p}_i - q_i \int_0^1 \mathrm{d}\sigma\, \sigma \mathbf{B}[\mathbf{r}_{\mathrm{O}} + \sigma(\mathbf{r}_i - \mathbf{r}_{\mathrm{O}})] \times (\mathbf{r}_i - \mathbf{r}_{\mathrm{O}})\right)^2}{2m_i} \\ &+ \sum_{i \neq j} \frac{q_i q_j}{8\pi\varepsilon_0 |\mathbf{r}_i - \mathbf{r}_j|} + \frac{1}{2\varepsilon_0} \int \mathrm{d}^3 r\, \left(\mathbf{P}^{\perp}\right)^2 \\ &+ \int \mathrm{d}^3 r \left[\frac{\left(\mathbf{\Pi}^{\perp}\right)^2}{2\varepsilon_0} + \frac{\varepsilon_0 c^2}{2} \mathbf{B}^2\right] + \frac{1}{\varepsilon_0} \int \mathrm{d}^3 r\, \mathbf{P}^{\perp} \cdot \mathbf{\Pi}^{\perp}, \end{aligned} \tag{2.38}$$

where, in line with the ideas of section 2.1.2, the momentum operators no longer represent the original canonical momenta. Instead, they represent new

momentum variables:

$$\mathbf{p}_i \to m_i\dot{\mathbf{r}}_i + q_i \int_0^1 \mathrm{d}\sigma\, \sigma \mathbf{B}[\mathbf{r}_\mathrm{O} + \sigma(\mathbf{r}_i - \mathbf{r}_\mathrm{O})] \times (\mathbf{r}_i - \mathbf{r}_\mathrm{O}) \quad \text{and} \tag{2.39a}$$

$$\mathbf{\Pi}^\perp \to -\mathbf{D}^\perp = -\left(\varepsilon_0 \mathbf{E}^\perp + \mathbf{P}^\perp\right) = -(\varepsilon_0 \mathbf{E} + \mathbf{P}), \tag{2.39b}$$

where $\mathbf{D}$ is the displacement field, and we have used that $\varepsilon_0 \nabla \cdot \mathbf{E}^\parallel = \rho = -\nabla \cdot \mathbf{P}^\parallel$ to identify $\varepsilon_0 \mathbf{E}^\parallel$ with $-\mathbf{P}^\parallel$ and arrive at the last equality. Accordingly, the light and matter DOF are shared between both the charges and field momenta in this representation, while in the minimal coupling one the field canonical momentum made reference to the EM field. This reshuffling of DOF results in a new form for the light-matter interaction encoded in two different terms. First, the charges interact with the displacement field through the last contribution in eq. (2.38). Additionally, the kinetic part of the charges contains the magnetic field $\mathbf{B}$ in the square. If expanded, the square gives rise to terms similar to those in eq. (2.13), with something that can be identified as some vector potential different from $\mathbf{A}^\perp$. Indeed, the PZW transformation can be alternatively conceived as a gauge transformation to the so-called Poincaré gauge, which defines the potentials in terms of the fields [14, 173].

Yet, some extensions of the PZW transformation are not compatible with a change of gauge. This is the case, for instance, when $\mathbf{P}$ includes multiple charge origins $\mathbf{r}_{\mathrm{O}_i}$ describing different atoms or molecules.

An important feature of eq. (2.38) is the appearance in the second line of the so-called polarization self-energy (PSE) term. The PSE has been the topic of much debate recently in the literature regarding its presence or absence in certain contexts [177, 178, 180, 181]. One of the goals of this thesis is to shed light on these questions (see chapter 5). Besides that debate, the truth is that the PSE term can be uncomfortable, as it is slightly ill-defined when eq. (2.37) is chosen as polarization: it essentially involves integrating the square of a delta function. Nevertheless, we will show in the next sections that it is not a problem any more than the diamagnetic term of the minimal coupling Hamiltonian. Instead, a careful handling of the PSE takes us simply to the limits of non-relativistic QED, which, unsurprisingly, fails to account for the interaction between matter and photons of sufficiently large energy.

We finish our exposition of the multipolar Hamiltonian by briefly discussing two slight modifications to the PZW transformation, besides those arising from the freedom in $\mathbf{P}^\perp$, that will play a role in chapter 5. The details are provided there, to keep this section's more general aim. In the first one, only a subset of the charges is included in $\mathbf{P}$. This *partial PZW transformation* makes sense when there are physically distinct subsets of charges that, for mathematical convenience, we want to treat differently. The second is the *multicenter PZW transformation*, and is reasonable when the charges are clumped in smaller subsets, all of which we want to describe in the multipolar framework.

The "multicenter" then comes from including different charge centers in $\mathbf{P}$:

$$\begin{aligned}\mathbf{P}(\mathbf{r}) &= \sum_n \mathbf{P}_n(\mathbf{r}) \\ &= \sum_n \sum_{i\in C_n} q_i\big(\mathbf{r}_i - \mathbf{r}_{\mathrm{O}_n}\big)\int_0^1 \mathrm{d}\sigma\; \delta^{(3)}\big[\mathbf{r} - \mathbf{r}_{\mathrm{O}_n} - \sigma\big(\mathbf{r}_i - \mathbf{r}_{\mathrm{O}_n}\big)\big],\end{aligned} \tag{2.40}$$

where $\mathbf{r}_{\mathrm{O}_n}$ is the center associated to the nth subset of charges, and C_n contains the charge indices in it. A particularly noteworthy feature of the multicenter transformation is that no direct Coulomb coupling between different subsets of charges appears explicitly in the Hamiltonian. More explicitly, it is canceled by the crossed terms in the PSE:

$$\begin{aligned}\frac{1}{\varepsilon_0}\int \mathrm{d}^3r\; \mathbf{P}_n^{\perp}\cdot\mathbf{P}_m^{\perp} &= \frac{1}{\varepsilon_0}\Big[\int \mathrm{d}^3r\; \mathbf{P}_n\cdot\mathbf{P}_m - \int \mathrm{d}^3r\; \mathbf{P}_n^{\parallel}\cdot\mathbf{P}_m^{\parallel}\Big] = -\frac{1}{\varepsilon_0}\int \mathrm{d}^3r\; \mathbf{P}_n^{\parallel}\cdot\mathbf{P}_m^{\parallel} \\ &= \varepsilon_0\int \mathrm{d}^3r\; \nabla\phi_{\mathrm{C},n}\cdot\mathbf{E}_m^{\parallel} = -\varepsilon_0\int \mathrm{d}^3r\; \phi_{\mathrm{C},n}\nabla\cdot\mathbf{E}_m^{\parallel} \\ &= -\int \mathrm{d}^3r\; \rho_m\phi_{\mathrm{C},n} = -\sum_{i\in C_n}\sum_{j\in C_m}\frac{q_iq_j}{4\pi\varepsilon_0\big|\mathbf{r}_i - \mathbf{r}_j\big|},\end{aligned} \tag{2.41}$$

which exactly cancels the Coulomb interaction between the charges in C_n and C_m, with $n \neq m$. To arrive at the above expression, we have assumed that the different polarization fields $\mathbf{P}_n$ do not overlap. Next, we used that $\mathbf{P}_n^{\parallel} = -\varepsilon_0\mathbf{E}_n^{\parallel} = \varepsilon_0\nabla\phi_{\mathrm{C},n}$, where the subscript n restricts the Coulomb field and potential to those produced by the charges in C_n. Then, integration by parts and eq. (2.1a) suffice to find the last line.

2.1.3 Mode expansions: photons are harmonic oscillators

Up to this point, we have kept the discussion in rather abstract EM terms. We now bring the above concepts to the physicists' prime comfort zone: the harmonic oscillator. We first discuss general properties of mode expansions of transverse fields, which will offer more insight into the EM state space. Then, we show how to manipulate the modes in a way that simplifies matters.

We begin by expanding the transverse fields into a basis of non-interacting normal modes [194]. In more detail, we perform separation of variables on eq. (2.8b), which is reduced to

$$\frac{1}{c^2}\ddot{\mathbf{A}}^{\perp} - \nabla^2\mathbf{A}^{\perp} = \frac{1}{\varepsilon_0 c^2}\mathbf{j}^{\perp} \tag{2.42}$$

in the Coulomb gauge and using the continuity equation. Next, we choose

transverse mode functions $\boldsymbol{\psi}_\lambda$ that solve the spatial part of eq. (2.42):

$$\nabla^2 \boldsymbol{\psi}_\lambda = -\left(\frac{\omega_\lambda}{c}\right)^2 \boldsymbol{\psi}_\lambda, \tag{2.43a}$$

We assume here that the mode functions are real, which they can be chosen to be. For instance, we choose to work with sines and cosines rather than with complex exponentials.

and expand the vector potential as

$$\mathbf{A}^\perp = \sum_\lambda A_\lambda \boldsymbol{\psi}_\lambda. \tag{2.43b}$$

These mode functions $\boldsymbol{\psi}_\lambda$ form an orthonormal and complete basis of the space of transverse vector fields, that is,

$$\int \mathrm{d}^3 r\, \boldsymbol{\psi}_\lambda \cdot \boldsymbol{\psi}_{\lambda'} = \delta_{\lambda\lambda'} \quad \text{and} \quad \sum_\lambda \boldsymbol{\psi}_\lambda(\mathbf{r}) \otimes \boldsymbol{\psi}_\lambda(\mathbf{r}') = \boldsymbol{\delta}^\perp(\mathbf{r}-\mathbf{r}'). \tag{2.43c}$$

Another important property of these mode functions is the following:

$$\nabla^2(\nabla \times \boldsymbol{\psi}_\lambda) = \nabla \times (\nabla^2 \boldsymbol{\psi}_\lambda) = \left(\frac{\omega_\lambda}{c}\right)^2 (\nabla \times \boldsymbol{\psi}_\lambda). \tag{2.43d}$$

Thus, for every $\boldsymbol{\psi}_\lambda$, there exists another mode function $\boldsymbol{\psi}_{\lambda'} = \frac{c}{\omega_\lambda}\nabla \times \boldsymbol{\psi}_\lambda$ with the same frequency, $\omega_\lambda = \omega_{\lambda'}$, and the prefactor $\frac{c}{\omega_\lambda}$ ensures that the new mode $\boldsymbol{\psi}_{\lambda'}$ is properly normalized. The last remark concerning the mode expansion is that the discrete sum notation has been used for simplicity only. In general, our index λ hides at least one continuous and one discrete label, which implies that the $\delta_{\lambda\lambda'}$ on the left relation of eq. (2.43c) actually contains a Dirac delta. For instance, for plane waves λ becomes the wave vector and polarization, while it becomes the norm of the wave vector, the polarization, and angular momentum indices for spherical waves.

After their introduction, we may choose the variables A_λ as our canonical field "positions", such that their canonical conjugates turn out to be precisely Π_λ, the mode coefficients of the canonical momentum $\boldsymbol{\Pi}^\perp = \sum_\lambda \Pi_\lambda \boldsymbol{\psi}_\lambda$. Accordingly, we can directly quantize by promoting these scalar variables to operators. The advantage of working with a mode expansion is that the field Hamiltonian no longer hides its true colors:

$$H_\mathrm{f} = \int \mathrm{d}^3 r \left[\frac{\left(\boldsymbol{\Pi}^\perp\right)^2}{2\varepsilon_0} + \frac{\varepsilon_0 c^2}{2}\left(\nabla \times \mathbf{A}^\perp\right)^2\right] = \sum_\lambda \left[\frac{\Pi_\lambda^2}{2\varepsilon_0} + \frac{\varepsilon_0 \omega_\lambda^2}{2} A_\lambda^2\right], \tag{2.44}$$

that is, the field variables are nothing but a collection of harmonic oscillators. Accordingly, we may apply the ladder-operator machinery and define an an-

nihilation and creation operator for each mode:

$$\begin{cases} A_\lambda = \sqrt{\dfrac{\hbar}{2\varepsilon_0\omega_\lambda}}\left(a_\lambda^\dagger + a_\lambda\right) \\ \Pi_\lambda = i\sqrt{\dfrac{\hbar\varepsilon_0\omega_\lambda}{2}}\left(a_\lambda^\dagger - a_\lambda\right) \end{cases} \implies \begin{cases} a_\lambda = \sqrt{\dfrac{\varepsilon_0\omega_\lambda}{2\hbar}}\left(A_\lambda + \dfrac{i}{\varepsilon_0\omega_\lambda}\Pi_\lambda\right) \\ a_\lambda^\dagger = \sqrt{\dfrac{\varepsilon_0\omega_\lambda}{2\hbar}}\left(A_\lambda - \dfrac{i}{\varepsilon_0\omega_\lambda}\Pi_\lambda\right) \end{cases}, \tag{2.45}$$

with the well-known commutation relation $\left[a_\lambda, a_{\lambda'}^\dagger\right] = \delta_{\lambda\lambda'}$. With these operators, we can bring H_f to its final form

$$H_\mathrm{f} = \sum_\lambda \hbar\omega_\lambda\left[a_\lambda^\dagger a_\lambda + \frac{1}{2}\right]. \tag{2.46}$$

Then, it is straightforward to see from eq. (2.16) that the equation of motion of a_λ is

$$\dot{a}_\lambda = -i\omega_\lambda a_\lambda + \frac{i}{\sqrt{2\varepsilon_0\hbar\omega_\lambda}} S[j_\lambda] \quad \text{or} \tag{2.47a}$$

$$\dot{a}_\lambda = -i\omega_\lambda a_\lambda + \frac{i\omega_\lambda}{\sqrt{2\varepsilon_0\hbar\omega_\lambda}} P_\lambda, \tag{2.47b}$$

depending on whether the minimal coupling or the multipolar coupling picture is used at the start. Here, j_λ and P_λ are the expansion coefficients of $\mathbf{j}^\perp = \sum_\lambda j_\lambda \boldsymbol{\psi}_\lambda$ and $\mathbf{P}^\perp = \sum_\lambda P_\lambda \boldsymbol{\psi}_\lambda$. The reason for the different equations of motion is found in section 2.1.2: the fact that $\mathbf{\Pi}$ represents a different physical quantity in either picture is directly inherited by the a_λ obtained. Still, as one would expect, in the absence of charges both equations become the same, emphasizing that the multiplicity lies in the interaction. In that case, the modes oscillate in time, with ω_λ corresponding to the free-space oscillation frequency. In the presence of matter, however, the current acts as a source to the field modes.

STRUCTURE OF THE HILBERT SPACE

Let us now take a look at the state space. Naturally, it is built as a tensor product of the charge's and transverse EM field's Hilbert spaces: $\mathcal{H}_\mathrm{QED} = \mathcal{H}_\mathrm{c} \otimes \mathcal{H}_\mathrm{f}$. We occupy ourselves with the transverse fields here, while the charges will be discussed in some more detail later in section 2.3. Since we have expanded the fields in modes, and these modes are a set of harmonic oscillators, we know that there is a lowest-energy state, the vacuum or ground state, defined by

$$a_\lambda|\{0\}\rangle = 0 \quad \forall\lambda. \tag{2.48a}$$

From the vacuum, we can use the creation operators to climb the excitation ladder of any mode an integer number of times:

$$\left(a_\lambda^\dagger\right)^{n_\lambda}|\{0\}\rangle = \sqrt{n_\lambda!}|n_\lambda\rangle, \tag{2.48b}$$

where $\langle n_\lambda|m_\lambda\rangle = \delta_{n_\lambda m_\lambda}$. Combining the equations above, and taking into account that $\left[a_\lambda, \left(a_\lambda^\dagger\right)^n\right] = n\left(a_\lambda^\dagger\right)^{n-1}$, we also have

$$a_\lambda|n_\lambda\rangle = \sqrt{n_\lambda}|n_\lambda - 1\rangle. \tag{2.48c}$$

Then, we can build a basis for the whole $\mathcal{H}_\mathrm{f}$ through tensor products of the form

$$\bigotimes_\lambda |n_\lambda\rangle \equiv |\dots, n_{\lambda-1}, n_\lambda, n_{\lambda+1}, \dots\rangle,\ n_\lambda \in \mathbb{N}\ \forall\lambda, \tag{2.49}$$

and it becomes natural to interpret the number states in terms of the amount of photons present in each mode. The final remark is that the states $|\dots, n_\lambda, \dots\rangle$ are eigenstates of H_f such that

$$H_\mathrm{f}|\dots, n_\lambda, \dots\rangle = \left[\sum_\lambda \hbar\omega_\lambda n_\lambda\right]|\dots, n_\lambda, \dots\rangle. \tag{2.50}$$

As is customary, we have removed the divergent, but inconsequential, zero-point energy from H_f. The eigenvalues eq. (2.50) reinforce thus the interpretation in terms of photons, that is, quanta of light of energy $\hbar\omega_\lambda$. Note that the nature of these excitations will be "purely photonic" in the minimal coupling picture only. In the multipolar coupling picture they will instead correspond to mixed light-matter excitations.

Simplification of the mode structure

We have introduced an arbitrary mode expansion and, from that, revealed the properties of the state space. We have been deliberate in keeping the above discussion general, as there is no fundamental reason to prefer one set of $\boldsymbol{\psi}$ functions over another. Nevertheless, some functions might be better suited for certain purposes. For example, introductory accounts of the quantization of the EM field tend to favor the plane-wave expansion. Other situations call for slightly more sophisticated options, as can be the spherical-wave functions that will be important in chapter 5. Throughout this thesis, we will be interested in describing the interaction between photons and localized atoms. A natural question is, then, if there exists a basis of functions particularly well-suited for these scenarios. The answer is positive, and we discuss here a gen-

eral procedure to find a "minimal" set of relevant modes [180, 195–200]. We then illustrate it by applying these ideas to the concrete interaction Hamiltonian between an atom and the free-space EM field, extracting the coupling strength to this particular set of modes, and reaching the so-called free-space spectral density.

Let us work, for concreteness, in the multipolar coupling picture, and assume that the atom is localized in a region of space much smaller than the important wavelengths involved. Then, we can apply the long-wavelength approximation to eq. (2.38). By further neglecting magnetic effects, the light-matter interaction in the multipolar coupling Hamiltonian becomes

$$H'_{\text{int}} = -\frac{1}{\varepsilon_0}\mathbf{d}\cdot\mathbf{D}^{\perp}(\mathbf{0}), \tag{2.51}$$

where the atom sits at the origin, and $\mathbf{d} = \sum_i q_i \mathbf{r}_i$ is its dipole moment. For simplicity of exposition, let us momentarily assume that the relevant transition of the atom has a transition dipole moment pointing along the z axis; we will soon see how to lift this restriction. If we expand the displacement field

$$\mathbf{D}^{\perp}(\mathbf{0}) = \sum_{\lambda} i\sqrt{\frac{\hbar\varepsilon_0\omega_\lambda}{2}}\boldsymbol{\psi}_\lambda(\mathbf{0})\left(a_\lambda^\dagger - a_\lambda\right), \tag{2.52}$$

we can write

$$H'_{\text{int}} = -i\hbar(\mathbf{d}\cdot\mathbf{u}_z)\sum_{\lambda} g_{z,\lambda}\left(a_\lambda^\dagger - a_\lambda\right), \tag{2.53}$$

with

$$g_{z,\lambda} \equiv \sqrt{\frac{\omega_\lambda}{2\hbar\varepsilon_0}}(\mathbf{u}_z\cdot\boldsymbol{\psi}_\lambda(\mathbf{0})), \tag{2.54}$$

which summarizes how strongly the emitter's transition is coupled to the mode a_λ. We may now formally combine all degenerate modes (with the same frequency ω) into a set of *bright* modes

$$b_z(\omega) = \frac{i}{g_z(\omega)}\sum_{\lambda} g_{z,\lambda}a_\lambda\delta(\omega-\omega_\lambda), \tag{2.55}$$

where

$$g_z^2(\omega) = \sum_{\lambda} g_{z,\lambda}^2\delta(\omega-\omega_\lambda), \tag{2.56}$$

and many orthogonal *dark* modes $d_{z,\eta}(\omega)$, uncoupled from the atomic transition. These dark modes still exist, but they cannot communicate with the atom

Note that there are a continuously infinite amount of dark modes at each frequency in an unbound space.

at all and evolve freely. By construction, the transformation

$$\{a_\lambda\} \to \left\{b_z(\omega), d_{z,\eta}(\omega)\right\} \tag{2.57}$$

is orthogonal, and translates into an interaction Hamiltonian where we sum over a frequency index, with only one mode at each frequency:

$$H'_{\text{int}} = \hbar(\mathbf{d}\cdot\mathbf{u}_z)\sum_\omega g_z(\omega)\left(b_z^\dagger(\omega) + b_z(\omega)\right). \tag{2.58}$$

Thus, we have decoupled, at each frequency, all modes but one, which bears the whole coupling strength. Of course, the transformation carries over to H_{f} straightforwardly:

$$H'_{\text{f}} = \sum_\lambda \hbar\omega_\lambda a_\lambda^\dagger a_\lambda = \sum_\omega \hbar\omega\left[b_z^\dagger(\omega)b_z(\omega) + \sum_\eta d_{z,\eta}^\dagger(\omega)d_{z,\eta}(\omega)\right]. \tag{2.59}$$

We are now ready to lift the previous restriction to a single Cartesian component. If we were to repeat the procedure above for the x and y components, we would reach three sets of modes $b_j(\omega)$ $(j = x, y, z)$. However, it is generally not true that these new modes are orthogonal, that is,

The same goes for the dark modes, but we have left them out of the description.

$$\left[b_j(\omega), b_{j'}^\dagger(\omega')\right] \neq \delta_{jj'}\delta(\omega-\omega'). \tag{2.60}$$

If that is the case, one needs to additionally orthogonalize them at each frequency and reach a final set of modes $c_k(\omega)$ given by

$$c_k(\omega) = \sum_{j\in\{x,y,z\}} V_{kj}(\omega)b_j(\omega), \tag{2.61}$$

where $\mathbf{V}(\omega)$ are 3×3 matrices with the orthogonalization coefficients. For a complete implementation of this full process, see [180].

Now, we illustrate the procedure of finding a minimal set of modes for an atom interacting with the free-space EM field. For concreteness, we choose to start from the transverse and real plane-wave basis

$$\boldsymbol{\psi}_\lambda(\mathbf{r}) \to \begin{cases} \boldsymbol{\psi}_p^{\text{c}}(\mathbf{k},\mathbf{r}) = \dfrac{\sqrt{2}\cos(\mathbf{k}\cdot\mathbf{r})}{(2\pi)^{3/2}}\boldsymbol{\epsilon}_p(\mathbf{k}) \\ \boldsymbol{\psi}_p^{\text{s}}(\mathbf{k},\mathbf{r}) = \dfrac{\sqrt{2}\sin(\mathbf{k}\cdot\mathbf{r})}{(2\pi)^{3/2}}\boldsymbol{\epsilon}_p(\mathbf{k}) \end{cases}, \tag{2.62}$$

where c and s denote the particular trigonometric functions involved, $\mathbf{k}$ sweeps one half of the full reciprocal space, $\boldsymbol{\epsilon}_p(\mathbf{k})$ are polarization unit-vectors perpen-

dicular to $\mathbf{k}$ and to each other, labeled with $p = 1, 2$. We choose to work with these functions rather than the simpler and more common complex exponentials because, by ensuring that they are real, we can simply factor them out in, e.g., eq. (2.52) and avoid complex conjugated quantities that lengthen those expressions. The small price to pay is that the mode functions themselves are not quite as simple to write down. These mode functions are properly normalized according to

$$\int \mathrm{d}^3 r \, \boldsymbol{\psi}_p^f(\mathbf{k}, \mathbf{r}) \cdot \boldsymbol{\psi}_{p'}^{f'}(\mathbf{k}', \mathbf{r}) = \delta_{ff'} \delta_{pp'} \delta^{(3)}(\mathbf{k} - \mathbf{k}'), \tag{2.63}$$

and their free-space oscillation frequency is $\omega_p^f(\mathbf{k}) = c|\mathbf{k}|$. Because our generic λ index has now become $(\mathbf{k}, p, f)$, the interaction Hamiltonian involves summing over p and f, and a three-dimensional integral. However, since the mode functions have to be evaluated at $\mathbf{r} = \mathbf{0}$, only those with $f = \mathrm{c}$ contribute. Following the procedure described above, we can find three sets of Cartesian free-space modes $b_j(\omega)$ $(j = x, y, z)$, whose coupling strengths are obtained by adapting eq. (2.56):

$$\begin{aligned} g_j^2(\omega) &= \frac{\omega}{16\pi^3 \hbar \varepsilon_0} \int_{1/2} \mathrm{d}^3 k \, \sum_p \Big(\sqrt{2} \mathbf{u}_j \cdot \boldsymbol{\epsilon}_p(\mathbf{k}) \Big)^2 \delta(\omega - |\mathbf{k}|c) \\ &= \frac{\omega}{16\pi^3 \hbar \varepsilon_0 c} \int_\Omega \mathrm{d}\Omega \int_0^\infty \mathrm{d}k \, k^2 \big[1 - \big(\hat{\mathbf{k}} \cdot \mathbf{u}_j \big) \big] \delta(\omega/c - k) \\ &= \frac{\omega^3}{8\pi^2 \hbar \varepsilon_0 c^3} \int_0^\pi \mathrm{d}\vartheta \, \sin\vartheta \big[1 - \cos^2\vartheta \big] = \frac{\omega^3}{6\pi^2 \hbar \varepsilon_0 c^3} \equiv g^2(\omega). \end{aligned} \tag{2.64}$$

Here, $\int_{1/2} \mathrm{d}^3 k$ indicates that the integration domain is a half space. We have used spherical coordinates, the fact that $\delta(f(x)) = \frac{\delta(x - x_0)}{|f'(x_0)|}$ for a zero x_0 of f, and the completeness relation $\sum_p \boldsymbol{\epsilon}_p \otimes \boldsymbol{\epsilon}_p + \hat{\mathbf{k}}\hat{\mathbf{k}} = \mathbf{1}$. Because free space is isotropic, the total coupling strength does not depend on the Cartesian index, and the free-space bright modes $b_j(\omega)$ are orthogonal; in other words, $\big[b_j(\omega), b_{j'}^\dagger(\omega') \big] = \delta_{jj'} \delta(\omega - \omega')$.

It is not hard to check that the Cartesian free-space bright modes are orthogonal explicitly.

$$H'_{\mathrm{int}} = \hbar \sum_j \mathbf{d} \cdot \mathbf{u}_j \int_0^\infty \mathrm{d}\omega \, \sqrt{\frac{\omega^3}{6\pi^2 \hbar \varepsilon_0 c^3}} \big(b_j^\dagger(\omega) + b_j(\omega) \big). \tag{2.65}$$

For future reference, we mention here that

$$J^{\perp,0}(\omega) \equiv \frac{\omega^3}{6\pi^2 \hbar \varepsilon_0 c^3} \tag{2.66}$$

is the so-called spectral density of free space. The superscript $\perp$ emphasizes the transversality of free-space photon mode functions. It can be shown with

similar arguments that more general EM environments, such as those discussed in section 2.2, have their own associated spectral density $J(\omega)$ [180]. The coupling between the atom and the (macroscopic) EM fields can thus be rewritten in terms of $J(\omega)$, like in eq. (2.65). Accordingly, much of this thesis revolves around spectral densities viewed from different angles. We finish by noting that these arguments to find "minimal" sets of modes can be extended even further [201]. The key realization is that any set of modes capable of describing a given spectral density will affect the emitter in the exact same way. Although these extensions are not a main concern of the thesis, we will make use of some methodological corollaries from the results therein. Therefore, section 2.4.4 will briefly highlight the most relevant aspects from the perspective of the theory of open quantum systems.

2.2 Macroscopic QED: A theory of photons, atoms and bodies

In the previous section, we have framed molecular QED as a theory of charges and transverse EM fields, or photons. As long as the energies involved allow for the non-relativistic treatment of matter, every electromagnetic phenomenon is included therein except for the interaction between the particles' spin and $\mathbf{B}$. In the following, the matter component is further split into smaller units, usually emitters (atoms, molecules...) and macroscopic bodies. This separation is a matter of practicality; while macroscopic bodies or structures are nothing but large collections of charges, the amount of DOF they entail far exceeds the computational capabilities of any physicist or computer. Such systems are effectively out of reach, which only becomes even more unfortunate after realizing that the quantities of interest tend to concern a reduced and much more manageable subsystem. However, in this realization lies the solution: it is imperative to develop a framework that describes the EM response of the larger structure with a lower degree of detail. Luckily, such an approach already exists and is usually known as macroscopic QED (MQED) [202–204], which is, in some sense, a quantum theory built to be compatible with classical macroscopic electrodynamics. In this section, we outline its premises and definitions, and offer some final words of caution regarding gauge transformations.

2.2.1 Classical macroscopic electrodynamics

Let us begin with an overview of the relevant concepts of macroscopic electrodynamics. We first note that media develop a polarization $\mathbf{P}$ (incompletely defined by $\nabla \cdot \mathbf{P} = -\rho$) or magnetization $\mathbf{M}$, due to the internal currents induced by an incoming field, $\mathbf{j}_{\text{in}} = \dot{\mathbf{P}} + \nabla \times \mathbf{M}$. It is through these quantities that media are generally described. Accordingly, it is more convenient to write the inhomogeneous Maxwell equations, eqs. (2.1a) and (2.1d), in their "macroscopic" form

$$\nabla \cdot \mathbf{D} = 0 \quad \text{and} \quad \nabla \times \mathbf{H} = \dot{\mathbf{D}}, \tag{2.67a}$$

where $\mathbf{D}$ and $\mathbf{H}$ are the displacement and magnetic excitation fields, respectively, defined as

$$\mathbf{D} = \varepsilon_0 \mathbf{E} + \mathbf{P} \quad \text{and} \quad \mathbf{H} = \frac{1}{\mu_0}\mathbf{B} - \mathbf{M}. \tag{2.67b}$$

For simplicity, we limit ourselves to the case of media whose response to the EM field is linear, isotropic and local, which means that the constitutive equations that relate $\mathbf{P}$ and $\mathbf{M}$ to $\mathbf{E}$ and $\mathbf{B}$ are

For MQED, we need only keep the linear response assumption. In non-isotropic media, the susceptibilities are tensors. Also, at sufficiently small length scales, relaxing the response's locality still provides an adequate description. Then, the constitutive relations are spatial convolutions of the field and the response functions.

$$\mathbf{P}(\mathbf{r}, t) = \int_0^\infty \mathrm{d}\tau\, \chi(\mathbf{r}, \tau)\mathbf{E}(\mathbf{r}, t-\tau) \quad \text{and} \tag{2.68a}$$

$$\mathbf{M}(\mathbf{r}, t) = \int_0^\infty \mathrm{d}\tau\, \zeta(\mathbf{r}, \tau)\mathbf{B}(\mathbf{r}, t-\tau). \tag{2.68b}$$

Here, χ and ζ are the electric and magnetic susceptibility of the medium, respectively. Indeed, these relations are linear, and the susceptibilities are given by scalars that only depend on $\mathbf{r}$, which makes the response isotropic and local. Additionally, it proves convenient to work in the frequency domain. To that end, we define the frequency components through

$$f(\omega) = \frac{1}{\sqrt{2\pi}} \int_{-\infty}^\infty \mathrm{d}t\, f(t) e^{i\omega t} \tag{2.69}$$

and, therefore,

$$f(t) = \frac{1}{\sqrt{2\pi}} \int_{-\infty}^\infty \mathrm{d}\omega\, f(\omega) e^{-i\omega t}. \tag{2.70}$$

Note that this definition of the frequency components corresponds to the common time-frequency Fourier transform sign convention, opposite to the one used throughout this thesis and given in appendix A. This convention is followed here to recover expressions with the familiar sign choices.

Then, the constitutive equations become

$$\mathbf{P}(\omega) = \varepsilon_0 \chi(\omega)\mathbf{E}(\omega) \quad \text{and} \quad \mathbf{M}(\omega) = \frac{1}{\mu_0}\zeta(\omega)\mathbf{B}(\omega). \tag{2.71}$$

As above, these quantities usually depend on the spatial point at which they are evaluated, save for the case of homogeneous media. Nevertheless, in this

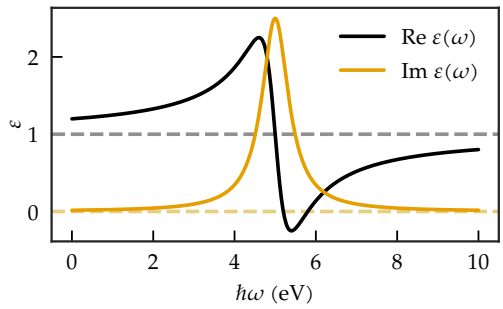

Figure 2.1: Illustration of the permittivity associated to an electric susceptibility given by $\chi(\omega) = \frac{-1}{\omega - \omega_r + i\gamma_r}$, with the parameters chosen to be $\hbar\omega_r = 5$ eV and $\hbar\gamma_r = 0.4$ eV. The dashed lines highlight the vertical positions of 0 and 1 along the plot.

1

thesis we tend to omit the explicit $\mathbf{r}$ dependence from both the fields and sucep-tibilities to simplify the notation, except to stress it in particular expressions. With these constitutive relations, we can write

$$\mathbf{D}(\omega) = \varepsilon_0(1 + \chi(\omega))\mathbf{E}(\omega) = \varepsilon_0\varepsilon(\omega)\mathbf{E}(\omega) \quad \text{and} \tag{2.72a}$$

$$\mathbf{H}(\omega) = \frac{1}{\mu_0}(1 - \zeta(\omega))\mathbf{B}(\omega) = \frac{1}{\mu(\omega)}\mathbf{B}(\omega), \tag{2.72b}$$

where we have introduced the relative permittivity ε and permeability μ to more compactly write the constitutive relations and for convenience.

The response functions cannot depend on ω arbitrarily. Indeed, we want the response of the medium to be causal, which means that only past times affect the current state of the medium. It can be seen that, in frequency space, the requirement of causality implies that

$$\operatorname{Re}\varepsilon(\omega) = 1 + \frac{1}{\pi}P\int_{-\infty}^{\infty} \mathrm{d}\omega' \, \frac{\operatorname{Im}\varepsilon(\omega')}{\omega' - \omega} \quad \text{and} \tag{2.73a}$$

$$\operatorname{Im}\varepsilon(\omega) = -\frac{1}{\pi}P\int_{-\infty}^{\infty} \mathrm{d}\omega' \, \frac{\operatorname{Re}\varepsilon(\omega') - 1}{\omega' - \omega}, \tag{2.73b}$$

that is, the Kramers-Kronig relations for dielectrics, and μ fulfills similar equations. Here, P denotes the principal value integral. It has been assumed that $\varepsilon(\omega)$ has no poles on the real axis. Metals, however, are usually described by

$$\varepsilon_{\text{metal}}(\omega) = \varepsilon_1(\omega) + \frac{i\sigma(\omega)}{\omega}, \tag{2.74}$$

where $\sigma(\omega)$ is the metal's conductivity. The associated susceptibility exhibits a simple pole at the origin, which must be accounted for separately [205]. An important consequence of eq. (2.73), schematically illustrated in fig. 2.1, is that variations of Re ε in frequency space bring non-zero Im ε with them. In other words, dispersion and absorption are two faces of the causality coin.

If we include a source current $\mathbf{j}_s$, the macroscopic Maxwell equations can

be condensed into the Helmholtz equation for the electric field:

$$\left[\nabla\times\frac{1}{\mu}\nabla\times\ -\frac{\omega^2}{c^2}\varepsilon(\omega)\right]\mathbf{E}(\omega)=i\mu_0\omega\mathbf{j}_{\mathrm{s}}(\omega). \tag{2.75}$$

This equation can be formally solved by introducing the EM Green tensor, customarily denoted by $\mathbf{G}$, defined by

$$\left[\nabla\times\frac{1}{\mu}\nabla\times\ -\frac{\omega^2}{c^2}\varepsilon(\mathbf{r},\omega)\right]\mathbf{G}(\mathbf{r},\mathbf{r}',\omega)=\boldsymbol{\delta}(\mathbf{r}-\mathbf{r}') \tag{2.76}$$

and the boundary condition $\mathbf{G}(\mathbf{r},\mathbf{r}',\omega)\to\mathbf{0}$ when $|\mathbf{r}-\mathbf{r}'|\to\infty$. Here, it is clear that ∇ takes a derivative with respect to $\mathbf{r}$. Still, when we consider equations with more coordinates it can be unclear to which one ∇ refers. In such cases, we will specify it with either a prime or a subscript. We can generally split $\mathbf{G}$ as a sum of a free-space and scattering contributions $\mathbf{G}^0$ and $\mathbf{G}^{\mathrm{s}}$, respectively, where $\mathbf{G}^{\mathrm{s}}$ is the one due to the presence of media.

The Green tensor allows us to write the solution to the Helmholtz equation as simply

$$\mathbf{E}(\mathbf{r},\omega)=i\mu_0\omega\int\mathrm{d}^3r'\ \mathbf{G}(\mathbf{r},\mathbf{r}',\omega)\cdot\mathbf{j}_{\mathrm{s}}(\mathbf{r}',\omega). \tag{2.77}$$

Together with Maxwell's equations and the constitutive relations, the other fields can also be straightforwardly written in terms of $\mathbf{G}$, which emphasizes the power of the Green tensor. Indeed, it summarizes the full EM properties of the macroscopic medium, including its composition and geometry through $\varepsilon(\mathbf{r},\omega)$ and $\mu(\mathbf{r},\omega)$, and has a simple physical interpretation as the electric field at point $\mathbf{r}$ produced by an oscillating point dipole at point $\mathbf{r}'$, modulo some constants. The downside is that, as is usually the case, with great power comes little analytical insight. In fact, finding a closed form for $\mathbf{G}$ is only possible in highly symmetric configurations, and the resulting expressions tend to be quite involved, so one is often forced to resort to numerical methods. More specifically, it is $\mathbf{G}^{\mathrm{s}}$ that generally requires a numerical approach, as $\mathbf{G}^0$ follows an analytical expression (see appendix C). Still, there are a number of convenient properties that $\mathbf{G}$ fulfills, some of which will prove extremely useful for MQED and for some calculations presented in this thesis. We highlight a few here for reference [204]:

$$\mathbf{G}^*(\mathbf{r},\mathbf{r}',\omega)=\mathbf{G}(\mathbf{r},\mathbf{r}',-\omega^*), \tag{2.78a}$$

$$\mathbf{G}^{\mathrm{t}}(\mathbf{r},\mathbf{r}',\omega)=\mathbf{G}(\mathbf{r}',\mathbf{r},\omega)\quad\text{and} \tag{2.78b}$$

$$\operatorname{Im}\mathbf{G}(\mathbf{r},\mathbf{r}',\omega)=\int\mathrm{d}^3s\left\{-\frac{\operatorname{Im}\mu(\mathbf{s},\omega)}{|\mu(\mathbf{s},\omega)|^2}[\nabla_{\mathbf{s}}\times\mathbf{G}(\mathbf{s},\mathbf{r},\omega)]^{\mathrm{t}}\cdot[\nabla_{\mathbf{s}}\times\mathbf{G}^*(\mathbf{s},\mathbf{r}',\omega)]\right.$$

$$+\frac{\omega^2 \mathrm{Im}\,\varepsilon(\mathbf{s},\omega)}{c^2}\mathbf{G}^{\mathrm{t}}(\mathbf{s},\mathbf{r},\omega)\cdot\mathbf{G}^{*}(\mathbf{s},\mathbf{r}',\omega')\Big\}, \tag{2.78c}$$

where the superscript "t" denotes matrix transposition. The complicated look of the last identity can be made conceptually simpler by noticing that $\mathbf{G}$ is, by definition, the inverse of the Helmholtz differential operator in eqs. (2.75) and (2.76), which we may represent here by $\mathbf{H}$:

$$\mathbf{H}(\mathbf{r},\mathbf{r}') = \delta(\mathbf{r}-\mathbf{r}')\left[\nabla_{\mathbf{r}}\times\frac{1}{\mu}\nabla_{\mathbf{r}}\times -\frac{\omega^2}{c^2}\varepsilon(\mathbf{r},\omega)\right]. \tag{2.79}$$

Then, eq. (2.76) can be succinctly written as $\mathbf{H}\cdot\mathbf{G}=\mathbf{1}$, where the dot product involves a spatial integration, and the $\mathbf{1}$ represents $\delta(\mathbf{r}-\mathbf{r}')$. With this compact notation, eq. (2.78c) follows from

$$\mathrm{Im}\,\mathbf{G} = \frac{\mathbf{G}-\mathbf{G}^{\dagger}}{2i} = \frac{\mathbf{G}\cdot\mathbf{H}^{\dagger}\cdot\mathbf{G}^{\dagger}-\mathbf{G}\cdot\mathbf{H}\cdot\mathbf{G}^{\dagger}}{2i} = \frac{\mathbf{G}\cdot\left(\mathbf{H}^{\dagger}-\mathbf{H}\right)\cdot\mathbf{G}^{\dagger}}{2i} \tag{2.80}$$

where the † involves complex conjugation and transposition of both spatial and position (continuous) indices (see appendix A in [206] for a more detailed account of these manipulations).

2.2.2 Quantization of macroscopic electrodynamics

After the overview of macroscopic electrodynamics, a natural question to ask is what happens if one tries to quantize it directly. The most direct quantization route directly mirrors section 2.1, and would require finding a classical Lagrangian with the macroscopic Maxwell equations as equations of motion. At that point, quantization would be straightforward by passing to the Hamiltonian formalism. Indeed, this idea was pursued since the early days of QED for lossless dielectrics [207–209], and with some success at that. The problem came when it was attempted to extend the same idea to dissipative media. As we have pointed out before, the Kramers-Kronig relations establish an intimate relation between dissipation and dispersion. The reason for the problem is readily seen in the constitutive relations. If χ depends non-trivially on ω, with the ensuing dissipation, Fourier-transforming eq. (2.72a) to the time domain yields a relation between $\mathbf{D}$ and $\mathbf{E}$ that is non-local in time. Since the effective Lagrangian depends on both, it becomes non-local as well, which hinders its quantization [210].

Macroscopic QED offers an elegant solution to the problems caused by the dissipation. In a display of premonitory prowess, Hillery and Mlodinow concluded in ref. [208] that "the best way to proceed is to consider a microscopic

theory, i.e., fields plus matter, and to see if an effective macroscopic theory can be developed" and that "this effective theory should have as its basic objects collective matter-field modes". Actually, this observation would become the basis for MQED. Huttner and Barnett published in 1992 an article showing how to include a microscopic model for matter in the problem [210]. More specifically, as sketched in fig. 2.2, they described the matter part through its polarization field, decomposed into harmonic oscillators b_μ. Then, each polarization oscillator is coupled to both the EM modes a_μ and a reservoir of matter modes $c_\mu(\omega)$ that takes care of the dissipation in the material. The main idea of the Huttner-Barnett model is to diagonalize the full light-matter problem, reaching a new set of matter-field (polaritonic) modes $f_\mu(\omega)$. Conceptually, this model is a close precursor to the modern view of MQED, which resulted from a number of works refining and extending the theory to linear and dispersive magneto-dielectrics [206, 211–215], even with non-local and non-reciprocal responses [216]. We next review the basic definitions of MQED [204].

The fundamental building blocks of the theory are the vector bosonic operators $\mathbf{f}_\lambda^{(\dagger)}(\mathbf{r},\omega)$ that generalize the $f_\mu^{(\dagger)}(\omega)$ of the Huttner-Barnett model, which satisfy the usual commutation relations:

$$\left[\mathbf{f}_\lambda(\mathbf{r},\omega),\mathbf{f}_{\lambda'}^\dagger(\mathbf{r}',\omega')\right] = \delta_{\lambda\lambda'}\boldsymbol{\delta}(\mathbf{r}-\mathbf{r}')\delta(\omega-\omega') \quad \text{and} \tag{2.81a}$$

$$\left[\mathbf{f}_\lambda(\mathbf{r},\omega),\mathbf{f}_{\lambda'}(\mathbf{r}',\omega')\right] = \left[\mathbf{f}_\lambda^\dagger(\mathbf{r},\omega),\mathbf{f}_{\lambda'}^\dagger(\mathbf{r}',\omega')\right] = \mathbf{0}. \tag{2.81b}$$

Each scalar component of these operators annihilates (creates) an excitation, which can be either electric ($\lambda = \mathrm{e}$) or magnetic ($\lambda = \mathrm{m}$) in nature, at $\mathbf{r}$ along one Cartesian axis, such that:

$$\mathbf{u}\cdot\mathbf{f}_\lambda^\dagger(\mathbf{r},\omega)|0\rangle = \sum_i u_i|1_{\lambda,i}(\mathbf{r},\omega)\rangle \tag{2.82}$$

for any vector $\mathbf{u}$ with coordinates u_i. These excitations, which possess a mixed light-matter character, build together the medium-assisted fields. Finally, because the polaritonic operators diagonalize the light-media Hamiltonian, their

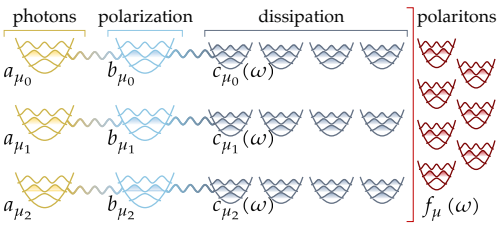

Figure 2.2: Schematic depiction of the light and matter modes of the Huttner-Barnett model. The situation is conceptually similar in MQED.

dynamics is dictated by the Hamiltonian

$$H_{\mathrm{f}} = \sum_{\lambda} \int \mathrm{d}^3 r \int_0^\infty \mathrm{d}\omega\, \hbar\omega\, \mathbf{f}_\lambda^\dagger(\mathbf{r},\omega)\cdot\mathbf{f}_\lambda(\mathbf{r},\omega). \tag{2.83}$$

Up to a prefactor that fixes the dimensions, one can think of $\mathbf{f}_{\mathrm{e}}$ and $\mathbf{f}_{\mathrm{m}}$ as infinitesimal oscillating electric or magnetic dipoles, respectively, that create both electric and magnetic fields. Therefore, the EM fields are built as expansions in the polaritonic operators:

$$\mathbf{E}(\mathbf{r}) = \sum_{\lambda} \int \mathrm{d}^3 r' \int_0^\infty \mathrm{d}\omega\, \mathbf{G}_\lambda(\mathbf{r},\mathbf{r}',\omega)\cdot\mathbf{f}_\lambda(\mathbf{r}',\omega) + \mathrm{H.c.}, \tag{2.84}$$

and similarly for the other fields, where the coefficients are related to the Green tensor through

One might try to directly test whether free-space QED is contained in MQED by taking the $\mathrm{Im}\,\varepsilon = \mathrm{Im}\,\mu = 0$ limit in these equations. However, the coefficients $\mathbf{G}_\lambda$ become zero and the analysis loses its meaning. Instead, the correct free-space limit must be taken a posteriori, after performing all spatial integrations.

$$\mathbf{G}_{\mathrm{e}}(\mathbf{r},\mathbf{r}',\omega) = i\frac{\omega^2}{c^2}\sqrt{\frac{\hbar}{\pi\varepsilon_0}\mathrm{Im}\,\varepsilon(\mathbf{r}',\omega)}\mathbf{G}(\mathbf{r},\mathbf{r}',\omega) \quad \text{and} \tag{2.85a}$$

$$\mathbf{G}_{\mathrm{m}}(\mathbf{r},\mathbf{r}',\omega) = i\frac{\omega}{c}\sqrt{\frac{\hbar}{\pi\varepsilon_0}\frac{\mathrm{Im}\,\mu(\mathbf{r}',\omega)}{|\mu(\mathbf{r}',\omega)|^2}}[\nabla'\times\mathbf{G}(\mathbf{r}',\mathbf{r},\omega)]^{\mathrm{t}}. \tag{2.85b}$$

These coefficients, which allow us to more compactly write eq. (2.78c) as

$$\sum_{\lambda}\int \mathrm{d}^3 s\, \mathbf{G}_\lambda(\mathbf{r},\mathbf{s},\omega)\cdot\mathbf{G}_\lambda^{*\mathrm{t}}(\mathbf{r}',\mathbf{s},\omega) = \frac{\hbar\omega^2}{\pi\varepsilon_0 c^2}\mathrm{Im}\,\mathbf{G}(\mathbf{r},\mathbf{r}',\omega), \tag{2.86}$$

essentially tell us how the field propagates from its sources, at $\mathbf{r}'$, to $\mathbf{r}$, as sketched in fig. 2.3. After contemplating eq. (2.84), it is interesting to recall from section 2.1 that $\mathbf{E}^\perp$ and $\mathbf{E}^\parallel$ are fundamentally different fields, with the former being related to photons while the latter to the charges in the medium. Still, in spite of their disparity, they are both expressed in terms of the same $\mathbf{f}_\lambda$ operators, which reinforces the fact that the $\mathbf{f}_\lambda$ are the polaritonic eigenmodes of the full light-medium system. It is, therefore, not surprising that both longitudinal and transverse excitations are captured by them. Nevertheless, we can separate them through the left-longitudinal and left-transverse components of the Green tensor:

$$\mathbf{E}^{\parallel/\perp}(\mathbf{r}) = \sum_{\lambda}\int \mathrm{d}^3 r' \int_0^\infty \mathrm{d}\omega\, {}^{\parallel/\perp}\mathbf{G}_\lambda(\mathbf{r},\mathbf{r}',\omega)\cdot\mathbf{f}_\lambda(\mathbf{r}',\omega) + \mathrm{H.c.}, \tag{2.87}$$

where

$${}^{\parallel/\perp}\mathbf{G}_\lambda(\mathbf{r},\mathbf{r}',\omega) = \int \mathrm{d}^3 s\, \boldsymbol{\delta}^{\parallel/\perp}(\mathbf{r}-\mathbf{s})\cdot\mathbf{G}_\lambda(\mathbf{s},\mathbf{r}',\omega). \tag{2.88}$$

This way, it becomes clear that the left-longitudinal and left-transverse coeffi-

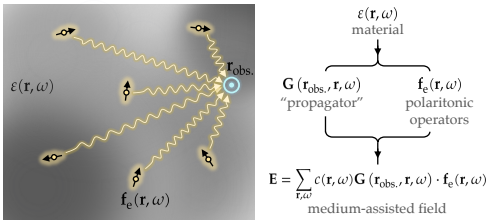

Figure 2.3: Schematic view of the physical meaning of MQED. A material charaterized by $\varepsilon(\mathbf{r},\omega)$ is described through the fundamental polaritonic operators $\mathbf{f}_e(\mathbf{r},\omega)$, that create an electric field at the observation position $\mathbf{r}_{\text{obs.}}$ according to the full Green tensor $\mathbf{G}(\mathbf{r}_{\text{obs.}},\mathbf{r},\omega)$.

cients project the operators from the hybrid light-matter basis $(\mathbf{f}_\lambda(\mathbf{r},\omega))$ onto the purely material and purely photonic DOF.

We finish our presentation of the relation between the polaritonic operators and the fields by writing the expressions for the Coulomb vector and scalar potentials:

$$\mathbf{A}^\perp(\mathbf{r}) = \sum_\lambda \int \mathrm{d}^3r' \int_0^\infty \mathrm{d}\omega\, \frac{1}{i\omega}\,{}^\perp\mathbf{G}_\lambda(\mathbf{r},\mathbf{r}',\omega)\cdot\mathbf{f}_\lambda(\mathbf{r}',\omega) + \text{H.c.} \quad \text{and} \tag{2.89a}$$

$$-\nabla\phi_C(\mathbf{r}) = \mathbf{E}^\parallel(\mathbf{r}) = \sum_\lambda \int \mathrm{d}^3r' \int_0^\infty \mathrm{d}\omega\, {}^\parallel\mathbf{G}_\lambda(\mathbf{r},\mathbf{r}',\omega)\cdot\mathbf{f}_\lambda(\mathbf{r}',\omega) + \text{H.c.} \tag{2.89b}$$

By using the explicit formula for $\boldsymbol{\delta}^\parallel$ given in appendix A.3, we can also find

$$\phi_C(\mathbf{r}) = -\frac{1}{4\pi}\sum_\lambda \int \mathrm{d}^3r'\,\mathrm{d}^3s\,\nabla_{\mathbf{s}}\left(\frac{1}{|\mathbf{r}-\mathbf{s}|}\right)\cdot\mathbf{G}_\lambda(\mathbf{s},\mathbf{r}',\omega)\cdot\mathbf{f}_\lambda(\mathbf{r}',\omega) + \text{H.c.} \tag{2.89c}$$

Like eq. (2.87), these expressions reinforce the interpretation of ${}^{\parallel/\perp}\mathbf{G}_\lambda$ as the projection coefficients onto photonic and material DOF. The expansion of $\mathbf{A}^\perp$ above also implies that, as in free-space,

$$\left[\mathbf{A}^\perp(\mathbf{r}), \mathbf{E}^\perp(\mathbf{r})\right] = i\hbar\boldsymbol{\delta}^\perp(\mathbf{r}-\mathbf{r}'). \tag{2.90}$$

Thus far, we have discussed the building blocks of the theory, as well as how they fit together to recover observables from macroscopic electrodynamics. In the process, we have placed much of the emphasis on the $\mathbf{f}_\lambda$ as the operators that diagonalize the light-medium Hamiltonian, generalizing the conceptual approach of the Huttner-Barnett model. However, we have not discussed the precise steps from which the $\mathbf{f}_\lambda$ follow. There are two main options. The first one is the canonical approach to MQED [217], conceptually closer to the Huttner-Barnett model. In it, the starting point is a Lagrangian that includes the medium reservoirs, and whose equations of motion describe macroscopic

electrodynamics. Then, the constrained theory is quantized and, finally, diagonalized to recover the $\mathbf{f}_\lambda$. The other approach is more phenomenological in that it builds the theory in order to fulfill three physically motivated requirements: (i) the equations of motion of the fields must be Maxwell's equations in matter; (ii) the commutation relations of $\mathbf{E}^\perp$ and $\mathbf{B}$ must agree with the free-space theory, since they are purely photonic DOF; and (iii) the EM quantum fluctuations must comply with the fluctuation-dissipation theorem that connects both phenomena. These conditions can be satisfied by introducing a "noise" current $\mathbf{j}$ that can be decomposed into polarization and magnetization currents

$$\mathbf{j}(\mathbf{r},\omega) = -i\omega\mathbf{P}(\mathbf{r},\omega) + \nabla\times\mathbf{M}(\mathbf{r},\omega). \tag{2.91}$$

The following vacuum fluctuations are then imposed on the quantum currents

$$\left\langle S\big[\Delta\mathbf{P}(\mathbf{r},\omega)\Delta\mathbf{P}^\dagger(\mathbf{r}',\omega')\big]\right\rangle = \frac{\hbar}{2\pi}\varepsilon_0 \operatorname{Im}\chi(\mathbf{r},\omega)\delta(\mathbf{r}-\mathbf{r}')\delta(\omega-\omega') \tag{2.92a}$$

$$\left\langle S\big[\Delta\mathbf{M}(\mathbf{r},\omega)\Delta\mathbf{M}^\dagger(\mathbf{r}',\omega')\big]\right\rangle = \frac{\hbar}{2\pi}\frac{\operatorname{Im}\zeta(\mathbf{r},\omega)}{\mu_0}\delta(\mathbf{r}-\mathbf{r}')\delta(\omega-\omega') \tag{2.92b}$$

in accordance with the fluctuation-dissipation theorem. These can be enforced by relating $\mathbf{P}$ and $\mathbf{M}$ to some bosonic operators through

$$\mathbf{P}(\mathbf{r},\omega) = i\sqrt{\frac{\hbar\varepsilon_0}{\pi}\operatorname{Im}\varepsilon(\mathbf{r},\omega)}\mathbf{f}_\mathrm{e}(\mathbf{r},\omega) \quad \text{and} \tag{2.93a}$$

$$\mathbf{M}(\mathbf{r},\omega) = \sqrt{\frac{\hbar}{\pi\mu_0}\frac{\operatorname{Im}\mu(\mathbf{r},\omega)}{|\mu(\mathbf{r},\omega)|^2}}\mathbf{f}_\mathrm{m}(\mathbf{r},\omega), \tag{2.93b}$$

and, of course, these turn out to be the MQED polaritonic operators. Finally, the classical EM Green tensor translates the currents to the fields via equations like eq. (2.84). The resulting expressions are the same in either approach, albeit reached from a different set of assumptions.

Before concluding our quick overview of the fundamentals of MQED, we must point out a detail that has made some physicists wary of the theory. If one pays close attention to the coefficients that appear in the field expansions $\mathbf{G}_\lambda$ defined in eq. (2.85), one can observe that they are proportional to $\sqrt{\operatorname{Im}\varepsilon(\mathbf{r},\omega)}$ and $\sqrt{\operatorname{Im}\mu(\mathbf{r},\omega)}$. As a result, directly taking the free-space limit through $(\varepsilon,\mu)\to(1,1)$ yields $\mathbf{E}=\mathbf{0}$, and similarly for the other fields; that is clearly not the correct free-space limit. The workaround argument is that the limit should be taken after all the spatial integrations have been performed, such that $\operatorname{Im}\varepsilon$ and $\operatorname{Im}\mu$ are no longer present in the final expressions. Then, the limit reproduces the free-space fields. Nevertheless, not everyone finds this procedure convincing enough, which has prompted an alternative ap-

proach that shares its starting point with the canonical version in [217]. The difference is that the medium and free-space regions are kept, to some extent, separate, providing explicit control over the limit $(\varepsilon, \mu) \to (1, 1)$ [218–220]. The final result, however, seems to be equivalent to the formulation of MQED provided above, especially given the central role that $\mathrm{Im}\,\mathbf{G}$ ends up playing in both. In the next sections, we will discuss the coupling of atoms to the medium-assisted fields and some aspects of gauge freedom.

2.2.3 Atoms and MQED fields

Up to this point, we have seen how MQED accounts for the EM fields supported by material structures. It is now time to turn our focus to the interaction of those medium-assisted fields with additional charges besides the macroscopic media. In practice, these charges can be atomic or molecular systems, or other kinds of emitters. Their only particular feature is that they must be small enough that they can be treated explicitly, rather than effectively as the larger material structures are. For brevity, we will write atoms throughout this section to refer to the quantum emitters, and, for convenience, we first extract the center-of-mass and relative coordinates and momenta of the atomic system of charges [202]:

$$\mathbf{r}_{\mathrm{at}} = \sum_i \frac{m_i}{m_{\mathrm{at}}} \mathbf{r}_i, \qquad \bar{\mathbf{r}}_i = \mathbf{r}_i - \mathbf{r}_{\mathrm{at}} \quad \text{and} \tag{2.94a}$$

$$\mathbf{p}_{\mathrm{at}} = \sum_i \mathbf{p}_i, \qquad \bar{\mathbf{p}}_i = \mathbf{p}_i - \frac{m_i}{m_{\mathrm{at}}} \mathbf{p}_{\mathrm{at}}, \tag{2.94b}$$

where $m_{\mathrm{at}} = \sum_i m_i$, and the only "non-standard" commutation relation is

$$\left[\bar{\mathbf{r}}_i, \bar{\mathbf{p}}_j\right] = i\hbar \mathbf{1} \left(\delta_{ij} - \frac{m_j}{m_{\mathrm{at}}} \right). \tag{2.94c}$$

The above commutator follows from the fact that, with the addition of the center-of-mass variable, we have included three more coordinates for the same system. Thus, they cannot all be canonically independent. Interestingly, there is an alternative choice of variables, namely, the center-of-mass coordinates and the electronic coordinates relative to the nucleus. This choice does not carry any non-standard commutation relation, but brings with it an additional so-called mass polarization term [221], whose effect is usually negligible. For example, if we consider an atom with a single nucleus, the mass polarization term is

$$\frac{1}{m_{\mathrm{nuc}}} \sum_{i<j}^{\text{electrons}} \bar{\mathbf{p}}_i \cdot \bar{\mathbf{p}}_j. \tag{2.95}$$

Given our current goal of explaining the formalism, the choice is not really important, although, in practice, the difference can matter. For concreteness, we follow [204] here and set the coordinates to be those given in eq. (2.94).

The atomic polarization and magnetization, referred to the center-of-mass coordinate $\mathbf{r}_{\mathrm{at}}$ are defined as

$$\mathbf{P}_{\mathrm{at}}(\mathbf{r}) = \sum_i q_i \bar{\mathbf{r}}_i \int_0^1 \mathrm{d}\sigma\, \delta^{(3)}(\mathbf{r} - \mathbf{r}_{\mathrm{at}} - \sigma\bar{\mathbf{r}}_i) \quad \text{and} \tag{2.96a}$$

$$\mathbf{M}_{\mathrm{at}}(\mathbf{r}) = \sum_i q_i \int_0^1 \mathrm{d}\sigma\, \sigma S\big[\bar{\mathbf{r}}_i \times \dot{\bar{\mathbf{r}}}_i \delta^{(3)}(\mathbf{r} - \mathbf{r}_{\mathrm{at}} - \sigma\bar{\mathbf{r}}_i)\big]. \tag{2.96b}$$

In the following, we express the atom-field interaction in the minimal coupling and multipolar coupling pictures.

Minimal coupling in MQED

According to the minimal coupling prescription, the MQED Hamiltonian of an atom interacting with the medium-assisted fields is, in the Coulomb gauge,

$$\begin{aligned} H = &\sum_i \frac{\big(\mathbf{p}_i - q_i \mathbf{A}^{\perp}(\mathbf{r}_i)\big)^2}{2m_i} + \sum_{i\neq j} \frac{q_i q_j}{8\pi\varepsilon_0 |\mathbf{r}_i - \mathbf{r}_j|} \\ &+ \underbrace{\sum_\lambda \int \mathrm{d}^3 r \int_0^\infty \mathrm{d}\omega\, \hbar\omega\, \mathbf{f}_\lambda^\dagger(\mathbf{r},\omega)\cdot\mathbf{f}_\lambda(\mathbf{r},\omega)}_{H_{\mathrm{f}}} - \int \mathrm{d}^3 r\, \mathbf{P}_{\mathrm{at}}\cdot\mathbf{E}^{\parallel}. \end{aligned} \tag{2.97a}$$

Expanding the square yields

$$\begin{aligned} H = &\sum_i \frac{\mathbf{p}_i^2}{2m_i} + \sum_{i\neq j} \frac{q_i q_j}{8\pi\varepsilon_0 |\mathbf{r}_i - \mathbf{r}_j|} + H_{\mathrm{f}} - \int \mathrm{d}^3 r\, \mathbf{P}_{\mathrm{at}}\cdot\mathbf{E}^{\parallel} \\ &- \sum_i \frac{q_i}{m_i}\mathbf{p}_i\cdot\mathbf{A}^{\perp}(\mathbf{r}_i) + \sum_i \frac{q_i^2}{2m_i}\big(\mathbf{A}^{\perp}(\mathbf{r}_i)\big)^2, \end{aligned} \tag{2.97b}$$

which becomes, in the long-wavelength limit,

$$\begin{aligned} H = &\frac{\mathbf{p}_{\mathrm{at}}}{2m_{\mathrm{at}}} + \sum_i \frac{\bar{\mathbf{p}}_i^2}{2m_i} + \sum_{i\neq j} \frac{q_i q_j}{8\pi\varepsilon_0 |\bar{\mathbf{r}}_i - \bar{\mathbf{r}}_j|} + H_{\mathrm{f}} - \mathbf{d}\cdot\mathbf{E}^{\parallel}(\mathbf{r}_{\mathrm{at}}) \\ &- \sum_i \frac{q_i}{m_i}\bar{\mathbf{p}}_i\cdot\mathbf{A}^{\perp}(\mathbf{r}_{\mathrm{at}}) + \sum_i \frac{q_i^2}{2m_i}\big(\mathbf{A}^{\perp}(\mathbf{r}_{\mathrm{at}})\big)^2, \end{aligned} \tag{2.97c}$$

where $\mathbf{d}$ is the atomic dipole moment operator:

$$\mathbf{d} = \sum_i q_i \mathbf{r}_i = \sum_i q_i \bar{\mathbf{r}}_i. \tag{2.97d}$$

Note that the second equality holds for neutral atoms only. This will be the limit of interest for the results presented in this thesis.

Multipolar coupling in MQED

Like in non-relativistic QED, we can change the quantum picture as well through the MQED version of the PZW transformation with the atomic polarization:

$$T = \exp\left\{-\frac{i}{\hbar}\int \mathrm{d}^3 r\, \mathbf{P}_{\mathrm{at}} \cdot \mathbf{A}^{\perp}\right\}. \tag{2.98}$$

Conceptually, this operator implements a "partial PZW" transformation, in that the charges in the macroscopic structure are excluded. Of course, it would not be very useful to include them in this PZW transformation, as they are already neatly bundled together with the purely photonic DOF in MQED.

Performing the transformation is a lengthy and instructive endeavor whose details can be found in appendix D. Here, we restrict ourselves to writing the multipolar coupling Hamiltonian

$$\begin{aligned} H = &\sum_i \frac{1}{2m_i} S\Big[\mathbf{p}_i + \int \mathrm{d}^3 r\, \boldsymbol{\Xi}_i \times \mathbf{B}\Big]^2 + \sum_{i\neq j} \frac{q_i q_j}{8\pi\varepsilon_0 |\mathbf{r}_i - \mathbf{r}_j|} + \frac{1}{2\varepsilon_0}\int \mathrm{d}^3 r\, \left(\mathbf{P}_{\mathrm{at}}^{\perp}\right)^2 \\ &+ H_{\mathrm{f}} - \frac{1}{\varepsilon_0}\int \mathrm{d}^3 r\, \mathbf{P}_{\mathrm{at}} \cdot \mathbf{D}_{(\mathrm{at})}, \end{aligned} \tag{2.99}$$

where

$$\boldsymbol{\Xi}_i(\mathbf{r}) = \sum_j q_j \bar{\mathbf{r}}_j \left(\delta_{ij} - \frac{m_i}{m_{\mathrm{at}}}\right) \int_0^1 \mathrm{d}\sigma\, \sigma\left(\mathbf{r} - \mathbf{r}_{\mathrm{at}} - \sigma\bar{\mathbf{r}}_j\right) + \frac{m_i}{m_{\mathrm{at}}} \mathbf{P}_{\mathrm{at}}(\mathbf{r}). \tag{2.100}$$

A few features of the multipolar Hamiltonian stand out. First, there is an atomic PSE, analogous to the one in eq. (2.38), at the end of the first line. Additionally, the kinetic energy contains a term proportional to the magnetic field similar to the one in eq. (2.38). The fact that this term looks more complicated than its previous QED version is due to the particular choice of coordinates, as the difference can be traced back to the non-standard commutation relation between relative coordinates and momenta in eq. (2.94c). Last, the interaction

between the atom and the field involves

$$\mathbf{D}_{(\mathrm{at})} = \varepsilon_0 \mathbf{E}' + \mathbf{P}_{\mathrm{at}}^{\perp} \stackrel{!}{=} \varepsilon_0 \mathbf{E}. \tag{2.101}$$

Here, the last equality indicates that $\mathbf{D}_{(\mathrm{at})}/\varepsilon_0$ coincides with $\mathbf{E}$ as an expansion in terms of the operators $\mathbf{f}_\lambda$ in eq. (2.84). However, it does not represent the physical medium-assisted electric field in the multipolar coupling picture; that task is fulfilled by $\mathbf{E}'$. Instead, it physically corresponds to a sort of displacement field where only the transverse atomic polarization is included, thus the change of name and subscript.

We conclude this section on the coupling of atoms to the fields in MQED by making the long-wavelength approximation to eq. (2.99), and assuming that the atomic's magnetic response and center-of-mass motion are negligible:

$$\begin{aligned} H = {} & \frac{\mathbf{p}_{\mathrm{at}}}{2m_{\mathrm{at}}} + \sum_i \frac{\bar{\mathbf{p}}_i^2}{2m_i} + \sum_{i\neq j} \frac{q_i q_j}{8\pi\varepsilon_0 |\bar{\mathbf{r}}_i - \bar{\mathbf{r}}_j|} + \frac{1}{2\varepsilon_0} \int \mathrm{d}^3 r \, \left(\mathbf{P}_{\mathrm{at}}^{\perp}\right)^2 \\ & + H_{\mathrm{f}} - \frac{1}{\varepsilon_0} \mathbf{d} \cdot \mathbf{D}_{(\mathrm{at})}(\mathbf{r}_{\mathrm{at}}). \end{aligned} \tag{2.102}$$

As before, this is the limit that we will usually work with.

2.2.4 Gauge freedom in MQED

General discussions of gauge freedom in MQED have been few and far between, although some works in this direction have been published [222, 223]. Indeed, we only mentioned the potentials after introducing every other concept in section 2.2.2. A possible reason for this lack of attention is that, for most purposes, the minimal coupling or multipolar coupling Hamiltonians in the Coulomb gauge have been convenient enough, as in molecular QED. We do not aim at providing a comprehensive overview of gauge invariance in MQED. Rather, we analyze a particular gauge transformation that has, as we will see at the end, implications regarding published results [224].

As in section 2.1, the multipolar coupling picture can be seen as obtained through a gauge transformation, but it is not strictly necessary to change what we call **A** since the potentials are not explicit in the Hamiltonian.

Consider the following unitary transformation

$$T = \exp\left\{ \frac{i}{\hbar} \sum_i q_i \chi(\mathbf{r}_i) \right\} = \exp\left\{ \frac{i}{\hbar} \int \mathrm{d}^3 r \, \mathbf{P}_{\mathrm{at}} \cdot \nabla\chi \right\}, \tag{2.103}$$

where $\mathbf{P}_{\mathrm{at}}$ is the atom's polarization and

$$\nabla\chi(\mathbf{r}) = \sum_\lambda \int \mathrm{d}^3 r' \int \mathrm{d}\omega \, \frac{1}{i\omega} {}^{\parallel}\mathbf{G}_\lambda(\mathbf{r}, \mathbf{r}', \omega) \cdot \mathbf{f}_\lambda(\mathbf{r}', \omega) + \mathrm{H.c.} \tag{2.104}$$

As we have seen in section 2.1.2, this kind of unitary transformation can be seen to implement a gauge transformation, because it is of the form described in eq. (2.25). Starting from the Hamiltonian in eq. (2.97a), we transform the operators of the atom's kinetic energy:

$$T\mathbf{p}_i T^\dagger = \mathbf{p}_i - q_i \nabla_{\mathbf{r}_i} \chi(\mathbf{r}_i) \quad \text{and} \tag{2.105a}$$

$$T\mathbf{A}^\perp T^\dagger = \mathbf{A}^\perp. \tag{2.105b}$$

The momentum one results from a trivial application of eq. (A.46) that terminates at the first commutator. As for the transformation of the vector potential operator, its derivation is more involved, and done explicitly in appendix C.2. Remember that, in line with section 2.1.2, $\mathbf{p}_i$ is still the canonical momentum operator, which now represents a different quantity. With these relations, the atom's kinetic energy becomes

$$\sum_i \frac{\left[\mathbf{p}_i - q_i\left(\mathbf{A}^\perp(\mathbf{r}_i) + \nabla\chi(\mathbf{r}_i)\right)\right]^2}{2m_i}. \tag{2.106}$$

From eq. (2.106), we can read the vector potential that corresponds to the new gauge as

$$\mathbf{A}'(\mathbf{r}) = \sum_\lambda \int \mathrm{d}^3 r' \int_0^\infty \mathrm{d}\omega \, \frac{1}{i\omega} \mathbf{G}_\lambda(\mathbf{r}, \mathbf{r}', \omega) \cdot \mathbf{f}_\lambda(\mathbf{r}', \omega) + \text{H.c.}, \tag{2.107}$$

which corresponds to the expansion in eq. (2.89a), except for the absence of a transverse superscript. Hence, longitudinal fields are, to some degree at least, included in $\mathbf{A}$. Obviously, $T\mathbf{P}_{\text{at}}T^\dagger = \mathbf{P}_{\text{at}}$ and $T\mathbf{r}_i T^\dagger = \mathbf{r}_i$, and we also obtain

$$T\mathbf{f}_\lambda(\mathbf{r}, \omega)T^\dagger = \mathbf{f}_\lambda(\mathbf{r}, \omega) + \frac{1}{\hbar\omega} \int \mathrm{d}^3 s \, \mathbf{P}_{\text{at}}(\mathbf{s}) \cdot {}^{\parallel}\mathbf{G}_\lambda(\mathbf{s}, \mathbf{r}, \omega), \tag{2.108}$$

which can be seen as an application of the displacement operator, to transform the fields (see appendix A.4). With this relation, we have

$$\begin{aligned} T H_{\text{f}} T^\dagger = H_{\text{f}} &+ \int \mathrm{d}^3 r \, \mathbf{P}_{\text{at}} \cdot \mathbf{E}^{\parallel} + \frac{1}{2\varepsilon_0} \int \mathrm{d}^3 r \left(\mathbf{P}_{\text{at}}^{\parallel}\right)^2 \\ &+ \frac{1}{2\varepsilon_0} \int \mathrm{d}^3 r \, \mathrm{d}^3 s \, \mathbf{P}_{\text{at}}(\mathbf{r}) \cdot \left(\frac{\omega^2}{c^2} {}^{\parallel}\mathbf{G}^{\parallel}(\mathbf{r}, \mathbf{s}, \omega) \right)\Big|_{\omega=0} \cdot \mathbf{P}_{\text{at}}(\mathbf{s}) \quad \text{and} \end{aligned} \tag{2.109a}$$

$$\begin{aligned} T\mathbf{E}^{\parallel}(\mathbf{r})T^\dagger = \mathbf{E}^{\parallel}(\mathbf{r}) &+ \frac{1}{\varepsilon_0} \mathbf{P}_{\text{at}}^{\parallel}(\mathbf{r}) \\ &+ \frac{1}{\varepsilon_0} \int \mathrm{d}^3 s \left(\frac{\omega^2}{c^2} {}^{\parallel}\mathbf{G}^{\parallel}(\mathbf{r}, \mathbf{s}, \omega) \right)\Big|_{\omega=0} \cdot \mathbf{P}_{\text{at}}(\mathbf{s}), \end{aligned} \tag{2.109b}$$

where we have used eq. (2.86). Again, the detailed derivations are in appendix C.2. In this case, $\mathbf{E}^{\parallel}$ is expressed in terms of $\mathbf{f}_\lambda$ through eq. (2.87). However, the notation is unfortunate because, in the new picture, the operator $\mathbf{E}^{\parallel}$ no longer really represents the longitudinal component of the physical electric field. Instead, the full right-hand side of eq. (2.109b) does. Bringing everything together, we arrive at

$$\begin{aligned} H' &= \sum_i \frac{\left(\mathbf{p}_i - q_i \mathbf{A}'(\mathbf{r}_i)\right)^2}{2m_i} + \sum_{i\neq j} \frac{q_i q_j}{8\pi\varepsilon_0 |\mathbf{r}_i - \mathbf{r}_j|} + H_\mathrm{f} - \frac{1}{2\varepsilon_0} \int \mathrm{d}^3 r \left(\mathbf{P}_\mathrm{at}^{\parallel}\right)^2 \\ &\quad - \frac{1}{2\varepsilon_0} \int \mathrm{d}^3 r \, \mathrm{d}^3 s \, \mathbf{P}_\mathrm{at}(\mathbf{r}) \cdot \left(\frac{\omega^2}{c^2} {}^{\parallel}\mathbf{G}^{\parallel}(\mathbf{r}, \mathbf{s}, \omega) \right)\Big|_{\omega=0} \cdot \mathbf{P}_\mathrm{at}(\mathbf{s}) \\ &= \sum_i \frac{\left(\mathbf{p}_i - q_i \mathbf{A}'(\mathbf{r}_i)\right)^2}{2m_i} + \sum_{i\neq j} \frac{q_i q_j}{8\pi\varepsilon_0 |\mathbf{r}_i - \mathbf{r}_j|} + H_\mathrm{f} \\ &\quad - \frac{1}{2\varepsilon_0} \int \mathrm{d}^3 r \, \mathrm{d}^3 s \, \mathbf{P}_\mathrm{at}(\mathbf{r}) \cdot \left(\frac{\omega^2}{c^2} {}^{\parallel}\mathbf{G}^{\mathrm{s}\parallel}(\mathbf{r}, \mathbf{s}, \omega) \right)\Big|_{\omega=0} \cdot \mathbf{P}_\mathrm{at}(\mathbf{s}), \end{aligned} \tag{2.110}$$

where we have reached the last expression by noting that the Green tensor can be split into $\mathbf{G} = \mathbf{G}^0 + \mathbf{G}^\mathrm{s}$, and that the free-space term gives

$$\lim_{\omega\to 0} \frac{\omega^2}{c^2} {}^{\parallel}\mathbf{G}^{0\parallel}(\mathbf{r}, \mathbf{s}, \omega) = -\boldsymbol{\delta}^{\parallel}(\mathbf{r} - \mathbf{s}). \tag{2.111}$$

Accordingly, the free-space part cancels the last term in the first line, and only the scattering contribution stays in the last line. Notably, the final form of the transformed Hamiltonian H', which is necessarily equivalent to the Coulomb gauge Hamiltonian in eq. (2.97a), displays an interesting separation of longitudinal interactions. On one hand, $\mathbf{A}'$ contains longitudinal fields because the full $\mathbf{G}_\lambda$ appears in it, rather than ${}^{\perp}\mathbf{G}_\lambda$ alone. On the other, however, the last line in eq. (2.110) can be seen as a modification to the free-space atomic Coulomb interaction due to electrostatic image charges that form in the structure, i.e., another longitudinal effect. In fact, the last line can be rewritten as

$$-\frac{1}{2} \int \mathrm{d}^3 r \, \mathrm{d}^3 q \, \mathrm{d}^3 s \, \rho_\mathrm{at}(\mathbf{r}) \frac{\nabla_\mathbf{q} \cdot \left[\left(\frac{\omega^2}{c^2} \mathbf{G}^{\mathrm{s}\parallel}(\mathbf{q}, \mathbf{s}, \omega) \right)\Big|_{\omega=0} \cdot \mathbf{P}_\mathrm{at}(\mathbf{s}) \right]}{4\pi\varepsilon_0 |\mathbf{r} - \mathbf{q}|}, \tag{2.112}$$

which, despite its intimidating look, has a simple interpretation: the numerator without the divergence operator is, after integrating over $\mathbf{s}$, the electrostatic field at $\mathbf{q}$ due to the image charges in the structure. Its divergence then yields the induced charge density through eq. (2.1a), which creates a Coulomb potential at $\mathbf{r}$. The interaction is finally written as an integral of this potential over the atomic charge density.

Besides the intrinsic fundamental interest of the manipulations above, the final line in eq. (2.110) implies that the theoretical results of [224] are quantitatively incorrect. In that article, the authors compute energy shifts in atoms close to a graphene sheet. To do so, they claim to choose a particular gauge where

$$\phi' = 0 \quad \text{and} \tag{2.113a}$$

$$\mathbf{A}' = \int \mathrm{d}^3 r' \int_0^\infty \mathrm{d}\omega \, \frac{1}{i\omega} \mathbf{G}_\mathrm{e}(\mathbf{r}, \mathbf{r}', \omega) \cdot \mathbf{f}_\mathrm{e}(\mathbf{r}', \omega) + \mathrm{H.c.}, \tag{2.113b}$$

commonly known as the Weyl gauge or temporal gauge. The vector potential differs from eq. (2.107) in that only $\lambda = \mathrm{e}$ excitations are considered, which merely amounts to assuming that the medium is a dielectric with no magnetic response. Moreover, it is taken for granted that the longitudinal interactions are fully captured by $\mathbf{A}'$, since $\phi' = 0$, and the authors start their calculations from the following light-matter Hamiltonian:

$$H' = \sum_i \frac{\left(\mathbf{p}_i - q_i \mathbf{A}'(\mathbf{r}_i)\right)^2}{2m_i} + \sum_{i \neq j} \frac{q_i q_j}{8\pi\varepsilon_0 |\mathbf{r}_i - \mathbf{r}_j|} + H_\mathrm{f}. \tag{2.114}$$

The problem lies in the fact that their expression for $\mathbf{A}'$ coincides with the one that we have found through our unitary gauge transformation, but we have the additional term given by the last line in eq. (2.110), which is absent from eq. (2.114). Thus, it does not have the same spectrum. Therefore, it cannot be unitarily related to MQED in the Coulomb gauge and, hence, cannot actually reproduce the correct physics. Indeed, the energy shift formula reported in [224] does not agree with the well-established result discussed later on, in eq. (2.143) within section 2.4.1 (see, e.g., the expressions in [204, 225]). Accordingly, such a mismatch renders the quantitative results of that study incompatible with other energy-shift calculations within MQED. All this is to show that one can never be too cautious when playing around with choices of gauge.

2.3 Small quantum emitters: atoms

We have already dedicated some attention to charges clumped into atoms when considering their coupling to the medium-assisted fields of MQED in section 2.2.3. There, we defined the center-of-mass and relative coordinates and their associated momenta. In this section, we will focus on other aspects of atoms, paying special attention to the hydrogen atom in its non-relativistic

and relativistic limits.

2.3.1 Internal degrees of freedom of atoms

If we neglect the atomic center-of-mass motion, we are left with the following Hamiltonian:

$$H_{\text{at}} = \sum_i \frac{\bar{\mathbf{p}}_i^2}{2m_i} + \sum_{i\neq j} \frac{q_i q_j}{8\pi\varepsilon_0 \left|\bar{\mathbf{r}}_i - \bar{\mathbf{r}}_j\right|}. \tag{2.115}$$

Note that this is exactly the atomic Hamiltonian in the minimal coupling picture, although the relative canonical momenta do not coincide with the relative kinetic momenta there. Hence, the physical meaning of H_{at} is not really the same if one considers the atom on its own or interacting with the EM field. However, since it has the same mathematical form regardless, we can build the eigenenergies and eigenfunctions of H_{at} as though there were no photons and without additional considerations. Comparing with the atomic Hamiltonian in the multipolar coupling picture, general presentations on the topic usually include the polarization self-energy (PSE) term in it, as the PSE only depends on atomic operators (see, e.g., [14, 204, 225]). However, when discussing the free space Lamb shift, it is necessary to separately account for the PSE in the calculation. Then, in reality, the bare atomic energies that become corrected by the Lamb shift are, again, the eigenenergies of eq. (2.115), which, in practice, is the unperturbed/uncoupled atomic Hamiltonian. Unfortunately, this point has not always been clearly explained in the literature (see, for example, the last remarks of section 4.2 in [204]). Because the PSE already plays this perturbative role in the Lamb shift, we can regard eq. (2.115) as the bare atomic Hamiltonian.

The coordinates and momenta relative to the center-of-mass ones are not completely independent:

$$\sum_i \bar{\mathbf{p}}_i = \sum_i \left(\mathbf{p}_i - \frac{m_i}{m_{\text{at}}} \mathbf{p}_{\text{at}} \right) = \mathbf{0} \quad \text{and} \tag{2.116a}$$

$$\sum_i \frac{m_i}{m_{\text{at}}} \bar{\mathbf{r}}_i = \sum_i \frac{m_i}{m_{\text{at}}} (\mathbf{r}_i - \mathbf{r}_{\text{at}}) = \mathbf{0}, \tag{2.116b}$$

which again manifests in the non-standard commutation relation in eq. (2.94c). Still, atoms have N electrons bound to the Coulomb potential generated by a nucleus with charge Ne, and a mass more than 10^3 times larger than that of the electrons. Accordingly, the nuclear coordinate $\mathbf{r}_N$ relative to the center of mass will have a negligible dynamics. Furthermore, the center-of-mass coordinate $\mathbf{r}_{\text{at}}$ will be much slower than the internal electronic timescales, and

More precisely, the mass of the nucleons (protons or neutrons) in the nucleus is roughly 1840 times larger than the electron's mass.

can be treated adiabatically. As for the electrons, due to the large mass mismatch, the commutation relation in eq. (2.94c) is actually almost standard, up to deviations of the order of 0.05%.

Again, recall that there is an alternative choice of coordinates that has no non-standard commutation relations, but comes with the additional mass polarization interaction.

In any case, one can, in principle, diagonalize the Hamiltonian given in eq. (2.115) to find its many-body eigenstates $|a\rangle$ and eigenenergies $\hbar\omega_a$. It is generally useful to find the matrix elements of relevant variables in terms of these eigenstates, and we will do so in section 2.3.2. Still, we can already state two useful properties that follow from $[H_{\text{at}}, \bar{\mathbf{r}}_i] = -i\hbar\frac{\bar{\mathbf{p}}_i}{m_i}$ [204]:

$$\sum_i \frac{q_i}{m_i}\langle a|\bar{\mathbf{p}}_i|b\rangle = i\omega_{ab}\sum_i q_i\langle a|\bar{\mathbf{r}}_i|b\rangle = i\omega_{ab}\mathbf{d}_{ab} \quad \text{and} \tag{2.117a}$$

$$\hbar\sum_i \frac{q_i^2}{m_i}\mathbf{1} = \sum_c \omega_{ca}(\mathbf{d}_{ac}\mathbf{d}_{ca} + \mathbf{d}_{ca}\mathbf{d}_{ac}). \tag{2.117b}$$

Here, we have defined $\omega_{ab} = \omega_a - \omega_b$, $\mathbf{d}_{ab}$ is the atomic transition dipole moment, and we note that eq. (2.117b) is usually known as the Thomas-Reiche-Kuhn sum rule.

One last comment is that these eigenstates $|n\rangle$ would be the atomic stationary states if there were no other DOF for it to interact with. As the previous sections show, atoms are not completely isolated, but instead interact with, e.g., EM fields. However, it is still worth exploring the eigenvalue problem of eq. (2.115), as in many cases one can use its solutions as building blocks for the solutions of the full QED problem. To that end, we focus next on the simplest of atoms, the hydrogen atom, and analyze important properties of its spectrum and wave-functions.

2.3.2 The hydrogen atom

A hydrogen atom is a bound system comprised of an electron of mass m_e, position $\mathbf{r}_e$ and momentum $\mathbf{p}_e$, and a nucleus featuring a single proton with mass m_p, position $\mathbf{r}_p$ and momentum $\mathbf{p}_p$. Such a simplified scenario allows one to elegantly deal with the internal and center-of-mass DOF without any non-standard commutation relation or mass polarization term in the Hamiltonian. To that end, we chose the following center-of-mass and relative coordinates:

$$\mathbf{r}_{\text{at}} = \frac{m_p\mathbf{r}_p + m_e\mathbf{r}_e}{m_{\text{at}}} \quad \text{and} \quad \mathbf{r} = \mathbf{r}_e - \mathbf{r}_p. \tag{2.118a}$$

Here, $m_{\text{at}} = m_p + m_e$ and there is only one relative coordinate defined as the distance between the charges themselves, rather than two coordinates relative

to the center of mass. Their conjugate momenta are

$$\mathbf{p}_{\text{at}} = m_{\text{at}}\dot{\mathbf{r}}_{\text{at}} = \mathbf{p}_p + \mathbf{p}_e \quad \text{and} \quad \mathbf{p} = \mu\dot{\mathbf{r}} = \frac{m_p\mathbf{p}_e - m_e\mathbf{p}_p}{m_{\text{at}}}, \tag{2.118b}$$

where $\mu = m_e m_p/m_{\text{at}} \approx 0.9995 m_e$ is the so-called reduced mass. These variables satisfy the commutation relations

$$[\mathbf{r}, \mathbf{p}] = [\mathbf{r}_{\text{at}}, \mathbf{p}_{\text{at}}] = i\hbar\mathbf{1} \quad \text{and} \quad [\mathbf{r}_{\text{at}}, \mathbf{p}] = [\mathbf{p}_{\text{at}}, \mathbf{r}] = \mathbf{0}. \tag{2.118c}$$

With this (canonical) coordinate change, the Hamiltonian of the hydrogen atom becomes

$$H = \frac{\mathbf{p}_{\text{at}}^2}{2m_{\text{at}}} + \frac{\mathbf{p}}{2\mu} + \frac{e^2}{4\varepsilon_0|\mathbf{r}|}. \tag{2.119}$$

The center-of-mass part describes a particle of mass m_{at} moving at constant velocity, while the relative DOF represents a charged particle in a Coulomb potential centered at $\mathbf{r} = \mathbf{0}$. Since these center-of-mass and relative DOF are decoupled, we may discuss here the solutions to the relative part only.

Of course, there is a continuum spectrum of unbound states with positive energy that significantly contribute in certain observables, and are crucial for photoelectron spectroscopies and attosecond physics in general.

The bound-state solutions to the time-independent Schrödinger equation for the relative coordinate are well known [226–228]:

$$\langle \mathbf{r}|nlm_l\rangle = \psi_{nlm_l}(\mathbf{r}) = R_{nl}(|\mathbf{r}|)Y_l^{m_l}(\vartheta,\varphi), \tag{2.120a}$$

where the wave-function is expressed in spherical coordinates $(|\mathbf{r}|, \vartheta, \varphi)$, and the principal, angular and magnetic quantum numbers n, l and m_l, respectively, are integers constrained by

$$n = 1, 2, 3\ldots, \quad 0 \le l \le n-1 \quad \text{and} \quad -l \le m_l \le l. \tag{2.120b}$$

Concretely, l and m specify the orbital angular momentum $\mathbf{L} = \mathbf{r}\times\mathbf{p}$ of a given wave-function according to

$$\mathbf{L}^2|nlm_l\rangle = \hbar l(l+1)|nlm_l\rangle \quad \text{and} \quad L_z|nlm_l\rangle = \hbar m_l|nlm_l\rangle. \tag{2.120c}$$

For historical reasons, states are often named using their spectroscopic notation, whereby different values of l are assigned a letter: $l = 0 \to s$, $l = 1 \to p$, $l = 2 \to d$, $l = 3 \to f$, $l = 4 \to g$, and so on. The radial and angular parts of ψ_{nlm_l} are

$$R_{nl}(|\mathbf{r}|) = \sqrt{\left(\frac{2}{na_0^*}\right)^3 \frac{(n-l-1)!}{2n(n+l)!}} e^{-\frac{|\mathbf{r}|}{na_0^*}} \left(\frac{2|\mathbf{r}|}{na_0^*}\right)^l L_{n-l-1}^{2l+1}\left(\frac{2|\mathbf{r}|}{na_0^*}\right) \quad \text{and} \tag{2.120d}$$

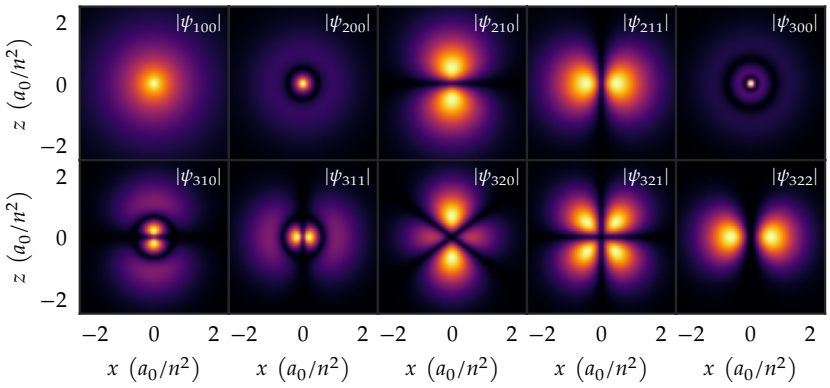

Figure 2.4: Cuts along the $x-z$ plane of the probability densities associated some hydrogenic wave-functions in eq. (2.120a). For visual purposes, the axes are scaled with n^2.

$$Y_l^{m_l}(\vartheta,\varphi) = -\sqrt{\frac{(l-m_l)!}{(l+m_l)!}\frac{(2l+1)}{4\pi}}P_l^{m_l}(\cos\vartheta)e^{im_l\varphi}, \tag{2.120e}$$

where $Y_l^{m_l}$ are the spherical harmonics. $L_\lambda^\mu(x)$ and $P_\lambda^\mu(x)$ denote the generalized Laguerre functions and associated Legendre polynomials, respectively, defined in appendix A.1. The constant

$$a_0^* = \frac{4\pi\varepsilon_0\hbar^2}{e^2\mu} \approx 0.53\ \text{Å} = 5.3\cdot 10^{-11}\ \text{m} \tag{2.121}$$

is the reduced Bohr radius. Since the above expressions are not particularly revealing, we plot the wave-functions in fig. 2.4. Additionally, these atomic states satisfy

$$H|nlm_l\rangle = -\frac{\mu e^4}{32\pi^2\varepsilon_0^2\hbar^2}\frac{1}{n^2}|nlm_l\rangle = -\frac{\alpha^2\mu c^2}{2}\frac{1}{n^2}|nlm_l\rangle \approx -\frac{13.6\ \text{eV}}{n^2}|nlm_l\rangle, \tag{2.122}$$

where $\alpha = \frac{e^2}{4\pi\varepsilon_0\hbar c} \simeq \frac{1}{137}$ is the well-known "fine structure" constant. This implies that the eigenenergies only depend on the principal quantum number. Nevertheless, we will see in the next subsection that this degeneracy is actually not exact due to the so-called fine structure of the spectrum, an effect arising from relativistic considerations.

Note that the smallness of α is compensated by the large rest energy of the electron μc^2. Indeed, in atomic units, $c = \alpha^{-1}$, which makes the compensation evident.

As seen in sections 2.1 and 2.2, the interaction of atoms with the fields depends crucially on the matrix elements of the dipole operator, in the long-wavelength approximation. With the above wave-functions, these transition dipole moments can be readily calculated. For the hydrogen atom, this es-

sentially reduces to knowing the matrix elements of the relative coordinate $\mathbf{r} = (x, y, z)$. More conveniently, we have

$$|\mathbf{r}|Y_1^0(\vartheta,\varphi) = \sqrt{\frac{3}{4\pi}}z \quad \text{and} \tag{2.123a}$$

$$|\mathbf{r}|Y_1^{\pm1}(\vartheta,\varphi) = \mp\sqrt{\frac{3}{4\pi}}\frac{x \pm iy}{\sqrt{2}}, \tag{2.123b}$$

which allows us to write

$$\left\langle nlm_l\middle|\begin{Bmatrix}\mp\dfrac{x \pm iy}{\sqrt{2}}\\ z\end{Bmatrix}\middle|n'l'm_l'\right\rangle = (-1)^{m_l}\sqrt{\frac{4\pi}{3}}\int_0^\infty \mathrm{d}r\, r^3 R_{nlm_l}(r)R_{n'l'm_l'}(r) \times \int_\Omega \mathrm{d}\Omega\, Y_l^{-m_l}\begin{Bmatrix}Y_1^{\pm1}\\ Y_1^0\end{Bmatrix}Y_{l'}^{m_l'}. \tag{2.124}$$

These conditions, also known as "dipole selection rules", summarize the possible atomic transitions mediated by external fields within the long-wavelength approximation.

The angular integrals vanish except if

$$l - l' = \pm1 \ \text{ and } \ m_l - m_l' = 0 \ \text{ (for } z\text{)} \ \text{ or } \ m_l - m_l' = \pm1 \ \text{ (for } x \text{ and } y\text{)}. \tag{2.125}$$

In the case that $l' = l + 1$, the angular integrals yield

$$(-1)^{m_l}\sqrt{\frac{4\pi}{3}}\int_\Omega \mathrm{d}\Omega\, Y_l^{-m_l}Y_1^{-1}Y_{l+1}^{m_l+1} = -\sqrt{\frac{(l+m_l+1)(l+m_l+2)}{2(2l+1)(2l+3)}}, \tag{2.126a}$$

$$(-1)^{m_l}\sqrt{\frac{4\pi}{3}}\int_\Omega \mathrm{d}\Omega\, Y_l^{-m_l}Y_1^{1}Y_{l+1}^{m_l-1} = \sqrt{\frac{(l-m_l+1)(l-m_l+2)}{2(2l+1)(2l+3)}} \quad \text{and} \tag{2.126b}$$

$$(-1)^{m_l}\sqrt{\frac{4\pi}{3}}\int_\Omega \mathrm{d}\Omega\, Y_l^{-m_l}Y_1^{0}Y_{l+1}^{m_l} = \sqrt{\frac{(l+m_l+1)(l-m_l+1)}{(2l+1)(2l+3)}}. \tag{2.126c}$$

The radial integral is, unfortunately, not so simple, even if it admits a closed expression in terms of the hypergeometric function [226, 229]. In any case, the hydrogenic transition dipole moments can be calculated numerically. In fig. 2.5, we select the states $|721\rangle$ and $|921\rangle$, for illustration purposes, and represent the square of their transition dipole moments to other states $|a\rangle$. Each shaded region corresponds to a different principal quantum number of $|a\rangle$, n_a, as indicated with the numbers on top of the figure. An important feature is that the magnitudes decrease as the difference in n increases, and that the maximum value is, by far, reached for intra-level transitions. This does not mean that the intra-level transitions will be the most important ones in general, as there are other elements to factor in, such as the EM density of states at the transition frequencies. However, intra-level transitions will have noticeable

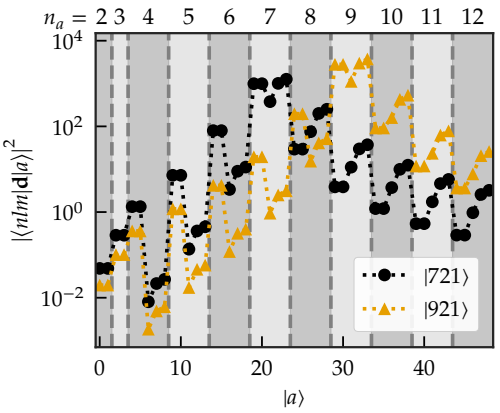

Figure 2.5: Scaling of the dipole moment matrix elements with n. Black dots and orange triangles represent the magnitude squared of the transition dipole moments associated to the Bohr states $|721\rangle$ and $|921\rangle$, respectively. We separate with shaded areas the principal quantum numbers of the states $|a\rangle$, which are explicitly written on top of the figure.

1

consequences in chapter 4.

In summary, we have written the eigenstates of eq. (2.119) in terms of three quantum numbers n, l and m_l. We have also seen that the energy levels of the bound states only depend on n. Once the eigenvalue problem's solution has been revisited, we have found expressions for the allowed transition dipole moments. This is, however, far from the complete picture, even without including the interaction with the fields. Indeed, the above discussion only captures the "gross structure" of the hydrogen atom. Up to this point in the chapter, we have emphasized several times that a non-relativistic treatment for the atoms is enough. However, it turns out that there are spectroscopic features known as the "fine structure" coming from relativistic corrections that will play an important role in chapter 4. Therefore, we next focus on these relativistic effects to more accurately describe the physics.

2.3.3 Relativistic corrections to the hydrogen atom

In 1928, [230, 231] Dirac derived a relativistic equation for the electron. In the case of an electron under the effect of a central Coulomb potential, the equation reads

$$\left[\beta m_e c^2 + \boldsymbol{\alpha}\cdot\mathbf{p}c - \frac{e^2}{4\pi\varepsilon_0|\mathbf{r}|}\right]u = i\hbar\frac{\partial u}{\partial t} = Eu \tag{2.127}$$

for stationary states u. Here, u is a *Dirac spinor*, a quantity with 4 components that accommodates both the spin and the positron, and β and $\boldsymbol{\alpha}$ are matrices

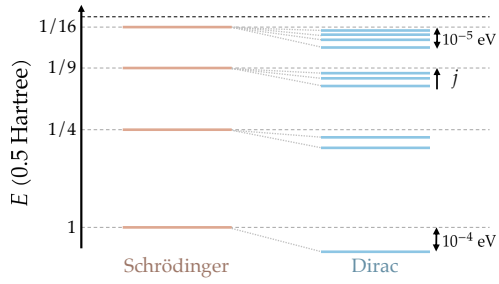

Figure 2.6: Energy spectra of the non-relativistic (Schrödinger) and relativistic (Dirac) descriptions of the hydrogen atom. Each Bohr level n splits in n fine-structure spectral lines according to the value of j, due to the relativistic effects included in the Dirac equation, eq. (2.127).

in spinor space. They can be chosen as

$$\beta = \begin{bmatrix} I_2 & 0 \\ 0 & -I_2 \end{bmatrix} \quad \text{and} \quad \alpha_i = \begin{bmatrix} 0 & \sigma_i \\ -\sigma_i & 0 \end{bmatrix}. \tag{2.128}$$

Here, I_2 is the 2×2 identity matrix and σ are the Pauli matrices defined as

$$\sigma_x = \begin{pmatrix} 0 & 1 \\ 1 & 0 \end{pmatrix}, \quad \sigma_y = \begin{pmatrix} 0 & -i \\ i & 0 \end{pmatrix} \quad \text{and} \quad \sigma_z = \begin{pmatrix} 1 & 0 \\ 0 & -1 \end{pmatrix}. \tag{2.129a}$$

Note that the spin operator $\mathbf{S}$ acts on the spinor indices and is defined through

$$S_i = \frac{\hbar}{2} \begin{bmatrix} \sigma_i & 0 \\ 0 & \sigma_i \end{bmatrix}. \tag{2.129b}$$

Due to the rotational symmetry of eq. (2.127), eigenstates of the Dirac Hamiltonian in eq. (2.127) can be classified according to its total angular momentum $\mathbf{J} = \mathbf{L} + \mathbf{S}$ through j and m_j, where

$$\mathbf{J}^2 \left| njm_j \right\rangle = \hbar j(j+1) \left| njm_j \right\rangle \quad \text{and} \quad J_z \left| njm_j \right\rangle = \hbar m_j \left| njm_j \right\rangle. \tag{2.130}$$

These quantum numbers take on the half-integer values $j = 1/2, 3/2 \ldots$ and $-j \leq m_j \leq j$. Interestingly, in the fully relativistic case, l is not a good quantum number, but only very close to being one [226].

As it turns out, the eigenvalue problem of eq. (2.127) can be solved analyt-

ically. Its eigenenergies are given by

$$E_{nj} = m_e c^2 \left[1 + \left(\frac{\alpha}{n - j - \frac{1}{2} + \sqrt{\left(j + \frac{1}{2}\right)^2 - \alpha^2}} \right)^2 \right]^{-\frac{1}{2}}$$
$$\approx m_e c^2 - \frac{\alpha^2 m_e c^2}{2n^2} - \frac{\alpha^4 m_e c^2}{2n^3} \left[\frac{1}{j + \frac{1}{2}} - \frac{3}{4n} \right] + \ldots \tag{2.131}$$

The series expansion indicates that, besides the rest energy of the electron, the energy spectrum consists of the gross structure $O(\alpha^2 m_e c^2)$, corresponding to the non-relativistic result obtained above, plus a much smaller correction $O(\alpha^4 m_e c^2)$. This is the fine structure of the hydrogen atom that we mentioned earlier. Notably, the energies now depend on n and j, rather than on n alone. Therefore, the hydrogenic energy degeneracies are partially lifted by the Dirac equation, as shown in fig. 2.6. Compared to eq. (2.122), m_e appears in eq. (2.131) rather than μ, which assumes that the mass of the proton is effectively infinite. Here, directly replacing m_e with μ is not strictly correct. Instead, there are further "recoil corrections" even to $O(\alpha^4 m_e c^2)$, as shown in [232, 233]. In any case, these terms are negligible since they carry at least additional μ/m_{at} factors. For our purposes, directly replacing $m_e \to \mu$ will provide accurate enough results.

The eigenfunctions are more complicated, so we restrict ourselves to Pauli's approximate treatment [226]. In it, one extracts from eq. (2.127) the approximate Hamiltonian

$$H_{\text{Pauli}} = \frac{\mathbf{p}^2}{2m_e} - \frac{e^2}{4\pi\varepsilon_0 |\mathbf{r}|} - \frac{\mathbf{p}^4}{8m_e^3 c^2} + \frac{1}{m_e^2 c^2} \frac{e^2}{4\pi\varepsilon_0 |\mathbf{r}|^2} \left[\frac{\mathbf{L} \cdot \mathbf{S}}{2|\mathbf{r}|} - i \frac{\hat{\mathbf{r}} \cdot \mathbf{p}}{\hbar} \right], \tag{2.132}$$

where $\hat{\mathbf{r}}$ is the radial unit vector. Then, treating the entire second line as a perturbation, one can find that

$$H_{\text{Pauli}} \left| nlsjm_j \right\rangle \approx -m_e c^2 \left[\frac{\alpha^2}{2n^2} + \frac{\alpha^4}{2n^3} \left(\frac{1}{j + \frac{1}{2}} - \frac{3}{4n} \right) \right] \left| nlsjm_j \right\rangle \tag{2.133}$$

to first order, which coincides with the exact spectrum of the Dirac equation to $O(\alpha^4 m_e c^2)$, save for the trivial and constant rest energy of the electron $m_e c^2$. Thus, the eigenfunctions are characterized by n, l, s, j and m_j, although we will generally omit s, as it always equals $1/2$. The first two quantum numbers n and l obey the same constraints written in eq. (2.120b) and, following the rules to combine angular momenta, either $j = l + 1/2$ or $j = l - 1/2$. Last, m_j can take the usual values: from $-j$ to j. In spectroscopic notation, the states are

abbreviated as $n\mathrm{L}_j$. An important consequence of the $\mathbf{L}\cdot\mathbf{S}$ contribution, also called the spin-orbit coupling term, is that neither L_z nor S_z commute with the Hamiltonian. Accordingly, the quantum numbers m_l and m_s are not good quantum numbers. Instead, they have been replaced by j and m_j. This implies that the angular part of the wave-functions has been modified to account for spin:

$$\left\langle \mathbf{r}\middle| nl, j = l + 1/2, m_j \right\rangle = R'_{nl}\left[\sqrt{\frac{l + m_j + \frac{1}{2}}{2l+1}} Y_l^{m_j - \frac{1}{2}} |m_s = +1/2\rangle \right. \\ \left. + \sqrt{\frac{l - m_j + \frac{1}{2}}{2l+1}} Y_l^{m_j + \frac{1}{2}} |m_s = -1/2\rangle \right], \tag{2.134a}$$

$$\left\langle \mathbf{r}\middle| nl, j = l - 1/2, m_j \right\rangle = R'_{nl}\left[-\sqrt{\frac{l - m_j + \frac{1}{2}}{2l+1}} Y_l^{m_j - \frac{1}{2}} |m_s = +1/2\rangle \right. \\ \left. + \sqrt{\frac{l + m_j + \frac{1}{2}}{2l+1}} Y_l^{m_j + \frac{1}{2}} |m_s = -1/2\rangle \right]. \tag{2.134b}$$

The coefficients in front of the spherical harmonics are the well-konwn Clebsch-Gordan coefficients [226, 234]. The radial functions R'_{nl} are, in principle, not exactly equal to R_{nl}. However, their modification is very small and quite inconsequential compared to the new arrangement of orbital and spin angular momenta. Therefore, we will simply replace R'_{nl} with R_{nl}, such that the transition dipole moments will be combinations of the ones discussed in the previous non-relativistic account of the hydrogen atom.

To finish this part, we note that the hydrogen atom will be a main character of the results shown in chapter 4. There, the fine structure spectrum will be the starting point upon which we will study more effects arising from the interaction with the medium-assisted fields. The theoretical details concerning those radiative effects are given next, in section 2.4.

2.4 Open quantum systems: the atom in an environment

In the previous section, we have focused on the atomic charges and their mutual interaction only, as if they formed an isolated system. However, real atoms exist in constant interaction with external elements. Due to the interaction of atoms with external DOF, the eigenstates and eigenenergies of the

isolated atom will no longer represent eigenstates or eigenenergies of the joint Hamiltonian that describes the full system. Then, depending on the interaction strength compared to the bare energies, different coupling regimes are achieved. If the interaction is weak enough, it is to be expected that the atom will keep some of its individuality. Then, we will be able to describe the effect of the environment through further corrections to the atomic parameters. If the coupling strength is increased by, e.g., placing atoms close to larger material bodies, the perturbative description becomes not directly applicable.

The formalism of OQS provides us with a general tool to describe systems coupled to larger environments. As such, it will prove very useful for our purposes here to explore its theoretical foundations. We begin this section with a first calculation of the perturbative energy shift due to medium-assisted fields within MQED. Then, we adopt a more general approach to OQS and adapt it to the EM field as an environment. Last, we discuss some more recent ideas that have been built on the foundations of OQS.

2.4.1 Atoms surrounded by media

Before turning our attention to the case in which there are macroscopic bodies near the atom, let us consider an atom in free space. According to section 2.1, such an atom is in constant interaction with the EM field through eq. (2.97a) (minimal coupling) or eq. (2.99) (multipolar coupling). From this interaction, a free space energy shift, now referred to as the Lamb shift, is expected. This was known in the early days of quantum mechanics, but the result of the calculation of these *radiative corrections* diverged [235]. However, during the 1930s, some measurements seemed to indicate that the fine structure described in the previous section was not completely accurate [236–238]. In particular, the $2S_{1/2}$ and $2P_{1/2}$ states appeared to be non-degenerate, contrary to Dirac's spectrum in eq. (2.131). These results were not yet precise enough to raise anything more than mild suspicions about the theory. The situation drastically changed in 1947 when the experiment of Lamb and Retherford measured the alleged shift with unprecedented clarity and precision [17]. The shift became known as the Lamb shift, and was about 10% of the fine structure splitting between $2P_{1/2}$ and $2P_{3/2}$ according to eq. (2.131).

The experiment, together with Kramers' mass-renormalization ideas [11], prompted Bethe to attempt a non-relativistic calculation of the Lamb shift that, remarkably, was only about 5% off the measured value. Schematically, the argument is as follows [13, 239]. On one hand, an unbound electron has its energy shifted due to its $\mathbf{p} \cdot \mathbf{A}^{\perp}$ interaction with the field by an amount equal

to

$$\Delta_a^{\text{free}} = -\frac{2\hbar\alpha}{3\pi}\left(\frac{1}{m_e c}\right)^2 (\mathbf{p}^2)_{aa} \int_0^\infty \mathrm{d}\omega, \tag{2.135}$$

which is a linearly divergent expression. However, measured unbound electrons do not display such an energetic divergence. Such an observation led to the proposal that the infinite shift could be canceled by the bare parameters of the theory, in this case, by the bare (unobserved) mass of the electron m_0. In practice, the measured mass should be equal to the bare mass plus some correction δm known as electromagnetic mass, that is, the additional inertia that the motion of a charged point particle exhibits due to the radiation reaction field [13]:

$$\delta m = \frac{4\hbar\alpha}{3\pi c^2} \int_0^\infty \mathrm{d}\omega. \tag{2.136}$$

Then, somewhat informally,

$$\frac{\mathbf{p}^2}{2m_0} = \frac{\mathbf{p}^2}{2(m_e - \delta m)} \simeq \frac{\mathbf{p}^2}{2m_e} + \frac{\delta m}{2m_e^2}\mathbf{p}^2. \tag{2.137}$$

When accounting additionally for the energy shift Δ_a^{free}, it turns out that only the observed kinetic energy $\frac{\mathbf{p}^2}{m_e}$ remains. In other words, when we start with $\frac{\mathbf{p}^2}{m_e}$ as the electron's kinetic energy, we are already implicitly accounting for Δ_a^{free}. If we were to calculate and add this shift, we would be unawarely including it twice.

The energy shift in the case of a bound electron follows a different expression:

$$\Delta_a^{\text{bound}} = \frac{2\hbar\alpha}{3\pi}\left(\frac{1}{m_e c}\right)^2 \sum_b |\mathbf{p}_{ab}|^2 \int_0^\infty \mathrm{d}\omega \, \frac{\omega}{\omega_{ab} - \omega}, \tag{2.138}$$

where $\mathbf{d}_{ab} = \langle a|\mathbf{d}|b\rangle$ and $\hbar\omega_{ab} = E_a - E_b$ are the transition dipole moments and energies, respectively, and which still diverges linearly. However, if we write its kinetic energy with the measured mass m_e, we have to subtract the free-electron, mass renormalization term Δ_a^{free} from Δ_a^{bound}. Subtracting two linearly divergent integrals yields a logarithmically divergent one, and Bethe reached thus his logarithmic formula:

$$\Delta_a^0 = -\frac{1}{6\pi^2\varepsilon_0 c^3} \sum_{a\neq b} |\mathbf{d}_{ab}|\omega_{ab}^3 \log\left(\frac{m_e c^2}{|\hbar\omega_{ab}|}\right), \tag{2.139}$$

where the superscript 0 denotes that this shift comes from the interaction between the atom and the free-space fields. The rest energy of the electron in the logarithm comes from a high-energy cutoff, "stupidly or boldly" assumed by Bethe [13, 240], which meant that only photons with energies below $m_e c^2$

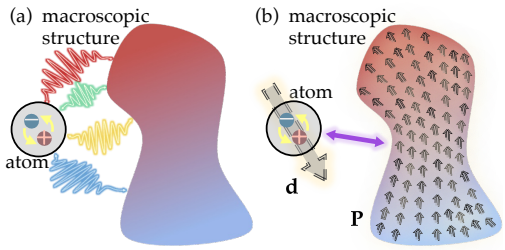

Figure 2.7: Schematic illustration of the CP interaction.

(a) Exchange of virtual MQED light-matter excitations.

(b) Fluctuation-induced dipole moment ($\mathbf{d}$) and polarization field ($\mathbf{P}$) in the atom and structure, respectively.

should significantly contribute to the Lamb shift. This result would be later cemented by fully relativistic treatments that complemented eq. (2.139) with the contribution of high-energy photons [11, 226, 241], and eventually lead to the formalization of QED and the renormalization procedure.

The precise way to do this turned out to be a very delicate matter that, initially, eluded the efforts of Feynman and Schwinger by some small numerical factors [11].

In chapter 4, we will occupy ourselves with the modification of the free-space Lamb shift when the atom is placed next to a macroscopic body. In that situation, MQED allows us to find an expression for the energy shift that depends on the new EM properties of the environment, summarized in the Green tensor $\mathbf{G}$, and commonly referred to as the Casimir-Polder (CP) shift [16, 204]. The CP shift was first calculated in [16], and was subsequently given two alternative interpretations. The more "exotic" one alludes to the modification of the EM vacuum due to the macroscopic medium, while the more "mundane" explanation relies on quantum-mechanical fluctuations in the charges of both the atom and the larger structure that induce dipole moments [13] (see fig. 2.7 for a visual interpretation of these words). It can be hardly overstated how important these dispersive interactions are across science; as S. Y. Buhmann puts it, "[t]hey are the weakest and at the same time the most persistent of all electromagnetic interactions" [204].

It has also been argued that it is not fundamentally correct to ascribe Casimir forces in general to the EM vacuum [242, 243], though it may all be a matter of terminology.

Here, we perform a first calculation of the CP shift in MQED, in the multipolar coupling picture. Nevertheless, the calculation can be done in the minimal coupling scheme and gives rise to the same result [204]. The reasons for this choice are that (i) the actual procedure is somewhat simpler than starting from the minimal coupling Hamiltonian, and (ii) it allows us to discuss the role of the polarization self-energy (PSE), which has been mentioned in passing earlier, and which will be needed to support part of the discussion in chapter 5. The terms in eq. (2.102) whose contribution we need to obtain are the PSE and the $-\mathbf{d}\cdot\mathbf{D}_{(\mathrm{at})}(\mathbf{r}_{\mathrm{at}})/\varepsilon_0$ interaction. The first one provides a shift $O(e^2)$ to first order in perturbation theory, while the second requires us to go

to second order in perturbation theory:

$$\Delta_a^{(1)} = \frac{1}{2\varepsilon_0}\int \mathrm{d}^3 r\, \langle a|\big(\mathbf{P}_{\mathrm{at}}^{\perp}\big)^2|a\rangle = \frac{1}{6\pi^2\varepsilon_0 c^2}\sum_b |\mathbf{d}_{ba}|^2 \int_0^\infty \mathrm{d}\omega\, \omega^2 \quad \text{and} \tag{2.140}$$

$$\begin{aligned}\Delta_a^{(2)} &= \frac{1}{\varepsilon_0^2\hbar}\sum_b\sum_{\lambda i}\int \mathrm{d}^3 r \int_0^\infty \mathrm{d}\omega \\ &\quad\times \frac{\big\langle a,0|\mathbf{d}\cdot\mathbf{D}_{\mathrm{at}}(\mathbf{r}_{\mathrm{at}})|b,1_{\lambda,i}(\mathbf{r},\omega)\big\rangle\big\langle b,1_{\lambda,i}(\mathbf{r},\omega)|\mathbf{d}\cdot\mathbf{D}_{\mathrm{at}}(\mathbf{r}_{\mathrm{at}})|a,0\big\rangle}{\omega_{ab}-\omega} \\ &= \frac{1}{\pi\varepsilon_0 c^2}\sum_b \int_0^\infty \mathrm{d}\omega\, \frac{\omega^2 \mathbf{d}_{ab}\cdot \operatorname{Im}\mathbf{G}(\mathbf{r}_{\mathrm{at}},\mathbf{r}_{\mathrm{at}},\omega)\cdot\mathbf{d}_{ba}}{\omega_{ab}-\omega},\end{aligned} \tag{2.141}$$

where i is a spatial index that indicates the polarization of the light-matter excitation, and we have made use of eqs. (2.84) and (2.86) for $\Delta_a^{(2)}$. It is quite apparent that eq. (2.140) diverges in a dramatic way. In the following, we discuss its role and how to turn it into a divergence that we can tolerate.

We can decompose eq. (2.141) into its free-space and scattering parts $\Delta_a^{(2),0}$ and $\Delta_a^{(2),s}$, respectively. Let us deal with the free-space part first. Using eq. (C.1), we have

$$\Delta_a^{(2),0} = \frac{1}{6\pi^2\varepsilon_0 c^3}\sum_b |\mathbf{d}_{ab}|^2 \int_0^\infty \mathrm{d}\omega\, \frac{\omega^3}{\omega_{ab}-\omega}. \tag{2.142a}$$

Adding the above equation to $\Delta_a^{(1)}$ yields

$$\Delta_a^{(2),0} + \Delta_a^{(1)} = \frac{1}{6\pi^2\varepsilon_0 c^3}\sum_b |\mathbf{d}_{ab}|^2 \omega_{ab} \int_0^\infty \mathrm{d}\omega\, \frac{\omega^2}{\omega_{ab}-\omega}, \tag{2.142b}$$

in which the degree of divergence has been lowered by one. Next, using the Thomas-Reiche-Kuhn sum rule in eq. (2.117b) we extract a state-independent contribution that will play no role and may be discarded. Then, only

$$\Delta_a^{(2),0} + \Delta_a^{(1)} \equiv \frac{1}{6\pi^2\varepsilon_0 c^3}\sum_b |\mathbf{d}_{ab}|\omega_{ab}^2 \int_0^\infty \mathrm{d}\omega\, \frac{\omega}{\omega-\omega_{ab}} \tag{2.142c}$$

remains, where the degree of divergence has again been lowered by one, but it is still linearly divergent. From this point on we can directly follow Bethe's mass-renormalization argument and thus recover eq. (2.139), as was to be expected. We take a moment here to highlight the role of the PSE in this perturbative calculation: it merely lowers the degree of divergence and, in doing so, allows us to retrieve Bethe's logarithm.

With the free-space contribution under control, we can now study the left-

over scattering part. Unless more is said about the macroscopic media that surround the atom, we can only write

$$\Delta_a^{(2)} = \frac{1}{\pi\varepsilon_0 c^2}\sum_b \int_0^\infty \mathrm{d}\omega\, \frac{\omega^2 \mathbf{d}_{ab}\cdot \mathrm{Im}\,\mathbf{G}^{\mathrm{s}}(\mathbf{r}_{\mathrm{at}},\mathbf{r}_{\mathrm{at}},\omega)\cdot\mathbf{d}_{ba}}{\omega_{ab}-\omega}, \tag{2.143}$$

where the total Green tensor has been simply replaced by the scattering component. This part alone is the CP shift, and its spatial dependence gives rise to the CP forces. These shifts will play a key role in chapter 4; however, the EM environment will affect individual atoms in other ways as well. To tackle this issue, we develop a more systematic OQS approach in the following section.

2.4.2 Mathematical foundations and physical interpretation

The theory of OQS is a framework whose goal is to treat manageable and interesting quantum systems that are coupled to typically unmanageable and uninteresting quantum environments. The idea is to try to find a new equation of motion for the interesting, and usually small, component that effectively includes the effects of the environment, without keeping track of its disproportionately large number of DOF. Such an equation is generally known as *master equation*, and the most widespread one is, by far, the Lindblad master equation (LME). Let us start by elucidating the mathematical properties that make the LME so well-regarded among physicists. Accordingly, we momentarily change the tone to a more mathematical register.

Mathematical basis

Consider a generic finite quantum system with Hilbert space $\mathcal{H}_{\mathrm{s}}$ ($\dim\mathcal{H}_{\mathrm{s}} = N$), whose state is specified by the density matrix ρ_{s}. In $\mathcal{H}_{\mathrm{s}}$, we may call a dynamical map a one parameter family of transformations $\mathcal{M}_t$ that act on a density matrix and evolve it in time according to some rule: $\rho_{\mathrm{s}}(t_0+t) \equiv \mathcal{M}_t[\rho_{\mathrm{s}}(t_0)]$ [244]. There are three conditions that we demand of our dynamical maps on physical grounds:

$$\text{(I)}\quad \mathrm{Tr}\{\mathcal{M}_t[\rho_{\mathrm{s}}(t_0)]\} = \mathrm{Tr}\{\rho_{\mathrm{s}}(t_0)\}. \tag{2.144a}$$

$$\text{(II)}\quad \text{If } A\in\mathcal{H}, \text{ such that } A\geq 0,\ B\in\mathcal{H}' \text{ and } \dim\mathcal{H}' = D,$$
$$\text{then } \{\mathcal{M}_t\otimes I'\}(A\otimes B) \equiv \mathcal{M}_t[A]\otimes B \geq 0\ \forall D\in\mathbb{N}. \tag{2.144b}$$

$$\text{(III)}\quad \mathcal{M}_{t_2}\circ\mathcal{M}_{t_1} = \mathcal{M}_{t_1+t_2}, \text{ where } t_1>0, \text{ and } t_2>0. \tag{2.144c}$$

Condition (I) states that $\mathcal{M}_t$ is *trace preserving*. Next, condition (II) indicates that the map should be *completely positive*. It can be surprising that simple positivity (if $A \geq 0$, then $\mathcal{M}[A] \geq 0$) is not enough to ensure physicality of the map $\mathcal{M}$, even if it guarantees that the populations remain non-negative. Instead, we must imagine that there is an auxiliary system with Hilbert space $\mathcal{H}'$ ($\dim \mathcal{H}' = D$) that undergoes independent Hamiltonian evolution according to $\mathcal{N}_t[\rho'(t_0)] = e^{-iH't/\hbar}\rho'(t_0)e^{iH't/\hbar}$, for simplicity. Then, we expect from physics that the composite dynamical map should be positive:

$$\{\mathcal{M}_t \otimes \mathcal{N}_t\}[\rho_s(t_0) \otimes \rho'(t_0)] = \mathcal{M}_t[\rho_s(t_0)] \otimes \mathcal{N}_t[\rho'(t_0)] \geq 0. \tag{2.145}$$

Using the identities I and I' of $\mathcal{H}$ and $\mathcal{H}'$, respectively, we can decompose the total map into $\{\mathcal{M}_t \otimes I'\} \circ \{I \otimes \mathcal{N}_t\}$, where the second term is positive. Because positivity is closed under composition, to guarantee eq. (2.145) we must demand $\mathcal{M}_t \otimes I'$ to be positive $\forall D = \dim \mathcal{H}'$ or, equivalently, $\mathcal{M}_t$ to be completely positive. The distinction between positivity and complete positivity stems from the fact that positivity of $\mathcal{M}_t$ alone does not imply its complete positivity, that is, positivity of $\mathcal{M}_t \otimes I'$ [245, 246]. Any map that fulfills (I) and (II) is called completely positive and trace preserving (CPTP).

As for condition (III), due to the lack of negative values for the time parameter, it states that the dynamics is irreversible, and there is no inverse $\mathcal{M}_{-t}$. The precise mathematical term that describes the algebraic relation of different elements of the family $\mathcal{M}_t$ is *semigroup*. It also implies that the instantaneous evolution of $\rho_s(t)$ only depends on $\rho_s(t)$, and not on its previous history:

Incidentally, we mention here that we allow t to take the value 0, as many people do, then there is an identity element in the family and the precise term is actually *monoid*.

$$\rho_s(t + \delta t) = \mathcal{M}_{\delta t}[\rho_s(t)] \tag{2.146}$$

for arbitrarily small δt. The dynamical map $\mathcal{M}_t$ is then said to describe a *Markovian* process. From the semigroup structure and some continuity requirements [245, 247, 248], it follows the existence of a linear (super)operator $\mathcal{L}$ such that

$$\frac{\mathrm{d}}{\mathrm{d}t}\{\mathcal{M}_t[\rho_s(0)]\} = \mathcal{L}\{\mathcal{M}_t[\rho_s(0)]\} \implies \dot{\rho}_s(t) = \mathcal{L}[\rho_s(t)], \tag{2.147}$$

whose formal solution is $\mathcal{M}_t = e^{\mathcal{L}t}$. Accordingly, $\mathcal{L}$ is the so-called generator of the dynamical map $\mathcal{M}_t$.

After physically motivating the three conditions in eq. (2.144) and fixing some mathematical terminology, we are ready to tackle Lindblad's theorem: the generator $\mathcal{L}$ of the most general Markovian and CPTP map always acts on

density matrices as

$$\dot{\rho}_{\mathrm{s}} = \mathcal{L}[\rho_{\mathrm{s}}] = -\frac{i}{\hbar}\sum_{ij}^{N^2} h_{ij}\left[\sigma_i^\dagger \sigma_j, \rho_{\mathrm{s}}\right] + \sum_{ij}^{N^2} \gamma_{ij}\left(\sigma_j \rho_{\mathrm{s}} \sigma_i^\dagger - \frac{1}{2}\left\{\sigma_i^\dagger \sigma_j, \rho_{\mathrm{s}}\right\}\right), \quad (2.148)$$

where the coefficient matrix γ_{ij}, commonly known as Kossakowski matrix, must be symmetric and positive semi-definite, and $H_{\mathrm{s}} \equiv \sum_{ij} h_{ij}\sigma_i^\dagger \sigma_j$ is Hermitian. Here, the dynamical map is unequivocally determined by the Hamiltonian $\tilde{H}_{\mathrm{s}}$, the matrix γ_{ij}, and the operators σ_i, which are a complete basis of operators in $\mathcal{H}_{\mathrm{s}}$, orthonormal according to the inner product

$$\left\langle \sigma_i, \sigma_j \right\rangle \equiv \mathrm{Tr}\left\{\sigma_i^\dagger \sigma_j\right\} = \delta_{ij}. \quad (2.149)$$

For compactness, let us define the *dissipator* $\mathcal{D}_{A,B}[C] = BCA^\dagger - \frac{1}{2}\{A^\dagger B, C\}$, such that eq. (2.148) becomes

$$\dot{\rho}_{\mathrm{s}} = -\frac{i}{\hbar}[H_{\mathrm{s}}, \rho_{\mathrm{s}}] + \sum_{ij} \gamma_{ij}\mathcal{D}_{\sigma_i,\sigma_j}[\rho_{\mathrm{s}}]. \quad (2.150)$$

This is the general form of the so-called LME. Note that the properties of the Kossakowski matrix imply that it is diagonalizable, which allows us to write eq. (2.148) in its standard form

$$\dot{\rho}_{\mathrm{s}} = \mathcal{L}[\rho_{\mathrm{s}}] = -\frac{i}{\hbar}[H_{\mathrm{s}}, \rho_{\mathrm{s}}] + \sum_{k}^{N^2} \Gamma_k \mathcal{D}_{\Sigma_k,\Sigma_k}[\rho_{\mathrm{s}}], \quad (2.151)$$

where Γ_k are the non-negative eigenvalues of γ_{ij}, $\Sigma_k = \sum_j U_{kj}\sigma_j$, and the diagonalization matrix $\mathbf{U}$ fulfills $\sum_k U_{ki}^* \Gamma_k U_{kj} = \gamma_{ij}$.

We make now one last interesting mathematical remark. In the usual matrix representation of quantum mechanics states are vectors and operators are matrices. This, of course, very neatly captures the essence of linear algebra present in quantum mechanics. We have now found a new kind of object that acts linearly on operators and, more interestingly, on density matrices. These objects are known as *superoperators*, and include the dynamical maps or their generators $\mathcal{L}$. Due to their linear action, we can find a new enlarged "matrix", or rather tensor representation, whereby they are assigned a four index tensor. Thus, eq. (2.148) transforms into

$$\dot{\rho}_{\mathrm{s},ab} = \sum_{cd} \mathcal{L}_{abcd}\rho_{\mathrm{s},cd}, \quad (2.152)$$

where, if $\sigma_{i,ab} = \langle a|\sigma_i|b\rangle$, $\hbar\omega_{ab} = E_a - E_b$ and $\mathcal{L}_{abcd} = |a\rangle\langle b|\mathcal{L}[|c\rangle\langle d|]$, then

$$\mathcal{L}_{abcd} = -i\omega_{ab}\delta_{ac}\delta_{bd} + \sum_{ij}^{N^2}\gamma_{ij}\left[\sigma_{j,ac}\sigma^\dagger_{i,db} - \sum_e\left(\frac{\delta_{bd}}{2}\sigma^\dagger_{i,ae}\sigma_{j,ec} + \frac{\delta_{ac}}{2}\sigma^\dagger_{i,de}\sigma_{j,eb}\right)\right]$$

Physical intuition

After reviewing the desirable mathematical properties of the LME above, we should discuss what each term physically represents. For now, we assume that an equation like eq. (2.148) can actually describe the dynamics of a system including the effects of a larger environment. We will later see how and when this is true. The commutator term then corresponds to the usual unitary evolution generated by a Hamiltonian $\tilde{H}_\mathrm{s}$. In general, as anticipated by our previous calculation of the CP shifts in eq. (2.143), $\tilde{H}_\mathrm{s}$ will contain the free-evolution Hamiltonian of the system H_s plus some contribution Δ due to the environment, thus $\tilde{H}_\mathrm{s} = H_\mathrm{s} + \Delta$. The second term corresponds to the dissipation of the system's initial excitations (decay) and coherence (dephasing) into the environment. The precise way in which these effects are encoded can be far from intuitive, except for relatively simple systems. Nevertheless, we can leave the complications for later and see how decay and dephasing are included in two elementary models. For these examples, we consider our system to be a two-level atom (2LA) with basis vectors $|0\rangle$ and $|1\rangle$. The σ_i operators can be chosen as

$$\sigma_0 = \frac{I}{\sqrt{2}}, \quad \sigma_1 = \frac{\sigma_x + i\sigma_y}{2} = |0\rangle\langle 1|, \quad \sigma_2 = \frac{\sigma_x - i\sigma_y}{2} = |1\rangle\langle 0|, \quad \sigma_3 = \frac{\sigma_z}{\sqrt{2}}. \tag{2.153a}$$

Here, $\sigma_{x/y/z}$ are the Pauli matrices as defined in eq. (2.129a). For simplicity, we take here $\Delta = 0$ such that

$$\tilde{H}_\mathrm{s} = H_\mathrm{s} = \frac{\hbar\omega}{2}(I - \sigma_z) = \hbar\omega|1\rangle\langle 1|, \tag{2.153b}$$

and denote the states by $H_\mathrm{s}|0\rangle = 0$ and $H_\mathrm{s}|0\rangle = \hbar\omega|1\rangle$. With that, the most general density matrix is $\rho_\mathrm{s} = \sum_{ab}\rho_{\mathrm{s},ab}|a\rangle\langle b|$.

Example 1: decay in a TLA To analyze this phenomenon, we consider that only $\gamma_{11} = \gamma \neq 0$. Then, eq. (2.148) becomes

$$\dot{\rho}_\mathrm{s} = -i\omega\Big(\rho_{\mathrm{s},10}|1\rangle\langle 0| - \mathrm{H.c.}\Big) + \gamma\left(\rho_{\mathrm{s},11}(|0\rangle\langle 0| - |1\rangle\langle 1|) - \frac{\rho_{\mathrm{s},10}|1\rangle\langle 0| + \mathrm{H.c.}}{2}\right)$$

or, for each matrix element individually,

$$\begin{aligned}
\dot{\rho}_{s,00} &= \gamma\rho_{s,11} && \Longrightarrow \rho_{s,00} = \rho_{00}(0) + \rho_{s,11}(0)\big(1 - e^{-\gamma t}\big), \\
\dot{\rho}_{s,11} &= -\gamma\rho_{s,11} && \Longrightarrow \rho_{s,11} = \rho_{s,11}(0)e^{-\gamma t} \quad \text{and} \\
\dot{\rho}_{s,10} &= \left(-i\omega - \frac{\gamma}{2}\right)\rho_{s,10} && \Longrightarrow \rho_{s,10} = \rho_{s,10}(0)e^{-i\omega t - \frac{\gamma}{2}t}.
\end{aligned} \tag{2.154}$$

From the above equations, it is clear that the dissipative timescale is given by γ^{-1}, and γ is thus the decay rate. More specifically, we see that the $\sigma_j\rho_s\sigma_i^\dagger$ term takes care of the population that flows into the ground state. For this reason, it is sometimes known as the "refilling" term; another common name is the "quantum jump" term. As for the anticommutator, it makes sure of (i) the dissipation of the excited state population and (ii) the decay of the off-diagonal elements of ρ (coherences) at the same rate. Among other things, the decay of the coherence takes care of preserving the positivity of ρ_s through time. For illustration purposes, the solution is graphically presented in figs. 2.8a and 2.8c, for $\gamma = \omega/10$ and $|\psi(0)\rangle = \frac{2|0\rangle+|1\rangle}{\sqrt{5}}$ as initial state. Note that the coherence decays at half the rate of the populations, $\gamma/2$, as seen in eq. (2.154).

Example 2: pure dephasing in a TLA In this case, we take only $\gamma_{33} = \gamma \neq 0$. With this choice, eq. (2.148) turns into

$$\dot{\rho}_s = -i\omega\big(\rho_{s,10}|1\rangle\langle 0| - \text{H.c.}\big) - \gamma\big(\rho_{s,10}|1\rangle\langle 0| + \text{H.c.}\big).$$

Again, one element at a time:

$$\begin{aligned}
\dot{\rho}_{s,00} &= 0 && \Longrightarrow \rho_{s,00}(t) = \rho_{s,00}(0), \\
\dot{\rho}_{s,11} &= 0 && \Longrightarrow \rho_{s,11}(t) = \rho_{s,11}(0) \quad \text{and} \\
\dot{\rho}_{s,10} &= (-i\omega - \gamma)\rho_{s,10} && \Longrightarrow \rho_{s,10}(t) = \rho_{s,10}(0)e^{-i\omega t - \gamma t}.
\end{aligned} \tag{2.155}$$

Now the populations do not change, while the coherence's decay comes from both the refilling term and the anticommutator in equal measure. Indeed, for long enough times, the TLA's state becomes a *classical mixture* of states $|0\rangle$ and $|1\rangle$ with the original probabilities. Again, we illustrate the decoherence behavior with figs. 2.8b and 2.8d, with the same parameters as before. In this case, the populations do not change with time, while the coherences decay with rate γ.

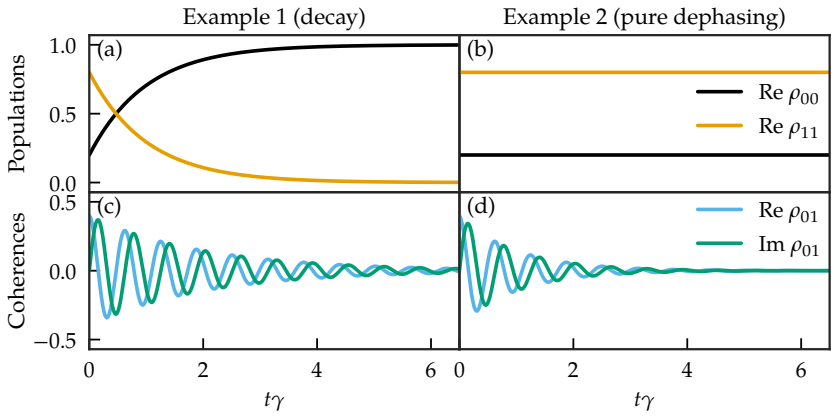

Figure 2.8: Temporal evolution of populations (top) and coherences (bottom) for examples 1 (left) and 2 (right). In both cases the initial state is $|\psi(0)\rangle = \frac{|1\rangle+2|0\rangle}{\sqrt{5}}$.

2.4.3 General systems in general environments

In section 2.4.2, we have developed a formalism and assumed that it will be useful to describe some aspects of the quantum world. We just saw with two examples that this at least seems plausible. Indeed, most uses of LMEs in the literature take a rather phenomenological approach, in the sense that the system in question is assumed to have some sensible decay channels and decay rates and then an adequate LME is "postulated", rather than actually derived. In this section we do not assume anymore, and dive into the precise arguments that can be used to extract a LME from a microscopic model of the system, the environment and their interaction. Following [249], our starting point will be the Hamiltonian

$$H = H_\mathrm{s} + H_\mathrm{b} + H_\mathrm{int}, \tag{2.156a}$$

where, generally,

$$H_\mathrm{int} = \sum_r S_r B_r. \tag{2.156b}$$

Here, S_i and B_i are Hermitian system and bath operators. In the interaction picture, the dynamics of the full system are

$$\dot{\rho}^I(t) = -\frac{i}{\hbar}\big[H_\mathrm{int}(t), \rho^I(t)\big], \tag{2.156c}$$

with the density matrix of the full system $\rho^I = e^{-i(H_\mathrm{s}+H_\mathrm{b})t/\hbar}\rho e^{i(H_\mathrm{s}+H_\mathrm{b})t/\hbar}$ and the interaction Hamiltonian $H_\mathrm{int}(t) = e^{i(H_\mathrm{s}+H_\mathrm{b})t/\hbar}H_\mathrm{int}e^{-i(H_\mathrm{s}+H_\mathrm{b})t/\hbar}$. We can formally integrate eq. (2.156c), substitute the result back in, and take the partial

trace over the environment to obtain

$$\dot{\rho}_{\mathrm{s}}^{I}(t) = -\frac{i}{\hbar}\mathrm{Tr}_{\mathrm{b}}\{\big[H_{\mathrm{int}}(t), \rho^{I}(0)\big]\} - \frac{1}{\hbar^2}\int_0^t \mathrm{d}\tau\ \mathrm{Tr}_{\mathrm{b}}\{\big[H_{\mathrm{int}}(t), \big[H_{\mathrm{int}}(\tau), \rho^{I}(\tau)\big]\big]\}. \tag{2.157}$$

So far, we have merely rewritten the von Neumann equation. Next, we make a physical assumption known as the *Born approximation*. Taken at face value, it amounts to stating that $\rho^{I}(t) \approx \rho_{\mathrm{s}}^{I}(t) \otimes \rho_{\mathrm{b}}^{I}$, i.e., the environment does not "feel" the system and, therefore, does not evolve in the interaction picture. Furthermore, the Born approximation neglects any system-bath correlation build-up through time, as the total state is always separable. As stated, this approximation seems to be somewhat crude and not necessarily realistic. For instance, consider an excited atom that, through its interaction with the EM continuum, releases a photon and relaxes to its ground state. The field's state changes significantly; there is a new photon in it. However, the photon propagates away from the atom and, crucially, never comes back. Thus, from the atom's perspective, it can be reasonable to approximate the environment's state as unchanged. This example illustrates the real physical condition that our perturbative OQS approach requires. The Born approximation is a simple way to remove any back-action from the environment, although, strictly speaking, it does more than that. An immediate consequence of the Born approximation is that we can straightforwardly eliminate the first commutator: it either vanishes or can be "reabsorbed" elsewhere by replacing

$$H_{\mathrm{s}} \to H_{\mathrm{s}}' = H_{\mathrm{s}} + \sum_r \mathrm{Tr}_{\mathrm{b}}\{B_r\rho_{\mathrm{b}}\}S_r \quad \text{and} \quad B_r \to B_r' = B_r - \mathrm{Tr}_{\mathrm{b}}\{\rho_{\mathrm{b}}B_r\}. \tag{2.158}$$

Thus, we have

$$\dot{\rho}_{\mathrm{s}}^{I}(t) = -\frac{1}{\hbar^2}\int_0^t \mathrm{d}\tau\ \sum_{rt} \mathrm{Tr}_{\mathrm{b}}\{\big[S_r(t)B_r(t), \big[S_t(\tau)B_t(\tau), \rho_{\mathrm{s}}^{I}(\tau)\otimes\rho_{\mathrm{b}}^{I}\big]\big]\}. \tag{2.159}$$

The validity of the Born approximation can be intuitively understood on the basis that the environment is much larger than the system, and is thus expected to remain relatively unaffected by the system. However, this explanation is not completely satisfactory if not complemented by another key assumption: the *Markov approximation*. Consider the minimum timescale of environment-induced effects in the system τ_{s}. If the environment typically dissipates excitations and correlations among its many DOF in times $\tau_{\mathrm{b}} \ll \tau_{\mathrm{s}}$, then the system cannot keep up and will not notice the relatively fast changes in the environment's state. Intuitively, this hierarchy of timescales

Due to the connection between the Born and Markov approximations, they are often presented together as the Born-Markov approximation.

induces an irreversible flow of excitations from the system into the environment, and allows us to find a "coarse-grained" description of the system's dynamics. A schematic view is presented in fig. 2.9, where the red curve indicates the system's environment-induced evolution, with timescale τ_s, while the blue exponential tails represent the bath's memory, τ_b, over which the integrand in eq. (2.159) is non-negligible. There are two mathematical implications of the Markov approximation. The first one is that we can replace $\rho_s^I(\tau) \to \rho_s^I(t)$, because $\rho_s^I(\tau)$ will be multiplied in the integrals by terms of the form $\mathrm{Tr}_b\{B_r(t)B_t(\tau)\rho_b^I\}$, which quickly decay for $\tau < t - \tau_b$. For the same reason, we can take the lower integration limit to $-\infty$ and change the integration variable to arrive at

$$\begin{aligned}\dot{\rho}_s^I(t) &= -\frac{1}{\hbar^2}\int_0^\infty \mathrm{d}\tau \sum_{rt} \mathrm{Tr}_b\{\big[S_r(t)B_r(t), \big[S_t(t-\tau)B_t(t-\tau), \rho_s^I(t)\otimes\rho_b^I\big]\big]\} \\ &= \mathcal{R}^I[\rho_s^I]. \end{aligned} \tag{2.160}$$

The above equation is known as the Bloch-Redfield equation (BRE), and we have defined the interaction-picture Redfield superoperator $\mathcal{R}^I$. It is simple to verify that $\mathcal{R}^I$ generates Markovian and trace-preserving maps. Unfortunately, as we will see later explicitly, it does not respect the complete positivity of the map. As we argued in section 2.4.2, complete positivity is a physically meaningful requirement. There is a systematic procedure, known as *secularization* or *secular approximation*, that restores complete positivity in eq. (2.160), turning $\mathcal{R}^I$ into the generator of a CPTP map. The secular approximation is a key step in standard LME derivations in OQS textbooks, and we will review it in the next part. However, we note at this point that it has some important limitations, which are addressed in chapter 3, where we find an alternative procedure that involves less crude approximations. In the following, we will manipulate eq. (2.160) to write it in a form where the idea behind the secular approximation becomes transparent. Then, we will finally retrieve a LME after secularization, and briefly comment on its shortcomings. Last, we will particularize the equations for the case of an atom interacting with medium-assisted fields.

Massaging the BRE

The goal of this part is to derive a more explicit expression for $\mathcal{R}[\rho_s]$. To that end, we start by introducing the eigenstates of the system's Hamiltonian $H_s|a\rangle = \hbar\omega_a|a\rangle$ and defining its transition operators $\sigma_i = |a_i\rangle\langle b_i|$, with transition frequencies $\delta_i = \omega_{b_i} - \omega_{a_i}$. With this convention, lowering (raising)

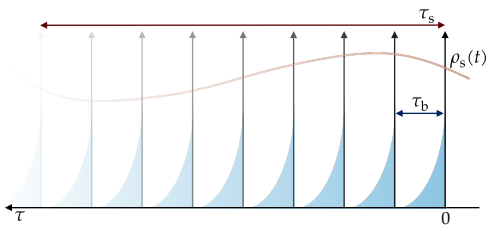

Figure 2.9: Graphical justification of the Markov approximation. The light red curve represents the evolution of the system due to environment-induced effects. The blue exponential tails correspond to the bath correlation functions, whose temporal extension indicates the bath's "memory".

transition operators have positive (negative) frequency. We can use the σ_i to expand S_r as

$$S_r = \sum_i S_{r,i}\sigma_i = \sum_i S^*_{r,i}\sigma_i^\dagger, \tag{2.161}$$

where $S_{r,i} = \mathrm{Tr}_s\{\sigma_i^\dagger S_r\}$. Because the transitions are between eigenstates of the unperturbed Hamiltonian, the interaction picture operators $S_r(t)$ are

$$S_r(t) = \sum_i S_{r,i}e^{-i\delta_i t}\sigma_i = \sum_i S^*_{r,i}e^{i\delta_i t}\sigma_i^\dagger. \tag{2.162}$$

Then, separating the terms in the nested commutator of eq. (2.160), we have

$$\begin{aligned}\dot\rho_s^I = -\frac{1}{\hbar^2}\sum_{rt,ij}\int_0^\infty \mathrm{d}\tau\,\Big[&S^*_{r,i}C_{rt}(\tau)S_{t,j}e^{i\delta_j\tau}\,\sigma_i^\dagger\sigma_j\rho_s^I\,e^{i(\delta_i-\delta_j)t}\\ &+S^*_{t,i}C_{tr}(-\tau)S_{r,j}e^{-i\delta_i\tau}\,\rho_s^I\sigma_i^\dagger\sigma_j\,e^{i(\delta_i-\delta_j)t}\\ &-S^*_{t,i}C_{tr}(-\tau)S_{r,j}e^{-i\delta_i\tau}\,\sigma_j\rho_s^I\sigma_i^\dagger\,e^{i(\delta_i-\delta_j)t}\\ &-S^*_{r,i}C_{rt}(\tau)S_{t,j}e^{i\delta_j\tau}\,\sigma_j\rho_s^I\sigma_i^\dagger\,e^{i(\delta_i-\delta_j)t}\Big]\end{aligned} \tag{2.163}$$

where

$$C_{rt}(\tau) = \mathrm{Tr}_b\{B_r(t)B_t(t-\tau)\rho_b^I\} = \langle B_r(t)B_t(t-\tau)\rangle = \langle B_r(\tau)B_t(0)\rangle \tag{2.164}$$

are the environment correlation functions. We have assumed that these functions are homogeneous in time such that they only depend on the time difference τ, which is the case for stationary environment states. Now, we isolate the τ integrals and define two frequency-dependent Hermitian matrices γ_{rt} and λ_{rt} through

$$\frac{\gamma_{rt}(\delta)}{2} + i\lambda_{rt}(\delta) = \frac{1}{\hbar^2}\int_0^\infty \mathrm{d}\tau\, C_{rt}(\tau)e^{i\delta\tau}. \tag{2.165}$$

Specifically,

$$\begin{aligned}\gamma_{rt}(\delta) &= \frac{1}{\hbar^2}\Big[\int_0^\infty \mathrm{d}\tau\, C_{rt}(\tau)e^{i\delta\tau} + \int_0^\infty \mathrm{d}\tau\, C^*_{tr}(\tau)e^{-i\delta\tau}\Big] \\ &= \frac{1}{\hbar^2}\Big[\int_0^\infty \mathrm{d}\tau\, C_{rt}(\tau)e^{i\delta\tau} \int_{-\infty}^0 \mathrm{d}\tau\, C_{rt}(\tau)e^{i\delta\tau}\Big] \\ &= \frac{1}{\hbar^2}\int_{-\infty}^\infty \mathrm{d}\tau\, C_{rt}(\tau)e^{i\delta\tau}, \end{aligned} \tag{2.166}$$

where we have used that $C^*_{tr}(\tau) = C_{rt}(-\tau)$, which follows from the definition of the correlation functions and their homogeneity in time. Note that, as we show in appendix A.2, γ_{rt} and λ_{rt} satisfy a Kramers-Kronig-like relation, i.e.,

$$\lambda_{rt}(\delta) = \frac{1}{2\pi} P\int_{-\infty}^\infty \mathrm{d}\omega\, \frac{\gamma_{rt}(\omega)}{\delta-\omega}. \tag{2.167}$$

With these functions, we perform the r and t summations by introducing

$$\Gamma_{ij}(\delta) = \sum_{rt} S^*_{r,i}\gamma_{rt}(\delta)S_{t,j} \quad \text{and} \tag{2.168a}$$

$$\Lambda_{ij}(\delta) = \sum_{rt} S^*_{r,i}\lambda_{rt}(\delta)S_{t,j}, \tag{2.168b}$$

and finally write eq. (2.163) in the Schrödinger picture:

$$\begin{aligned}\dot\rho_\mathrm{s} = -\frac{i}{\hbar}[H_\mathrm{s},\rho_\mathrm{s}] + \sum_{ij}\Big\{ &- i\big(\Lambda_{ij}(\delta_j)\sigma_i^\dagger\sigma_j\rho_\mathrm{s} - \rho_\mathrm{s}\Lambda_{ij}(\delta_i)\sigma_i^\dagger\sigma_j\big) \\ &+ i\big(\Lambda_{ij}(\delta_j) - \Lambda_{ij}(\delta_i)\big)\sigma_j\rho_\mathrm{s}\sigma_i^\dagger \\ &- \frac{1}{2}\big(\Gamma_{ij}(\delta_j)\sigma_i^\dagger\sigma_j\rho_\mathrm{s} + \rho_\mathrm{s}\Gamma_{ij}(\delta_i)\sigma_i^\dagger\sigma_j\big) \\ &+ \frac{1}{2}\big(\Gamma_{ij}(\delta_j) + \Gamma_{ij}(\delta_i)\big)\sigma_j\rho_\mathrm{s}\sigma_i^\dagger\Big\}. \end{aligned} \tag{2.169}$$

This is the final form of the BRE, a master equation that connects the effective description with the underlying microscopic model through its parameters Λ_{ij} and Γ_{ij}.

To some extent, one can recognize elements that look almost like they could be cast into a LME. Indeed, the first, third and fourth lines are close to being a commutator, an anticommutator and the refilling term, respectively. The resemblance is further evidenced by noticing that eq. (2.169) can also be expressed as

$$\dot\rho_\mathrm{s} = -\frac{i}{\hbar}[H_\mathrm{s},\rho_\mathrm{s}] + \sum_{ij}\Big\{ - \frac{K^+_{ij}(\delta_j) - K^-_{ij}(\delta_i)}{2}\big[\sigma_i^\dagger\sigma_j,\rho_\mathrm{s}\big]$$

$$+\left[K_{ij}^{+}(\delta_j)+K_{ij}^{-}(\delta_i)\right]\mathcal{D}_{\sigma_i,\sigma_j}[\rho_{\mathrm{s}}]\Big\}, \tag{2.170}$$

where $K_{ij}^{\pm}(\delta)=\Gamma_{ij}(\delta)/2\pm i\Lambda_{ij}(\delta)$, and the identity

$$aO_1O_2+bO_2O_1=\frac{a+b}{2}\{O_1,O_2\}+\frac{a-b}{2}[O_1,O_2] \tag{2.171}$$

has been used. Still, the Kossakowski matrix of this master equation is not positive semi-definite in general, which is why the BRE fails to be a genuine LME. Regardless, the BRE has proven very useful and accurate, as long as the underlying assumptions are respected [250, 251]. Still, one would naturally prefer if the requirement of complete positivity could be fulfilled.

Secularizing the BRE

As mentioned before, there exists a general procedure to turn the BRE into a LME: the secular approximation. The secularization procedure amounts to removing terms in eq. (2.169) where $\delta_i\neq\delta_j$. Therefore, only terms where $\Lambda_{ij}(\delta_j)=\Lambda_{ij}(\delta_i)$ are kept, which removes the asymmetry in each line of eq. (2.169). The rationale behind the approximation is that terms with large values of $|\delta_i-\delta_j|$, which oscillate quickly in the interaction picture, average out. In this regard, the secular approximation is very similar conceptually to the well-known RWA. When applied to the BRE, we straightforwardly obtain

$$\dot{\rho}_{\mathrm{s}}=-\frac{i}{\hbar}[H_{\mathrm{s}},\rho_{\mathrm{s}}]+\sum_{ij}^{(\delta_i=\delta_j)}\Big(-i\Lambda_{ij}(\delta_i)\left[\sigma_i^{\dagger}\sigma_j,\rho_{\mathrm{s}}\right]+\Gamma_{ij}(\delta_i)\mathcal{D}_{\sigma_i,\sigma_j}[\rho_{\mathrm{s}}]\Big). \tag{2.172}$$

The positive semi-definiteness of $\Gamma_{ij}(\delta_i)$ is directly related to that of $\gamma_{rt}(\delta_i)$, which follows from a theorem by Bochner [249]. See [252] for a short proof of $\gamma\geq 0$. The way in which $\Lambda_{ij}(\delta_i)$ and $\Gamma_{ij}(\delta_i)$ appear in eq. (2.172) cements their interpretation as shifts to the Hamiltonian and decay rates, respectively.

Since we have just derived a LME whose parameters are connected to the microscopic model of the environment, it would appear as though we had reached the pinnacle of OQS. This is not true for several reasons. First, we can consider situations where one or more of the underlying assumptions in our derivation stop being valid. This is true in, for example, highly structured environments or in the strong coupling regime. In such cases, the master equations derived in the last few pages, eqs. (2.169) and (2.172), have no chance of properly describing the dynamics. Yet, there are extensions to the "traditional" OQS theory that make an OQS approach work even in those situations, which

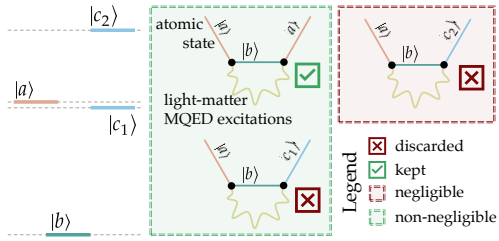

Figure 2.10: Graphical representation of the terms included and neglected by the secular approximation. Left: schematic level structure of the atom. Right: relation of physical processes to the secular approximation. Bottom right: symbol legend.

will be discussed briefly in section 2.4.4.

The second reason why there is more to OQS is that the secular approximation has been shown to be inaccurate in many situations, e.g., when there are some pairs of transition frequencies where $\delta_i \neq \delta_j$, but which are close enough compared with the environment-induced frequency scales. The failure of the secular approximation is succinctly summarized in that populations and coherences of non-degenerate states become completely decoupled. A more intuitive picture can be provided with the following argument (see fig. 2.10 for a graphical illustration): if the system is in state $|a\rangle$, the second-order effects due to the environment will induce virtual transitions to some other state $|b\rangle$ and back. If there is no state $|c\rangle$ such that $\omega_c \approx \omega_a$, then these virtual transitions cannot (meaningfully) happen any other way. However, if there is some state $|c_1\rangle$ close enough to $|a\rangle$, then the excitation might reach $|c_1\rangle$ instead of $|a\rangle$ on its way back from $|b\rangle$. This way, the environment-induced virtual transitions give rise to an indirect, second order coupling between $|a\rangle$ and $|c_1\rangle$. The secular approximation accurately discards it for states that lie far apart in the energy spectrum, like $|a\rangle$ and $|c_2\rangle$. However, it also neglects this coupling between non-degenerate states that are, nevertheless, close to each other, like $|a\rangle$ and $|c_1\rangle$. There is a whole line of research dedicated to finding alternative prescriptions that transform the BRE into a LME, and this is the topic of chapter 3.

Particularizing the BRE

For the purposes of chapter 4, it is convenient to find the environment correlation functions $\gamma_{rt}(\delta)$ when the environment is given by the medium-assisted fields of MQED. For that, we start from the multipolar coupling Hamiltonian in the long-wavelength approximation in eq. (2.102). There, the interaction is

$$H_{\text{int}} = -\frac{\mathbf{d}\cdot\mathbf{D}_{(\text{at})}(\mathbf{r}_{\text{at}})}{\varepsilon_0}$$

$$= -\mathbf{d} \cdot \sum_\lambda \int \mathrm{d}^3 r \int_0^\infty \mathrm{d}\omega\, \mathbf{G}_\lambda(\mathbf{r}_{\mathrm{at}}, \mathbf{r}, \omega) \cdot \mathbf{f}_\lambda(\mathbf{r}, \omega) + \mathrm{H.c.} \tag{2.173}$$

With the general notation above, the operators S_r and B_r are the components of $\mathbf{d}$ and $\mathbf{D}_{(\mathrm{at})}(\mathbf{r}_{\mathrm{at}})/\varepsilon_0$. The $-$ sign does not matter, as the effects discussed arise from terms quadratic in H'_{int}. In the interaction picture, we have

$$\frac{\mathbf{D}_{(\mathrm{at})}(\mathbf{r}_{\mathrm{at}}, t)}{\varepsilon_0} = \sum_\lambda \int \mathrm{d}^3 r \int_0^\infty \mathrm{d}\omega\, \mathbf{G}_\lambda(\mathbf{r}_{\mathrm{at}}, \mathbf{r}, \omega) \cdot \mathbf{f}_\lambda(\mathbf{r}, \omega) e^{-i\omega t} + \mathrm{H.c.} \tag{2.174}$$

Next, we may assume that the environment is approximately in a thermal state with sufficiently low temperature that we can, for all purposes, set it to zero: $k_{\mathrm{B}}T \ll \hbar\delta_i$. This is easily satisfied if the transitions have optical frequencies, whose associated temperatures are $O(10^4\ \mathrm{K})$. Consequently, ρ_{b} is the medium-assisted ground state and the fundamental expectation values become

The finite temperature case is a direct generalization involving the appearance of the bosonic thermal occupation at each frequency [249].

$$\left\langle \mathbf{f}_\lambda(\mathbf{r}, \omega) \mathbf{f}_{\lambda'}(\mathbf{r}', \omega') \right\rangle = \left\langle \mathbf{f}^\dagger_\lambda(\mathbf{r}, \omega) \mathbf{f}^\dagger_{\lambda'}(\mathbf{r}', \omega') \right\rangle = \left\langle \mathbf{f}^\dagger_\lambda(\mathbf{r}, \omega) \mathbf{f}_{\lambda'}(\mathbf{r}', \omega') \right\rangle = \mathbf{0} \tag{2.175a}$$

$$\left\langle \mathbf{f}_\lambda(\mathbf{r}, \omega) \mathbf{f}^\dagger_{\lambda'}(\mathbf{r}', \omega') \right\rangle = \delta_{\lambda\lambda'} \boldsymbol{\delta}(\mathbf{r} - \mathbf{r}') \delta(\omega - \omega'). \tag{2.175b}$$

Then, the time correlator that defines $\gamma_{rt}(\delta)$ is

$$\frac{\left\langle \mathbf{D}_{(\mathrm{at})}(\mathbf{r}_{\mathrm{at}}, \tau) \mathbf{D}_{(\mathrm{at})}(\mathbf{r}_{\mathrm{at}}, 0) \right\rangle}{\varepsilon_0^2} = \int_0^\infty \mathrm{d}\omega\, \frac{\hbar\omega^2}{\pi\varepsilon_0 c^2} \mathrm{Im}\, \mathbf{G}(\mathbf{r}_{\mathrm{at}}, \mathbf{r}_{\mathrm{at}}, \omega) e^{-i\omega\tau}, \tag{2.176}$$

where again eq. (2.86) has proven useful. Now, according to eq. (2.166), we have

$$\begin{aligned} \gamma_{rt}(\delta) &= \int_{-\infty}^\infty \mathrm{d}\tau \int_0^\infty \mathrm{d}\omega\, \frac{\omega^2}{\pi\hbar\varepsilon_0 c^2} \mathrm{Im}\, G_{rt}(\mathbf{r}_{\mathrm{at}}, \mathbf{r}_{\mathrm{at}}, \omega) e^{i(\delta-\omega)\tau} \\ &= 2\pi J_{rt}(\delta), \end{aligned} \tag{2.177}$$

where

$$\mathbf{J}(\omega) = \frac{\omega^2}{\pi\hbar\varepsilon_0 c^2} \mathrm{Im}\, \mathbf{G}(\mathbf{r}_{\mathrm{at}}, \mathbf{r}_{\mathrm{at}}, \omega) \tag{2.178}$$

is the spectral density of a general electromagnetic environment. Recall that we already encountered its free-space limit at the end of section 2.1.3. Finally, the functions Γ_{ij} that appear in eq. (2.169) are, in this particular case,

$$\Gamma_{ij}(\delta) = 2\pi \mathbf{d}_i^* \cdot \mathbf{J}(\delta) \cdot \mathbf{d}_j. \tag{2.179}$$

As for the λ_{rt} and Λ_{ij} functions, eq. (2.167) straightforwardly relates them to γ_{rt} and Γ_{ij}.

From the expressions above, it seems like the CP shift from eq. (2.143) will also appear here. Indeed, if we look at the secularized Lindblad master equation in eq. (2.172) and focus on transitions where $\sigma_i^\dagger \sigma_j = |a\rangle\langle a|$, for some atomic state $|a\rangle$, we see that the environment-induced energy shift is

$$\Delta_a = \frac{1}{\pi\varepsilon_0 c^2} \sum_b \int_0^\infty \mathrm{d}\omega \, \frac{\omega^2 \mathbf{d}_{ba}^* \cdot \mathrm{Im}\, \mathbf{G}(\mathbf{r}_{\mathrm{at}}, \mathbf{r}_{\mathrm{at}}, \omega) \cdot \mathbf{d}_{ba}}{\omega_{ab} - \omega}, \tag{2.180}$$

which is exactly eq. (2.141). As explained in section 2.4.1, only the scattering part will be considered here, as $\mathbf{G}^0$, in combination with the polarization self-energy (PSE), gives rise to free-space Lamb shifts that are significantly smaller than the effects studied here. Therefore, we will replace $\mathbf{G}$ with $\mathbf{G}^{\mathrm{s}}$ in λ_{rs} and Λ_{ij}, and discard the PSE from the atomic Hamiltonian. Nevertheless, the first line of eq. (2.169) contains more terms where $\sigma_i^\dagger \sigma_j = |a\rangle\langle c|$ for some $|a\rangle \neq |c\rangle$. Those additional contributions, which the secular approximation neglects except when $\omega_{ac} = 0$, provide coherent couplings between $|a\rangle$ and $|c\rangle$ that were missing from our initial calculation of the CP shift. Notably, the Purcell enhancement of the atomic decay rates γ_a of each state $|a\rangle$, which is captured by the appearance of $\mathbf{G} = \mathbf{G}^0 + \mathbf{G}^{\mathrm{s}}$ in $\gamma_{rt}(\delta)$, is also supplemented by corresponding incoherent couplings between different states. The impact of these off-diagonal terms on the atom's dynamics will be studied in chapter 4.

2.4.4 Recent additions to the OQS toolbox

Consider an environment whose spectral density is characterized by a very sharp peak around some atomic transition (see fig. 2.11a). The sharp peak may be identified as an EM resonance of the macroscopic body surrounding the atom, like the plasmonic dipolar resonance of a metallic sphere. Because $J(\omega)$ is proportional to the Fourier transform of the field correlators, it is evident that very sharp frequency features will correspond to very long-lived correlations. This directly confronts the Markovian approximation made in the derivation of the BRE. Indeed, the phenomenology associated with such a spectral density includes the coherent energy exchange between the atom and the EM resonance, a primary signature of the SC regime.

The inadequacy of the OQS formalism to straightforwardly account for these issues can be remedied by simply redefining what is meant by the system. The simplest way is to assign a single bosonic mode a for the EM resonance

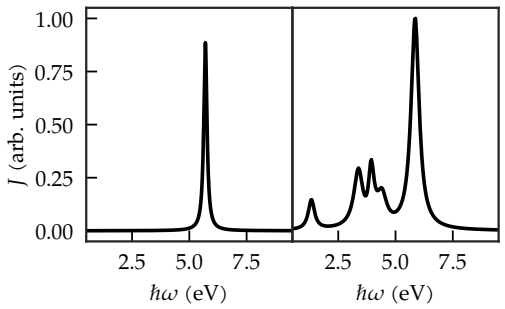

Figure 2.11: Examples of spectral densities.

(a) A non-Markovian environment characterized by a single sharp resonance

(b) A complex, highly-structured environment with five resonances.

1

at ω_r, with some finite decay rate κ_r associated to the width of the resonance and a coupling strength parameter g_r between the system and the resonance. Then, the system's Hilbert space is $\mathcal{H}_s = \mathcal{H}_{at} \otimes \mathcal{H}_a$ and one can tentatively write down the following LME

$$\dot{\rho}_s = -\frac{i}{\hbar}\left[H_{at} + \hbar\omega_r a^\dagger a + d\hbar g_r\left(a^\dagger + a\right), \rho_s\right] + \kappa_r \mathcal{D}_{a,a}[\rho_s], \tag{2.181}$$

where d is the atom's interaction operator. The use of this kind of phenomenological LME has been widely extended in cavity QED and QO, and is supported on the formal equivalence between a Lorentzian spectral density and a model of a single bosonic mode coupled to a set of perfectly Markovian environment oscillators [253]. More explicitly, the atom's dynamics generated by

$$H = H_{at} + \int \mathrm{d}\omega \left[\hbar\omega a^\dagger(\omega)a(\omega) + d\hbar\sqrt{J_L(\omega)}\left(a^\dagger(\omega) + a(\omega)\right)\right], \tag{2.182a}$$

where

$$J_L(\omega) = \frac{g_r^2}{\pi}\frac{\kappa_r/2}{(\omega-\omega_r)^2 + (\kappa_r/2)^2}, \tag{2.182b}$$

and

$$\begin{aligned} H_{model} = {} & H_{at} + \hbar\omega_r a^\dagger a + d\hbar g_r\left(a^\dagger + a\right) \\ & + \int \mathrm{d}\Omega \left[\hbar\Omega b^\dagger(\Omega)b(\Omega) + \hbar\sqrt{\frac{\kappa_r}{2\pi}}\left(a^\dagger b(\Omega) + a b^\dagger(\Omega)\right)\right], \end{aligned} \tag{2.182c}$$

are identical and, since the Markov approximation is exact for flat environment-system couplings, eq. (2.181) is the exact equation of motion of the atom-mode system.

In spite of such a convenient relation between a Lorentzian bath and a single bosonic mode, it has been known for some time that the simple LME in eq. (2.181) brings with it a number of unphysical effects, such as production

of excitations in the system at zero temperature or incorrect photon correlations [165, 254] for large values of g_r. The origin of these issues lies in the negative frequency tail of the Lorentzian line shape, which is effectively a source of incoherent pumping. There are several ways to go about this problem. The way that is most in line with a "traditional" OQS approach is to turn back to the microscopic derivations, which require the knowledge of the system's eigenstates and eigenenergies. If the atom and resonance are ultrastrongly coupled, then the coupled eigenstates will necessarily be very different from the uncoupled bare ones. It is then clear that a more consistent derivation needs to account for the fact that the atom and the mode interact with each other. The first solution, derived in [165], is the so-called "dressed" master equation, because it uses the coupled (or dressed) excitations of the system. Subsequent generalizations have been proposed since then [166], to overcome some remaining limitations, but the underlying idea has always been to extend the system to astutely include the non-Markovian part of the environment. Still, these models are generally not well suited to describe environments with a very complex mode structure (see fig. 2.11b), where resonances might not even look like Lorentzian functions.

We next describe another powerful solution to attack this issue that has a number of advantages: the few-mode quantization approach [201]. It works for arbitrary coupling strengths, in any general EM setup, and it is exact up to the numerical convergence of one step. The idea is something that has been mentioned before (at the end of section 2.1.3) and that generalizes the equivalence mentioned in the single mode picture from above, namely, that any set of modes that reproduces a given spectral density induces the same dynamics in the emitter. Specifically, one replaces the whole MQED continuum of modes with a set of N coupled discrete modes a_α, with frequencies and couplings summarized in $\omega_{\alpha\beta}$, and N continua $b_\alpha(\Omega)$. The discrete modes are additionally coupled to independent continua (one per mode) with a frequency-independent parameter $\sqrt{\frac{\kappa_\alpha}{2\pi}}$. Then, the atom is coupled to the discrete modes with some coupling strengths g_α, through the operator d. Accordingly, the total Hamiltonian of the model is

$$\begin{aligned} H = H_{\text{at}} &+ \sum_{\alpha\beta} \hbar\omega_{\alpha\beta} a_\alpha^\dagger a_\beta + d \sum_\alpha \hbar g_\alpha \left(a_\alpha^\dagger + a_\alpha\right) \\ &+ \sum_\alpha \int \mathrm{d}\Omega \left[\hbar\Omega b_\alpha^\dagger(\Omega) b_i(\Omega) + \hbar\sqrt{\frac{\kappa_i}{2\pi}} \left(a_\alpha^\dagger b_\alpha(\Omega) + a_\alpha b_\alpha^\dagger(\Omega)\right) \right]. \end{aligned} \tag{2.183}$$

With these conditions, there are two key realizations that give the method its power. The first is that the parameters ω_α, $\omega_{\alpha\beta}$, κ_α and g_α can be chosen to fit

any realistic spectral density. If the spectral density for the single-mode model was a Lorentzian function, in this generalized framework it is

$$J_{\mathrm{m}}(\omega) = \frac{1}{\pi}\mathbf{g}\cdot \mathrm{Im}\left[(\mathbf{h}-\omega I_N)^{-1}\right]\cdot \mathbf{g}^{\mathrm{t}}, \tag{2.184}$$

where $\mathbf{g} = (g_1, \dots, g_N)$ and $h_{\alpha\beta} = \omega_{\alpha\beta} - i\delta_{\alpha\beta}\kappa_\alpha/2$ contain the model's parameters. By choosing them judiciously, one can make J_{m} fit any arbitrary spectral density. The second realization is that it can be proven that the dynamics of the atom plus the discrete modes are exactly given by the LME

$$\dot{\rho}_{\mathrm{s}} = -\frac{i}{\hbar}\left[H_{\mathrm{at}} + \sum_{\alpha\beta}\hbar\omega_{\alpha\beta}a_\alpha^\dagger a_\beta + d\sum_\alpha \hbar g_\alpha\left(a_\alpha^\dagger + a_\alpha\right), \rho_{\mathrm{s}}\right] + \sum_\alpha \kappa_\alpha \mathcal{D}_{a_\alpha, a_\alpha}[\rho_{\mathrm{s}}]. \tag{2.185}$$

Thus, we have a LME that represents the dynamics of the system exactly. To obtain the atom's evolution, one simply takes the partial trace over the discrete modes. The only step where any approximation is made is the choice of the parameter values to fit the target spectral density, but even here one can always reach a sufficiently converged spectral density J_{m} by adding enough modes. Nevertheless, actual implementations of the method show that a moderate amount of modes is usually enough [167, 255], and additional work has been made to reduce it even further [256].

In the work presented in chapters 3 and 4, we use either the few-mode quantization approach or the single-mode model from above as a fast and affordable way to compute the exact dynamics against which other methods are compared. In particular, in chapter 3 the parameters of the few-mode model are given random values to sample the space of physically consistent atom-environment interactions, and from there extract further statistical conclusions.

Chapter Three | Taming the Bloch-Redfield equation

Where there's a whip, there's a way!

Orcs marching song in the 1980 animated movie The Return of the King, *by Glenn Yarbrough*

Chapter summary In the last section of chapter 2, we described the ideal kind of master equation that, in principle, everyone would like to have: the LME. We also saw that, unfortunately, direct derivations of master equations from microscopic models fail to yield a LME, instead resulting in the BRE. In this chapter, we delve deeper into the reasons why an LME is preferable over the BRE, and discuss the inadequacy of the standard procedure to turn the BRE into a LME: the secular approximation. Next, we describe a recent and simple approach that aims to retrieve a LME from the BRE, referred to as $g\Lambda - g\Gamma$. After that, we identify two flaws of that procedure that preclude the final equation from being a genuine LME in arbitrary scenarios. Finally, we present a minimal modification of the $g\Lambda - g\Gamma$ method that guarantees that the resulting master equation is an accurate and true LME. The results shown in this chapter have been published in [257].

3.1 Notation and preliminary considerations

Let us start by refreshing the notation. We consider a system interacting with its environment through

$$H_{\text{int}} = \sum_r S_r B_r, \tag{3.1}$$

where S_r and B_r are Hermitian system and environment operators, respectively. For concreteness, we will take an atom as the system such that its den-

sity matrix is ρ_{at}. Note, however, that this is done only to set a notation that is convenient throughout the chapter, and choosing an atom is not a real imposition. We denote the atom's eigenstates and eigenfrequencies as $|a\rangle$ and ω_a, where the state index $a = 1, \dots, \dim \mathcal{H}_{\text{at}}$. In order to retrieve a simpler index structure in the equations, we switch from state indices a to transition indices i defining $\sigma_i = |a_i\rangle\langle b_i|$, where $i = 1, \dots, (\dim \mathcal{H}_{\text{at}})^2$. To any given transition σ_i, we associate the transition frequency $\delta_i \equiv \omega_{b_i} - \omega_{a_i}$, which is positive (negative) when σ_i is a lowering (raising) operator. With this notation, the BRE, also in eq. (2.169), can be written as

$$\begin{aligned}\dot{\rho}_{\text{at}} = -\frac{i}{\hbar}[H_{\text{at}}, \rho_{\text{at}}] + \sum_{ij} \Big\{ &- i\big(\Lambda_{ij}(\delta_j)\sigma_i^\dagger\sigma_j\rho_{\text{at}} - \rho_{\text{at}}\Lambda_{ij}(\delta_i)\sigma_i^\dagger\sigma_j\big) \\ &+ i\big(\Lambda_{ij}(\delta_j) - \Lambda_{ij}(\delta_i)\big)\sigma_j\rho_{\text{at}}\sigma_i^\dagger \\ &- \frac{1}{2}\big(\Gamma_{ij}(\delta_j)\sigma_i^\dagger\sigma_j\rho_{\text{at}} + \rho_{\text{at}}\Gamma_{ij}(\delta_i)\sigma_i^\dagger\sigma_j\big) \\ &+ \frac{1}{2}\big(\Gamma_{ij}(\delta_j) + \Gamma_{ij}(\delta_i)\big)\sigma_j\rho_{\text{at}}\sigma_i^\dagger\Big\}. \end{aligned} \tag{3.2}$$

In this equation, Λ_{ij} and Γ_{ij} are related to the atomic coupling operators (S_r) and bath correlation functions λ_{rt} and γ_{rt} through

$$\Gamma_{ij}(\delta) = \sum_{rt} \langle a_i|S_r|b_i\rangle^* \gamma_{rt}(\delta)\big\langle a_j\big|S_t\big|b_j\big\rangle \quad \text{and} \tag{3.3a}$$

$$\Lambda_{ij}(\delta) = \sum_{rt} \langle a_i|S_r|b_i\rangle^* \lambda_{rt}(\delta)\big\langle a_j\big|S_t\big|b_j\big\rangle, \tag{3.3b}$$

where

$$\frac{\gamma_{rt}(\delta)}{2} + i\lambda_{rt}(\delta) = \frac{1}{\hbar^2}\int_0^\infty \mathrm{d}\tau\, \langle B_r(\tau)B_t(0)\rangle e^{i\delta\tau}. \tag{3.3c}$$

As we have done in other places throughout the thesis, we introduce here the spectral density $J_{rt}(\delta) = \gamma_{rt}(\delta)/2\pi$. Finally, as we mentioned in section 2.4.3, the secular approximation consists in eliminating from the BRE every single term where $\delta_i \neq \delta_j$, which yields

$$\dot{\rho}_{\text{at}} = -\frac{i}{\hbar}[H_{\text{at}}, \rho_{\text{at}}] - i\sum_{ij}^{\delta_i=\delta_j} \Lambda_{ij}(\delta_i)\big[\sigma_i^\dagger\sigma_j, \rho_{\text{at}}\big] + \sum_{ij}^{\delta_i=\delta_j} \Gamma_{ij}(\delta_i)\mathcal{D}_{\sigma_i,\sigma_j}[\rho_{\text{at}}], \tag{3.4}$$

that is, a genuine LME.

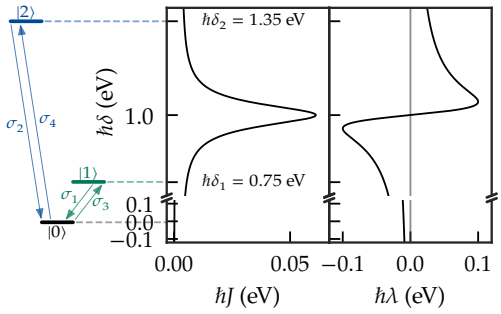

Figure 3.1: V-type three-level atom coupled to its environment, characterized by a Lorentzian spectral function $\gamma(\delta)$. Adapted from [257].

1

3.1.1 Bloch-Redfield equation: non-positive evolution

Traditionally, the attitude of physicists towards the BRE has leaned to the side of wariness, due to its failure to generate a completely positive map. This can be traced back to the fact that the Kossakowski matrix of the BRE, as read from eq. (2.170), is not positive semidefinite. In fact, the BRE generally fails to preserve the positivity of the populations, meaning that it does not just miss complete positivity, but simple positivity as well. We next show that this is the case by solving the BRE in a particular example. Consider a three-level atom (3LA) like the one depicted in fig. 3.1, where the allowed transitions make it a V-type system. Thus, a transition index $i = 1, 2, 3, 4$ is enough, where

$$\sigma_1 = |0\rangle\langle 1| \qquad \sigma_2 = |0\rangle\langle 2| \qquad \sigma_3 = |1\rangle\langle 0| \qquad \sigma_4 = |2\rangle\langle 0|, \tag{3.5}$$

such that δ_1 and δ_2 are positive, while $\delta_3 = -\delta_1$ and $\delta_4 = -\delta_2$ are negative. The 3LA interacts with a reservoir of harmonic oscillators through

$$H_{\text{int}} = \sum_i \sigma_i \int_0^\infty \mathrm{d}\omega \, \sqrt{J(\omega)}\big(b^\dagger(\omega) + b(\omega)\big). \tag{3.6a}$$

We take the environment's spectral density $J(\omega)$ to be characterized by a Lorentzian line shape, such that the correlation functions $\gamma(\delta) = 2\pi J(\delta)$ and $\lambda(\delta)$ are given by

$$\gamma(\delta) = g_{\text{r}}^2 \frac{\kappa_{\text{r}}}{(\delta - \omega_{\text{r}})^2 + (\kappa_{\text{r}}/2)^2} \quad \text{and} \tag{3.6b}$$

$$\lambda(\delta) = g_{\text{r}}^2 \frac{\delta - \omega_{\text{r}}}{(\delta - \omega_{\text{r}})^2 + (\kappa_{\text{r}}/2)^2}. \tag{3.6c}$$

Here, ω_{r} and κ_{r} are the resonant frequency and width (FWHM) of the peak, and g_{r} controls its maximum value via $\max_\delta \gamma(\delta) = 4g^2/\kappa_{\text{r}}$. For concreteness, we now set $\hbar\omega_{\text{r}} = 1$ eV, $\hbar\kappa_{\text{r}} = 0.1$ eV, $\hbar\delta_1 = 0.75$ eV, $\hbar\delta_2 = 1.35$ eV, and the

initial state to $|\psi(0)\rangle = (|1\rangle - |2\rangle)/\sqrt{2}$, and solve the temporal evolution as a function of g_r/κ_r using the BRE. The dynamics of the populations $\rho_{at,00}$, $\rho_{at,11}$ and $\rho_{at,22}$ are shown in fig. 3.2, as a function of g_r/κ_r in the top panels, and for a fixed value of $g_r = \kappa_r$ in the lower panels. In the color maps, blue and red denote negative and positive values, respectively, and, in the line plots, the shaded blue regions indicate negative populations. In the first column, besides some oscillatory behavior, figs. 3.2a and 3.2d feature a very noticeable negative population of the ground state $|0\rangle$. Since the BRE does preserve the trace of the density matrix, this negative ground state population also manifests itself in the small initial bumps observed in figs. 3.2e and 3.2f: the horizontal dashed lines highlight the fact that $\rho_{at,11}$ and $\rho_{at,22}$ simultaneously surpass the 0.5 mark.

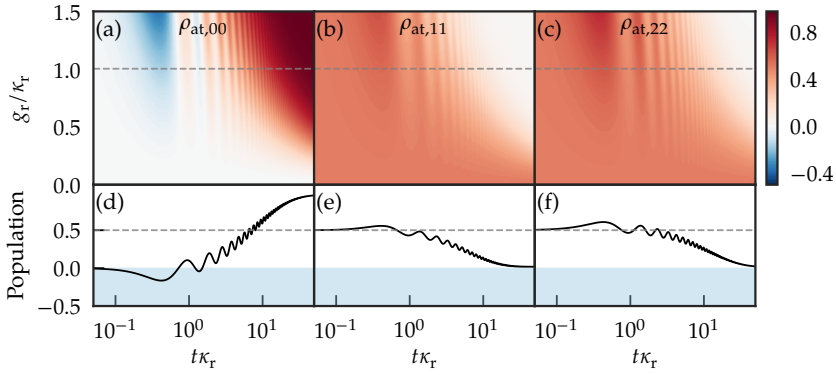

Figure 3.2: Populations of a three-level atom according to the BRE. Top row: as a function of time and the coupling strength g_r. From left to right, populations of $|0\rangle$, $|1\rangle$ and $|2\rangle$. Bottom row: Cuts of the color maps at $g_r = \kappa_r$. The shaded blue region indicates negative values. Adapted from [257].

With fig. 3.2, we have seen that the BRE can return unphysical predictions. In all fairness, however, as long as the underlying physical approximations (see section 2.4.3 for the details) hold to a high enough degree, the BRE should produce physically accurate results. In that sense, it has been proposed that the lack of positivity of the BRE can be used to identify regimes in which, e.g., the Markov approximation fails [251]. As a matter of fact, over the last few years, the BRE has been vindicated by some studies that shed light on different misconceptions about it [250, 251].

Nevertheless, it can be argued that a true Lindblad equation is still preferable, as not only does it always give physically sensible evolution, but it also presents some computational advantages. For example, the LME can be simulated with quantum Monte Carlo methods, as it admits a quantum trajectory

unraveling, whereas this is not the case for the BRE. The "text book" way to turn the BRE into a LME is the secular approximation. We already mentioned in section 2.4.3 that it can be inadequate, as it can miss relevant effects, and the next section is devoted to clarifying why and how the secular approximation works.

We note that some recent work has derived a pseudo-Lindblad quantum trajectory method to address this issue [258].

3.2 Failure of the secular approximation

The reason why the secular approximation generally fails to capture the dynamics can be succinctly summarized as follows: the couplings between populations and coherences from different degenerate subspaces are discarded. As concise as this statement is, it surely requires some further discussion to clarify its implications. We first make more explicit what this assertion means in the secularized master equation by taking a look at the terms that are included in it. However, the secular condition as expressed above is not the most adequate to this end. To express everything in the most convenient way, we first write everything in state indices again. Then, eq. (3.4) is equivalent to

$$\dot{\rho}_{\mathrm{at},ab} = \sum_{cd}^{\omega_{ab}=\omega_{cd}} [-i\omega_{ab}\delta_{ac}\delta_{bd} + \mathcal{R}_{abcd}]\rho_{\mathrm{at},cd}, \tag{3.7}$$

where $\rho_{\mathrm{at},ab} = \langle a|\rho_{\mathrm{at}}|b\rangle$ and the Bloch-Redfield tensor is

$$\begin{aligned}\mathcal{R}_{abcd} = \sum_{rt}\Bigg\{ & S^*_{r,bd}\left[\frac{\gamma_{rt}(\omega_{ca}) + \gamma_{rt}(\omega_{db})}{2} + i(\lambda_{rt}(\omega_{ca}) - \lambda_{rt}(\omega_{db}))\right]S_{t,ac} \\ & - \delta_{bd}\sum_n S^*_{r,na}\left(\frac{\gamma_{rt}(\omega_{cn})}{2} + i\lambda_{rt}(\omega_{cn})\right)S_{t,nc} \\ & - \delta_{ac}\sum_n S^*_{r,nd}\left(\frac{\gamma_{rt}(\omega_{dn})}{2} + i\lambda_{rt}(\omega_{dn})\right)S_{t,nb}\Bigg\}.\end{aligned} \tag{3.8}$$

The condition over the summation symbol in eq. (3.7) means that only terms with $\omega_{ab} = \omega_{cd}$ are kept. Technically speaking, this is not exactly the same condition from before, $\delta_i = \delta_j$, where δ_i is the oscillation frequency of σ_i in the interaction picture, not even when translating the transition indices i and j to pairs of eigenstate indices ab and cd. This is a subtle matter that could potentially cause index mismatches. Fortunatelly, the $\delta_i = \delta_j$ and $\omega_{ab} = \omega_{cd}$ conditions can actually be shown to be equivalent, as we explicitly do line by line below. To that end, we simply read the states that correspond to the σ_i and σ_j transitions from the matrix elements of S_r according to eq. (3.3):

1st: Here, $\delta_i = \omega_{db}$ and $\delta_j = \omega_{ca}$. Therefore, $0 = \delta_i - \delta_j = \omega_{db} - \omega_{ca} =$

$\omega_{ab} - \omega_{cd}$.

2nd: Now, $\delta_i = \omega_{an}$, $\delta_j = \omega_{cn}$, and the Kronecker delta ensures that $0 = \delta_i - \delta_j = \omega_{an} - \omega_{cn} - \omega_{bd} = \omega_{ab} - \omega_{cd}$.

3rd: Last, $\delta_i = \omega_{dn}$, $\delta_j = \omega_{bn}$, and the Kronecker delta implies that $0 = \delta_i - \delta_j = \omega_{dn} - \omega_{bn} - \omega_{ac} = \omega_{ab} - \omega_{cd}$.

We can now revert to transition indices through $ab \to k$ and $cd \to l$. We change the names of the transition indices compared to earlier (i and j) to emphasize that these transition indices are not directly the same as those appearing in eq. (3.2) or eq. (3.4). There, as we have discussed above, i and j refer to the transition frequency of the operators $sigma_i$ and σ_j through which the action of the corresponding superoperator is defined. Here, they come from expanding ρ in terms of the same basis of transition operators $\{\sigma_k\}$. Regardless of these subtleties, we can compactly write the secularized BRE as

$$\dot{\rho}_{\mathrm{at},k} = \sum_{l}^{\delta_k=\delta_l} [-i\omega_k \delta_{kl} + \mathcal{R}_{kl}]\rho_{\mathrm{at},l}, \tag{3.9}$$

Even if the secular condition has the same formal expression, the renewed interpretation of its elements δ_k and δ_k allows us to mathematically understand which terms are kept and discarded in the secularized LME. Let us first focus on a matrix element of ρ_{at} where both states belong to the same degenerate subspace: $\rho_{\mathrm{at},k}$ with $\delta_k = 0$. Then, these matrix elements are only coupled to similarly degenerate matrix elements because $\delta_l = 0$. In the other possible case, $\delta_k \neq 0$, the coherence $\rho_{\mathrm{at},k}$ is only affected by coherences with the same transition energy δ_l. The couplings included in the secularized LME are visually represented in the schematic figures in fig. 2.10. Not much more insight can be drawn from the most general considerations, so we assume next that there are no degeneracies in the spectrum of H_{at}. The discussion in the preceding lines implies that populations (coherences) are only influenced by populations (coherences), which circles back to the opening statement of this section.

The above considerations show that only the terms in the BRE satisfying strict frequency conditions are kept after the secular approximation, which has unfortunate effects. However, the generality of the presentation so far makes it hard to grasp the real consequences of the secular approximation on the dynamics, a difficulty directly inherited from the intricacies of the BRE. To provide a more tangible demonstration, we first devote our attention to the atomic Hamiltonian and, afterwards, to the Kossakowski matrix.

Environment-induced Hamiltonian correction After the secular approximation, part of the dynamics included in the secularized Bloch-Redfield tensor $\mathcal{R}$ is unitary and generated by the following shift Hamiltonian:

$$\Delta = -\hbar \sum_{ij}^{\delta_i=\delta_j} \Lambda_{ij}(\delta_i)\sigma_i^\dagger \sigma_j. \tag{3.10}$$

Due to the secular approximation, the matrix representation of this operator will be structured in blocks that correspond to each degenerate subspace, and with no couplings between them:

$$\Delta = \begin{pmatrix} \omega = \omega_1 & 0 & 0 \\ 0 & \omega = \omega_2 & 0 \\ 0 & 0 & \ddots \end{pmatrix}. \tag{3.11}$$

For concreteness, imagine that our system of interest is a three-level atom with a V-type energy spectrum as the one in fig. 3.1. Depending on whether $|1\rangle$ and $|2\rangle$ are degenerate or not, we have

$$\Delta = \hbar \begin{pmatrix} \Lambda_{00} & 0 \\ 0 & \Lambda_{11} \quad \Lambda_{12} \\ & \Lambda_{21} \quad \Lambda_{22} \end{pmatrix} \tag{3.12}$$

or

$$\Delta = \hbar \begin{pmatrix} \Lambda_{00} & 0 & 0 \\ 0 & \Lambda_{11} & 0 \\ 0 & 0 & \Lambda_{22} \end{pmatrix}, \tag{3.13}$$

respectively. The difference between these corrections to the Hamiltonian highlights the problems of the secular approximation: when $|1\rangle$ and $|2\rangle$ are degenerate, there is an environment-induced coupling between them, which disappears abruptly due to the secular approximation. Physically, the off-diagonal coupling Λ_{12} will induce Rabi-like oscillations between $|1\rangle$ and $|2\rangle$ in the degenerate case, with a frequency equal to $\Omega_R = \sqrt{(\Lambda_{11} - \Lambda_{22})^2 + 4\Lambda_{12}^2}$. Meanwhile, there are no oscillations at all as soon as one breaks the degeneracy. However, the timescale of the Rabi oscillations is $\sim |\Lambda_{ij}|^{-1}$ and the timescale at which the non-degeneracy becomes noticeable is $|\omega_{12}|^{-1}$. Hence, whenever $|\omega_{12}| \ll |\Lambda_{ij}|$, the system will undergo many Rabi cycles before "realizing" that the states were not quite degenerate.

Environment-induced dissipation The dissipative part of the secularized LME suffers from similar disappearances, which strongly affect the decay channels present in the atom, encoded in the eigenvectors and eigenvalues of the Kossakowski matrix $\mathbf{K}$. For the present V-type 3LA, $\mathbf{K}$ is a 9×9 matrix. However, if we assume that $\gamma(\omega) = 0$ for $\omega \leq 0$ (we only have decay, and no thermal pumping) and V-type non-zero transition matrix elements, almost all entries of the Kossakowski matrix are zero except for a few elements. Thus, we only write here the non-vanishing block of $\mathbf{K}$. In the degenerate case ($\omega_{10} = \omega_{20}$), we have

$$\mathbf{K}_{2\times 2} = \begin{pmatrix} \langle 0|S|1\rangle^* \gamma(\omega_{10}) \langle 0|S|1\rangle & \langle 0|S|1\rangle^* \gamma(\omega_{10}) \langle 0|S|2\rangle \\ \langle 0|S|2\rangle^* \gamma(\omega_{20}) \langle 0|S|1\rangle & \langle 0|S|2\rangle^* \gamma(\omega_{20}) \langle 0|S|2\rangle \end{pmatrix}, \tag{3.14}$$

while the same block becomes

$$\mathbf{K}_{2\times 2} = \begin{pmatrix} \langle 0|S|1\rangle^* \gamma(\omega_{10}) \langle 0|S|1\rangle & 0 \\ 0 & \langle 0|S|2\rangle^* \gamma(\omega_{20}) \langle 0|S|2\rangle \end{pmatrix}, \tag{3.15}$$

in the non-degenerate case ($\omega_{10} \neq \omega_{20}$). In the first case, because $\det \mathbf{K} = 0$, we have only one non-zero eigenvalue equal to $\mathrm{Tr}\, \mathbf{K}$. The eigenvector associated to the vanishing decay rate corresponds to a combination of $|1\rangle$ and $|2\rangle$ that does not decay at all, i.e., it is decoupled from the environment, while the orthogonal combination decays with the sum of the "individual decay rates" of $|1\rangle$ and $|2\rangle$ if they were independent. However, when the states are non-degenerate, the off-diagonal terms again vanish abruptly, and no smooth transition between the degenerate and non-degenerate regimes is recovered.

We end this section with a more graphic and suggestive description of the physical processes described above. For a V-type atom initially in $|1\rangle$, virtual excitations will be emitted into the environment, and subsequently reabsorbed. If $|1\rangle$ and $|2\rangle$ are very far from each other in energy, the excitation will only be able to take the atom back into $|1\rangle$. This translates into the shift and decay rate of $|1\rangle$. If, instead, $|1\rangle$ and $|2\rangle$ are completely degenerate, the excitation will see both states on its way back, and the atom will end up in either one, which in turn induces Rabi-like oscillations and is responsible for the combined dissipation channels. Last, in the quasidegenerate case, the virtual excitation from the environment is again able to drive Rabi-like oscillations, although not as efficiently as in the degenerate case. As for the decay, the individual decay rates give us the bandwidth of environmental modes that the levels directly interact with. If the levels are not quite degenerate, but there is still a noticeable overlap between the affected environmental modes, then something like the combined dissipative channels will still play a role in describ-

ing the atom's dissipative behavior. The clear implication is that we expect a smoother transition between the degenerate and completely non-degenerate regimes, in which the secular approximation does provide accurate results. Going beyond the secular approximation means finding a prescription that interpolates between both extremes and accurately describes the quasidegenerate case. The rest of the chapter deals with ways to include these additional effects, which do not straightforwardly conform to a genuine Lindblad form.

3.3 Current status of the issue

We have seen already that the secular approximation, the simplest way to turn the BRE into a LME, is expected to fail when there are quasidegenerate subspaces in the energy spectrum. Indeed, it has been questioned in several works [250, 259, 260]. Since the LME has advantages over the BRE, a surge of research activity trying to find alternatives has been going on for some time [259, 261–265]. In these articles, positivity is restored through various approaches, such as temporal coarse graining or frequency clustering. Such procedures can, occasionally, require detailed knowledge of the system's energy spectrum and, perhaps, a different implementation for different systems. Here, we highlight the approach proposed by McCauley and coworkers [266], whose method cleanly avoids the secular approximation and can be implemented in a simple manner. Unfortunately, their idea potentially runs into two problems when one considers relatively complex and general systems and environments, failing to retrieve a LME in those scenarios. We will explain in section 3.4 what these problems are, the conditions under which they arise, and then provide a minimal solution to both that guarantees a final LME. To that end, we begin by describing the method devised in [266].

3.3.1 A simple (but flawed) LME prescription

We adapt the procedure of [266] to the notation introduced in sections 2.4.3 and 3.1. In doing so, we already slightly generalize the method of [266]. There, the authors consider a system (here, an atom) interacting with its environment through

$$H = H_{\text{at}} + S \int \mathrm{d}\omega \, \sqrt{J(\omega)}\big[b^\dagger(\omega) + b(\omega)\big] + \int \mathrm{d}\omega \, \hbar\omega \, b^\dagger(\omega) b(\omega), \tag{3.16}$$

and applied the RWA approximation to the system-bath coupling to derive the master equation. Our present exposition does not rely on the RWA at all,

and includes the case where there are several interaction terms:

$$H_{\text{int}} = \sum_r S_r B_r = \sum_r S_r \int \mathrm{d}\omega \, \sqrt{J_{rr}(\omega)} \left[b_r^\dagger(\omega) + b_r(\omega) \right], \tag{3.17}$$

By the way, this possibility is at the heart of one of the potential problems of the LME of [266] discussed in this chapter.

which allows for cross-correlations in the environment's B_r operators. At the end of section 2.4.3, we showed that in arbitrary EM environments $\boldsymbol{\gamma} \propto \mathbf{J} \propto \operatorname{Im} \mathbf{G}$, which has non-diagonal elements except in sufficiently symmetric configurations. In this interaction Hamiltonian, the off-diagonal elements J_{rt} would be encoded in $\left[b_r(\omega), b_t^\dagger(\omega') \right] = f_{rt}\delta(\omega - \omega')$, where $f_{rt} = J_{rt}/\sqrt{J_{rr}J_{tt}}$ (see section 2.4 of [180] for a more detailed discussion).

From this somewhat generalized interaction, the prescription proposed in [266] is to take the BRE (eq. (3.2)) and replace

$$\Lambda_{ij}(\delta_i) \text{ and } \Lambda_{ij}(\delta_j) \to \tilde{\Lambda}_{ij} = \sqrt{\Lambda_{ij}(\delta_i)}\sqrt{\Lambda_{ij}(\delta_j)} \quad \text{and} \tag{3.18a}$$

$$\Gamma_{ij}(\delta_i) \text{ and } \Gamma_{ij}(\delta_j) \to \tilde{\Gamma}_{ij} = \sqrt{\Gamma_{ij}(\delta_i)}\sqrt{\Gamma_{ij}(\delta_j)}, \tag{3.18b}$$

that is, replace the coefficients of the BRE with suitable geometric averages. For concreteness, we will refer to this method as $g\Lambda - g\Gamma$, as a geometric average appears for both Λ and Γ. The immediate effect of this substitution is that we eliminate the asymmetry in the i and j indices in eq. (3.2) that prevents us from (i) writing the first line as a commutator, (ii) eliminating the second line, (iii) expressing the third line as an anticommutator, and (iv) finding a refilling term with the appropriate coefficient:

$$\dot{\rho}_{\text{at}} = -\frac{i}{\hbar}[H_{\text{at}}, \rho_{\text{at}}] - i \sum_{ij} \tilde{\Lambda}_{ij} \left[\sigma_i^\dagger \sigma_j, \rho_{\text{at}} \right] + \sum_{ij} \tilde{\Gamma}_{ij} \mathcal{D}_{\sigma_i, \sigma_j}[\rho_{\text{at}}]. \tag{3.19}$$

This "recipe" seemingly eliminates all the mathematical problems of the BRE at once, in a very simple and elegant way, although we discuss in section 3.4 that this is not actually the case in general environments.

Still, a question remains: Why is this geometric mean replacement supposed to accurately describe the actual dynamics of the atom? We can answer it by analyzing possible scenarios:

1st: In the degenerate transition case, $\delta_i = \delta_j$ so $\tilde{\Lambda}_{ij} = \Lambda_{ij}(\delta_i) = \Lambda_{ij}(\delta_j)$ and $\tilde{\Gamma}_{ij} = \Gamma_{ij}(\delta_i) = \Gamma_{ij}(\delta_j)$.

2nd: In the quasidegenerate transition case, we have that

$$\left| \delta_i - \delta_j \right| \lesssim \max_{\delta \in \{\delta_i, \delta_j\}} (\Lambda_{ij}(\delta), \Gamma_{ij}(\delta)).$$

Accordingly, it is important to keep these terms, as the premise for the secular approximation is not fulfilled. If the correlation functions are "flat" enough, that is, the environment is sufficiently Markovian, then $\Lambda_{ij}(\delta_i) \approx \Lambda_{ij}(\delta_j) \approx \tilde{\Lambda}_{ij}$, and likewise for $\tilde{\Gamma}_{ij}$.

3rd: As the difference $\left|\delta_i - \delta_j\right|$ grows and surpasses the scale of environment-induced effects given by $\max_{\delta\in\{\delta_i,\delta_j\}}(\Lambda_{ij}(\delta), \Gamma_{ij}(\delta))$, the effect of these terms in the BRE becomes less relevant, until the secular approximation is indeed accurate. In such cases, $\tilde{\Lambda}_{ij}$ and $\tilde{\Gamma}_{ij}$ can be very different from the original values, but the accuracy of the equation does not suffer from it since we are replacing a term that does not influence the dynamics with another that does not do so either. Indeed, we could simply eliminate these terms through a "partial" secular approximation. However, keeping them makes the procedure more direct and provides neater final expressions in certain cases.

Therefore, the replacement is indeed accurate when it is relevant. Another advantage of this prescription is that, if no cross-correlations between different environment operators B_r exist, i.e., $\lambda_{rt} = 0$ for $r \neq t$, and H_{int} can be written in a way where every transition operator σ_i is contained in only one S_r, then the LME can be written as

$$\dot{\rho}_{\text{at}} = -\frac{i}{\hbar}[H_{\text{at}}, \rho_{\text{at}}] - i\sum_r [A_r^\dagger A_r, \rho_{\text{at}}] + \sum_r \mathcal{D}_{\Sigma_r,\Sigma_r}[\rho_{\text{at}}]. \tag{3.20a}$$

In this equation, we have defined collective operators

$$A_r = \sum_j \sqrt{\lambda_{rr}(\delta_j)} S_{r,j}\sigma_j \quad \text{and} \quad \Sigma_r = \sum_j \sqrt{\gamma_{rr}(\delta_j)} S_{r,j}\sigma_j, \tag{3.20b}$$

which accurately reflect the ways in which the atom develops energy shifts and its decay channels.

3.4 Fixing the flaws

In this section, we reveal the problems which can arise with the geometric mean prescription for complex environments and systems. In short, it can happen that the energy shift Hamiltonian is *non-Hermitian*, that the Kossakowski matrix is *non-positive semidefinite*, or both. We point out the origin of each problem and describe simple fixes that solve both issues separately.

3.4.1 Non-Hermitian energy shift

One of the hypotheses in Lindblad's theorem (eq. (2.148)) is that the commutator term generates unitary dynamics, i.e.,

$$\tilde{H}_{\text{at}} = H_{\text{at}} + \Delta = H_{\text{at}} + \hbar \sum_{ij} \tilde{\Lambda}_{ij} \sigma_i^\dagger \sigma_j \tag{3.21}$$

must be Hermitian. Hence, whatever procedure we follow starting at the BRE, the corresponding energy shift Δ should be Hermitian. In this case, Δ is trivially a Hermitian operator when the matrix $\tilde{\Lambda}_{ij}$ is Hermitian as well. While Δ can in principle be Hermitian even if $\tilde{\Lambda}$ is not, this would require very fortuitous cancellations involving system and environment properties. Hence, for all practical purposes, we can gauge the Hermiticity of Δ through that of $\tilde{\Lambda}_{ij}$.

Even if the risk of confusion may be minimal, we note that the Hermiticity of Δ and $\tilde{\Lambda}_{ij}$ is considered in different spaces: $\mathcal{H}_{\text{at}}$ and the space of linear operators of $\mathcal{H}_{\text{at}}$, respectively.

As can probably be guessed, the geometric mean procedure does not guarantee that $\tilde{\Lambda}_{ij}$, and therefore Δ, is Hermitian. We illustrate the origin of the non-Hermiticity with the same 3LA and environment used in section 3.1.1 to show negative populations predicted by the BRE. First, we note that the Hamiltonian correction is

$$\Delta = \hbar \begin{pmatrix} \tilde{\Lambda}_{33} + \tilde{\Lambda}_{44} & 0 & 0 \\ 0 & \tilde{\Lambda}_{11} & \tilde{\Lambda}_{12} \\ 0 & \tilde{\Lambda}_{21} & \tilde{\Lambda}_{22} \end{pmatrix}. \tag{3.22}$$

Consider now a situation such as the one depicted in fig. 3.1, where the function λ takes different signs when evaluated at δ_1 or δ_2: $\lambda(\delta_1)\lambda(\delta_2) < 0$. Then, following the geometric mean prescription, $\tilde{\Lambda}_{12} = \sqrt{\lambda(\delta_1)}\sqrt{\lambda(\delta_2)} = i|\tilde{\Lambda}_{12}| = \tilde{\Lambda}_{21}$, such that $\tilde{\Lambda}_{ij}$ is not Hermitian due to its off-diagonal elements. Hence, Δ becomes

$$\Delta = \hbar \begin{pmatrix} \tilde{\Lambda}_{33} + \tilde{\Lambda}_{44} & 0 & 0 \\ 0 & \tilde{\Lambda}_{11} & i|\tilde{\Lambda}_{12}| \\ 0 & i|\tilde{\Lambda}_{12}| & \tilde{\Lambda}_{22} \end{pmatrix}, \tag{3.23}$$

where the off-diagonal terms fail to be complex conjugates of each other, and thus Δ is not Hermitian.

An important point here is that, because γ_{rt} typically has resonances and λ_{rt} is essentially its conjugate via a Hilbert transform, λ_{rt} is generally expected to have sign changes around the resonances. If the system and environment are tuned so that their spectral features overlap, it follows that this situation should happen frequently, such that non-Hermitian Hamiltonians would not be uncommon. A significant remark at this point is that effective non-Hermitian Hamiltonians can be useful to perform certain kinds of analysis, as

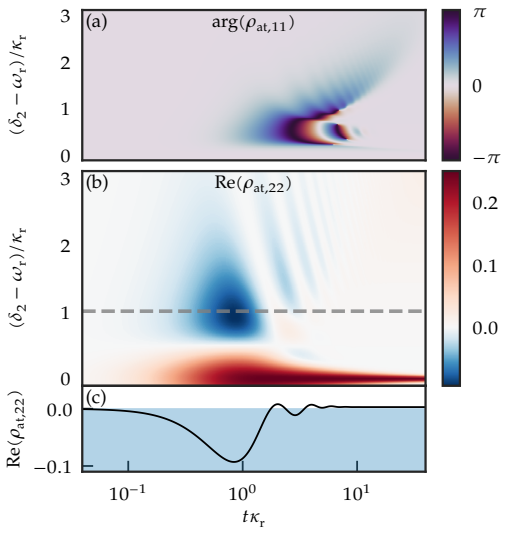

Figure 3.3: Breakdown of the $g\Lambda - g\Gamma$ prescription of [266] due to the non-Hermiticity of Δ. Adapted from [257].

(a) Non-trivial complex phase of $\rho_{at,11}$ owing to the loss of Hermiticity of eq. (3.23).

(b) Real part of $\rho_{at,22}$, as obtained with eq. (3.19). Blue and red regions represent positive and negative values, respectively.

(c) Horizontal cut of (b) at Population of $|2\rangle$ at $\delta_2 - \omega_r = \kappa_r$. As in the previous plots, the blue shaded region indicates negative populations.

1

done in chapter 4, with an evolution given by

$$\dot{\rho}_{at} = -\frac{i}{\hbar}\left(H_{eff}\rho_{at} - \rho_{at}H_{eff}^{\dagger}\right). \tag{3.24}$$

Indeed, it is an economical way to include dissipation, without worrying about the lower levels being filled. This is not the case for the non-Hermitian Hamiltonians discussed here because (i) the would-be decay rates can be negative, while dissipation requires positive rates, and (ii) the effective equation of motion is a pure commutator, not the modified commutator that takes the Hermitian conjugate of H_{eff} when it acts from the right in eq. (3.24). Instead, the effect of these non-Hermitian Hamiltonians is showcased in fig. 3.3. To obtain it, we have simulated the same 3LA setting $\hbar\omega_r = 1$ eV, $\hbar\kappa_r = 0.1$ eV and $\hbar g_r = 0.1$ eV. The transition frequencies have been chosen to be symmetrically located around ω_r, such that $\delta_1 + \delta_2 = 2\omega_r$, and then swept over. Last, the initial state is taken to be $|\psi(0)\rangle = |1\rangle$. The top panel shows the complex phase of $\rho_{at,11}$. Since it is a population, it must be a real number (a positive one, in fact); however, we see that it undergoes complete oscillations in the complex plane. Hence, these non-Hermitian Hamiltonians do not preserve the Hermiticity of ρ_{at} itself. In fig. 3.3b, we plot Re $(\rho_{at,22})$, and see large negative regions, further evidenced by the cut at $\delta_2 - \omega_r = \kappa_r$ in fig. 3.3c. Incidentally, Im $\rho_{at,22}$ is also different from zero, but it is much smaller than the real part.

With fig. 3.3, we have showed that the cure can be worse than the disease in some ways: at least the BRE preserves the Hermiticity of ρ_{at}. Nevertheless, this deficiency of the $g\Lambda - g\Gamma$ does not automatically imply that eq. (3.19) with

a non-Hermitian Δ is never going to accurately describe the system's dynamics. Just like the BRE, this LME can be precise if the underlying approximations are valid. Still, it would be desirable to find a way to restore the Hermiticity of Δ and ρ_{at} in all cases.

3.4.2 Restoring Hermiticity

After describing the non-Hermiticity problem, we propose two possible solutions in the following. We illustrate them using again the V-type atom and environment of fig. 3.1, as only the non-Hermiticity issue can occur in this setup.

Solution 1: frequency clustering As has been proposed in other studies mentioned in section 3.3, the first possible approach is to group all states that are sufficiently close to each other (quasidegenerate). Then, we may treat each cluster as though its states were degenerate in deriving the master equation. For that reason, we will refer to this method as $d\Lambda - d\Gamma$. With this approach, the correlation functions are evaluated at the average frequency of each cluster, and the cross-cluster interactions can be safely discarded. In practice, this solution amounts to replacing

$$\Lambda_{ij}(\delta_i) \text{ and } \Lambda_{ij}(\delta_j) \to \tilde{\Lambda}_{ij} = \Lambda_{ij}\left(\frac{\delta_i + \delta_j}{2}\right) \quad \text{and} \tag{3.25a}$$

$$\Gamma_{ij}(\delta_i) \text{ and } \Gamma_{ij}(\delta_j) \to \tilde{\Gamma}_{ij} = \Gamma_{ij}\left(\frac{\delta_i + \delta_j}{2}\right), \tag{3.25b}$$

within the quasidegenerate clusters. In particular, for our 3LA here, this solution takes $|1\rangle$ and $|2\rangle$ to be degenerate as far as the correlation functions are concerned. Thus, the energy shift is

$$\Delta^d = \hbar \begin{pmatrix} 2\lambda\left(-\frac{\delta_1+\delta_2}{2}\right) & 0 & 0 \\ 0 & \lambda\left(\frac{\delta_1+\delta_2}{2}\right) & \lambda\left(\frac{\delta_1+\delta_2}{2}\right) \\ 0 & \lambda\left(\frac{\delta_1+\delta_2}{2}\right) & \lambda\left(\frac{\delta_1+\delta_2}{2}\right) \end{pmatrix}, \tag{3.26}$$

which is obviously Hermitian. Also, since the correlation functions are evaluated as though $|1\rangle$ and $|2\rangle$ were degenerate, the Kossakowski matrix is positive semidefinite, just like in the secularized LME for degenerate levels. This replacement is expected to work well when $\delta_1 \approx \delta_2$, that is, when $|1\rangle$ and $|2\rangle$ are indeed quasidegenerate. However, it can fail when δ_1 and δ_2 are very different, since $|1\rangle$ and $|2\rangle$ should in reality decay independently with rates given

by $\gamma(\delta_1)$ and $\gamma(\delta_2)$, which are in general different from each other and from $\gamma\left(\frac{\delta_1+\delta_2}{2}\right)$. Also, one can foresee that this solution will be harder to implement than $g\Lambda - g\Gamma$ when the system's size grows and its energy spectrum becomes more intricate, as separating clusters of energy levels can be a less clear-cut task.

Solution 2: arithmetic mean By observing that the problem arises from taking the square root of negative numbers, we propose in the second approach to replace the geometric mean with the arithmetic one for Λ_{ij}. At the same time, we leave Γ_{ij} untouched, as it has no relation to the issue we are trying to fix right now. Put more concisely, we now have

$$\Lambda_{ij}(\delta_i) \text{ and } \Lambda_{ij}(\delta_j) \to \tilde{\Lambda}_{ij} = \frac{\Lambda_{ij}(\delta_i) + \Lambda_{ij}(\delta_j)}{2} \tag{3.27a}$$

while still keeping

$$\Gamma_{ij}(\delta_i) \text{ and } \Gamma_{ij}(\delta_j) \to \tilde{\Gamma}_{ij} = \sqrt{\Gamma_{ij}(\delta_i)}\sqrt{\Gamma_{ij}(\delta_j)}. \tag{3.27b}$$

With these replacements, our 3LA Hamiltonian becomes shifted by

$$\Delta^a = \hbar \begin{pmatrix} \lambda(-\delta_1) + \lambda(-\delta_2) & 0 & 0 \\ 0 & \lambda(\delta_1) & \frac{\lambda(\delta_1)+\lambda(\delta_2)}{2} \\ 0 & \frac{\lambda(\delta_1)+\lambda(\delta_2)}{2} & \lambda(\delta_2) \end{pmatrix}, \tag{3.28}$$

which is, by construction, Hermitian. Note that, while the arithmetic mean works well for the energy shifts Λ, meaning that Δ becomes Hermitian, it would not help in restoring the positivity of the master equation. Indeed, the arithmetic mean replacement in the dissipative rates Γ would not yield a positive semidefinite Kossakowski matrix $\mathbf{K}^a$, because

$$\mathbf{K}^a = \begin{pmatrix} \gamma(\delta_1) & \frac{\gamma(\delta_1)+\gamma(\delta_2)}{2} & \frac{\gamma(\delta_1)+\gamma(\delta_3)}{2} & \frac{\gamma(\delta_1)+\gamma(\delta_4)}{2} \\ \frac{\gamma(\delta_2)+\gamma(\delta_1)}{2} & \gamma(\delta_2) & \frac{\gamma(\delta_2)+\gamma(\delta_3)}{2} & \frac{\gamma(\delta_2)+\gamma(\delta_4)}{2} \\ \frac{\gamma(\delta_3)+\gamma(\delta_1)}{2} & \frac{\gamma(\delta_3)+\gamma(\delta_2)}{2} & \gamma(\delta_3) & \frac{\gamma(\delta_3)+\gamma(\delta_4)}{2} \\ \frac{\gamma(\delta_4)+\gamma(\delta_1)}{2} & \frac{\gamma(\delta_4)+\gamma(\delta_2)}{2} & \frac{\gamma(\delta_4)+\gamma(\delta_3)}{2} & \gamma(\delta_4) \end{pmatrix}, \tag{3.29}$$

belongs to a family of matrices that can be shown to always have a negative eigenvalue equal to

$$\Gamma_- = \frac{1}{2}\sum_i \gamma(\delta_i) - \frac{1}{2}\sqrt{n\sum_i \gamma^2(\delta_i)} < 0. \tag{3.30}$$

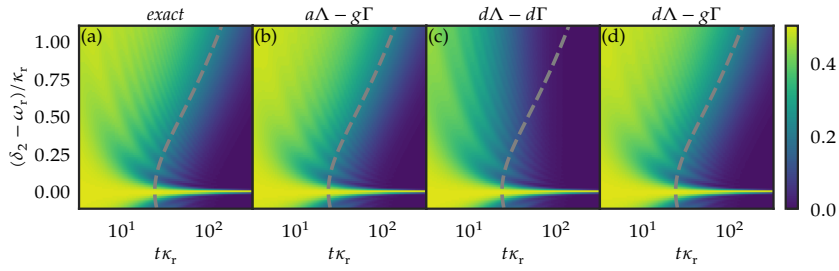

Figure 3.4: Temporal evolution of $\rho_{at,22}$ according to (a) the exact solution, and the (b) $a\Lambda - g\Gamma$ and (c) $d\Lambda - d\Gamma$ methods. The dashed line follows $1/J(\delta_2)$, which corresponds to the local dissipation timescale of $|2\rangle$. (d) "Manual" correction of $d\Lambda - d\Gamma$ to include the information about the detuning between δ_1 and δ_2 in the dissipative part by reverting to the geometric mean of [266]. Adapted from [257].

See appendix A.5 for an elementary proof of this fact. Hence, we call this method $a\Lambda - g\Gamma$, reflecting which mathematical mean is used in each term. Unlike the previous one, this solution does retain the information about the fine details of H_{at}'s energy spectrum.

Comparison These approaches eliminate the issue of the non-Hermitian Hamiltonian corrections by avoiding taking the square root of negative numbers. We benchmark here the performance of each solution by numerically solving the LME in eq. (3.19) using eqs. (3.25) and (3.27) for the 3LA and environment of fig. 3.1, and compare with the *exact* result given by

$$\dot{\rho}_s = -\frac{i}{\hbar}\left[H_{at} + \hbar\omega_r a^\dagger a + d\hbar g_r\left(a^\dagger + a\right), \rho_s\right] + \kappa_r \mathcal{D}_{a,a}[\rho_s] \tag{3.31a}$$

and

$$d = \sum_{i=1}^{4} \sigma_i = \sum_{i=1}^{2}\left(\sigma_i + \sigma_i^\dagger\right). \tag{3.31b}$$

To obtain the *exact* atomic density matrix, we take the partial trace with respect to the single bosonic mode a: $\rho_{at} = \mathrm{Tr}_a \rho_s$. For concreteness, we choose the following parameters: $\hbar\omega_r = 1$ eV, $\hbar\kappa_r = 0.1$ eV, $g_r = 0.05\kappa_r$, and again the symmetric configuration where $\delta_1 + \delta_2 = 2\omega_r$. The initial state is now set to $|\psi(0)\rangle = (|1\rangle - |2\rangle)/\sqrt{2}$, for the approximate methods being discussed, and $|\psi(0)\rangle \otimes |0\rangle$ for the exact approach. In figs. 3.4a to 3.4c, we show the dynamics of $\rho_{at,22}$ as calculated with the *exact*, $a\Lambda - g\Gamma$ and $d\Lambda - d\Gamma$ methods. We notice a prominent feature in all plots at $\delta_2 = \omega_r$, where the population does not decay. This happens because $|1\rangle$ and $|2\rangle$ are degenerate, and $|\psi(0)\rangle$ is precisely the superposition of $|1\rangle$ and $|2\rangle$ that is decoupled from the envi-

ronment. In the *exact* and $a\Lambda - g\Gamma$ approaches, when the detuning between $|1\rangle$ and $|2\rangle$ increases, $\rho_{\mathrm{at},22}$ decays on a timescale approximately equal to $1/J(\delta_2)$, marked by the dashed line. This is in stark contrast to $d\Lambda - d\Gamma$, where the dissipation timescale quickly converges to $1/J(\omega_\mathrm{r})$. Of course, this disparity can be traced back to the frequency clustering in $\tilde{\Gamma}_{ij}$. Accordingly, we can retrieve an accurate description of the dissipation by retaining the geometric mean replacement for $\tilde{\Gamma}_{ij}$, and clustering frequencies for $\tilde{\Lambda}_{ij}$ only. In our naming convention, we would call this method $d\Lambda - g\Gamma$. In fig. 3.4d, we see that the dissipative behavior of $d\Lambda - g\Gamma$ indeed converges to the *exact* and $a\Lambda - g\Gamma$ cases.

From fig. 3.4, we conclude that both $a\Lambda - g\Gamma$ and $d\Lambda - g\Gamma$ work well to describe the dissipation, with only minimal performance differences. Still, there are two deciding factors that incline us to select $a\Lambda - g\Gamma$ over $d\Lambda - g\Gamma$

1. The energy shift part in $d\Lambda - g\Gamma$ assumes no natural detuning between the excited states, while in reality there is a non-zero difference. It is, therefore, natural to envision some specific setups where the accuracy of $d\Lambda - g\Gamma$ might be compromised compared to $a\Lambda - g\Gamma$, which includes the finer details of the atom's energy spectrum without further considerations. Hence, in the wide landscape of possible systems susceptible to a description like the one discussed here, it is to be expected that $a\Lambda - g\Gamma$ should outperform $d\Lambda - g\Gamma$, even if only slightly.
2. From the point of view of the practical implementation, the need for a classification of the transition frequencies in particular clusters is an additional step of $d\Lambda - g\Gamma$, not required by $a\Lambda - g\Gamma$. Additionally, for large systems without a clear "gross" structure, this step can become quite unclear. In this regard, $a\Lambda - g\Gamma$ avoids dealing with such contemplations, as it accepts the transition frequencies for what they are, not trying to mold them into something they are not.

With that in mind, we conclude that the $a\Lambda - g\Gamma$ approach provides the best solution. It (i) successfully reproduces the exact solution for weakly coupled Markovian environments, (ii) straightforwardly addresses the non-Hermiticity issue associated with the geometric mean prescription, and (iii) seamlessly incorporates the finer energetic features of the system without additional supervision. This makes the $a\Lambda - g\Gamma$ method robust and effective at describing the energy shift of complex quantum systems.

3.4.3 Non-positive semidefinite Kossakowski matrix

We next turn our focus to the other problem that can arise from the geometric mean prescription: the Kossakowski matrix can come out non-positive semidefinite. A notable situation is that of a single system-environment interaction term, the case treated in [266]. There, the authors show that the final Kossakowski matrix is positive semidefinite by construction. In the more general case of $H_{\text{int}} = \sum_r S_r B_r$, we can consider two scenarios. If there are no cross-correlations, one can simply treat the baths independently and repeat the procedure of [266] for the dissipative part due to each environment operator. We considered such an example in [267], which is presented in more detail in chapter 4. The opposite scenario, which is certain to occur in EM environments lacking a high enough degree of symmetry, requires some more work. We anticipate already that this section has less analytical insight, instead making heavier use of numerical simulations to both present and substantiate the claims. Therefore, let us first clarify the key methodological tools to be employed.

Methodology In this part, we are going to randomly generate an atom and environment pair, and then calculate the associated Kossakowski matrix for several approximate master equations. For later reference, we explain the procedure to generate random systems and environments in some generality, as it will be useful in section 3.4.4 too. We work with a generic L-level atom coupled to its environment through M interaction terms $H_{\text{int}} = \sum_{r=1}^{M} d_r B_r$. The environment is, thus, characterized by an $M \times M$ spectral density. To make sure that the environment is physically plausible, we profit from the few-mode quantization technique developed in [201], and described at the end of section 2.4.4. Accordingly, we take N lossy coupled bosonic modes a_α with frequencies and couplings $\omega_{\alpha\beta}$ and loss rates κ_α. The few-mode spectral density is

$$\mathbf{J}_{\text{m}}(\omega) = \frac{1}{\pi}\mathbf{g} \cdot \text{Im}\left[(\mathbf{h} - \omega \mathbf{I}_N)^{-1}\right] \cdot \mathbf{g}^{\text{t}}, \tag{3.32}$$

where $\mathbf{g}$ is an $M \times N$ matrix and $\mathbf{h}$ is an $N \times N$ matrix that contains the model's parameters through $h_{\alpha\beta} = \omega_{\alpha\beta} - i\delta_{\alpha\beta}\kappa_\alpha/2$. A convenient feature of $\mathbf{J}_{\text{m}}$ as the spectral density is that $\boldsymbol{\lambda}_{\text{m}}$ can also be written down analytically as

$$\boldsymbol{\lambda}_{\text{m}}(\omega) = -\mathbf{g} \cdot \text{Re}\left[(\mathbf{h} - \omega \mathbf{I}_N)^{-1}\right] \cdot \mathbf{g}^{\text{t}}, \tag{3.33}$$

and that provides us with all the information that we need regarding the environment. The conceptual shift with respect to [167, 201, 255, 256] is that

instead of choosing the parameters to fit some existing spectral density, we choose here both the environment and system parameters randomly, sampled using the `Python` library `NumPy` (version 1.26.2). The initial state is initialized through random phases and amplitudes for each coefficient $c_a(0)$ in $|\psi(0)\rangle = \sum_{a=1}^{L} c_a(0)|a\rangle$. Next, we ensure that the system's and environments energy scales overlap by confining $\hbar\omega_a$ to $[0.1\text{ eV}, 5.0\text{ eV}]$ and the discrete mode energies $\hbar\omega_{\alpha\alpha}$ to $[0.3\text{ eV}, 2.0\text{ eV}]$, while the mode couplings $\hbar\omega_{\alpha\beta}$ form a symmetric matrix whose elements belong to $[0.0\text{ eV}, 1.0\text{ eV}]$, and the decay rates $\hbar\kappa_\alpha$ to $[0.2\text{ eV}, 0.5\text{ eV}]$. The atom's transition operators are constructed as Hermitian matrices with vanishing diagonal elements and values in $[0, 1]$ off the diagonal. The dimensions of these operators have been absorbed in the atom's environment coupling strengths, $\hbar g_\alpha$, which have been sampled uniformly within $[0.0\text{ meV}, 1.5\text{ meV}]$. These parametrization ranges ensured a diverse set of systems for our analysis.

Once we have the system-environment pairs, we simulate them through several dynamical equations in order to test and compare them. In particular, we implement the following methods: *BRE* and $a\Lambda - g\Gamma$, which simply correspond to the BRE and the master equation that we ended up with at the end of the last part. Neither one of these master equations is generally a LME at this point, because of the possible negative eigenvalues of their Kossakowski matrices. For that reason, we also modify them by directly removing these negative eigenvalues. These new methods are labeled as $BRE(+)$ and $a\Lambda - g\Gamma(+)$, reflecting their forced positivity. In a way, discarding the negative eigenvalues amounts to replacing the method's corresponding Kossakowski matrix $\mathbf{K}_\text{m}$ with its unique *positive approximant* $\mathbf{K}_\text{m}^{(+)}$ with respect to the Frobenius norm, i.e., the positive semidefinite matrix such that $\left\|\mathbf{K}_\text{m} - \mathbf{K}_\text{m}^{(+)}\right\|_F$ is minimized, as shown in [268]. Concretely, the Hermiticity of $\mathbf{K}_\text{m}$ allows us to concisely write

$$\mathbf{K}_\text{m}^{(+)} = \frac{\mathbf{K}_\text{m} + \sqrt{\mathbf{K}_\text{m}^2}}{2}. \tag{3.34}$$

As a consequence of this replacement, $BRE(+)$ and $a\Lambda - g\Gamma(+)$ are, indeed, genuine LMEs. Whether they are accurate is another matter that we will find out soon.

Finally, in order to check the validity of each method, we compare them with the exact solution of the system's dynamics, which is directly given by the few-mode quantization technique used to generate the system-environment pairs. Indeed, if our environment is described through $\mathbf{J}_\text{m}$ and $\boldsymbol{\lambda}_\text{m}$, the *exact*

solution is directly available as the solution of

$$\dot{\rho}_{\mathrm{s}} = -\frac{i}{\hbar}\left[H_{\mathrm{at}} + \sum_{\alpha\beta}\hbar\omega_{\alpha\beta}a_{\alpha}^{\dagger}a_{\beta} + \sum_{r} d_{r}\sum_{\alpha}\hbar g_{r\alpha}\left(a_{\alpha}^{\dagger} + a_{\alpha}\right), \rho_{\mathrm{s}}\right] + \sum_{\alpha}\kappa_{\alpha}\mathcal{D}_{a_{\alpha},a_{\alpha}}[\rho_{\mathrm{s}}], \tag{3.35}$$

where the *exact* atomic density matrix is $\rho_{\mathrm{at}} = \mathrm{Tr}_{\{a_\alpha\}}\rho_{\mathrm{s}}$. We will use the exact result to test and compare the following methods: *BRE*, *BRE*$(+)$, $a\Lambda - g\Gamma$ and $a\Lambda - g\Gamma(+)$.

Particular example With these tools, we generate an $L = 3$-level atom coupled to an environment through $M = 2$ operators, and with $N = 2$ modes characterizing the spectral density, with randomly generated parameters. We take $|\psi(0)\rangle = \left(|1\rangle + \sqrt{2}|2\rangle\right)/\sqrt{3}$. We display the system and correlation functions in figs. 3.5a and 3.5b, respectively. Then, we may compute the Kossakowski matrix of each master equation. For the BRE, we read the Kossakowski matrix from eq. (2.170), while for $a\Lambda - g\Gamma$ it is simply $\tilde{\Gamma}_{ij}$. For the current 3LA, these matrices are 9×9 and, accordingly, have 9 eigenvalues. We present the most significant ones in ascending order (first two and last two) in table 3.1. Let us focus on the BRE row first, where the largest negative eigenvalues are comparable to their positive counterparts. For that reason, it is to be expected that the negative eigenvalues of the BRE will play an important role. Nevertheless, if we now turn our attention to the $a\Lambda - g\Gamma$ row, we see that the negative eigenvalues are about 100 times smaller than the positive ones. This seems to imply that the geometric mean procedure greatly softens the impact of the negative eigenvalues. To check this statement, we solve the dynamics of the

Table 3.1: Negative (blue) and positive (red) eigenvalues of the corresponding Kossakowski matrices. We show only the 4 largest in absolute value, out of the 9 total eigenvalues for $L = 3$, rounded to the first significant digit.

Method	**Eigenvalues** (meV/$\hbar$)				
	1st	2nd	...	8th	9th
BRE	-5	$-9 \cdot 10^{-2}$		$2 \cdot 10^{-1}$	9
$a\Lambda - g\Gamma$	$-3 \cdot 10^{-2}$	$-1 \cdot 10^{-5}$		$1 \cdot 10^{-2}$	4

system with the *exact*, *BRE*, *BRE*$(+)$, $a\Lambda - g\Gamma$ and $a\Lambda - g\Gamma(+)$ methods and plot the results in fig. 3.5c. As can be seen, only the *BRE*$(+)$ master equation fails to reproduce the *exact* dynamics, while the rest come very close to the exact populations. This fact is further evidenced by fig. 3.5c, where the "error" of

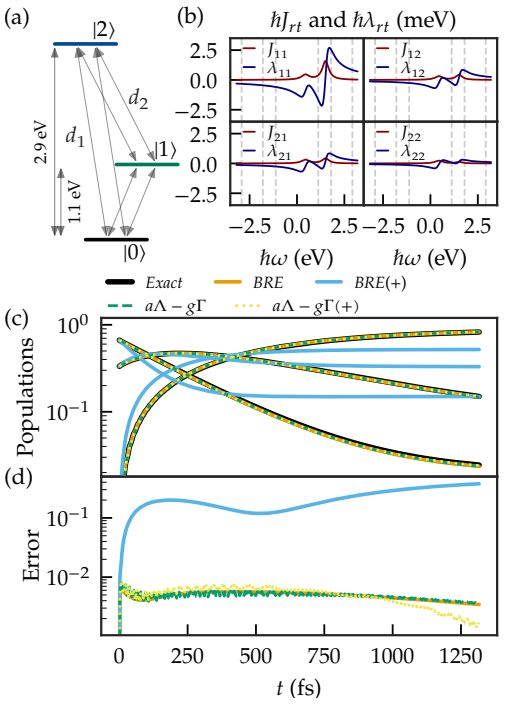

Figure 3.5: Particular instance of a random system-environment pair. Adapted from [257].

(a) Level structure and allowed transitions due to the transition operators d_r.

(b) 2×2 matrices of the spectral functions of the environment, $\mathbf{J}$ and $\boldsymbol{\lambda}$, with cross-correlations in the off-diagonal panels. The vertical lines represent the atom's allowed transitions.

(c) Populations obtained with the *exact*, *BRE*, *BRE*(+), $a\Lambda - g\Gamma$ and $a\Lambda - g\Gamma(+)$ methods.

(d) Deviation with respect to the exact solution of the approximate *BRE*, *BRE*(+), $a\Lambda - g\Gamma$ and $a\Lambda - g\Gamma(+)$ master equations.

1

each approximate master equation is measured with the Frobenius norm for matrices:

$$\left\|\rho_{\text{at}}^{(\text{method})}(t) - \rho_{\text{at}}^{(exact)}(t)\right\|_F = \sqrt{\sum_{ab}\left|\rho_{\text{at},ab}^{(\text{method})}(t) - \rho_{\text{at},ab}^{(exact)}(t)\right|^2}. \tag{3.36}$$

In agreement with the observation based on the eigenvalues alone, *BRE*(+) is the only one to significantly deviate from the exact evolution, which is followed by all other methods with great accuracy. Remarkably, this confirms that the negative eigenvalues of the Kossakowski matrix associated to $a\Lambda - g\Gamma$ are essentially irrelevant, so that discarding them yields a genuine LME which, in addition, is accurate. So far, everything points at $a\Lambda - g\Gamma(+)$ as a solution to the non-Hermiticity and non-positive semidefiniteness problems. However, unlike the non-Hermiticity problem, we have thus far found a practical solution that we know to work only in the particular example analyzed in this section. It remains to be seen how well this procedure works in the general case, that is, by how much the negative eigenvalues from *BRE* are reduced after the geometric mean replacement. If the geometric mean systematically decreases the negative eigenvalues by a few orders of magnitude, then we will have reached our goal, and showing so is the purpose of the next section.

3.4.4 Restoring positive semidefiniteness

The methodology described above lends itself very naturally to a statistical study. We begin by generating a large sample of system-environment pairs with random parameters. Next, in each system, we obtain and diagonalize the Kossakowski matrix with the BRE and the $a\Lambda - g\Gamma$ master equation, and study whether the negative eigenvalues become smaller, as seen in the particular example from section 3.4.3. To that end, we have generated a sample of 1000 random systems and environments with the same parameter ranges as before, and the eigenvalues of their respective Kossakowski matrices are represented in figs. 3.6a and 3.6b, for the *BRE* and $a\Lambda - g\Gamma$ methods. There, blue bars correspond to negative eigenvalues, while the positive ones are colored with red. Since we can order the eigenvalues in each system, fig. 3.6 actually contains many histograms: one for the first eigenvalue, another for the second, and so on. These partial histograms are differentiated from each other through their color shade, with darker tones indicating larger absolute values. Notice that the horizontal axes features a negative and positive logarithmic scale, broken at $\pm 10^{-12.5}$.

There are several differences between figs. 3.6a and 3.6b. For instance, the *BRE* histogram is more ordered, with many eigenvalues that are essentially zero (out of the range), and two positive and negative peaks that approximately mirror each other. After the geometric mean procedure, however, the eigenvalues become more scattered throughout the whole logarithmic range. Nevertheless, there is a particularly important difference: while the first peak of the *BRE* method clusters around -1, in agreement with the first row of table 3.1, the same peak in $a\Lambda - g\Lambda$ master equation has shifted about 3 orders of magnitude closer to zero on average. Clearly, the geometric mean replacement has significantly reduced the negative eigenvalues across the whole random sample of 1000 system-environment pairs.

To end this section, we explore the breakdown of the master equations due to the onset of the strong coupling regime. With that goal, we simply introduce a dimensionless numerical coupling strength factor to scale up the system-environment interaction for each random instance, covering a wide range of orders of magnitude. For each system, we calculate its dynamics with every method and compare with the exact solution, with a random initial state. We measure the deviation by taking the temporal average of the Frobenius norm of the difference between the density matrices:

$$\Delta^{(\text{method})} = \frac{1}{T}\int_0^T \mathrm{d}t \left\| \rho_{\text{at}}^{(exact)}(t) - \rho_{\text{at}}^{(\text{method})}(t) \right\|_F. \tag{3.37}$$

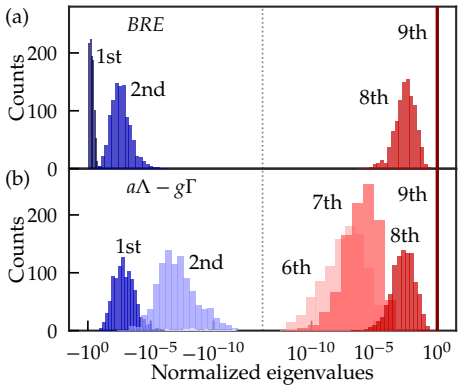

Figure 3.6: Histogram with the negative and positive eigenvalues, in logarithmic scales and normalized to the largest positive one. Adapted from [257].

(a) Eigenvalues of the Kossakowski matrices obtained from the BRE as read from eq. (2.170).

(b) Eigenvalues of the Kossakowski matrices corresponding to the geometric prescription of [266].

1

Then, we can average this quantity across the 1000 systems at each value of the coupling strength factor to gauge their robustness and breaking point. In practice, however, it makes more sense to study the statistical properties of $\log \Delta^{(\text{method})}$, to account for the skewness of $\Delta^{(\text{method})}$, which is due to the deviation being either small or large, but always positive.

The results are condensed in fig. 3.7, where we plot $\exp(\langle \log \Delta^{(\text{method})} \rangle)$ to present the results in the more intuitive form of Δ and not $\log \Delta$. Several things stand out in the figure. First, any approximate method fails to reproduce the exact dynamics when the strength factor becomes sufficiently large, as expected. In the weak coupling limit, however, we see with the continuous lines that the "full" methods, including both positive and negative eigenvalues, converge to the exact solution. Meanwhile, from the positive versions of the methods, the deviation of $BRE(+)$ stabilizes above the dotted line and never converges. This behavior is consistent with the results shown in fig. 3.6, as the large negative eigenvalues of the BRE's Kossakowski matrix are expected to be of great impact on the dynamics. As for $a\Lambda - g\Gamma(+)$, it manages to follow the trend of convergence, which again is to be expected since fig. 3.6 showed a marked reduction in the size of the negative eigenvalues of the Kossakowski matrix. Accordingly, figs. 3.6 and 3.7 support that our proposed master equation, $a\Lambda - g\Gamma(+)$, fixes both the non-Hermiticity and non-positive semidefiniteness problems of the one developed in [266].

Note that this is equivalent to a geometric average of $\Delta^{(\text{method})}$ over random systems, but we refrain from using that nomenclature here for clarity, as the geometric mean is already a main character of the chapter.

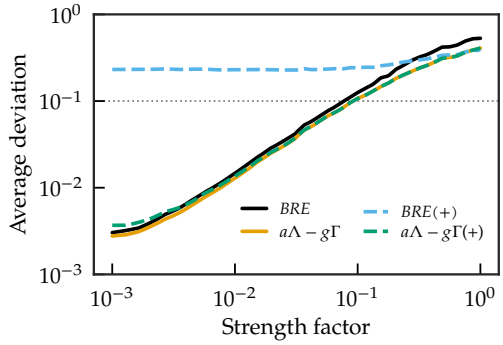

Figure 3.7: Statistical average over random systems of the time-averaged deviation of the dynamics (eq. (3.37)), as a function of the coupling strength factor. The horizontal dotted line indicates the point beyond which any method undoubtedly breaks down. Adapted from [257].

1

3.5 Final Lindblad master equation and conclusions

In the preceding sections, we have discussed the need to go beyond the secular approximation when attempting to turn the BRE into a LME, with some methods already available [259, 261–265]. In this spirit, we have slightly generalized the geometric approach developed in [266]. Then, we have realized that it has two potential flaws, the non-Hermiticity of the energy shift and the presence of negative eigenvalues in the Kossakowski matrix. Either of these precludes the $g\Lambda - g\Gamma$ master equation from being a genuine LME already in scenarios of moderate complexity. We next show in the chapter how both difficulties can be solved with minimal modifications. To restore the Hermiticity of the energy shift, we merely replace the geometric mean with the arithmetic mean in the energy shift terms, such that

$$\tilde{\Lambda}_{ij} = \frac{\Lambda_{ij}(\delta_i) + \Lambda_{ij}(\delta_j)}{2}. \tag{3.38}$$

As for the negative eigenvalues of the Kossakowski matrix, we simply discard the negative eigenvalues, which are much smaller than in the BRE after the geometric mean procedure. In a way, as we have discussed before, we are replacing the Kossakowski matrix of the $a\Lambda - g\Gamma$ master equation $\mathbf{K}$ with

$$\mathbf{K}^{(+)} = \frac{\mathbf{K} + \sqrt{\mathbf{K}}^2}{2}. \tag{3.39}$$

These two modifications to the equation of [266] ensure that the final equation, $a\Lambda - g\Gamma(+)$, is a true LME, under any circumstance, for arbitrary systems and environments.

Regarding the properties of the $a\Lambda - g\Gamma(+)$ equation, it is designed to accu-

rately describe the dynamics as long as the BRE also delivers physically sensible results. Note that the approach $BRE(+)$, while also a genuine LME, generally fails to reproduce the correct dynamics, which highlights the significance of the intermediate geometric mean step. With the status of LME, $a\Lambda - g\Gamma(+)$ enjoys a number of advantages over the BRE. First, it is, by design, free from negative populations. Second, because the $a\Lambda - g\Gamma(+)$ master equation is a true LME, it generates a completely positive map, which means that its lifted dynamics is positive for any additional subsystem too. Last, the $a\Lambda - g\Gamma(+)$ LME admits a quantum trajectory interpretation of the dynamics with non-negative jump probabilities, which has additional computational benefits.

Chapter Four | Vacuum-field-induced state mixing

I'm not confused. I'm just well mixed.

Robert Frost

Chapter summary In this chapter, we build upon the ideas presented in the context of chapter 3 to accurately describe the dynamics of the hydrogen atom in the vicinity of an AlN dielectric nanoparticle. For the reader's convenience, we start in section 4.1 with a brief reminder about some concepts regarding atoms and macroscopic QED introduced in chapter 2. In particular, we will focus on the temporal evolution and eigenstate mixing effects that arise within a single fine-structure, quasidegenerate multiplet. To do so, off-diagonal couplings between quasidegenerate states must be taken into account, such that the standard secular approximation is not adequate. Therefore, we write in section 4.2 an appropriate LME following the discussion in chapter 3, and extract an effective, non-Hermitian Hamiltonian. Through it, not only are the relevant aspects of the dynamics fully captured, but the analysis itself also becomes significantly simpler in section 4.3. Our results show that, owing to the nanoparticle's presence, the hydrogenic eigenstates become mixtures of the original fine-structure eigenstates, and the precise mixtures depend on the atom-nanoparticle separation. This mixing arises from the off-diagonal terms that are completely missed by a secularized LME, and has marked consequences in the atomic dynamics. For instance, we observe that, under certain circumstances, quantum interferences due to the off-diagonal couplings can revert the expected Purcell enhancement of the spontaneous emission rates. The results presented here have been published in [267].

4.1 Reminder about atoms and nanoparticles in MQED

Throughout chapter 2, we have emphasized that atoms see their properties modified due to the EM environment that surrounds them. In particular, this part of the thesis deals with phenomena in the weak light-matter coupling regime. If the EM field is in its vacuum state, only two effects are expected to take place: an energy shift of the atomic energy levels and a finite decay rate. When atoms are placed close to a much larger nanostructure, the MQED vacuum field modifies both effects, as described at the end of section 2.4.3. The present chapter is concerned with such scenarios. Thus, we must use the results of the end of section 2.4.3 to obtain an appropriate master equation. There, we saw that the multipolar coupling interaction Hamiltonian in the long-wavelength approximation,

$$H_{\text{int}} = -\frac{\mathbf{d}\cdot\mathbf{D}_{(\text{at})}(\mathbf{r}_{\text{at}})}{\varepsilon_0}, \tag{4.1}$$

yields the following expressions for the parameters of the BRE:

$$\gamma(\delta) = 2\pi\mathbf{J}(\delta) = 2\pi\frac{\omega^2}{\pi\hbar\varepsilon_0 c^2}\text{Im}\,\mathbf{G}(\mathbf{r}_{\text{at}},\mathbf{r}_{\text{at}},\omega), \tag{4.2a}$$

$$\boldsymbol{\lambda}(\delta) = \frac{1}{\pi\hbar\varepsilon_0 c^2}P\int_0^\infty \mathrm{d}\omega\,\frac{\omega^2\text{Im}\,\mathbf{G}^{\text{s}}(\mathbf{r}_{\text{at}},\mathbf{r}_{\text{at}},\omega)}{\delta-\omega}, \tag{4.2b}$$

$$\Gamma_{ij}(\delta) = \mathbf{d}_i^*\cdot\gamma(\delta)\cdot\mathbf{d}_j = 2\pi\mathbf{d}_i^*\cdot\mathbf{J}(\delta)\cdot\mathbf{d}_j \quad \text{and} \tag{4.2c}$$

$$\Lambda_{ij}(\delta) = \mathbf{d}_i^*\cdot\boldsymbol{\lambda}(\delta)\cdot\mathbf{d}_j. \tag{4.2d}$$

Here, $\mathbf{G}$ is the EM Green tensor; note that the $\boldsymbol{\lambda}$ and Λ_{ij} only include its scattering contribution $\mathbf{G}^{\text{s}}$, as the free-space energy shifts formally diverge but become negligible compared with the effects treated here after an appropriate renormalization procedure. In the physical scenario considered here, such position-dependent energy shifts are commonly referred to as CP shifts. In the spirit of chapter 3, these are the functions that must be geometrically or arithmetically averaged in order to retrieve a LME from the BRE for atoms in medium-assisted EM fields. For simplicity and concreteness, we consider a hydrogen atom placed next to a dielectric nanoparticle, sketched in fig. 4.1, whose details are explained next.

Hydrogen atom As elaborated upon in section 2.3, the energy spectrum of the hydrogen atom has a distinctive "gross" structure characterized by the

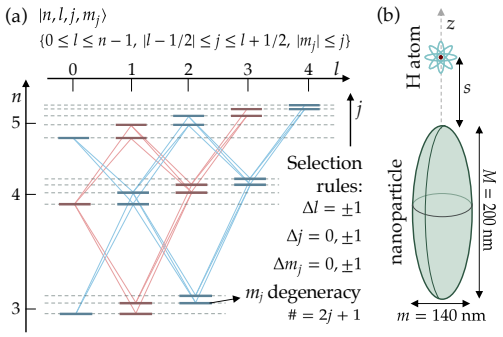

Figure 4.1: (a) Sketch of the fine-structure corrections to the Bohr energies (not to scale). The diagonal lines indicate the dipole-allowed transitions.

(b) Depiction of the system under study: hydrogen atom located on the symmetry axis of a spheroidal nanoparticle.

Adapted from [267].

Bohr energy levels $O(\alpha^2 m_e c^2)$, each of which comprises a manifold of states. There are a number of smaller corrections of various physical origins that shift each state in the manifolds differently, breaking the Bohr level's degeneracy. In the absence of external electric or magnetic fields, the most important effects are the relativistic contributions included in the Dirac equation, described in section 2.3.3, which give rise to the fine structure of the energy spectrum, $O(\alpha^4 m_e c^2)$. To a very good approximation, the eigenstates are characterized by the following quantum numbers:

- n: principal quantum number (labels Bohr levels).
- l: orbital angular momentum, $0 \le l \le n-1$.
- s: electron spin, $s = \frac{1}{2}$. We will generally omit it as it can only take this value.
- j: total angular momentum, $\frac{1}{2} \le j = l \pm \frac{1}{2}$.
- m_j: vertical axis projection of the total angular momentum, $-j \le m_j \le j$.

More concretely, the relation between the coupled and uncoupled angular momentum bases is

$$\begin{aligned} \left|j = l - 1/2, m_j\right\rangle &= c_- \left|m_l = m_j + 1/2, m_s = -1/2\right\rangle \\ &\quad + c_+ \left|m_l = m_j - 1/2, m_s = 1/2\right\rangle \qquad (4.3a) \\ \left|j = l + 1/2, m_j\right\rangle &= c_+ \left|m_l = m_j + 1/2, m_s = -1/2\right\rangle \\ &\quad - c_- \left|m_l = m_j - 1/2, m_s = 1/2\right\rangle. \qquad (4.3b) \end{aligned}$$

Here, $c_\pm$ are Clebsch-Gordan coefficients that can be read from eq. (2.134b). These combinations imply that dipole selection rules in the coupled basis are

$$l - l' = \pm 1,\ j - j' = 0, \pm 1 \text{ and } m_j - m_j' = 0 \text{ (for } z\text{) or } m_j - m_j' = \pm 1 \text{ (for } x \text{ and } y\text{)}. \qquad (4.3c)$$

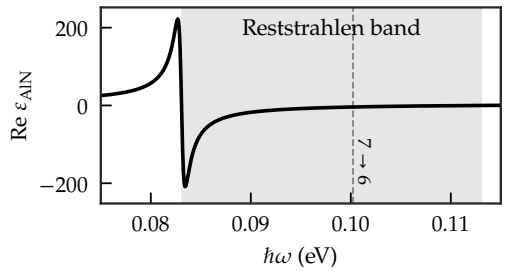

Figure 4.2: Real part of the permittivity of AlN, as a function of the frequency. The shaded area represents the Reststrahlen band, where $\mathrm{Re}\,\varepsilon_{\mathrm{AlN}} < 0$ and phonon-polaritonic resonances are expected to occur. The dashed vertical line indicates the energy of the $n = 7 \to n = 6$ transition.

1

As for the eigenenergies, we have $H_{\mathrm{at}}|nljm_j\rangle = E_{nj}|nljm_j\rangle$, with

$$E_{nj} \simeq -\frac{\alpha^2\mu c^2}{2n^2} - \frac{\alpha^4\mu c^2}{2n^3}\left[\frac{1}{j+\frac{1}{2}} - \frac{3}{4n}\right], \tag{4.4}$$

where μ is the reduced mass. In these energies, the degeneracy is explicitly broken for the j quantum number. Accordingly, for the nth Bohr level, a total of n closely separated lines appear in the spectrum, as sketched in fig. 4.1a. The next important correction to the hydrogenic spectrum is the well-known free-space Lamb shift. For $j = \frac{1}{2}$ states, it is roughly one order of magnitude smaller than the fine structure, while for $j > \frac{1}{2}$ states it becomes at least two or three orders of magnitude smaller [226]. On top of that, there is the so-called hyperfine structure due to effects like the interaction of the electron and the nuclear spin, also smaller than the fine structure. As will become clear in the following parts of the chapter, we are interested in a regime where the nanoparticle-induced shifts are comparable or larger than the fine structure. For that reason, we neglect all corrections but the fine structure. In the next sections, we will study the dynamics of a hydrogen atom within a single fine-structure multiplet, whose states lie within a thin energy window of width Δ_{fs}.

Dielectric nanoparticle We place the hydrogen atom close to a nanoparticle that supports EM resonances, adequately described through MQED. For the purposes of this chapter, we want the nanostructure's resonances to be narrow and to match the frequency of a particular $n \to n-1$ transition in the atom. With that in mind, there are two considerations to be made when choosing the nanoparticle: the material and the geometry.

Material: The material will be one of the key factors in determining the frequency range at which the nanostructure will support resonances.

One possible natural choice would be a metallic nanoparticle, where the resonances are plasmon-polaritonic excitations, that is, the result of electronic motion. Therefore, the resonant frequencies depend both on the metal's own plasma frequency and the concrete shape of the particle. However, metals are known to be relatively lossy, which can come into conflict with the narrow resonance requirement. Furthermore, we will look into relatively high n values, which enriches the phenomenology as more states participate in the simulations. This means that the target atomic transitions' frequencies will belong to the infrared range, where plasmonic nanoparticles become less efficient at supporting highly confined EM fields [269]. For these reasons, we turn our attention to polar covalent semiconductors that exhibit phonon-polaritonic excitations due to vibrations in the ionic lattice, typically in the infrared part of the spectrum. Their dielectric function is approximately of the form [269, 270]

$$\varepsilon_{\text{ionic}}(\omega) \simeq \varepsilon_\infty \frac{\omega_{\text{LO}}^2 - \omega^2 - i\omega\gamma_{\text{LO}}}{\omega_{\text{TO}}^2 - \omega^2 - i\omega\gamma_{\text{TO}}}. \tag{4.5}$$

Here, ω_{LO} and ω_{TO} are the longitudinal and transverse optical phonon frequencies, while γ_{LO} and γ_{TO} are related to the damping forces in the ionic oscillations. The real part of such permittivities becomes negative within a narrow frequency range known as the *Reststrahlen* band, where the phonon-polariton resonances are contained [271]. Even if the Reststrahlen band is not a very tunable property for any material, its precise location and the much lower losses of phonon-polaritons compared to plasmon-polaritons make these materials a good choice. From the permittivities parametrized in [269] for different phonon-polaritonic materials, we observe that the Reststrahlen band of aluminum nitride (AlN) contains the frequency associated to the $n = 7 \to n = 6$ transitions, $E_{n=7}^{\text{Bohr}} - E_{n=6}^{\text{Bohr}} \simeq 0.1$ eV, as illustrated in fig. 4.2. Encouraged by the numerical coincidence, we settle on AlN as the nanoparticle's material, and we pay special attention to the $n = 7 \to n = 6$ transition.

To be more precise, the EM response of AlN is slightly anisotropic [269]. We neglect this effect here for simplicity.

Geometry: For reasons that will become clear in section 4.3, we also want the nanoparticle to have an axis-symmetric prolate shape. In particular, we choose a spheroid whose major and minor axes are $M = 200$ nm and $m = 140$ nm, as depicted in fig. 4.1b. We place the atom on top of the nanoparticle, along the symmetry axis, the z axis in the

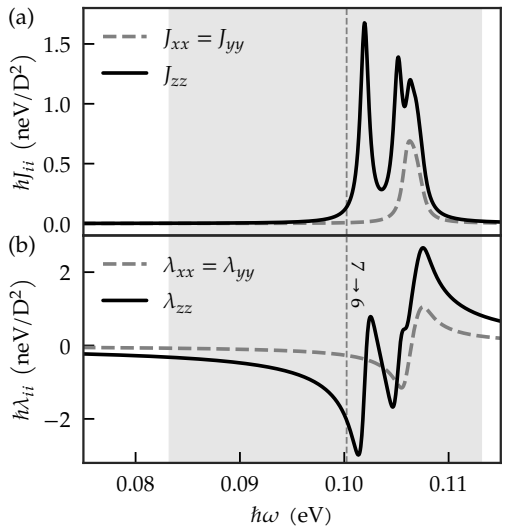

Figure 4.3: Spectral functions that characterize the EM environment due to the dielectric nanoparticle. The vertical dashed line and the shaded area represent the energy of the $n = 7 \to n = 6$ transition and the Reststrahlen band, respectively. Adapted from [267].

(a) Diagonal components of $\mathbf{J}$ for an atom placed at $s = 50$ nm.

(b) Diagonal components of $\boldsymbol{\lambda}$ for an atom placed at $s = 50$ nm.

Their units are eV/D^2, where 1 D $\approx 0.208\, e \cdot$ Å stands for Debye.

1

sketch, at a distance s from the surface. Such an arrangement implies that the cross-correlations between different environment operators vanish or, equivalently, that γ, $\mathbf{J}$ and $\boldsymbol{\lambda}$ are diagonal matrices, which simplifies matters in section 4.2. Still, the main reason for selecting such a nanoparticle is that, for an atom placed along the symmetry axis, the interaction due to $\hat{\mathbf{z}} \cdot \mathbf{d}$ will be significantly enhanced compared to the orthogonal components of the dipole moment; this choice is particularly well suited to illustrate some effects discussed in section 4.3.

With the above considerations, we characterize the environment through its spectral density $\mathbf{J}$ and its Hilbert conjugate $\boldsymbol{\lambda}$, using eqs. (4.2a) and (4.2b). For the specified geometry and material, and an atom placed $s = 50$ nm away from the nanoparticle's surface, these quantities are depicted in figs. 4.3a and 4.3b, respectively. As we anticipated earlier, the phonon-polaritonic resonances are clearly within the Reststrahlen band, as is the targeted transition. Also, in agreement with the geometric considerations, the zz components are larger than the others, and there is a richer peak structure to it. These quantities have been obtained numerically, using the boundary element method implemented in scuff-em [272, 273].

4.2 Master equation and non-Hermitian Hamiltonian

In this section, we will develop an effective Hamiltonian description from an appropriate LME. In doing so, we go from a simplified dynamical equation, the LME, to an even more simplified one in the effective non-Hermitian Hamiltonian, which will render the analysis in section 4.3 direct. After chapter 3, the most straightforward approach would be to simply start from the method developed there, a LME that we have called $a\Lambda - g\Gamma(+)$. Such a master equation avoids the secular approximation, thus keeping environment-induced off-diagonal couplings between different, off-resonant atomic states, and does so generalizing the one proposed in [266]. However, we are not going to start from there, but from $g\Lambda - g\Gamma$. As mentioned in section 3.3.1, this master equation already introduces two slight generalizations to the work of [266], namely, it dispenses with the RWA and allows for multiple system-environment interaction terms. However, it is not guaranteed that the resulting master equation is a true LME. Still, we start from $g\Lambda - g\Gamma$, rather than $a\Lambda - g\Gamma(+)$, for three reasons stated here and more thoroughly explained in the next subsections.

1. The energy structure of the hydrogen atom allows us to perform a partial secular approximation that eliminates the couplings between states in different Bohr levels. These terms can be safely discarded because the energy shifts and decay rates will be far from the orders of magnitude associated with the gross structure. As a consequence, we will be able to ensure that the energy shift is Hermitian in all cases, and the geometric mean needs not be replaced with the arithmetic version.

2. Due to the symmetric placement of the atom and the nanoparticle, we can express the interaction in a basis that ensures that (i) there are no environment cross-correlations and (ii) each emitter transition is mediated by only one dipole moment component. Indeed, we can write

$$H'_{\text{int}} = \frac{d_0 D_{(\text{at}),0} + d_{+1} D_{(\text{at}),-1} + d_{-1} D_{(\text{at}),+1}}{\varepsilon_0}, \tag{4.6a}$$

where the ± 1 components are the right and left circularly-polarized polarizations. More explicitly,

$$\begin{pmatrix} v_{+1} \\ v_{-1} \\ v_0 \end{pmatrix} = \begin{pmatrix} \frac{-1}{\sqrt{2}} & \frac{-i}{\sqrt{2}} & 0 \\ \frac{1}{\sqrt{2}} & \frac{-i}{\sqrt{2}} & 0 \\ 0 & 0 & 1 \end{pmatrix} \begin{pmatrix} v_x \\ v_y \\ v_z \end{pmatrix}, \tag{4.6b}$$

for the components of a generic vector $\mathbf{v}$. In terms of the new "spherical" components, the matrices $\boldsymbol{\gamma}$, $\mathbf{J}$ and $\boldsymbol{\lambda}$ remain the same, as the transformation affects only the $\{x, y\}$ subspace, which is degenerate in each of those matrices due to the symmetry. Therefore, $\gamma_{+1,+1} = \gamma_{-1,-1} = \gamma_{xx} = \gamma_{yy}$, and $\gamma_{+1,-1} = \gamma_{xy}$, and likewise for the other quantities. Note, however, that the components of the dipole moment operators that appear in the BRE's parameters are no longer Hermitian, as $d_{+1} = d_{-1}^{\dagger}$. Thus, we actually have

$$\Gamma_{ij}(\delta) = \mathrm{Tr}_{\mathrm{at}}\left(\mathbf{d}^{\dagger}\sigma_i\right) \cdot \boldsymbol{\gamma}(\delta) \cdot \mathrm{Tr}_{\mathrm{at}}\left(\mathbf{d}\sigma_j^{\dagger}\right), \tag{4.6c}$$

where $\mathrm{Tr}_{\mathrm{at}}\left(\mathbf{d}^{\dagger}\sigma_i\right)$ is no longer equal to $\mathrm{Tr}_{\mathrm{at}}\left(\mathbf{d}\sigma_i^{\dagger}\right)^{*}$, and likewise for Λ_{ij}. In any case, using the spherical components will allow us to prove in section 4.2.2 that the Kossakowski matrix is positive semidefinite, such that no negative eigenvalues must be explicitly removed.

3. The last reason is that the studies that lead to the results presented in chapters 3 and 4 were carried out in the opposite temporal order compared to the order of presentation here. We did not have at the time a solution to the potential problems of [266], nor was finding a solution our main preoccupation. Since we were able to show that the master equation used in this study is a true LME, we took it and analyzed the physical consequences of the off-diagonal couplings. The only drawback is that this chapter is restricted to the case where the atom lies on the symmetry axis of the nanoparticle, as any deviation would automatically incur the problems discussed in chapter 3. In any case, such a limitation was automatically lifted by the method proposed in chapter 3, and we have started work exploring this direction.

4.2.1 Details of the master equation

In order to derive the LME that will be the basis of our upcoming analysis, we start from the BRE in state-index notation:

$$\begin{aligned}
\dot{\rho}_{\mathrm{at}} = &-\frac{i}{\hbar}[H_{\mathrm{at}}, \rho_{\mathrm{at}}] \\
&+ \sum_{abcd}\Bigg[-i\Big(\Lambda_{ca,db}(\omega_{bd})|a\rangle\langle c|d\rangle\langle b|\rho_{\mathrm{at}} - \Lambda_{ca,db}(\omega_{ac})\rho_{\mathrm{at}}|a\rangle\langle c|d\rangle\langle b|\Big) \\
&\qquad + i[\Lambda_{ca,db}(\omega_{bd}) - \Lambda_{ca,db}(\omega_{ac})]|d\rangle\langle b|\rho_{\mathrm{at}}|a\rangle\langle c| \\
&\qquad - \frac{1}{2}\Big(\Gamma_{ca,db}(\omega_{bd})|a\rangle\langle c|d\rangle\langle b|\rho_{\mathrm{at}} + \Gamma_{ca,db}(\omega_{ac})\rho_{\mathrm{at}}|a\rangle\langle c|d\rangle\langle b|\Big)
\end{aligned}$$

$$+\frac{1}{2}[\Gamma_{ca,db}(\omega_{bd})+\Gamma_{ca,db}(\omega_{ac})]|d\rangle\langle b|\rho_{\mathrm{at}}|a\rangle\langle c|\Big]. \tag{4.7}$$

Here, a, b, c and d denote eigenstates of H_{at}, and, as in previous chapters,

$$\Gamma_{ca,db}(\omega)=\mathbf{d}^{\dagger}_{ac}\cdot\boldsymbol{\gamma}(\omega)\cdot\mathbf{d}_{db} \quad \text{and} \tag{4.8a}$$

$$\Lambda_{ca,db}(\omega)=\mathbf{d}^{\dagger}_{ac}\cdot\boldsymbol{\lambda}(\omega)\cdot\mathbf{d}_{db}. \tag{4.8b}$$

Note that we have kept $\mathbf{d}^{\dagger}$, foreseeing that the non-Hermitian spherical components of the atomic dipole moment will be used later. The first step is a partial secularization, alluded to in the previous paragraphs, which involves discarding every term in which the timescale induced by the environment, $\tau_{\mathrm{E}}\sim\min\Big(\left|\mathbf{d}^2\lambda\right|^{-1},\left|\mathbf{d}^2\gamma\right|^{-1}\Big)$, is much larger than that of the atomic transitions $\tau_{\mathrm{at}}\sim|\omega_{ac}-\omega_{bd}|^{-1}=|\omega_{ab}-\omega_{cd}|^{-1}$. Let us analyze the effect of the partial secular approximation in more detail.

1. Of course, we keep the terms where $|a\rangle$ and $|b\rangle$ belong to the same Bohr level, $n_a=n_b$, and $|c\rangle$ and $|d\rangle$ both belong to Bohr level $n_c=n_d$.
2. In most other cases, τ_{at} is very short because $\hbar\tau_{\mathrm{at}}^{-1}$ is of the order of the gross structure of the hydrogen atom's spectrum, and the secular approximation discards those terms.
3. The only other case that we need to delicately take care of happens when $|a\rangle$ and $|c\rangle$ belong to the same Bohr level, $n_a=n_c$, and $|b\rangle$ and $|d\rangle$ both belong to Bohr level $n_b=n_d$. We consider here the dissipative and energy shift parts of the BRE separately. In the dissipative part of eq. (4.7), these terms can be discarded even if $\tau_{\mathrm{at}}\simeq\hbar/\Delta_{\mathrm{fs}}$ is large, because the environment-induced timescale is even larger. Indeed, τ_{E} is proportional to $\gamma^{-1}(\omega=\Delta_{\mathrm{fs}}/\hbar)$, where $\gamma(\omega)\to 0$ very fast as $\omega\to 0$ (see Appendix B of [204]). However, in the first two lines of eq. (4.7) this condition is not fulfilled because $\lambda(0)\neq 0$. Still, for these terms ($n_a=n_c$ and $n_b=n_d$), the second line of eq. (4.7) has a factor $\lambda(\omega\approx\Delta_{\mathrm{fs}}/\hbar)-\lambda(\omega\approx\Delta_{\mathrm{fs}}/\hbar)\approx 0$ and is therefore negligible. Then, we only need to include the terms where $n_a=n_c$ and $n_b=n_d$ in the first line of the BRE, where the factor $\langle c|d\rangle$ implies that all 4 states belong to the same Bohr state. These terms are then a particular case of the first item on this list, and thus we are keeping them automatically.

We next apply the geometric mean replacement discussed in chapter 3,

$$\Lambda_{ca,db}(\omega_{ac})\text{ and }\Lambda_{ca,db}(\omega_{bd})\to\tilde{\Lambda}_{ca,db}=\sqrt{\Lambda_{ca,db}(\omega_{ac})}\sqrt{\Lambda_{ca,db}(\omega_{bd})} \tag{4.9a}$$

and

$$\Gamma_{ca,db}(\omega_{ac}) \text{ and } \Gamma_{ca,db}(\omega_{bd}) \to \tilde{\Gamma}_{ca,db} = \sqrt{\Gamma_{ca,db}(\omega_{ac})}\sqrt{\Gamma_{ca,db}(\omega_{bd})}, \tag{4.9b}$$

and obtain

$$\begin{aligned}\dot{\rho}_{\text{at}} = &-\frac{i}{\hbar}[H_{\text{at}}, \rho_{\text{at}}] - i\Bigg[\sum_{abc}^{(n_a=n_b)} \tilde{\Lambda}_{ca,cb}|a\rangle\langle b|, \rho_{\text{at}}\Bigg] \\ &+ \sum_{abcd}^{(n_a=n_b, n_c=n_d)} \tilde{\Gamma}_{ca,db}\Bigg(|d\rangle\langle b|\rho_{\text{at}}|a\rangle\langle c| - \frac{1}{2}\Big\{|a\rangle\langle c|d\rangle\langle b|, \rho_{\text{at}}\Big\}\Bigg).\end{aligned} \tag{4.10}$$

After the geometric mean replacement, the CP energy shift Hamiltonian is simply $H_{\text{CP}} = \hbar\sum_{abc}^{(n_a=n_b)} \tilde{\Lambda}_{ca,cb}|a\rangle\langle b|$. It contains both diagonal and off-diagonal matrix elements, these last ones coupling only states within the same Bohr level. However, as we saw in chapter 3, this form of H_{CP} can be non-Hermitian precisely because of the off-diagonal couplings. As for the Kossakowski matrix, $\tilde{\Gamma}_{ca,db}$, it is not at all obvious whether the geometric replacement procedure should yield a positive semidefinite matrix. Failing to satisfy either of these requirements would prevent eq. (4.10) from being a LME. In the following, we verify that the combination of the symmetric geometry of the system and the partial secular approximation ensure that eq. (4.10) is, indeed, a LME.

4.2.2 Verification of the LME

Let us address both potential issues separately.

Hermitian Casimir-Polder energy shift H_{CP} is guaranteed to be Hermitian if $\lambda(\omega_{ac})$ and $\lambda(\omega_{bc})$ have the same sign. Because of the partial secularization, only terms where $n_a = n_b$ are kept, which means that $\hbar|\omega_{ac} - \omega_{bc}| \simeq \Delta_{\text{fs}}$, of $O(10^{-6})$ eV for $|a\rangle$ and $|b\rangle$ in the $n = 7$ Bohr level. Additionally, the lines in fig. 4.3b clearly show that the energy scale over which λ changes significantly and changes sign is $O(10^{-3})$ eV, or larger. Consequently, the non-Hermiticity problem can only arise if $n = 7$ multiplet lies directly on top of a sign change of λ, a coincidence that would be unfortunate and unlikely in equal parts. Furthermore, even if that was the case, the states with $n = 7$ would lie extremely close to the actual zero of $\lambda(\omega)$, which would effectively render these contributions negligible, regardless of the non-Hermiticity.

The non-Hermitian nature of H_{CP} would still be there, but it would only become noticeable long after the dissipation has cleared out any population in the $n = 7$ level.

Positive semidefinite Kossakowski matrix We recall here the spherical vector components introduced in eq. (4.6b). With them, we may write $\Gamma_{ca,db}$

as

$$\Gamma_{ca,db}(\omega) = \sum_{\ell=-1}^{+1} \mathbf{d}^{\dagger}_{\ell,ac} \cdot \gamma_{\ell\ell}(\omega) \cdot \mathbf{d}_{\ell,db}. \tag{4.11}$$

In the coupled angular momentum basis, our hydrogenic states are of the general form $\left|nl; jm_j\right\rangle = \alpha|nl; m_l m_s\rangle + \alpha'|nl; m_l' m_s'\rangle$, where $m_l + m_s = m_l' + m_s' = m_j$. Since (i) the dipole operator does not act on the spin degree of freedom, and (ii) d_ℓ connects states with m_l to states with $m_l + \ell$, we have that d_ℓ maps states with m_j to states with $m_j + \ell$ too. Accordingly, because all $|a\rangle$ and $|c\rangle$ have a definite value of m_j, each transition $|a\rangle\langle c|$ will be mediated by a single component of the dipole moment operator. Furthermore, the diagonal form of γ implies that the transition operators $(|a\rangle\langle c|)^\dagger$ and $|d\rangle\langle b|$ must be mediated by the same d_ℓ; otherwise $\Gamma_{ca,db}(\omega) = 0$. As a result, we can expand the dissipative part of eq. (4.10) as three separate sums, one for each value of ℓ, indicated in the expression below with the label ℓ on top of the second summation sign in the second line of

$$\begin{aligned}
&\sum_{abcd}^{(n_a=n_b,n_c=n_d)} \sqrt{\Gamma_{ac,db}(\omega_{bd})}\sqrt{\Gamma_{ac,db}(\omega_{ac})} \\
&\qquad\qquad \times \left[|d\rangle\langle b|\rho_{\text{at}}|a\rangle\langle c| - \frac{1}{2}\left\{|a\rangle\langle c|d\rangle\langle b|, \rho_{\text{at}}\right\}\right] \\
&= \sum_{\ell} \sum_{abcd}^{(n_a=n_b,n_c=n_d),\ell} d^{\dagger}_{\ell,ac} d_{\ell,db} \sqrt{\gamma_{\ell\ell}(\omega_{bd})}\sqrt{\gamma_{\ell\ell}(\omega_{ac})} \\
&\qquad\qquad \times \left[|d\rangle\langle b|\rho_{\text{at}}|a\rangle\langle c| - \frac{1}{2}\left\{|a\rangle\langle c|d\rangle\langle b|, \rho_{\text{at}}\right\}\right] \\
&= \sum_{\ell n}\left(\Sigma^{(n)}_{\ell}\rho_{\text{at}}\Sigma^{(n)\dagger}_{\ell} - \frac{1}{2}\left\{\Sigma^{(n)\dagger}_{\ell}\Sigma^{(n)}_{\ell}, \rho_{\text{at}}\right\}\right) = \sum_{\ell n} \mathcal{D}_{\Sigma^{(n)}_{\ell},\Sigma^{(n)}_{\ell}}[\rho_{\text{at}}].
\end{aligned} \tag{4.12}$$

In the first step, we have used that $\gamma_{\ell\ell}(\omega) \geq 0$ and that $d_{\ell,ac}$ is real for any pair of states $|a\rangle$ and $|b\rangle$ and ℓ (see eqs. (2.126) and (2.134b)). As for the second step, we have separated the sums over a, c and d, b to define

$$\Sigma^{(n_b)}_{\ell} \equiv \sum_{db}^{(n_b)} d_{\ell,db}\sqrt{\gamma_{\ell\ell}(\omega_{bd})}|d\rangle\langle b|, \tag{4.13}$$

which allows us to neatly factor the equation in a way that evidences that the Kossakowski matrix is positive semidefinite. Moreover, it has only three nonzero eigenvalues, one for each ℓ, for each Bohr level.

In principle, one has to be careful in this factorization, as we are manipulating square roots of quantities that can be positive or negative. At the end of the day, simply considering all possible cases is enough to see that it can be done.

We have thus seen that the resulting master equation is, indeed, a LME. There are two final remarks of some interest. The first one is that, with similar

manipulations, we can actually factor the CP energy shift Hamiltonian similarly and arrive at

$$H_{\mathrm{CP}} = \hbar \sum_{\ell n} \left(D_\ell^{(n)}\right)^\dagger D_\ell^{(n)}, \tag{4.14a}$$

where

$$D_\ell^{(n_b)} \equiv \sum_{db}^{(n_b)} d_{\ell,db} \sqrt{\lambda_{\ell\ell}(\omega_{bd})} |d\rangle\langle b|. \tag{4.14b}$$

Then, the final LME can be written as

$$\begin{aligned} \dot{\rho}_{\mathrm{at}} &= -\frac{i}{\hbar}[H_{\mathrm{at}}, \rho_{\mathrm{at}}] - i \sum_{\ell n} \left[\left(D_\ell^{(n)}\right)^\dagger D_\ell^{(n)}, \rho_{\mathrm{at}} \right] + \sum_{\ell n} \mathcal{D}_{\Sigma_\ell^{(n)}, \Sigma_\ell^{(n)}}[\rho_{\mathrm{at}}] \\ &= -\frac{i}{\hbar}[H_{\mathrm{at}} + H_{\mathrm{CP}}, \rho_{\mathrm{at}}] + \sum_{\ell n} \mathcal{D}_{\Sigma_\ell^{(n)}, \Sigma_\ell^{(n)}}[\rho_{\mathrm{at}}]. \end{aligned} \tag{4.15}$$

The second observation is that the dissipative part of the LME in eq. (4.12) can be written in terms of "Cartesian" operators. We use now the x, y and z components of the dipole moment, and define

$$\Sigma_i^{(n_b)} = \sum_{db}^{(n_b)} d_{i,db} \sqrt{\lambda_{ii}(\omega_{bd})} |d\rangle\langle b|. \tag{4.16}$$

Evidently, $\Sigma_z^{(n)} = \Sigma_0^{(n)}$. As for the x and y components, they can be combined using that

$$\begin{aligned} \left(\Sigma_x^{(n)}\right)^\dagger A \Sigma_x^{(n)} + \left(\Sigma_y^{(n)}\right)^\dagger A \Sigma_y^{(n)} &= \frac{1}{2}\Big[\left(-\Sigma_{+1}^{(n)} + \Sigma_{-1}^{(n)}\right)^\dagger A \left(-\Sigma_{+1}^{(n)} + \Sigma_{-1}^{(n)}\right) \\ &\quad + \left(\Sigma_{+1}^{(n)} + \Sigma_{-1}^{(n)}\right)^\dagger A \left(\Sigma_{+1}^{(n)} + \Sigma_{-1}^{(n)}\right) \Big] \\ &= \left(\Sigma_{+1}^{(n)}\right)^\dagger A \Sigma_{+1}^{(n)} + \left(\Sigma_{-1}^{(n)}\right)^\dagger A \Sigma_{-1}^{(n)} \end{aligned} \tag{4.17}$$

for any operator A, which follows from eq. (4.6b). That is to say, the dissipative part corresponds simply to what a separate treatment of each system-environment interaction term would have yielded, expressing the dot product in terms of Cartesian components. In this regard, it is the same dissipator that the procedure in [266] would give, applied three separate times. Note that it is not a priori obvious from eq. (4.10) and [266] that this coincidence will happen, as there are atomic transitions mediated by both d_x and d_y, and those terms will be of the form

$$\sqrt{\Gamma_{ca,db}(\omega_{ac})} \sqrt{\Gamma_{ca,db}(\omega_{bd})} \mathcal{D}_{|c\rangle\langle a|,|d\rangle\langle b|}, \tag{4.18}$$

where,

$$\sqrt{\Gamma_{ca,db}(\omega)} = \sqrt{\gamma_{xx}(\omega) d^\dagger_{x,ac} d_{x,db} + \gamma_{yy}(\omega) d^\dagger_{y,ac} d_{y,db}}. \tag{4.19}$$

Then, there is no way in general to extract dipole moment factors from the square root and reach the separate Cartesian dissipators. However, the precise symmetry of the system implies that $\gamma_{xx}(\omega) = \gamma_{yy}(\omega)$, and provides us with a relation between the matrix elements of d_x and d_y. Inverting the relation in eq. (4.6b), we have that

$$\begin{cases} \langle a|d_x|b\rangle = \dfrac{-1}{\sqrt{2}}\langle a|d_{+1}|b\rangle \\ \langle a|d_y|b\rangle = \dfrac{i}{\sqrt{2}}\langle a|d_{+1}|b\rangle \end{cases} \implies \langle a|d_x|b\rangle = -i\langle a|d_y|b\rangle \text{ if } m_j(b) = m_j(a) - 1 \tag{4.20a}$$

$$\begin{cases} \langle a|d_x|b\rangle = \dfrac{1}{\sqrt{2}}\langle a|d_{-1}|b\rangle \\ \langle a|d_y|b\rangle = \dfrac{i}{\sqrt{2}}\langle a|d_{-1}|b\rangle \end{cases} \implies \langle a|d_x|b\rangle = +i\langle a|d_y|b\rangle \text{ if } m_j(b) = m_j(a) + 1 \tag{4.20b}$$

Additionally, we know that the $|a\rangle \to |c\rangle$ and $|b\rangle \to |d\rangle$ transitions in any given term have the same Δm_j. Hence,

$$\begin{aligned} &\sqrt{\gamma_{xx}(\omega_{ac})\left(d^\dagger_{x,ac} d_{x,db} + d^\dagger_{y,ac} d_{y,db}\right)}\sqrt{\gamma_{xx}(\omega_{bd})\left(d^\dagger_{x,ac} d_{x,db} + d^\dagger_{y,ac} d_{y,db}\right)} \\ &\qquad \times \mathcal{D}_{|c\rangle\langle a|,|d\rangle\langle b|} \\ &= \sqrt{\gamma_{xx}(\omega_{ac})}\sqrt{\gamma_{xx}(\omega_{bd})} d^\dagger_{x,ac} d_{x,db} \sqrt{1 + (\pm i)^*(\pm i)}^2 \mathcal{D}_{|c\rangle\langle a|,|d\rangle\langle b|} \\ &= 2 d^\dagger_{x,ac} d_{x,db} \sqrt{\gamma_{xx}(\omega_{ac})}\sqrt{\gamma_{xx}(\omega_{bd})} \mathcal{D}_{|c\rangle\langle a|,|d\rangle\langle b|} \\ &= \sum_{i=x,y} d^\dagger_{i,ac} d_{i,db} \sqrt{\gamma_{ii}(\omega_{ac})}\sqrt{\gamma_{ii}(\omega_{bd})} \mathcal{D}_{|c\rangle\langle a|,|d\rangle\langle b|}, \end{aligned} \tag{4.21}$$

where we have used the relations in eq. (4.20), and the equality $\gamma_{xx} = \gamma_{yy}$. In the final line, we recover explicitly the independent Cartesian dissipators. Note that the above manipulations work because our basis states conspire with the dipole matrix elements in a way that is allowed by $\gamma_{xx}(\omega) = \gamma_{yy}(\omega)$. In a more general, i.e., less symmetric configuration, these factors cannot work together, and no Cartesian dissipators are retrieved. Finally, we note that the accuracy of the final LME in eq. (4.15) is checked explicitly in appendix B.

4.2.3 Derivation of the effective Hamiltonian

Here, we extract an effective non-Hermitian Hamiltonian description from the LME provided in eq. (4.15), which will notably simplify the analysis of the dynamics. We begin by observing that any Lindblad equation

$$\dot{\rho}_{\text{at}} = -\frac{i}{\hbar}[H_{\text{at}} + H_{\text{CP}}, \rho_{\text{at}}] + \sum_{ij} \gamma_{ij} \mathcal{D}_{\sigma_i,\sigma_j}[\rho_{\text{at}}] \tag{4.22}$$

can be expressed as

$$\dot{\rho}_{\text{at}} = -\frac{i}{\hbar}(H_{\text{eff}}\rho_{\text{at}} - \rho_{\text{at}}H_{\text{eff}}^\dagger) + \sum_{ij} \gamma_{ij}\sigma_j\rho_{\text{at}}\sigma_i^\dagger, \tag{4.23}$$

where

$$H_{\text{eff}} = H_{\text{at}} + H_{\text{CP}} - \frac{i}{2}\sum_{ij} \hbar\gamma_{ij}\sigma_i^\dagger\sigma_j \tag{4.24}$$

is an effective, non-Hermitian Hamiltonian, and the last term was called the "refilling" term in chapter 2. Even if H_{eff} is non-Hermitian, since its anti-Hermitian component is positive semidefinite, the imaginary part of its eigenvalues will correspond to physical decay, unlike in the non-Hermiticity found in chapter 3. The refilling term ensures that the population that flows out of some states flows into some other states. In the absence of incoherent pumping, such as that arising from an environment at a sufficiently high temperature, the refilling term only accounts for the filling of lower levels, whose populations do not affect the dynamics of the upper states. In such physical situations, the dynamics of the upper states are fully characterized by the eigenstates and eigenvalues of the effective Hamiltonian [274].

As has been mentioned before, we will focus on the dynamics of the $n = 7$ fine-structure multiplet in section 4.3. Hence, we can completely neglect the refilling part of the LME. Then, following the discussion above, the effective Hamiltonian is

$$H_{\text{eff}} = H_{\text{at}} + \hbar\sum_{\ell n}\left(D_\ell^{(n)}\right)^\dagger D_\ell^{(n)} - \frac{i\hbar}{2}\sum_{\ell n}\left(\Sigma_\ell^{(n)}\right)^\dagger\Sigma_\ell^{(n)} = \sum_n H_{\text{eff}}^{(n)} \tag{4.25}$$

which comes neatly separated in separate blocks corresponding to different values of n,

$$H_{\text{eff}}^{(n)} = P_n H_{\text{eff}} P_n, \tag{4.26}$$

where P_n projects into the n subspace. Accordingly, the dynamics of the states

with $n = 7$, determined by $\rho_{\text{at}}^{(7)} = P_7 \rho_{\text{at}} P_7$, arises from $H_{\text{eff}}^{(7)}$, and is given by

$$\dot{\rho}_{\text{at}}^{(7)} = -\frac{i}{\hbar}\left(H_{\text{eff}}^{(7)} \rho_{\text{at}}^{(7)} - \rho_{\text{at}}^{(7)} H_{\text{eff}}^{(7)\dagger}\right), \tag{4.27}$$

or, equivalently, by the Schrödinger equation $\partial_t |\psi(t)\rangle = -\frac{i}{\hbar} H_{\text{eff}}^{(n)} |\psi(t)\rangle$. In order to gauge the degree of simplification that comes from using the effective Hamiltonian for a given value of n, rather than solving the full master equation, we observe that including all states from $n = 1$ to $n = 7$ involves

$$\#_{n\leq m} = 2\sum_{n=1}^{m}\sum_{l=0}^{n-1}(2l+1) = 2\sum_{n=1}^{m} n^2 = \frac{m(m+1)(2m+1)}{3} \rightarrow \#_{n\leq 7} = 280 \tag{4.28}$$

states. Meanwhile, with the effective Hamiltonian description it suffices to explicitly describe "just" $2 \cdot 7^2 = 98$ states. That is still plenty of states; however, we will see now how to reduce it even further to a significantly more manageable 7 states.

Angular momentum conservation Within each Bohr level n, the projected effective Hamiltonian $H_{\text{eff}}^{(n)}$ is itself a block matrix, where each block has a concrete value of m_j. This is easy to see, because both $D_\ell^{(n)}$ and $\Sigma_\ell^{(n)}$ take m_j to $m_j + \delta$, and their Hermitian conjugates take $m_j + \delta$ back to m_j such that, overall, $H_{\text{eff}}^{(n)}$ preserves m_j. In words, it can be understood as a sort of conservation of the atomic angular momentum under virtual transitions. Actually, only the z projection of the *total* angular momentum including both the atom and real photons is conserved due to the axial symmetry of the setup. This is reflected in the complete master equation, as the refilling term does connect different m_j subspaces. Still, because the refilling term has been shown to be negligible in describing the dynamics of the $n = 7$ multiplet for our purposes, we can use the preservation of m_j by $H_{\text{eff}}^{(7)}$ and, by fixing its value, further reduce the size of our Hilbert subspace of interest to $2\left(n - m_j\right)$. For $m_j = 1/2$, we thus obtain only 13 states. Finally, we can reduce the number of relevant states even further by noticing that $H_{\text{eff}}^{(n)}$ also preserves the parity of l, as evidenced by the red and blue diagonal lines in fig. 4.1a. For the upcoming section, we settle on $m_j = 1/2$ and even l, such that the dimension of the reduced Hilbert space of interest is a mere 7, definitely more convenient than either 98 or 280.

Again, explicit checks of the numerical reliability of the non-Hermitian Hamiltonian are provided in appendix B. Given the superior simplicity of the effective Hamiltonian, together with the considerations that further reduce the number of states and its similar degree of accuracy, we resort to it, rather

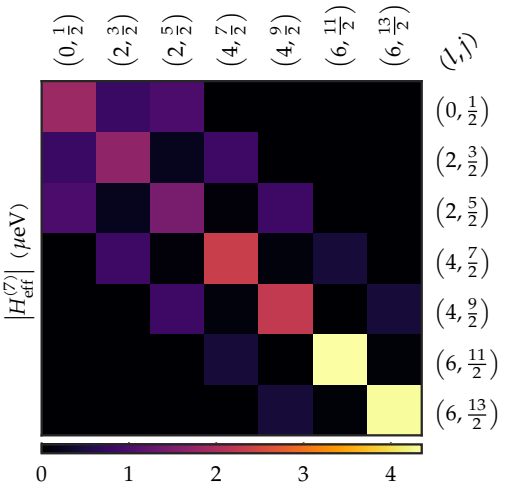

Figure 4.4: Modulus of the matrix elements of the effective Hamiltonian associated to the $n = 7$ level, for a fixed value of $m_j = 1/2$, at $d = 50$ nm (cf. fig. 4.1). The states defining each matrix element are denoted through their l and j values. The effective Hamiltonian displays a penta-diagonal structure due to the selection rules.

than to the LME, in the next part to substantiate our claims. In essence, this reduces the computational efforts to being able to numerically diagonalize the effective Hamiltonian, which, in turn, is calculated numerically with scuff-em [272, 273] at varying atom-nanoparticle separations.

4.3 Analysis and results

After the thorough explanation and derivation of the mathematical methods, we can analyze the dynamics within the relevant subset of states ($n = 7$, even l and $m_j = 1/2$). To that end, we calculate and study the effective Hamiltonian at varying atom-nanoparticle separations, d. For reference, fig. 4.4 depicts the magnitude of the matrix elements of $H_{\text{eff}}^{(7)}$ at $d = 50$ nm. The off-diagonal matrix elements $\langle a|H_{\text{eff}}^{(7)}|b\rangle$ are comparable to the differences between the diagonal elements $\left|\langle a|H_{\text{eff}}^{(7)}|a\rangle - \langle b|H_{\text{eff}}^{(7)}|b\rangle\right|$, which already hints at the decisive role that they will have in the atomic structure and dynamics. Such assessment can be more quantitatively explored by directly diagonalizing the effective Hamiltonian and looking at the eigenvalues and eigenstates at each separation. After looking at them, we select a concrete atom-nanoparticle separation and solve the dynamics restricted to the $n = 7$ subspace, as given by the effective non-Hermitian Hamiltonian. In the following calculations, we have included atomic levels up to $n = 10$ in the sums over intermediate states, which ensures that the results are converged.

4.3.1 Eigenvalues

Due to the non-Hermiticity of the effective Hamiltonian, its eigenvalues will be complex. The real and imaginary parts correspond to the new energies and decay rates of the hydrogenic states, respectively, as modified by the presence of the nanoparticle:

$$H_{\text{eff}}^{(7)}(d)|a(d)\rangle = \left(E_a(d) - \frac{i}{2}\hbar\Gamma_a(d)\right)|a(d)\rangle. \tag{4.29}$$

In fig. 4.5, we show the dependence of the effective Hamiltonian eigenvalues on the atom-nanoparticle separation d, and compare the results with the analogous quantities obtained with the completely secularized theory (dashed blue lines). The energies, in fig. 4.5a, are plotted relative to the average energy at each separation of the multiplet, to remove the overall attractive CP background potential reported in the inset figure. Accordingly, fig. 4.5a reveals the relative position of each spectral line. As $d \to \infty$, the energies converge to horizontal lines, which are simply the free-space fine-structure energies. As the atom approaches the nanoparticle, its eigenenergies start shifting relative to each other in both the full and secularized theories. However, the difference between these methods soon becomes noticeable upon close inspection: the secular energies merely cross each other, while the full energies feature marked avoided crossings. These tend to happen when the diagonal CP shift brings two states close to degeneracy, the situation in which the off-diagonal CP coupling has the largest significance. A notable remark is that these effects start appearing at relatively large separations, barely below 100 nm.

For comparison, the typical size of the $n = 7$ hydrogenic wave-functions is of the order of 5 nm, which makes these separations especially large.

The decay rates, presented in fig. 4.5b, also highlight the effect of the off-diagonal couplings included in the non-secularized theory. In particular, the secular lines increase monotonically as the atom-nanoparticle separation shrinks. This is a manifestation of the well-known Purcell enhancement phenomenon, whereby an increase in the EM density of states carries with it an enlargement of the decay rates of the atom. When the off-diagonal couplings are included, the decay rates display the crossings for separations as large as 120 nm. Nevertheless, the overall trend is increasing with smaller separations, like in the secularized case, except for a single line that, momentarily, escapes such behavior. Indeed, between $d = 40$ nm and 60 nm, one decay rate starts to actually decrease, contradicting the expectation based on a simple analysis of the Purcell factor. As a result, one new eigenstate of the hydrogen atom in the presence of the nanoparticle becomes noticeably subradiant. In some sense, the environment that induces the decay is also generating an internal atomic interaction that mixes the hydrogenic eigenstates leading to the formation of

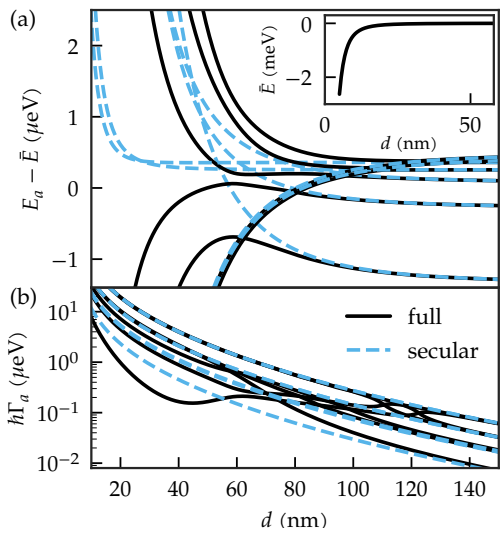

Figure 4.5: Evolution of the complex eigenvalues of $H_{\text{eff}}^{(7)}$ as a function of d, the separation between the atom and the nanoparticle. The continuous black lines represent the results with the full theory developed above, including off-diagonal terms. The dashed blue lines have been obtained from the effective Hamiltonian associated to the completely secularized theory, without off-diagonal elements. Adapted from [267].

(a) Energies relative to the multiplet's average energy at each separation d.

(b) Decay rates as a function of the separation d.

1

a "protected" state.

The explanation for the state-protection effect we just described goes back to our choice of the nanoparticle's shape and material. To better understand their roles, let us analyze an idealized scenario in which we can ignore (i) the fine structure, (ii) the atom-environment interaction due to d_x and d_y, and (iii) contributions of intermediate states outside the $n = 6$ Bohr level in the sums for the effective energy shift and decay. Then, the selection rules allow us to see the ideal system as 7 upper degenerate states $\{|u_i\rangle\}_{i=1}^{7}$ coupled to 6 lower degenerate states $\{|l_k\rangle\}_{k=1}^{6}$. Then, there must exist a superposition of the upper states, $|\psi\rangle = \sum_{i=1}^{7} a_i|u_i\rangle$ whose transition dipole moment matrix element to any lower state is zero, $\langle l_k|d_z|u_i\rangle a_i = 0$. This has to be the case, because it is equivalent to the fact that any seven vectors in a six dimensional space are linearly dependent. The conditions (i), (ii) and (iii) above are all approximately satisfied in our system, between $d = 40$ nm and 60 nm. For sufficiently close atom-nanoparticle separations, the CP shift is much larger than the fine structure, which renders the latter negligible. Furthermore, the nanoparticle's shape greatly favors the z component of the interaction over d_x and d_y, as revealed in fig. 4.3. Last, the effective contributions of the $n = 6$ Bohr level are expected to be larger than any other due to the coincidence of the $n = 7 \to n = 6$ transition energy with the phonon-polaritonic excitations of the material. Note that the last condition is not as simple as it seems. Indeed, the $n = 7$ intra-level transitions can be quite relevant too, despite the smaller value

If the second condition were not fulfilled, then there would be a different, uncoupled combination for each component of the dipole moment, which effectively yields no completely uncoupled combination.

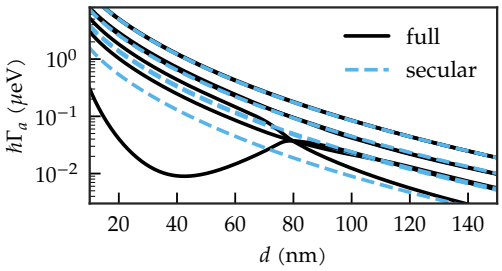

Figure 4.6: Evolution of the decay rates for the optimized geometry ($M = 200$ nm and $m = 120$ nm). The continuous black lines represent the results with the full, non-secularized theory. The dashed blue lines have been obtained from the completely secularized theory. Adapted from [267].

1

of $|\lambda(\omega \approx 0)|$, because the transition dipole moments are the largest for intra-level transitions. In the particular setup considered here, however, the $n = 6$ states indeed provide the largest contribution, as evidenced by the appearance of a subradiant state. In any case, the deviations from the idealized scenario act against the state protection effect.

Protected state optimization By changing the aspect-ratio of the nanoparticle, we can find the optimal shape that maximizes the environment-induced effect of state subradiance. After sweeping over the nanoparticle's width, we determine that reducing the minor axis from 140 nm to 120 nm significantly magnifies the effect, as shown in fig. 4.6. There, the ratio between the naive expectation of the lowest decay rate and the actual lowest decay rate reaches a value of approximately 20. Additionally, the range of separations in which the subradiant state defies the traditional Purcell enhancement is increased to between $d = 40$ nm and 80 nm.

4.3.2 Eigenstates

After dedicating some thought to the eigenvalues of the effective Hamiltonian, we now turn our attention to the eigenstates. Due to the off-diagonal couplings, the vacuum-field modified eigenstates $|a\rangle$ will be superpositions of the original hydrogenic states. Note that, due to the non-Hermiticity of $H_{\text{eff}}^{(7)}$, the new eigenstates are not orthogonal to each other, $\langle a|b\rangle \neq \delta_{ab}$. Thus, in any state expansion in terms of the eigenstates,

$$|\psi\rangle = \sum_a c_a |a\rangle, \tag{4.30}$$

the moduli squared of the coefficients c_a do not straightforwardly correspond to the probabilities. However, if we express the new eigenstates in terms of

Still, the eigenstates are almost orthogonal, because the Hermitian and anti-Hermitian parts of $H_{\text{eff}}^{(7)}$ are almost aligned for the same reasons leading to the subradiant state.

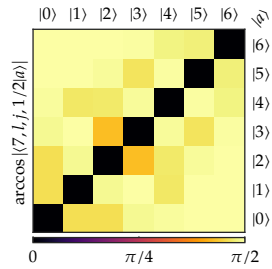

Figure 4.7: [1] Effective angle between different eigenstates.

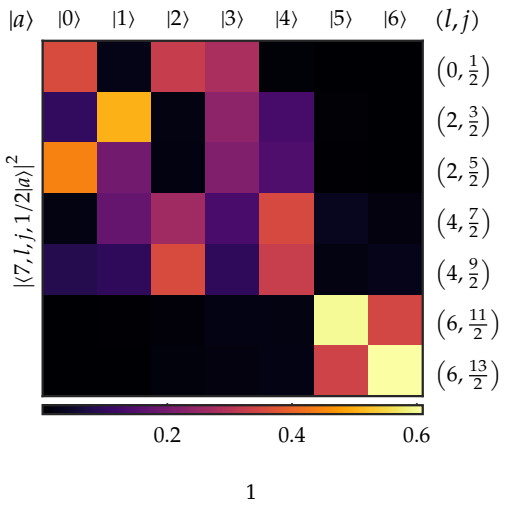

Figure 4.8: Degree of mixing of the eigenstates of $H_{\text{eff}}^{\langle 7\rangle}$ at an atom-nanoparticle separation of $d = 50$ nm, as indicated by the modulus squared of the expansion coefficients of the eigenstates $|a\rangle$ in terms of the fine-structure states $|7, l, j, 1/2\rangle$. Each column corresponds to an eigenstate, and each row to a fine-structure state.

the original fine-structure states as

$$|a\rangle = \sum_{l \text{ even}} \sum_{j=|l-1/2|}^{l+1/2} \langle 7, l, j, 1/2|a\rangle |a\rangle, \tag{4.31}$$

these coefficients do tell us how "mixed" the hydrogenic states have become, as a result of the nanoparticle-induced couplings. We illustrate the degree of mixing in fig. 4.8, where we plot $|\langle 7, l, j, 1/2|a\rangle|^2$ for the subspace where $n = 7$, l is even and $m_j = 1/2$, at an atom-nanoparticle separation of $d = 50$ nm, and with the initial nanoparticle shape ($M = 200$ nm and $m = 140$ nm). From fig. 4.8, the subspace is clearly separated in two blocks, one being 5×5 and the other 2×2. This fact could be anticipated from fig. 4.4, which has an almost degenerate 2×2 subspace in the lower-right corner, and the off-diagonal couplings become smaller as j increases. Within each block, the fine-structure state is very well mixed, with almost all coefficients noticeably larger than zero. In other words, simply by placing the atom in the vicinity of a dielectric nanoparticle, its fine structure becomes, for all intents and purposes, unrecognizable. Again in this part we remark that this strong effect happens relatively far from the nanoparticle, at experimentally realistic separations [112].

To more quantitatively assess the degree of mixing of the fine-structure states, we introduce the so-called participation ratio [275]. For a given orthonormal basis $\left\{|\phi_k\rangle_{k=1}^{n}\right\}$, it is defined as

$$P_a = \left(\sum_{k=1}^{n} |\langle \phi_k|a\rangle|^4 \right)^{-1}. \tag{4.32}$$

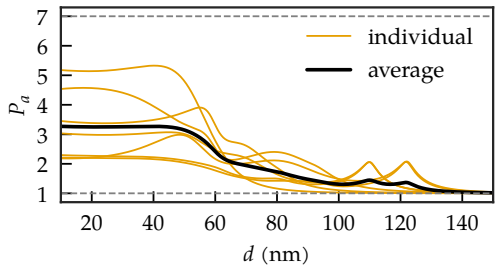

Figure 4.9: Evolution of the participation ratios P_a as a function of the atom-nanoparticle separation. The orange lines represent the individual participation ratios. The thick black line is the mean value. The horizontal dashed lines indicate the range of possible values.

1

The participation ratio is the inverse of the average of the probabilities $|\langle\phi_k|a\rangle|^2$, weighted by the same probabilities. Accordingly, it measures the number of basis states significantly "participating" in a given eigenstate. For instance, a maximally mixed state of the form $|\psi_{\max}\rangle = \sqrt{\frac{1}{n}}\sum_{k=1}^{n} e^{i\theta_k}|\phi_k\rangle$ has a participation ratio equal to

$$P_{\psi_{\max}} = \left(\sum_{k=1}^{n}\frac{1}{n^2}\right)^{-1} = n. \tag{4.33}$$

The participation ratio is, then, between 1 and n. We next calculate this ratio for the states in the subspace defined by $n = 7$, even l and $m_j = 1/2$, as a function of the atom-nanoparticle separation. The results are shown in fig. 4.9, where orange lines indicate the individual participation ratios of each eigenstate, and the black thicker black line represents the average value at each separation. In the figure, we see that state mixing is negligible for separations over $d = 140$ nm. Then, as the atom approaches the nanoparticle, the participation ratios develop distinct features. For instance, at around $d = 125$ nm and $d = 110$ nm, two participation ratios reach the value two. These peaks happen when the diagonal CP shift induces a degeneracy in two fine-structure states that remain approximately decoupled from the rest. Within this 2×2 subspace, the presence of off-diagonal couplings implies that the eigenstates are maximally mixed superpositions, that is, with participation ratios equal to 2. As d decreases even further, below $d = 100$ nm, the increased couplings start mixing more states, giving rise to a complex evolution of the participation ratios. The maximum value obtained is about 5.3, at around $d = 50$ nm. For separations under $d = 30$ nm, the participation ratios roughly stabilize, as now the dominant energies are the ones induced by the nanoparticle.

4.3.3 Dynamics

We finish our analysis of the nanoparticle-induced effects by explicitly solving the dynamics of the relevant states of the $n = 7$ multiplet. We present the

atomic populations in fig. 4.10 for an atom-nanoparticle separation of 40 nm, choosing, for illustration purposes, $\left|n = 7, l = 4, j = 9/2, m_j = 1/2\right\rangle$ as initial state. The shaded regions highlight two important features that follow from the discussion above. The gray region on the left, from 0 to 6 ns, displays a messy collection of lines with Rabi-like oscillations. These are a direct consequence of the off-diagonal couplings induced by the nanoparticle, and their convoluted appearance is due to the fact that all seven states are mixed to a reasonable degree. As time passes, the oscillation amplitudes become damped due to the non-Hermitian nature of the effective Hamiltonian, until, eventually, only a residual dissipation remains in the orange region. Indeed, beyond 6 ns, all populations decay at the same rate, as can be deduced from the lines becoming approximately parallel. The reason is that, at these long times, only the "protected" state in fig. 4.5 remains populated, and decays with its own rate.

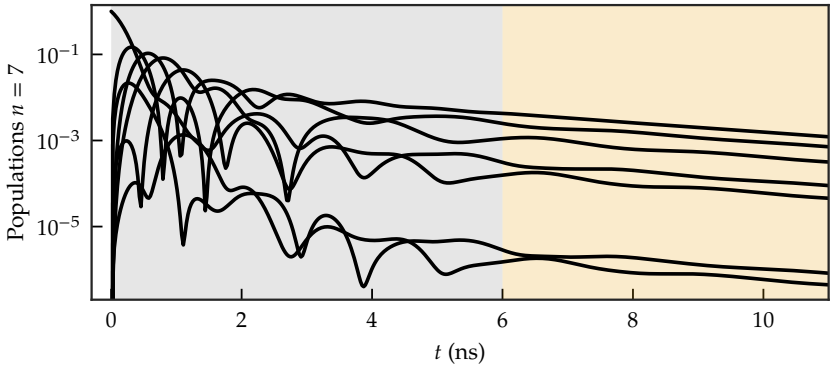

Figure 4.10: Evolution of the populations of the seven relevant fine-structure states in the $n = 7$ multiplet. The gray region on the left highlights Rabi-like oscillations early in the dynamics due to the off-diagonal couplings. The orange region, where the oscillations have dissipated, indicates the times when only the protected state remains populated.

4.4 Conclusions

In this chapter, we have seen that a secularized effective description of a hydrogen atom close to a nanoparticle is tremendously incomplete. In particular, we have shown that the environment does not only induce energy shifts and decay rates in the atom. Instead, it also results in effective couplings between atomic states, which can have very noticeable effects on the atomic dynamics and spectrum. In the preceding sections, we have derived an accurate way

to model the off-diagonal CP shift and dissipative rates, based on the LME developed in [266]. From the resulting LME, we have been able to further reduce the complexity of our dynamical equation by extracting an effective, non-Hermitian Hamiltonian in section 4.2. With it, we are able to very accurately describe the temporal evolution of the relevant states within a given fine-structure multiplet.

In section 4.3, we have used the methodology discussed in section 4.2 to analyze the properties of the $n = 7$ multiplet of a hydrogen atom interacting with the vacuum fields supported by a spheroidal prolate AlN nanoparticle. With these choices, we were able to ensure proper matching of energy scales and bring out specific effects due to the vacuum-field induced atomic interactions. Besides, the symmetric spatial arrangement of the system allowed for great simplifications; in fact, the final simulations only required the diagonalization of 7×7 effective Hamiltonians. Regarding the eigenvalues, we analyzed the real and imaginary parts separately, which correspond to the energies and widths of the spectral lines, respectively, as a function of the atom-nanoparticle separation. The energies display marked avoided crossings, a clear signature of the off-diagonal couplings, while the decay rates actually cross each other. Additionally, one of the decay rates managed to go against the naive expectation of Purcell enhancement, decreasing as the atom approaches the nanoparticle. This subradiant or protected state is a direct consequence of the particular material and geometrical features of the nanoparticle, as explained at the end of section 4.3.1.

The spectral features obtained from the eigenvalues of the effective non-Hermitian Hamiltonians strongly hint at the role that several fine-structure states must play in building the new eigenstates. This has been made more apparent in section 4.3.2, where we have defined the participation ratio as a way to measure the amount of fine-structure states that significantly contribute to a given eigenstate. Our results show that the original hydrogenic states become very well mixed due to the presence of the nanoparticle. From the perspective of atomic physics, it can be said that the hydrogen atom treated here becomes practically "unrecognizable", since the atomic structure and spectroscopic properties within each Bohr level dramatically change. Most strikingly, these effects start occurring at atom-nanoparticle separations of the order of 100 nm, well within experimental reality. Therefore, we are not merely dealing with a hypothetical effect that is expected to disappear as soon as realistic parameters are used.

The static analysis of the eigenvalue problem of the effective Hamiltonian presented in section 4.3 has concrete dynamical implications. Namely,

the temporal evolution of a hydrogen atom initially prepared in some fine-structure eigenstate will display marked Rabi-like oscillations, similar to those characteristic of the SC regime. However, unlike the SC regime between light and matter, the atom is here essentially an independent entity, with the SC-like effects induced by its weak coupling to the EM environment. We are, thus, led to the term "strong weak coupling" to label the particular regime described here. Another property of the dynamics is that, for appropriate parameters, the Rabi-like oscillations last up to 20 times longer than naively expected, due to the appearance of the subradiant state discussed above.

Finally, we note that, while we treat a specific scenario here for concreteness, the framework developed in section 4.3 is straightforwardly applicable to other nanostructures [224]. The emitters are also not limited to hydrogen, although some simplifying considerations made here might take a different quantitative form. One particularly relevant platform to study these effects would be to take advantage of the small energy splittings of the hyperfine structure of Rydberg atoms [275, 276]. Our work thus extends the regime where vacuum-field-induced shifts and decay rates are properly described and may lead to new strategies for developing quantum state manipulation platforms based on off-diagonal vacuum-induced effects.

Relation to other work In the interest of thoroughness, we note that similar effects have been reported in the literature. For example, in [277] an effective Hamiltonian is derived to account for the van der Waals interaction between two Rydberg atoms. There, state degeneracy plays a key role in accurately describing the system. A similar system is considered in [276], where the addition of a perfectly conducting half space modifies the interaction between the atoms. In those cases, the two-atom states develop additional, environment-induced interactions, whereas our work shows that these interactions can arise at the single-atom level. Another related work is [278], where a strong coupling approach to CP physics is used to study the mixing of states with different number of photons [195, 279]. As mentioned before, our work is far from the SC regime, and the main effects of this chapter are due to second order processes whereby virtual photons are emitted and absorbed. The last work that deserves mention in this paragraph is [280]. This one is conceptually closer to our approach, with the differences lying more so in the methodological aspects than in the physics. In this regard, our OQS approach seamlessly incorporates the dissipative effects, and the macroscopic structure used here is more realistically described and allows us to find surprising illustrations of the relevance of the off-diagonal couplings.

Chapter Five | There is no ultrastrong coupling with photons

> Things are often not what they seem. And then, sometimes they are. The trick is to learn what is real.
>
> *Thomas Lloyd Qualls*

Chapter summary In this chapter, we switch from the weak coupling regime of light-matter interactions to the ultrastrong coupling (USC) regime. We begin by revisiting the phenomenology usually attributed to USC physics, focusing on how the simplest model of quantized light-matter interactions, the Jaynes-Cummings model, fails to reproduce it. Instead, the slightly more general Rabi model is required to account for the USC regime. We then introduce the context of our work, namely, whether the USC regime is reached through the interaction with photons or through the Coulomb interaction between charges. To answer this question, we use a general argument to derive a bound on the emitter-photon coupling strength, under idealized circumstances that are more optimistic than what can realistically be achieved in experiments. Applied to the USC regime in cavities, the bound implies that photons cannot be responsible for achieving this regime and, in fact, that they have a negligible effect. Coulomb interactions are the only ones able to create the conditions for USC phenomena. As a corollary, through these results we shed light on the role of the PSE term in the multipolar coupling Hamiltonian. It turns out that if the USC regime is reached through direct charge-charge interactions, as in subwavelength cavities, the PSE plays no meaningful role in the actual dynamics. We end the chapter with a concrete illustration of these ideas, by solving a simple model for which we derive analytical expressions. Finally, we see how these closed formulas encapsulate the messages from the general argument.

5.1 Introduction

Without human design, the interaction between small quantum systems (from now on, quantum emitters) and the EM field is relatively weak, as summarized by the fine-structure constant, $\alpha \approx \frac{1}{137}$. As mentioned in section 1.1, this weak-coupling limitation can be remedied by surrounding the quantum emitters with some macroscopic structure that can "herd" photons and force them to interact more strongly with the emitter [15]. The conception and practical realization of such enhanced-coupling scenarios gave birth to the field of cavity QED, whose development bore the fruit of the strong coupling (SC) regime, in the 1980s and 1990s, and, more recently, the USC regime. In this first part, we are going to revisit the theoretical aspects of the USC description (section 5.1.1), and then explain the concrete context that this chapter addresses in section 5.1.2.

5.1.1 A tale of two models

Historically, two simple models have proved extremely effective in condensing the complexity of light-matter interactions: the Rabi and Jaynes-Cummings models. In fact, their usefulness throughout the exploration of the SC regime can hardly be overstated. The Rabi model describes a 2LA, with states $|g\rangle$ and $|e\rangle$, coupled to a single bosonic cavity mode, a, according to

In this part there is no explicit diamagnetic term, although it often appears in the discussion of the USC regime. The reason is that, as we will see in section 5.1.2, it can be removed through a Bogoliubov transformation that brings us to this Rabi Hamiltonian.

$$H_{\mathrm{R}} = \hbar\omega_{\mathrm{e}}|e\rangle\langle e| + \hbar\omega_{\mathrm{c}}a^{\dagger}a - \hbar g(|e\rangle\langle g| + |g\rangle\langle e|)(a^{\dagger} + a). \tag{5.1}$$

Here, $\hbar\omega_{\mathrm{e}}$ and $\hbar\omega_{\mathrm{c}}$ are the energies of the 2LA and the cavity mode, assumed to be close to each other, and g measures the interaction strength. The Jaynes-Cummings model is straightforwardly derived from eq. (5.1) by applying the RWA to the interaction term:

$$H_{\mathrm{JC}} = \hbar\omega_{\mathrm{e}}|e\rangle\langle e| + \hbar\omega_{\mathrm{c}}a^{\dagger}a - \hbar g\big(|e\rangle\langle g|a + |g\rangle\langle e|a^{\dagger}\big). \tag{5.2}$$

Note that Ref. [168] obtains a Jaynes-Cummings model through a unitary transformation rather than the RWA, which has been shown to be accurate in the USC as well.

In practice, we have neglected the so-called counter-rotating terms that simultaneously create or destroy a cavity and emitter excitation. To understand when the Jaynes-Cummings model is justified, we note that H_{JC} splits the Hilbert space in uncoupled subspaces labelled by the total number of excitations

$$\mathcal{H} = \bigoplus_{n} \mathcal{H}_n, \tag{5.3}$$

where $\mathcal{H}_n = \{|g,n\rangle, |e,n-1\rangle\}$. The counter-rotating terms, in turn, connect $\mathcal{H}_n$ with $\mathcal{H}_{n\pm2}$. In matrix notation, the Jaynes-Cummings Hamiltonian is a block diagonal matrix, whereas the Rabi Hamiltonian looks schematically like

$$H_{\mathrm{R}} = \begin{pmatrix} \ddots & 0 & \ddots & 0 & 0 \\ 0 & n-1 & 0 & \hbar g_{n-1,n+1} & 0 \\ \ddots & 0 & n & 0 & \ddots \\ 0 & \hbar g_{n+1,n-1} & 0 & n+1 & 0 \\ 0 & 0 & \ddots & 0 & \ddots \end{pmatrix}.$$

Hence, it is clear that the RWA approximation will be valid as long as the coupling between any pair of subspaces is much smaller than the energy difference between them. In the single-excitation subspace, the condition becomes $\frac{g}{\omega_{\mathrm{e}}+\omega_{\mathrm{c}}} \ll 1$. As long as it holds, the RWA works and the Jaynes-Cummings model suffices. Then, the dynamics is best described in terms of simple light-matter eigenstates

$$\begin{cases} |g,0\rangle (\text{ground state}) & \text{for } n=0 \quad \text{and} \\ |\psi_{n_\pm}\rangle = \alpha_{n_\pm}|g,n\rangle + \beta_{n_\pm}|e,n-1\rangle & \text{for } n>0 \end{cases} \tag{5.4}$$

with eigenvalues $H_{\mathrm{JC}}|g,0\rangle = 0$ and $H_{\mathrm{JC}}|\psi_{n_\pm}\rangle = E_{n_\pm}|\psi_{n_\pm}\rangle$. Of course, the coefficients $\alpha_{n_\pm}$ and $\beta_{n_\pm}$ depend on the values of the parameters. As a first approximation, dissipation can be accounted for with Lindblad dissipators of the form $\sqrt{\kappa_{\mathrm{c}}}\mathcal{D}_{a,a}[\rho_{\mathrm{s}}]$ and $\sqrt{\kappa_{\mathrm{e}}}\mathcal{D}_{|e\rangle\langle g|,|e\rangle\langle g|}[\rho_{\mathrm{s}}]$. Thus, two effects are at play. On one hand, if the initial state is not a polaritonic eigenstate, the misalignment between the uncoupled basis states $|g,n\rangle$ and $|e,n-1\rangle$ and the true eigenstates $|\psi_{n_\pm}\rangle$ gives rise to Rabi oscillations where the population flows back and forth between $|g,n\rangle$ and $|e,n-1\rangle$. On the other, these oscillations are damped due to the dissipative effect of the Lindblad terms. When the Rabi frequency is large enough that at least one oscillation can be distinguished before succumbing to the losses, then we say that the SC regime has been reached. With this, we have shown that the Jaynes-Cummings model can be very adequately applied to the SC regime, which explains why it was the theoretical backbone of much of cavity QED's development. Indeed, manufacturing cavities with larger and larger quality factors, i.e., lower and lower losses, made it possible to observe SC-related phenomena without needing to increase g beyond the applicability range of the RWA.

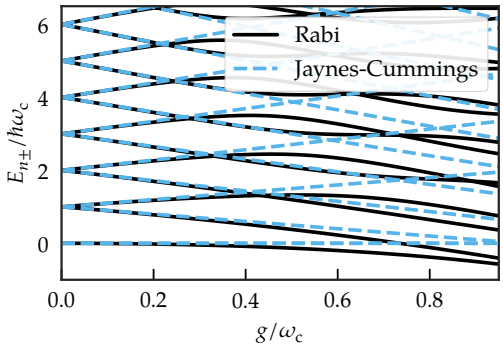

Figure 5.1: Energy spectrum of the Rabi and Jaynes-Cummings models, as a function of the coupling strength g. In this figure, the 2LA and the cavity mode are on resonance, that is, $\omega_e = \omega_c$, and up to 20 cavity excitations have been included.

When the light-matter interaction strength g becomes a significant fraction of $\omega_e \sim \omega_c$, customarily described as $\eta_{USC} = \frac{g}{\omega_e} \sim 0.1$, the counter-rotating terms begin to play a non-negligible role. The energy spectra presented in fig. 5.1 highlight the difference between the predictions of both models for a 2LA on resonance with the bosonic cavity excitations ($\omega_e = \omega_c$). With these conditions, the Jaynes-Cummings eigenenergies are straight lines given by $E_{n\pm} = n\hbar\omega_c \pm \sqrt{n}\hbar g$, while their Rabi counterparts bend due to the phenomenon of "level repulsion" or "avoided crossing". In particular, from the lines starting at 1, we see that the Rabi model predicts an asymmetric splitting, in contrast to the symmetry of the Jaynes-Cummings lines. Furthermore, the energy of the ground state is unchanged by the Jaynes-Cummings Hamiltonian, while the Rabi Hamiltonian predicts a negative shift, also known as the Bloch-Siegert shift, approximately given by

To be precise, the crossing of lines in the spectrum of H_{JC} implies that its true ground state experiences jumps in the excitation number. The first such jump occurs at $g = \omega_c$. Still, this only happens when H_{JC} is not physically meaningful anymore.

$$\Delta_{gs} = -\hbar\frac{g^2}{\omega_c + \omega_e}. \tag{5.5}$$

This is one of the prototypical examples of an effect beyond the RWA, that can only be described by correctly including the counter-rotating couplings. An important, but often overlooked, remark is that most of the phenomena usually associated to the USC regime are not at all resonant effects, unlike the SC regime, which accentuates the fundamental difference between the two. The denominator in the Bloch-Siegert shift is a direct illustration thereof, as the sum of frequencies appears, rather than the difference.

Indeed, if the mode and emitter are far off-resonant, the comparison between Δ_{gs} and ω_e is a more meaningful measure of the size of USC effects on the emitter than η_{USC}.

We can keep digging into ground-state-related phenomena by looking at the state itself. In the Jaynes-Cummings model, the ground state is simply $|gs_{JC}\rangle = |g, 0\rangle$. Meanwhile, just like the ground-state energy changes in the Rabi model, the ground state is also modified [52]. Because H_R preserves the

parity of the excitation number, the new ground state becomes of the form

$$|\mathrm{gs}_\mathrm{R}\rangle = \sum_n \alpha_{2n}|g, 2n\rangle + \sum_n \beta_{2n+1}|e, 2n+1\rangle. \tag{5.6}$$

The size of these coefficients depends on the coupling strength as shown in fig. 5.2. As expected, the odd excitation-number subspaces do not contribute, hence the black rows. Meanwhile, we notice that, the larger the coupling strength becomes, the more states become noticeably involved. A striking consequence is that the Rabi model's ground state includes what one would typically consider excited states and cavity photons, which is another hallmark of the USC regime. The conceptual resolution to this apparent conundrum is that the individual emitter and cavity excitations are no longer a good basis with which the full solutions can be easily expanded. Instead, the emitter and cavity cannot be effectively disentangled and put in intuitive terms in the USC regime. Actually, this is merely a mathematical consequence of the counter-rotating terms, regardless of the coupling strength. Of course, for sufficiently small values of g the effects of the counter-rotating terms are negligible, and the whole dynamics can be understood through the more intuitive and simpler co-rotating terms only. Besides, the mathematical solution to the Jaynes-Cummings model is almost trivial. However, the trade-off for the improved understanding of the Jaynes-Cumming model is that much of the real physics described by the Rabi Hamiltonian is swept under the rug. In the USC, when the simplified picture is no longer enough, one is irremediably forced to face the full consequences of the counter-rotating terms. Then, the presence of excitations, specifically photons, in the ground state has led physicists to propose mechanisms to observe them [55, 281–283]. The idea is to swiftly change the system's parameters, such that the USC ground state relaxes to the new ground state, with a lower photon content. Another consequence of the photons in the USC ground state is that a simple Lindblad dissipator of the form $\sqrt{\kappa_\mathrm{c}}\mathcal{D}_{a,a}[\rho_\mathrm{s}]$ is no longer valid, as it predicts ground state dissipation even without any rapid modification of the parameters. There are several ways to correct the treatment of dissipation in the USC [165–167], but, in all cases, a step back has to be taken to gain a better view of the problem. The newly acquired perspective, then, grants a deeper understanding that reveals a fix to the issue.

The above paragraphs illustrate the risk of extending a simplified model (Jaynes-Cummings) beyond its applicability range. The only effective approach in that respect is to resort back to the more complete model (Rabi). Then, it may be possible to explore the physics of the full model to understand the differences. If that proves challenging, perhaps a more sophisticated

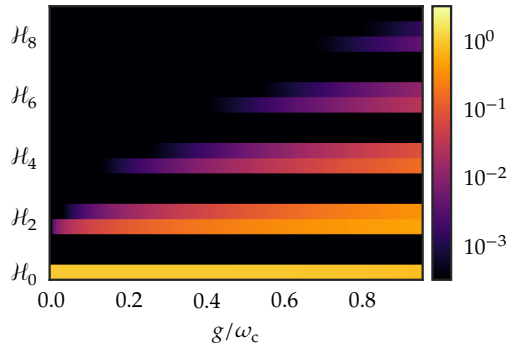

Figure 5.2: Modulus of the ground-state coefficients in eq. (5.6) for the Rabi model Hamiltonian as a function of the coupling strength in a logarithmic scale. In this figure, $\omega_e = \omega_c$, and up to 20 cavity excitations have been included. The black rows correspond to odd excitation-number subspaces, while colored lines indicate the coefficients from even excitation-number subspaces.

perturbative approach, based on, e.g., a Schrieffer-Wolff transformation, can reveal the new effects missing from the original simplified model, as done in the Bloch-Siegert Hamiltonian derived in [70, 165, 284]. The same happened when including dissipation in these models, as its correct treatment in the USC required taking a step back before moving forward. This is, in summary, the spirit of this chapter. We will next describe more concretely the theoretical question that we address, and the context in which it arises.

5.1.2 Photons or charges?

So far in this thesis, we have described the interaction between matter and light excitations. To that end, we have generally needed to start from the full light-matter Hamiltonian, and then applied some perturbative scheme. With this approach, we have been able to reach effective models with dynamical implications that a direct use of a simple model would have missed. With this sentence, we want to emphasize the importance of starting derivations from the appropriate place. Consider the classical scenario of cavity QED: an atom located between two mirrors that reflect photons back and forth. As a first approximation, one can assume that the mirrors impose hard boundary conditions on the electromagnetic field, which restricts the possible photon energies that can exist within them. Accordingly, the atom can only interact with those allowed photonic cavity modes. Assuming that one mode is very close to resonance with an atomic dipolar transition oriented along the z direction, we can discard the other photonic modes and the states that do not participate in the specific transition, thus keeping only $|g\rangle$ and $|e\rangle$. Then, in the long-wavelength approximation, the interaction between the transition and the cavity photon is essentially given by the Rabi model of eq. (5.1), or the Jaynes-Cummings

model if the RWA is applicable. In more detail,

$$\hat{\mathbf{z}} \cdot \mathbf{A}^{\perp}(\mathbf{r}_{\mathrm{at}}) = \sqrt{\frac{\hbar}{2\varepsilon_0 \omega_{\mathrm{c}} V}}\left(a^{\dagger} + a\right) = A_0\left(a^{\dagger} + a\right), \tag{5.7a}$$

where V is the quantization volume. Hence, the minimal coupling Hamiltonian is

$$H = \hbar\omega_{\mathrm{at}}|e\rangle\langle e| + \hbar\omega_{\mathrm{c}} a^{\dagger}a - \frac{q}{m} p_z A_0\left(a^{\dagger} + a\right) + \frac{q^2 A_0^2}{2m}\left(a^{\dagger} + a\right)^2. \tag{5.7b}$$

Through a Bogoliubov transformation of the bosonic operator, the Hamiltonian can be rewritten as [285]

$$H = \hbar\omega_{\mathrm{at}}|e\rangle\langle e| + \hbar\tilde{\omega}_{\mathrm{c}} c^{\dagger}c - \frac{q}{m} p_{z,eg} A_0 \sqrt{\frac{\omega_{\mathrm{c}}}{\tilde{\omega}_{\mathrm{c}}}}\left(|e\rangle\langle g| + |g\rangle\langle e|\right)\left(c^{\dagger} + c\right), \tag{5.7c}$$

where $\tilde{\omega}_{\mathrm{c}}^2 = \omega_{\mathrm{c}}^2 + \frac{2q^2 A_0^2 \omega_{\mathrm{c}}}{\hbar m}$ and $c^{\dagger} + c = \sqrt{\frac{\tilde{\omega}_{\mathrm{c}}}{\omega_{\mathrm{c}}}}\left(a^{\dagger} + a\right)$. Indeed, as we just mentioned, this is a Rabi model. Notice that the physical interpretation of all operators is clear: $|g\rangle\langle e|$ is an atomic lowering operator, and, more importantly, a annihilates cavity photons. Indeed, these cavity photons are really photons in the sense that they correspond to excitations of the transverse, propagating EM field, summarized in $\mathbf{A}^{\perp}$. The only real difference with free-space photons is that they are confined between the mirrors. Last, the bosonic c operator introduced to reach the Rabi-form of the Hamiltonian still represents a purely photonic degree of freedom, and just serves to remove the explicit A^2 contribution.

There is another way to look at this simplified light-matter interaction from which a Rabi model can also be extracted. In the spirit of section 2.1.2, we again start from eq. (5.7b) and apply a simplified version of the PZW unitary transformation $T = \exp\left[-\frac{i}{\hbar} q z A_0\left(a^{\dagger} + a\right)\right]$ to reach the multipolar coupling Hamiltonian:

$$\tilde{H} = \hbar\omega_{\mathrm{at}}|e\rangle\langle e| + \frac{q^2 A_0^2 \omega_{\mathrm{c}}}{\hbar} z^2 + \hbar\omega_{\mathrm{c}} a^{\dagger}a + iqz\omega_{\mathrm{c}} A_0\left(a^{\dagger} - a\right). \tag{5.8a}$$

Comparing eqs. (5.7b) and (5.8a), it becomes clear that we have replaced the A^2 term with a z^2 term. Now, to cast $\tilde{H}$ as a Rabi Hamiltonian we must first diagonalize the new atomic Hamiltonian, including the z^2 contribution, also known as dipole self-energy (DSE). As a result, a new excited eigenstate $|\tilde{e}\rangle$ emerges, with associated energy $\hbar\tilde{\omega}_{\mathrm{at}}$. Second, we have to rotate the a opera-

tors defining $\tilde{c} = ia$. Thus, we arrive at

$$\tilde{H} = \hbar\tilde{\omega}_{\mathrm{at}}|\tilde{e}\rangle\langle\tilde{e}| + \hbar\omega_{\mathrm{c}}\tilde{c}^{\dagger}\tilde{c} - qz\omega_{\mathrm{c}}A_0\big(\tilde{c}^{\dagger} + \tilde{c}\big), \tag{5.8b}$$

which, as anticipated, is a Rabi model.

In the previous paragraphs, we have seen that the atom-cavity interaction in the single-transition and single-mode approximations can be written as a Rabi model in both the minimal and multipolar coupling pictures. Accordingly, the Rabi model's versatility and simplicity have turned it into a cornerstone in the study of ultrastrongly coupled light-matter systems. However, an important consequence thereof is that the theoretical subtleties of light-matter interactions manifest in the Rabi model in ways that can go unnoticed to the untrained eye. For example, in eqs. (5.7b) and (5.7c), a, and later c, represent a purely photonic quantity, while the same is not true for a and $\tilde{c}$ in eqs. (5.8a) and (5.8b). Explicitly, we have

$$\hat{\mathbf{z}}\cdot\mathbf{A}^{\perp} = A_0\big(a^{\dagger} + a\big) \quad \text{and} \tag{5.9a}$$

$$\hat{\mathbf{z}}\cdot\mathbf{E}^{\perp} = -\hat{\mathbf{z}}\cdot\dot{\mathbf{A}}^{\perp} = -A_0\big(\dot{a}^{\dagger} + \dot{a}\big). \tag{5.9b}$$

In the minimal coupling picture,

$$\dot{a} = \frac{i}{\hbar}[H, a] = -i\omega_{\mathrm{c}}a + i\frac{qA_0}{m}\big(p_z - q\hat{\mathbf{z}}\cdot\mathbf{A}^{\perp}\big) \tag{5.10a}$$

and, thus,

$$\hat{\mathbf{z}}\cdot\mathbf{E}^{\perp} = -i\sqrt{\frac{\hbar\omega_c}{2\varepsilon_0 V}}\big(a^{\dagger} - a\big). \tag{5.10b}$$

Essentially, the vector potential and electric field are the quadratures of the a mode in the minimal coupling picture. In the multipolar coupling picture, however, things work out differently:

$$\dot{a} = \frac{i}{\hbar}\big[\tilde{H}, a\big] = -i\omega_{\mathrm{c}}a + \frac{\omega_{\mathrm{c}}A_0}{\hbar}qz \tag{5.11a}$$

and

$$\hat{\mathbf{z}}\cdot\left(\mathbf{E}^{\perp} + \frac{\mathbf{P}^{\perp}_{\mathrm{at}}}{\varepsilon_0}\right) = \frac{\hat{\mathbf{z}}\cdot\mathbf{D}^{\perp}}{\varepsilon_0} = -i\sqrt{\frac{\hbar\omega_{\mathrm{c}}}{2\varepsilon_0 V}}\big(a^{\dagger} - a\big) = \hat{\mathbf{z}}\cdot\mathbf{E}^{\perp} + \frac{qz}{\varepsilon_0 V}. \tag{5.11b}$$

That is to say, the field quadratures of a now include the displacement field, which incorporates the emitter through its polarization. In other words, while a (c) annihilates purely photonic excitations in the minimal coupling picture, the role of a ($\tilde{c}$) in the multipolar coupling picture is to annihilate mixed

emitter-photon excitations, even if it "looks" and "quacks" like the purely photonic cavity mode from the minimal coupling picture [286].

Note that these mixed excitations are not the polaritons that arise in the SC regime, but merely an artifact of the way the interaction is described. The same happens in the minimal coupling picture, where p_z does not correspond to an emitter-only quantity. See the opening remark in section 2.1.2.

With the very simple example above, we have seen that the same mathematical model can, in principle, describe different kinds of situations. Accordingly, it would be risky to directly start from the Rabi model without precisely specifying what each operator physically corresponds to. Again within the confines of the example, one could miss the photon frequency renormalization in eq. (5.7c) or the DSE correction in eq. (5.8b), leading to incorrect interpretations of experimental results. This is just one of the ways in which care must be taken when dealing with the description of light-matter systems, but, in general, many problems can arise when starting the theoretical discussion from too simplified models. Such circumstances have fueled plenty of works arguing for or against certain effects. For instance, the generalization of the Rabi model to N 2LAs, known as the Dicke model, predicts a superradiant phase transition in the USC regime, whereby the emitters radiate coherently and see an enhancement factor of $\sqrt{N}$ compared to the incoherent case [287, 288]. Shortly after that prediction, it was argued in [289] that the A^2 term precludes the existence of a superradiant phase. The debate was revitalized when the USC regime became accessible, which led to more works on the topic [192, 290–294] aimed at clarifying the ideas.

Another notable illustration of the problems derived from a hasty theoretical approach is found in the discussions concerning gauge ambiguities and consistency. In that regard, it was realized that the finite level truncation of the atomic Hilbert space brought with it an unfortunate consequence: gauge invariance was no longer a property of the simplified models [285]. Later, more detailed approaches were proposed to resolve the issue, again highlighting the importance of having a sufficiently nuanced perspective [168–170]. These examples capture the overall soul of the chapter, namely, that reaching conceptual clarity tends to demand a careful, "from-the-beginning" treatment.

After this momentary detour, we are ready to address the admittedly intriguing title of the chapter. So far, we have talked about debates arising from the use of simplified models beyond their range of validity. Here, we focus on shedding light on the role of longitudinal and transverse fields in the USC regime. While both are generally present, in practice the concrete experimental scenario considered can imply that one kind dominates over the other. For instance, in the classical Fabry-Pérot microcavity configuration, depicted in fig. 5.3a, the emitter is relatively far from the mirrors. Thus, the emitter is appreciably coupled to the photonic cavity modes confined between the mirrors, but does not directly feel in any significant way the charges that fundamentally

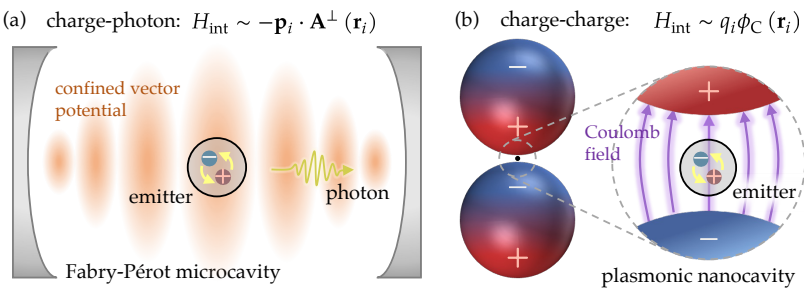

Figure 5.3: Sketches of the relevant limits of QED. (a) Fabry-Pérot microcavity where the longitudinal Coulomb interaction between the mirrors and the emitter is neglected. (b) Plasmonic nanocavity formed in the gap between two metallic nanoparticles, where the effect of the transverse fields is discarded.

build up the mirror. Hence, in the "microcavity description", the longitudinal interaction between the mirrors and the emitter can be discarded altogether, and a Hamiltonian like the one in eq. (5.7c) is recovered. Meanwhile, if the coupling strength is increased through the confinement of EM fields in subwavelength volumes, the emitters are necessarily much closer to the structure that forms the cavity. Such is the case in plasmonic nanocavities [175, 176, 181, 295, 296], as the one sketched in fig. 5.3b, or THz resonators [71, 297]. Then, the physics of the EM fields is, for all intents and purposes, quasistatic, meaning that the transverse, propagating fields have a negligible influence over the emitter. In those scenarios, the direct longitudinal interaction between the charges in the emitter and nanostructure arises as the main interaction mechanism, and a Hamiltonian like that in eq. (5.8b) can be found, albeit without the polarization self-energy term. Along these lines, we remark here that the difference between these situations is not just a matter of nomenclature. It does have very tangible consequences in the theoretical description, namely, some terms in the Hamiltonian are more relevant than others depending on the underlying physical reality [178, 179, 181, 291, 298]. An important example that will be explained in the section is the role of the polarization self-energy.

With the context provided above, the claim in the chapter's title is to be understood as meaning that USC can only arise from the longitudinal fields rather than from the transverse ones. We have already hinted at it, but we emphasize here that, by photons, we mean the excitations of the true dynamical variables of the pure EM field, i.e., the divergence-free (transverse) component $\mathbf{E}^{\perp}$. The curl-free (longitudinal) part $\mathbf{E}^{\parallel}$ has no dynamics of its own, and is merely an instantaneous function of the charges themselves through Gauss' law for the electric field written in eq. (2.1a). Hence, there is no ultrastrong

coupling with photons, which is instead reached through the direct longitudinal interaction between charges. To finish the chapter's introduction, we cannot in good faith avoid acknowledging that the direct charge-charge interaction can be thought of as resulting from the exchange of "longitudinal" and "scalar" photons. Indeed, if one quantizes the theory starting from the Lorentz gauge [14], the Coulomb interaction is not explicit, and instead these unphysical photons are effectively a reparametrization of the Coulomb interaction, but still do not represent true dynamical degrees of freedom. The resulting theory suffers from added complications that, of course, can be dealt with. Still, we dodge those difficulties and eliminate the unphysical photons from the start.

In the following, we revisit the main ingredients of non-relaticistic QED and, with them, provide a general argument that fundamentally limits the coupling strength between small emitters and photons. As a direct corollary, we find that the USC regime can only be reached through the direct charge-charge interactions, which has further consequences on terms as contentious as the polarization self-energy. Finally, we illustrate the rather abstract arguments with an analytically solvable example where the charge-charge and charge-photon interactions are simple to keep apart, and that still contains the relevant physics.

5.2 Fundamental bound on the emitter-photon coupling strength

We start here from the general picture of non-relativistic QED, as a theory of charges and photons, and prepare the expressions in the most convenient way for the argument that sets a limit to the coupling strength between photons and atoms. Finally, we apply this argument to the USC regime and derive further consequences. Note that, purposefully, we do not invoke macroscopic QED in order to show explicitly that the bounds we obtain are not a consequence of any assumptions or approximations in that theory.

5.2.1 Reminder of non-relativistic QED

The minimal coupling Hamiltonian is written in eq. (2.15) in the Coulomb gauge, but is reproduced here for reading ease:

$$H = \sum_i \frac{\mathbf{p}_i^2}{2m_i} + \sum_{i\neq j} \frac{q_i q_j}{8\pi\varepsilon_0 |\mathbf{r}_i - \mathbf{r}_j|} + \int \mathrm{d}^3 r \left[\frac{(-\varepsilon_0 \mathbf{E}^\perp)}{2\varepsilon_0} + \frac{\varepsilon_0 c^2}{2} (\nabla \times \mathbf{A}^\perp)^2 \right]$$

$$-\sum_i \frac{q_i}{m_i}\mathbf{p}_i\cdot\mathbf{A}^\perp(\mathbf{r}_i)+\sum_i\frac{q_i^2}{2m_i}\big(\mathbf{A}^\perp(\mathbf{r}_i)\big)^2. \tag{5.12}$$

Here the charges q_i are described through their positions $\mathbf{r}_i$ and canonical momenta $\mathbf{p}_i$, and photons are the excitations of the pure EM field position $\mathbf{A}^\perp$ and momentum $\mathbf{\Pi}^\perp=-\varepsilon_0\mathbf{E}^\perp$. In this formulation, the charges and photons interact with each other through the $\mathbf{p}_i\cdot\mathbf{A}^\perp$ term, and an additional $\big(\mathbf{A}^\perp\big)^2$ term appears that can be seen as a kind of photon-photon interaction mediated by the charges. The $\mathbf{E}^\parallel$ field is hidden in the second term, which can be rewritten as

$$\sum_{i\neq j}\frac{q_iq_j}{8\pi\varepsilon_0\big|\mathbf{r}_i-\mathbf{r}_j\big|}=\int \mathrm{d}^3r\,\rho\phi_\mathrm{C}-\mathcal{E}_\mathrm{C}=-\int\mathrm{d}^3r\,\mathbf{P}_\mathrm{c}^\parallel\cdot\mathbf{E}^\parallel-\mathcal{E}_\mathrm{C}, \tag{5.13}$$

where ϕ_C is the Coulomb scalar potential given in eq. (2.9), and the charge density $\rho=\sum_i q_i\delta^{(3)}(\mathbf{r}-\mathbf{r}_i)$. Integration by parts yields the second equality, with the longitudinal polarization field $\mathbf{P}_\mathrm{c}^\parallel$ completely determined by $\nabla\cdot\mathbf{P}_\mathrm{c}^\parallel=-\rho$. As for the constant $\mathcal{E}_\mathrm{C}$, it corresponds to the Coulomb self-energy that comes from setting $i=j$ in the Coulomb interaction. For point charges, $\mathcal{E}_\mathrm{C}$ is a formally divergent quantity that plays no role in the dynamics and will not be mentioned again. We start from this formulation, minimal coupling in the Coulomb gauge, because it is the one where the field variables ($\mathbf{A}^\perp$ and $\mathbf{E}^\perp$) are most directly related to the physical (transverse) photons.

We next particularize the system of charges to the situation in which it can be naturally split into one or more emitters and a nanostructure or cavity, as represented in fig. 5.4. According to eq. (5.12), the emitter and nanostructure will interact with each other through the longitudinal fields, and photons couple to both the emitter and nanostructure. Now, we narrow our attention to the emitter, whose interaction with the rest of the systems is the sum of the emitter-structure ($\mathrm{e}-\mathrm{s}$) and emitter-field ($\mathrm{e}-\mathrm{f}$) interaction Hamiltonians:

$$H_{\mathrm{e}-\mathrm{s}}+H_{\mathrm{e}-\mathrm{f}}=-\int\mathrm{d}^3r\,\mathbf{P}_\mathrm{e}^\parallel\cdot\mathbf{E}_\mathrm{s}^\parallel-\sum_{i\in C_\mathrm{e}}\frac{q_i}{m_i}\mathbf{p}_i\cdot\mathbf{A}^\perp(\mathbf{r}_i). \tag{5.14}$$

Here, $\mathbf{P}_\mathrm{e}$ is the emitter's polarization, $\mathbf{E}_\mathrm{s}^\parallel$ is the structure's longitudinal field, and the set C_e in the sum restricts the index i to the charges in the emitter. The advantage of the formulation chosen is made evident by eq. (5.14), since the longitudinal and transverse interactions are given by two independent terms in the Hamiltonian. As mentioned in the last paragraphs of section 2.1.2, this is not always guaranteed to occur (as it happens with the multicenter PZW transformation). We can make further progress by focusing on the transverse in-

teraction and expanding the transverse vector potential in terms of free-space photonic modes, as explained in section 2.1.3,

$$\mathbf{A}^{\perp} = \sum_{\lambda} A_{\lambda} \boldsymbol{\psi}_{\lambda}, \tag{5.15}$$

where λ is an abstract, generally continuous mode index. The mode functions $\boldsymbol{\psi}_{\lambda}$, which are chosen real for notational convenience, form an orthogonal and complete basis of the space of transverse vector fields. We also normalize them according to

$$\int \mathrm{d}^3 r \, \boldsymbol{\psi}_{\lambda} \cdot \boldsymbol{\psi}_{\lambda'} = \delta_{\lambda\lambda'}. \tag{5.16}$$

The expansion coefficients A_{λ} are Hermitian photon mode operators given by

$$A_{\lambda} = \sqrt{\frac{\hbar}{2\varepsilon_0 \omega_{\lambda}}} \left(a_{\lambda}^{\dagger} + a_{\lambda}\right), \tag{5.17}$$

with $a_{\lambda}^{(\dagger)}$ annihilating (creating) photons in the mode labelled by λ. Hence, the transverse interaction term of the emitter is, in the long-wavelength approximation,

$$\begin{aligned} H_{\mathrm{e-f}} &= -\sum_{i \in C_{\mathrm{e}}} \sum_{\lambda} \frac{q_i}{m_i} A_{\lambda} \mathbf{p}_i \cdot \boldsymbol{\psi}_{\lambda}(\mathbf{r}_{\mathrm{e}}) \\ &= \hbar \sum_{t} \sum_{\lambda} i \frac{\omega_t}{\omega_{\lambda}} g_{\lambda}^{\perp,0} \left[(\mathbf{d}_t \cdot \hat{\mathbf{u}}_{\lambda}) \sigma_t - (\mathbf{d}_t \cdot \hat{\mathbf{u}}_{\lambda})^* \sigma_t^{\dagger} \right] \left(a_{\lambda}^{\dagger} + a_{\lambda}\right). \end{aligned} \tag{5.18}$$

To obtain the last expression, we have expanded the emitter momentum operator in lowering and raising transitions, σ_t and $\sigma_t^{\dagger}$, respectively, with associated positive frequency ω_t. Next, we have used the relation

$$\mathrm{Tr}\left(\sigma_t^{\dagger} \mathbf{p}_i\right) = -i\omega_t m_i \mathrm{Tr}\left(\sigma_t^{\dagger} \mathbf{r}_i\right), \tag{5.19}$$

which comes from evaluating matrix elements in $[H_{\mathrm{at}}, \mathbf{r}_i] = -i\hbar \frac{\mathbf{p}_i}{m_i}$, to bring out the emitter's dipole moment $\mathbf{d}$, with $\mathbf{d}_t = \mathrm{Tr}\left(\sigma_t^{\dagger} \mathbf{d}\right)$. Finally, $\hat{\mathbf{u}}_{\lambda}$ is the polarization unit vector of $\boldsymbol{\psi}_{\lambda}(\mathbf{r}_{\mathrm{e}})$, and we have defined the coupling strength to free-space photons as

$$g_{\lambda}^{\perp,0} = \sqrt{\frac{\omega_{\lambda}}{2\hbar\varepsilon_0}} |\boldsymbol{\psi}_{\lambda}(\mathbf{r}_{\mathrm{e}})|, \tag{5.20}$$

where $\mathbf{r}_{\mathrm{e}}$ is the emitter's position. We emphasize that the long-wavelength approximation, while not necessary for the argument, is done for simplicity and will be justified a posteriori.

In the presence of nanostructures, their interaction with the free-space modes alters the temporal evolution of the oscillators A_{λ}. Conversely, the

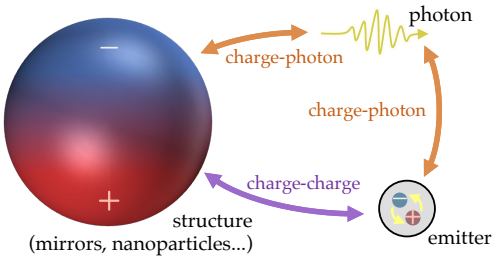

Figure 5.4: General scenario of a nanostructure and an emitter interacting with each other, through the Coulomb potential, and with photons, through the transverse EM fields.

nanostructure's charges themselves respond to the fields forming polarization currents. In the linear response regime, the behavior of these charges can be modeled through harmonic polarization oscillators. Accordingly, the interaction of the emitter with both the structure and the photons is most naturally thought of in terms of the joint photon-structure eigenmodes, from here on referred to as polaritonic eigenmodes. To that end, we formally diagonalize the photon-structure subsystem to find the polaritonic eigenmodes Σ_η with frequency ω_η. Introducing polaritonic annihilation and creation operators as

Note that the charges are not merely harmonic oscillators and, hence, the full response of the structure generally includes higher order terms. These non-linear terms, however, do not affect the polarization mode structure provided to us by the linear response.

$$\Sigma_\eta = \sqrt{\frac{\hbar}{2\varepsilon_0\omega_\eta}}\left(b_\eta^\dagger + b_\eta\right), \tag{5.21}$$

the emitter's transverse interaction reads

$$H_{\mathrm{e-f}} = \hbar\sum_t\sum_\eta i\frac{\omega_t}{\omega_\eta}g_\eta^\perp\left[\left(\mathbf{d}_t\cdot\hat{\mathbf{u}}_\eta\right)\sigma_t - \left(\mathbf{d}_t\cdot\hat{\mathbf{u}}_\eta\right)^*\sigma_t^\dagger\right]\left(b_\eta^\dagger + b_\eta\right), \tag{5.22}$$

which has the same form as eq. (5.18), but now the coupling strength function is

$$g_\eta^\perp\hat{\mathbf{u}}_\eta = \sum_\lambda\left(g_\lambda^{\perp,0}\hat{\mathbf{u}}_\lambda\right)M_{\lambda\eta} = \sqrt{\frac{\omega_\eta}{2\hbar\varepsilon_0}}\left|\sum_\lambda\sqrt{\frac{\omega_\eta}{\omega_\lambda}}M_{\lambda\eta}\boldsymbol{\psi}_\lambda(\mathbf{r}_\mathrm{e})\right|\hat{\mathbf{u}}_\eta, \tag{5.23}$$

and $\hat{\mathbf{u}}_\eta$ is a unit vector along the direction of $\sum_\lambda\sqrt{\frac{\omega_\eta}{\omega_\lambda}}M_{\lambda\eta}\boldsymbol{\psi}_\lambda(\mathbf{r}_\mathrm{e})$. The matrix $M_{\lambda\eta}$ arises from the diagonalization procedure, and implements the following Bogoliubov transformation:

$$a_\lambda^\dagger + a_\lambda = \sum_\eta M_{\lambda\eta}\left(b_\eta^\dagger + b_\eta\right). \tag{5.24}$$

Of course, $M_{\lambda\eta}$ is generally not easy to find. For reference, the MQED framework described in section 2.2 implements it through the $\mathbf{G}_\mathrm{e}$ and $\mathbf{G}_\mathrm{m}$ coefficients. Additionally, in section 5.3, we will solve a model where $M_{\lambda\eta}$ can be found analytically. Still, we can already provide a justification of the long-wavelength approximation. The new polaritonic modes b_η are combina-

tions of the photon modes a_λ, and the oscillators that model the response of the material structure. These material oscillators possess resonant frequencies in a given range, above which the structure cannot appreciable respond to photonic modes. Hence, above some frequency, the nanostructure and high-frequency photons do not hybridize efficiently, and, therefore, high-frequency polaritonic modes are essentially free-space photon modes. In terms of the transformation matrix, we have that $M_{\lambda\eta} \to \delta_{\lambda\eta}$ when $\omega_\lambda \big(= \omega_\eta\big)$ becomes sufficiently large. In the case of plasmonic particles, the relevant energy scale beyond which polaritons are merely photons is determined by interband transitions or, if we neglect them, by the metal's plasma frequency. The long-wavelength approximation, thus, will hold to describe the nanostructure-induced phenomena, which is the one of interest here, because we are interested in small emitters compared to the relevant wavelengths. As for the high-frequency photons, their correct treatment is known to account for minor corrections to the free-space Lamb shift, as briefly mentioned in section 2.4.1, and we discard such effects here.

The last step for our future purposes is to assign to each coupling strength function a transverse spectral density through

$$J_\nu^{\perp(,0)} = \sum_\mu \big(g_\mu^{\perp(,0)}\big)^2 \delta\big(\omega_\nu - \omega_\mu\big) \to J^{\perp(,0)}(\omega) = \sum_\mu \big(g_\mu^{\perp(,0)}\big)^2 \delta\big(\omega - \omega_\mu\big). \tag{5.25}$$

On the left, we have kept the abstract continuous-index notation with ν. However, throughout this chapter, it will sometimes be more "natural" to explicitly write these continuous indices in the usual continuous-function notation, as done on the right. We will use one or the other as appropriate. Thus defined, the spectral density is just an alternative way to characterize the transverse interaction strength to either the purely photonic $J^{\perp,0}$ or polaritonic $J^\perp$ modes. Indeed, in this context, the spectral density can be thought of as collecting the coupling strength to all modes with the same frequency, which are combined into a single interacting "bright" mode, with all orthogonal modes being uncoupled. This idea was also touched upon at the end of section 2.1.2. In addition, of course, the spectral density is also the main element that describes the environment in the theory of open quantum systems, as seen in section 2.4.

5.2.2 Derivation of the bound

After expressing the coupling strength in terms of spectral densities, we can obtain a bound to the total emitter-photon coupling strength. To do so, we use two basic EM constraints, such that the final result inherits a broad gener-

ality and validity. The first one, already mentioned while justifying the long-wavelength approximation, is that, at sufficiently high frequencies, any material becomes transparent to photons. The hybrid polaritonic modes will only differ from purely photonic modes below some "transparency" frequency scale, Ω_T. In terms of the spectral densities in eq. (5.25), this implies that

$$J_\nu^\perp \to J_\nu^{\perp,0} \quad \text{when} \quad \omega_\nu > \Omega_T. \tag{5.26a}$$

The second constraint can be derived from a Kramers-Kronig relation within the theory of electrodynamics [299]. Again expressed through the spectral density, the restriction is given by the following sum rule

$$\sum_\nu \frac{J_\nu^\perp - J_\nu^{\perp,0}}{J_\nu^{\perp,0}} \to \int_0^\infty \mathrm{d}\omega \, \frac{J^\perp(\omega) - J^{\perp,0}(\omega)}{J^{\perp,0}(\omega)} = 0, \tag{5.26b}$$

where the manifestly continous notation in the second equality emphasize the continuous nature of the index ν. In words, the sum rule implies that the transverse Purcell factor averages to 1, when integrated over a sufficiently broad frequency range. In [299], it had been shown for classical electromagnetism based on the properties of the dyadic Green's function. Therefore, the sum rule is directly applicable in the theory of macroscopic QED. In appendix E, however, we present an independent derivation within QED without resorting to arguments based on properties of the (classical) EM Green's function.

With these restrictions, we imagine, for the sake of the argument, the extreme case of a "perfect transverse cavity", that is, a cavity that concentrates the entire transverse coupling strength up to some transparency frequency Ω_T into a single, discrete "cavity" mode, resonant with some atomic transition t. The ensuing transverse spectral density is

$$J^\perp(\omega) = \left(G_t^\perp\right)^2 \delta(\omega - \omega_t) + J^{\perp,0}(\omega)\theta(\omega - \Omega_T), \tag{5.27}$$

where $G_t^\perp$ measures the coupling to the cavity mode with frequency ω_t, and θ is the unit step function that ensures that the first condition in eq. (5.26a) is fulfilled. Note that it also assumes a lossless cavity mode. Making it lossy would be achieved by replacing the Dirac delta function by a normalized Lorentzian line shape. This would not really modify the total coupling strength to the emitter, which is our primary concern here, while slightly complicating the final expressions. Introducing eq. (5.27) in eq. (5.25), the integral yields simply

$$G_t^\perp = \sqrt{\Omega_T J^{\perp,0}(\omega_t)} = \sqrt{\Omega_T \frac{\omega_t^3}{6\hbar\pi^2\varepsilon_0 c^3}}, \tag{5.28}$$

where $J_t^{\perp,0} = J^{\perp,0}(\omega_t)$ has been retrieved from eq. (2.66). Then, simply following the line of reasoning tells us that eq. (5.28) is an upper bound to the coupling enhancement that any kind of cavity can give rise to, and it is basically limited by the transparency frequency Ω_T and the relevant transition frequency ω_t.

5.2.3 Ultrastrong corollary

The total coupling strength to the idealized, discrete cavity mode includes the product of the dipole moment $|\mathbf{d}_t|$ and the cavity's transverse concentration factor $|G_t^{\perp}|$. With eq. (5.28), we have seen that two fundamental EM requirements constrain the size of $|G_t^{\perp}|$. We now invoke the Thomas-Reiche-Kuhn sum rule from eq. (2.117b) to find that

$$2|\mathbf{d}_t|^2\omega_t < \frac{\hbar e^2}{m_e}3n_e \implies |\mathbf{d}_t| < \sqrt{\frac{3\hbar e^2}{2m_e\omega_t}n_e}, \tag{5.29}$$

where e is the electron's charge, m_e is the electron's mass, and n_e is the number of electrons that participate in the transitions. Since we focus on small emitters, such as atoms or small molecules, $n_e \sim 1$. We finally put eqs. (5.28) and (5.29) together and arrive at an USC ratio equal to

$$\eta_{\text{USC}} = \frac{|\mathbf{d}_t|G_t^{\perp}}{\omega_t} < \sqrt{\frac{\Omega_T e^2}{4m_e\pi^2\varepsilon_0 c^3}} \approx 10^{-1}\sqrt{\frac{\hbar\Omega_T}{2\text{ MeV}}}, \tag{5.30}$$

which, remarkably, only depends on the transparency frequency of the structure's material. By convention, the USC regime is said to be reached whenever $\eta_{\text{USC}} \geq 0.1$. With eq. (5.30), we see that $\eta_{\text{USC}} \geq 0.1$ if $\hbar\Omega_T$ is larger than 2 MeV. Put more explicitly, the nanostructure must be able to reflect all photons with energies from zero up to larger than 2 MeV for the emitter to be ultrastrongly coupled to them. It cannot be overstated how unreasonably high this value is for any realistic material. For instance, plasmonic resonances happen below 10 eV, and phonon-polaritons are much lower yet. Furthermore, conventional cavity designs made with such a miraculous material would lead to cavity modes at frequencies also on the order of MeV, i.e., extremely far from the optical frequencies in the eV range of the emitters that we are mostly concerned with here. Such large detuning would, in practice, limit our ability to manipulate the emitter through the cavity vacuum fields. Conversely, the spatial extent of such an MeV-scale transverse cavity would have to be on the order of half the wavelength. For such large frequencies, the associated wavelengths are in the range of picometers, comparable to the typical size of atomic nuclei,

which only goes to show how inconceivable this kind of scenario is. For this reason, we conclude that no existing material can concentrate the coupling of enough free-space photon modes into one cavity resonance to bring the emitter and photons to the USC regime: there is no USC with photons. We must also not forget that the nanostructure already overestimates the total coupling strength, as we have assumed that a single, discrete mode appears in the spectral density. Accordingly, a more realistic scenario would yield a lower bound for $\hbar\Omega_T$ even beyond 2 MeV.

Before moving on to the last part of the section, we should point out that the USC regime has indeed been predicted and reached in microcavity-like configurations [52–54, 56, 58]. However, all those cases rely on coupling to collective matter excitations, which have an extremely large effective (collectively enhanced) dipole moment that scales with the number of constituents N as $\sqrt{N}$. Consequently, such collective excitations correspond to approximately bosonic material excitations, where the most striking effects of USC disappear.

5.2.4 Polarization self-energy in the USC regime

Recently, there has been some debate in the literature concerning the role and relevance of the PSE in the description of certain light-matter experiments. The PSE, also sometimes referred to as P^2 term, appears in the multipolar coupling picture after a partial Power-Zienau-Woolley transformation that affects the emitter's charges alone. In many ways, it replaces the A^2 term of the minimal coupling Hamiltonian, although the relation between the two is not direct. We use here the results obtained in the previous paragraphs to address the debate. Neglecting magnetic effects, the partial multipolar Hamiltonian is

$$\begin{aligned}\tilde{H} = &\sum_{i\in C_\mathrm{e}} \frac{\mathbf{p}_i^2}{2m_i} + \sum_{i\neq j\in C_\mathrm{e}} \frac{q_i q_j}{8\pi\varepsilon_0 |\mathbf{r}_i - \mathbf{r}_j|} + \frac{1}{2\varepsilon_0}\int \mathrm{d}^3 r \left(\mathbf{P}_\mathrm{e}^\perp\right)^2 \\ &+ \sum_{i\in C_\mathrm{s}} \frac{\left(\mathbf{p}_i - q_i \mathbf{A}^\perp(\mathbf{r}_i)\right)^2}{2m_i} + \sum_{i\neq j\in C_\mathrm{s}} \frac{q_i q_j}{8\pi\varepsilon_0 |\mathbf{r}_i - \mathbf{r}_j|} - \int \mathrm{d}^3\, \mathbf{P}_\mathrm{e}^\parallel \cdot \mathbf{E}_\mathrm{s}^\parallel \\ &+ \int \mathrm{d}^3 r \left[\frac{\left(\mathbf{\Pi}_\mathrm{e}^\perp\right)^2}{2\varepsilon_0} + \frac{\varepsilon_0 c^2}{2}\left(\nabla\times\mathbf{A}^\perp\right)^2\right] + \frac{1}{\varepsilon_0}\int \mathrm{d}^3 r\, \mathbf{P}_\mathrm{e}^\perp \cdot \mathbf{\Pi}_\mathrm{e}^\perp. \end{aligned} \tag{5.31}$$

Here, C_e and C_s are the emitter and structure charge subsets, the emitter's polarization is defined by the emitter's charge density through $\nabla\cdot\mathbf{P}_\mathrm{e} = -\rho_\mathrm{e}$, and $-\mathbf{\Pi}_\mathrm{e}^\perp$ physically corresponds to a "partial" displacement field given by $\mathbf{D}_{(\mathrm{e})}^\perp = \varepsilon_0\mathbf{E}^\perp + \mathbf{P}_\mathrm{e}^\perp$, as explained in the MQED multipolar picture section 2.2.3. Notice that, while the structure-field interaction is still in the minimal cou-

pling form, the emitter charges couple to the field's momentum, and the emitter's PSE appears as the last term of the first line. Physically, the emitter-field interaction includes more than just the emitter-photon coupling, as $\mathbf{\Pi}$ is not completely aligned with purely photonic DOF. Indeed, because $\mathbf{\Pi}_{\mathrm{e}}^{\perp}$ physically contains the emitter's transverse polarization as well, the emitter-field interaction and the $\left(\mathbf{\Pi}_{\mathrm{e}}^{\perp}\right)^2$ terms would cancel the PSE if we were to rewrite the Hamiltonian in terms of electric fields. Of course, doing so would not be beneficial at all, as the canonical field momentum is the most convenient to describe the dynamics.

Before we continue discussing the PSE, it is convenient to dedicate a brief moment to perform a mode expansion, like we did in section 2.1.3, as it will allow us to write the PSE in a very suggestive way. In particular, with

$$\mathbf{\Pi}_{\mathrm{e}}^{\perp} = \sum_{\lambda} \Pi_{\lambda} \boldsymbol{\psi}_{\lambda} \quad \text{and} \quad \mathbf{P}_{\mathrm{e}}^{\perp} = \sum_{\lambda} P_{\lambda} \boldsymbol{\psi}_{\lambda}, \tag{5.32}$$

the emitter-field interaction becomes

$$\tilde{H}_{\mathrm{e-f}} = \frac{1}{\varepsilon_0} \sum_{\lambda} P_{\lambda} \Pi_{\lambda} = i\hbar \sum_{\lambda} P_{\lambda} \sqrt{\frac{\omega_{\lambda}}{2\hbar\varepsilon_0}} (\tilde{a}_{\lambda}^{\dagger} - \tilde{a}_{\lambda}), \tag{5.33}$$

where we have used the relations in eqs. (2.43a) and (2.45) to reach the last expression. We have added the $\sim$ on top of the ladder operators to emphasize that these create "multipolar-coupling photons", and are thus physically different from the a_{λ} in the minimal coupling picture. In order to make progress, we need a concrete expression for the P_{λ}. The interesting thing about it is that the coefficients P_{λ} only depend on $\mathbf{P}_{\mathrm{e}}^{\perp}$, which is not a priori defined in the EM theory. In fact, $\nabla \cdot \mathbf{P}_{\mathrm{e}} = \nabla \cdot \mathbf{P}_{\mathrm{e}}^{\parallel} = -\rho_{\mathrm{e}}$ unequivocally determines solely the longitudinal component of the emitter's polarization. The transverse part, on the contrary, can be chosen freely, and each choice represents a different instance of the multipolar Hamiltonian. As mentioned in section 2.1.2, the most common expression for the polarizability is the Power form,

$$\mathbf{P}_{\mathrm{e}}(\mathbf{r}) = \sum_{i} q_i (\mathbf{r}_i - \mathbf{r}_{\mathrm{e}}) \int_0^1 \mathrm{d}\sigma \, \delta^{(3)}[\mathbf{r} - \mathbf{r}_{\mathrm{e}} - \sigma(\mathbf{r}_i - \mathbf{r}_{\mathrm{e}})], \tag{5.34}$$

which fixes the transverse component, and can be visualized as a chain of infinitesimal dipoles from $\mathbf{r}_{\mathrm{e}}$ to each charge. There is, however, an inconvenient downside to this polarization in that the PSE involves the integration over a squared Dirac delta, which unavoidably diverges. Actually, the divergence turns out to be less of a problem than one might initially think, given the role of the PSE in lowering the degree of divergence of the Lamb shift, as explained

in section 2.4.1, and thus allowing us to recover Bethe's logarithm formula [13, 204, 239]. In any case, with eq. (5.34) we can find

$$\begin{aligned} P_\lambda &= \int \mathrm{d}^3 r\, \mathbf{P}_\mathrm{e}^\perp \cdot \boldsymbol{\psi}_\lambda = \int \mathrm{d}^3 r\, \mathbf{P}_\mathrm{e} \cdot \boldsymbol{\psi}_\lambda \\ &= \sum_i \int_0^1 \mathrm{d}\sigma\, q_i(\mathbf{r}_i - \mathbf{r}_\mathrm{e}) \cdot \boldsymbol{\psi}_\lambda[\mathbf{r}_\mathrm{e} + \sigma(\mathbf{r}_i - \mathbf{r}_\mathrm{e})] \approx \mathbf{d} \cdot \boldsymbol{\psi}_\lambda(\mathbf{r}_\mathrm{e}). \end{aligned} \tag{5.35}$$

In the last step, we have performed the long-wavelength approximation. With it, the emitter-field interaction becomes

$$\begin{aligned} \tilde{H}_{\mathrm{e-f}} &= i\hbar \sum_\lambda \mathbf{d} \cdot \boldsymbol{\psi}_\lambda(\mathbf{r}_\mathrm{e}) \sqrt{\frac{\omega_\lambda}{2\hbar\varepsilon_0}} (\tilde{a}_\lambda^\dagger - \tilde{a}_\lambda) \\ &= \hbar \sum_t \sum_\lambda i\tilde{g}_\lambda^{\perp,0} \left[(\mathbf{d}_t \cdot \hat{\mathbf{u}}_\lambda)\sigma_t + (\mathbf{d}_t \cdot \hat{\mathbf{u}}_\lambda)^* \sigma_t^\dagger \right] (\tilde{a}_\lambda^\dagger - \tilde{a}_\lambda), \end{aligned} \tag{5.36}$$

where the multipolar and minimal coupling strengths have been defined to match each other

$$\tilde{g}_\lambda^{\perp,0} = \sqrt{\frac{\omega_\lambda}{2\hbar\varepsilon_0}} |\boldsymbol{\psi}_\lambda(\mathbf{r}_\mathrm{e})| = g_\lambda^{\perp,0}. \tag{5.37}$$

With the mode expansion above, we can reach an interesting conclusion regarding the PSE. Using eq. (5.32), the PSE can be written as

$$\begin{aligned} \tilde{H}_\mathrm{PSE} &= \frac{1}{2\varepsilon_0} \int \mathrm{d}^3 r \left(\mathbf{P}_\mathrm{e}^\perp\right)^2 = \frac{1}{2\varepsilon_0} \sum_\lambda P_\lambda^2 \approx \frac{1}{2\varepsilon_0} \sum_\lambda (\mathbf{d} \cdot \boldsymbol{\psi}_\lambda(\mathbf{r}_\mathrm{e}))^2 \\ &= \hbar \sum_\lambda \frac{\left(\tilde{g}_\lambda^{\perp,0}\right)^2}{\omega_\lambda} (\mathbf{d} \cdot \hat{\mathbf{u}}_\lambda)^2 \equiv H_\mathrm{DSE}. \end{aligned} \tag{5.38}$$

In other words, the PSE, or rather the DSE, can be expressed as a sum over the emitter-field multipolar coupling strength $\tilde{g}_\lambda^{\perp,0}$ in the long-wavelength approximation. An important remark is that the PSE (or DSE) does not depend on the cavity. It is obvious in the first equality, because $\mathbf{P}_\mathrm{e}^\perp$ is an emitter-dependent quantity, which we have chosen to match the Power form of the polarizability. However, it can be less clear in the subsequent mode expansion, because we express the DSE in terms of the coupling to each "photonic" mode, and the cavity is expected to modify the light-matter interaction. However, notice that what appears in eq. (5.38) is the coupling strength of the emitter to the $\tilde{a}_\lambda^{(\dagger)}$ operators, which does not change after including a nanostructure. Instead, the nanostructure modifies the dynamics of the $\tilde{a}_\lambda^{(\dagger)}$ themselves, in turn making the structure-photon polaritonic modes more appropriate. Naturally, the coupling to these polaritonic modes does depend on the structure, but it is nowhere to be seen in eq. (5.38). Thus, since the USC regime is a cavity-

We write "photonic" to stress that the multipolar coupling $\tilde{a}_\lambda^{(\dagger)}$ already does not create purely photonic excitations, as discussed in section 5.1.2.

dependent phenomenon, and the PSE is cavity-independent, it seems reasonable that the PSE should be irrelevant for USC physics.

Despite the above argument, some authors claim that the PSE is cavity-dependent, either implicitly or explicitly [178], and, therefore, has important consequences in the USC regime. To understand the line of reasoning behind those claims, let us consider a "perfect transverse cavity" like the one imagined before to derive the bound in section 5.2.2, with the following spectral density:

$$J^{\perp}(\omega) = \left(G_t^{\perp}\right)^2 \delta(\omega - \omega_t) + J^{\perp,0}(\omega)\theta(\omega - \Omega_T). \tag{5.39}$$

This transverse spectral density encodes the interaction between the emitter and the cavity-photon polaritonic eigenmodes, which, in this particular instance, are a single discrete mode and a continuum. Additionally, we show in appendix E.2 that the DSE can be expressed in terms of the transverse emitter-polariton coupling strength, just like it was written in terms of the free-space coupling strength $\tilde{g}_\lambda^{\perp,0}$ in eq. (5.38). Putting this fact together with the single-mode spectral density in eq. (5.39), we arrive at a DSE that is manifestly split into two contributions, one for the single-mode and another for the high-frequency continuum:

$$H_{\mathrm{DSE}} = \hbar \frac{\left(G_t^{\perp}\right)^2}{\omega_t} (\mathbf{d}\cdot\hat{\mathbf{u}}_t)^2 + \hbar \sum_{\lambda} \frac{\left(g_\lambda^{\perp,0}\right)^2}{\omega_\lambda} (\mathbf{d}\cdot\hat{\mathbf{u}}_\lambda)^2 \theta(\omega_\lambda - \Omega_T). \tag{5.40}$$

Here, $\hat{\mathbf{u}}_t$ is the unit vector that selects the components of $\mathbf{d}$ that interact with the single transverse cavity mode. The high-frequency continuum part, together with its corresponding modes, can be treated perturbatively and, after renormalization arguments, gives rise to a part of the free-space Lamb shift. Conversely, the single-mode part should, in principle, be kept, as its associated mode is treated explicitly and non-perturbatively. Finally, the single-mode multipolar coupling Hamiltonian becomes

$$\begin{aligned}\tilde{H} = &\sum_{i\in \mathrm{C_e}} \frac{\mathbf{p}_i^2}{2m_i} + \sum_{i\neq j\in \mathrm{C_e}} \frac{q_i q_j}{8\pi\varepsilon_0 |\mathbf{r}_i - \mathbf{r}_j|} + H'_{\mathrm{LS}} + \hbar \frac{\left(G_t^{\perp}\right)^2}{\omega_t} (\mathbf{d}\cdot\hat{\mathbf{u}}_t)^2 \\ &+ \hbar\omega_t b_\perp^\dagger b_\perp + i\hbar G_t^{\perp} \mathbf{d}\cdot\hat{\mathbf{u}}_t (b_\perp^\dagger - b_\perp),\end{aligned} \tag{5.41}$$

where $b_\perp$ is the discrete cavity-mode with frequency ω_t, in resonance with some transition in the emitter. The prime on the Lamb shift correction denotes that only part of the total free-space Lamb shift is included there, and is usually dropped or considered to be absorbed in the emitter Hamiltonian. We could have reached the same multipolar Hamiltonian by first truncating the modes,

that is, removing all but the discrete cavity mode in the minimal coupling Hamiltonian and, afterwards, performing a single-mode PZW transformation. In this alternative procedure, the full PSE never shows up; instead, only its single-mode contribution is explicit. In a compromise between precision and brevity, many works that follow the second approach call "PSE" to what we have described as its single-mode contribution here. Naturally, the "PSE" in those works will depend on the cavity, because $G_t^\perp$ measures the amount of coupling strength that the cavity concentrates at ω_t. Thus, the apparent disagreement is solved: while the single-mode PSE is cavity-dependent, the full one that takes the whole spectrum of modes into account is not.

Once this terminological conundrum has been clarified, we now address whether the single-mode PSE is relevant for the USC regime, as claimed in, e.g., [178], or not. If we take eq. (5.41) at face value, it is apparent that the single-mode DSE becomes more relevant the larger that $G_t^\perp$ is taken. In fact, if $G_t^\perp$ brings the emitter into the USC regime with the transverse cavity mode $b_\perp$, it will correspond to a contribution of the order of $\sim \eta_{\mathrm{USC}}^2 \hbar\omega_t$, definitely non-negligible. However, the key result of this chapter is that $G_t^\perp$ is inevitably restricted by fundamental EM constraints, as seen eq. (5.28). Furthermore, the dipole moments of small emitters are also bounded by the TRK sum rule in eq. (2.117b). Consequently, as concluded in section 5.2.3, the USC coupling regime cannot be achieved through transverse interactions. It is physically meaningless to take a sufficiently large value of $G_t^\perp$ to ensure that the USC regime is achieved with the transverse cavity mode in the theory, and, therefore, the single-mode DSE can be safely neglected. Instead, the USC regime can only be reached through the longitudinal Coulomb interaction between the emitter and structure charges, namely,

$$H_{\mathrm{e-s}} = -\int \mathrm{d}^3 r\, \mathbf{P}_{\mathrm{e}}^{\parallel} \cdot \mathbf{E}_{\mathrm{s}}^{\parallel}, \tag{5.42}$$

so long as the setup relies on subwavelength confinement. Moreover, if one can identify clear EM resonances in the structure, such as the dipolar resonance of a small metallic sphere, then the Coulomb interaction may be describable in terms of a single (or a few) longitudinal mode $b_\parallel$:

$$H_{\mathrm{e-s}} \sim \hbar(\mathbf{d}\cdot\hat{\mathbf{u}}_t) G_t^{\parallel}(b_\parallel^\dagger + b_\parallel). \tag{5.43}$$

The corresponding single-mode DSE will not depend on $G_t^\parallel$, but on the much smaller $\tilde{G}_t^\perp$, as we have shown above, and its ensuing impact is, therefore, largely overestimated if one assumes that $\tilde{G}_t^\perp$ is the one leading to USC. A posteriori, we see that singling out one field mode in the transverse interac-

tion, while possible in principle, can be more misleading than simplifying. Still, a consistency argument can be made for keeping the single-mode cavity-dependent part of the PSE that corresponds to the transverse cavity mode that is treated explicitly. For instance, even if the actual numerical contribution of the single-mode PSE is small, it connects the single-mode, multipolar coupling Hamiltonian with the single-mode minimal coupling Hamiltonian through a gauge (unitary) transformation, and maintaining gauge independence is desirable on theoretical grounds.

Note that we have assumed a single transverse cavity mode here for simplicity, but everything is straightforwardly generalized to the case of several such modes.

Before ending the discussion on the PSE, we address the claim that the DSE is important in the USC regime and provide a more direct counter-argument. It has been shown that, in the absence of DSE, ab-initio molecular simulations in the long-wavelength approximation display a lack of bound-states for sufficiently large computational boxes. In that setting, it has been pointed out that including the DSE restores the existence of molecular bound-states [177, 178], due to the additional quadratic potential that the DSE brings with it. Still, the arguments provided in this whole section imply that single- or few- emitter USC arises from the direct Coulomb interaction between the emitter and structure charges, where the DSE plays no role at all. Hence, the omission of the DSE cannot be physically responsible for the lack of molecular bound-states. It must come from the long-wavelength approximation used in those simulations, as it effectively corresponds to setting a constant electric field within the whole simulation box. It should then not come as a surprise that, for sufficiently large boxes, this constant electric field overcomes the molecular Coulomb interaction such that the charges are pulled apart. Naturally, the addition of the DSE's quadratic potential "fixes" the molecular dismemberment, but not in a physically meaningful way, as such scenarios are clearly not well-described within the long-wavelength approximation to begin with. Accordingly, a genuine fix requires going beyond the long-wavelength approximation in ab-initio simulations and, eventually, including the subwavelength cavity in the ab-initio description. We elaborate further on this issue in the next section. In conclusion, the PSE should be present in the full light-matter Hamiltonian, but its significance highly depends on the physical scenario that the theory is being used to describe. Specifically, it does not have the significance that other works have attributed to it in the USC regime.

5.3 Analytical illustration

In this section, we illustrate the general arguments from section 5.2 by solving the paradigmatic scenario of an emitter interacting with a metallic nanosphere.

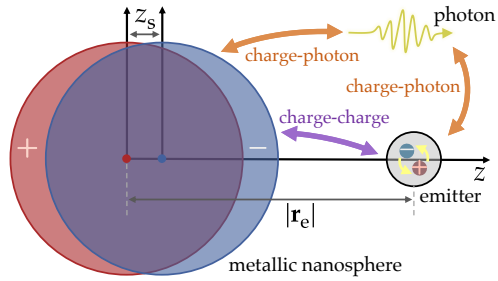

Figure 5.5: Sketch of the model. The metallic sphere is described as two overlapping and homogeneously charged spheres that represent the ionic lattice and conduction electrons. The emitter is placed along the z axis.

To make the calculations analytical, we resort to a few simplifying assumptions that, nevertheless, retain all the important physics we need to include. After discussing the required approximations, we proceed to the explicit diagonalization of the sphere and photons, and write the emitter interactions in terms of the new polaritonic eigenmodes, finding closed analytical expressions. From these coupling strengths, we straightforwardly obtain longitudinal and transverse spectral densities, from which it becomes clear that only the longitudinal one can account for USC effects. Last, we finish the section with a direct comparison with a MQED formulation of the problem, and a discussion on the role of the PSE.

5.3.1 Model

As shown in the sketch of fig. 5.5, we model the metallic sphere as two charged spheres of radius R_s, one describing the ionic lattice and the other for the conduction electrons. Both spheres are homogeneously charged, with charge densities ρ and $-\rho$ for the ionic and electronic spheres. Due to the large disparity in mass, the ionic sphere sits still at the origin, while the electronic sphere oscillates back and forth due to the Coulomb interaction between them. For simplicity, we restrict the motion of the electronic sphere to the z axis, and denote its displacement by z_s. We assume that the electronic sphere displacement is much smaller than the nanosphere's radius, i.e., $z_s \ll R_s$. Considering typical values of $R_s = 10$ nm, $\rho = 60\, e \cdot \text{nm}^{-3}$ and total energies around 1 eV, z_s can be estimated to be of the order of 1 pm, such that the small oscillation approximation holds with great accuracy. Intuitively, the two spheres are the simplest imitation of the dipolar resonance of a metallic nanosphere, which will be confirmed by the end of the section.

For the forthcoming parts of the chapter, a Hamiltonian description is

needed. To obtain it, we start from the usual light-matter Lagrangian

$$\begin{aligned} L = &\sum_{i\in C_e} \frac{m_i \dot{\mathbf{r}}_i^2}{2} - \sum_{i\neq j\in C_s} \frac{q_i q_j}{8\varepsilon_0 \left|\mathbf{r}_i - \mathbf{r}_j\right|} \\ &+ \frac{m_s \dot{z}_s^2}{2} + \int \mathrm{d}^3 r\, \rho \phi_+ - \frac{8\pi\rho^2 R_s^5}{15\varepsilon_0} - \sum_{i\in C_e} q_i \phi(\mathbf{r}_i) \\ &+ \frac{\varepsilon_0}{2} \int \mathrm{d}^3 r \left[\left(\dot{\mathbf{A}}^\perp\right)^2 - c^2 \left(\nabla \times \mathbf{A}^\perp\right)^2 \right] \\ &+ \sum_{i\in C_e} q_i \dot{\mathbf{r}}_i \cdot \mathbf{A}^\perp(\mathbf{r}_i) + \int \mathrm{d}^3 r\, \mathbf{j}_s \cdot \mathbf{A}^\perp. \end{aligned} \tag{5.44}$$

Here, the constant term in the fifth place simply accounts for the Coulomb self-energy of the spheres, which is finite. As for the electronic sphere, its mass is $m_s = \frac{4\pi R_s^3 \rho}{3e} m_e$, where m_e and e are the electron mass and charge, and its charge density is a step function, specifically $-\rho(\mathbf{r}) = -\rho\theta(R_s - |\mathbf{r} - z_s\hat{\mathbf{z}}|)$. The current density associated with its motion is $\mathbf{j}_s = -\rho(\mathbf{r})\dot{z}_s\hat{\mathbf{z}}$, and ϕ is the full sphere's Coulomb potential. As for the Coulomb potential due to the ionic sphere alone, ϕ_+, we have

$$\phi_+(\mathbf{r}) = \frac{\rho}{3\varepsilon_0} \begin{cases} \dfrac{3R_s^2 - |\mathbf{r}|^2}{2} & \text{if } |\mathbf{r}| \leq R_s, \\ \dfrac{R_s^3}{|\mathbf{r}|} & \text{if } |\mathbf{r}| > R_s. \end{cases} \tag{5.45}$$

The canonical momenta that correspond to this Lagrangian are

$$\mathbf{p}_i = m_i \dot{\mathbf{r}}_i + q_i \mathbf{A}^\perp(\mathbf{r}_i), \tag{5.46a}$$

$$p_s = m_s \dot{z}_s - \int \mathrm{d}^3 r\, \rho \left(\hat{\mathbf{z}} \cdot \mathbf{A}^\perp\right) \quad \text{and} \tag{5.46b}$$

$$\mathbf{\Pi} = \varepsilon_0 \dot{\mathbf{A}}^\perp = -\varepsilon_0 \mathbf{E}^\perp. \tag{5.46c}$$

Accordingly, the minimal coupling Hamiltonian of the model is

$$\begin{aligned} H &= \sum_i \mathbf{p}_i \cdot \dot{\mathbf{r}}_i + p_s \dot{z}_s + \int \mathrm{d}^3 r\, \mathbf{\Pi} \cdot \dot{\mathbf{A}}^\perp - L \\ &= \sum_{i\in C_e} \frac{\left(\mathbf{p}_i - q_i \mathbf{A}^\perp(\mathbf{r}_i)\right)^2}{2m_i} + \sum_{i\neq j\in C_e} \frac{q_i q_j}{8\pi\varepsilon_0 \left|\mathbf{r}_i - \mathbf{r}_j\right|} + \sum_{i\in C_e} q_i \phi(\mathbf{r}_i) \\ &\quad + \frac{\left(p_s + \int \mathrm{d}^3 r\, \rho \left(\hat{\mathbf{z}} \cdot \mathbf{A}^\perp\right)\right)^2}{2m_s} - \int \mathrm{d}^3 r\, \rho \phi_+ + \frac{8\pi\rho^2 R_s^5}{15\varepsilon_0} \\ &\quad + \int \mathrm{d}^3 r \left(\frac{\left(\mathbf{\Pi}^\perp\right)^2}{2\varepsilon_0} + \frac{\varepsilon_0 c^2}{2} \left(\nabla \times \mathbf{A}^\perp\right)^2 \right). \end{aligned} \tag{5.47}$$

An interesting remark is that the interaction between the sphere and the transverse photon field is a straightforward generalization of the minimal coupling term for point charges, simply integrating over an extended charge distribution.

5.3.2 Diagonalization steps

After reaching the Hamiltonian in eq. (5.47), we are ready to tackle the diagonalization of the sphere-photon oscillator Hamiltonian, H_{osc}, determined by the last two lines of eq. (5.47). Here, we first manipulate a few terms in order to obtain a more explicit version of H_{osc}. Next, we perform two consecutive canonical transformations that express the oscillator Hamiltonian in a way that is ready for a Fano diagonalization procedure [300], well-suited to diagonalize discrete systems coupled to a continuum. Finally, we carry out the diagonalization to find the polaritonic eigenmodes of the sphere-photon system.

More explicit oscillator Hamiltonian As shown in section F.1.1, the Coulomb interaction between the spheres is, in the limit of small oscillations,

$$-\int \mathrm{d}^3 r\, \rho\phi_+ = -\frac{8\pi\rho^2 R_{\text{s}}^5}{15\varepsilon_0} + \frac{2\pi\rho^2 R_{\text{s}}^3}{9\varepsilon_0} z_{\text{s}}^2 + O\Big(|z_{\text{s}}|^3\Big) \approx -\frac{8\pi\rho^2 R_{\text{s}}^5}{15\varepsilon_0} + \frac{m_{\text{s}}}{2}\frac{\Omega_{\text{P}}^2}{3} z_{\text{s}}^2. \tag{5.48}$$

In the final expression, the constant term cancels the Coulomb self-energy of the spheres, and we have introduced the plasma frequency $\Omega_{\text{P}} = \sqrt{\frac{\rho e}{m_{\text{e}}\varepsilon_0}}$, an intrinsic property of the metal that depends on the conduction electron density only. The electronic sphere is, therefore, in a harmonic potential with natural frequency equal to $\frac{\Omega_{\text{P}}}{\sqrt{3}}$, which is precisely the frequency of the dipolar resonance of a small metallic sphere with a lossless Drude permittivity, precisely the physics our model is designed to capture. The actual resonant frequency is slightly red-shifted due to the interaction with an environment of photons, as shown in appendix F.3.

The photon field Lagrangian and the sphere-photon interaction can be further simplified with a mode expansion. Due to the symmetry of the system, a convenient family of basis functions are the real spherical-wave functions, defined by

$$\boldsymbol{\psi}_{lm}^{(\text{te})}(\omega, \mathbf{r}) = \frac{\omega}{c}\sqrt{\frac{2}{l(l+1)\pi c}} j_l\Big(\frac{\omega|\mathbf{r}|}{c}\Big)\Big[\hat{\boldsymbol{\vartheta}}\frac{\partial_\varphi}{\sin\vartheta} - \hat{\boldsymbol{\varphi}}\partial_\vartheta\Big] Y_{lm}(\vartheta, \varphi) \quad \text{and} \tag{5.49a}$$

$$\boldsymbol{\psi}^{(\mathrm{tm})}_{lm}(\omega,\mathbf{r}) = \frac{c}{\omega}\nabla\times\boldsymbol{\psi}^{(\mathrm{te})}_{lm}(\omega,\mathbf{r}). \tag{5.49b}$$

Here, $\omega \in [0,\infty)$, $|\mathbf{r}|$, ϑ and φ are spherical coordinates, $l \geq 1$ and $m = -l, -l+1, \cdots, l$; the $l = 0$ is excluded because its associated functions vanish. The oscillating functions j_l are spherical Bessel functions, while Y_{lm} are the real (also known as tesseral) spherical harmonics (see appendix A.3). The abstract index λ from the conceptual argument is, in this case, replaced by p, l, m and ω. We have chosen the normalization constant to ensure that

$$\int \mathrm{d}^3r\, \boldsymbol{\psi}^{(p)}_{lm}(\omega)\cdot\boldsymbol{\psi}^{(\mathrm{p}')}_{l'm'}(\omega') = \delta_{pp'}\delta_{ll'}\delta_{mm'}\delta(\omega-\omega'). \tag{5.50}$$

If the vector potential and its canonical momentum are

$$\mathbf{A}^{\perp} = \sum_{p,lm}\int \mathrm{d}\omega\, A^{(p)}_{lm}(\omega)\boldsymbol{\psi}^{(p)}_{lm}(\omega) \tag{5.51a}$$

$$\boldsymbol{\Pi}^{\perp} = \sum_{p,lm}\int \mathrm{d}\omega\, \Pi^{(p)}_{lm}(\omega)\boldsymbol{\psi}^{(p)}_{lm}(\omega), \tag{5.51b}$$

then the photon field Hamiltonian becomes

$$\begin{aligned} H_{\mathrm{f}} &= \int \mathrm{d}^3r \left(\frac{\left(\boldsymbol{\Pi}^{\perp}\right)^2}{2\varepsilon_0} + \frac{\varepsilon_0 c^2}{2}\left(\nabla\times\mathbf{A}^{\perp}\right)^2 \right) \\ &= \frac{1}{2}\sum_{p,lm}\int \mathrm{d}\omega \left\{ \frac{1}{\varepsilon_0}\left[\Pi^{(p)}_{lm}(\omega)\right]^2 + \varepsilon_0\omega^2\left[A^{(p)}_{lm}(\omega)\right]^2 \right\}. \end{aligned} \tag{5.52}$$

As for the sphere-field interaction, we show it to be equal to

$$\int \mathrm{d}^3r\, \rho\left(\hat{\mathbf{z}}\cdot\mathbf{A}^{\perp}\right) = \frac{4\rho R_{\mathrm{s}}^2}{\sqrt{3c}}\sum_{p,lm}\int \mathrm{d}\omega\, A^{(p)}_{lm}(\omega) j_l\!\left(\frac{\omega R_{\mathrm{s}}}{c}\right)\delta_{p,\mathrm{tm}}\delta_{l1}\delta_{m0}, \tag{5.53}$$

in section F.1.2. A feature that immediately jumps out is the concatenation of Kronecker deltas, a consequence of the system's symmetry, which means that only "tm", $l = 1$ and $m = 0$ modes have to be taken into account to diagonalize the photon-sphere oscillator Hamiltonian. Hence, all other modes will essentially remain free-space modes with no modification due to the nanosphere, which will have consequences for the emitter-field interaction as well. Given the significance of the modes with non-vanishing interaction with the sphere, we grant them preferential treatment by stripping them from the discrete labels and keeping just the ω dependence: $A^{(\mathrm{tm})}_{10}(\omega) \equiv A(\omega)$, and likewise for Π. The advantage of working with the spherical-wave basis is thus revealed

here. After these steps, the oscillator Hamiltonian becomes

$$\begin{aligned} H_{\mathrm{osc}} = \frac{1}{2}{\sum_{p,lm}}' \int \mathrm{d}\omega \left\{ \frac{1}{\varepsilon_0}\left[\Pi_{lm}^{(p)}(\omega)\right]^2 + \varepsilon_0\omega^2\left[A_{lm}^{(p)}(\omega)\right]^2 \right\} \\ + \frac{\left[p_{\mathrm{s}} + \dfrac{4\rho R_{\mathrm{s}}^2}{\sqrt{3c}} \int \mathrm{d}\omega\, j_1\!\left(\dfrac{\omega R_{\mathrm{s}}}{c}\right) A(\omega)\right]^2}{2m_{\mathrm{s}}} + \frac{m_{\mathrm{s}}}{2}\frac{\Omega_{\mathrm{P}}^2}{3} z_{\mathrm{s}}^2 \\ + \frac{1}{2}\int \mathrm{d}\omega \left[\frac{\Pi^2(\omega)}{\varepsilon_0} + \varepsilon_0\omega^2 A^2(\omega) \right]. \end{aligned} \tag{5.54}$$

In this expression, the primed summation symbol means that the sum is to be taken excluding the "tm", $l = 1$ and $m = 0$ modes. Consequently, the first line is completely decoupled from the rest for the diagonalization. Therefore, we will drop it until the eigenmodes of the last two lines have been found.

Canonical transformations Explicitly diagonalizing eq. (5.54) is difficult because of the A^2 term, as it induces couplings between $A(\omega)$ and $A(\omega')$. Therefore, we switch to a multipolar coupling Hamiltonian with the following canonical transformation

$$p_{\mathrm{s}} \to p_{\mathrm{s}}' = p_{\mathrm{s}} + \frac{4\rho R_{\mathrm{s}}^2}{\sqrt{3c}} \int \mathrm{d}\omega\, j_1\!\left(\frac{\omega R_{\mathrm{s}}}{c}\right) A(\omega) \quad \text{and} \tag{5.55a}$$

$$\Pi(\omega) \to \Pi'(\omega) = \Pi(\omega) + \frac{4\rho R_{\mathrm{s}}^2}{\sqrt{3c}} j_1\!\left(\frac{\omega R_{\mathrm{s}}}{c}\right) z_{\mathrm{s}}. \tag{5.55b}$$

The oscillator Hamiltonian becomes

$$\begin{aligned} H_{\mathrm{osc}} = \frac{p_{\mathrm{s}}'^2}{2m_{\mathrm{s}}} + \frac{m_{\mathrm{s}}}{2}\left[\frac{\Omega_{\mathrm{P}}^2}{3} + \frac{16\rho^2 R_{\mathrm{s}}^4}{3\varepsilon_0 m_{\mathrm{s}} c} \int \mathrm{d}\omega\, j_1^2\!\left(\frac{\omega R_{\mathrm{s}}}{c}\right)\right] z_{\mathrm{s}}^2 \\ + \frac{1}{2}\int \mathrm{d}\omega \left[\frac{\Pi'^2(\omega)}{\varepsilon_0} + \varepsilon_0\omega^2 A^2(\omega) \right] - z_{\mathrm{s}} \int \mathrm{d}\omega\, \frac{4\rho R_{\mathrm{s}}^2}{\varepsilon_0\sqrt{3c}} j_1\!\left(\frac{\omega R_{\mathrm{s}}}{c}\right) \Pi'(\omega), \end{aligned} \tag{5.56}$$

where the unperturbed free-space modes have been dropped to alleviate the expressions, but we must not forget to include them at the end again. The second term in the square brackets on the first line is the sphere's finite PSE. It can be calculated explicitly with the expressions from appendix A.2, and yields a renormalized oscillator potential energy for the sphere given by

$$\frac{m_{\mathrm{s}}}{2}\left[\frac{\Omega_{\mathrm{P}}^2}{3} + \frac{16\rho^2 R_{\mathrm{s}}^4}{3\varepsilon_0 m_{\mathrm{s}} c} \int \mathrm{d}\omega\, j_1^2\!\left(\frac{\omega R_{\mathrm{s}}}{c}\right)\right] z_{\mathrm{s}}^2 = \frac{m_{\mathrm{s}}}{2}\Omega_{\mathrm{P}}^2 z_{\mathrm{s}}^2. \tag{5.57}$$

At face value, the sphere's oscillations seem to be massively shifted from $\frac{\Omega_P}{\sqrt{3}}$ to Ω_P, almost by a factor of 2. However, this is merely an artifact of the multipolar coupling Hamiltonian, which hides a compensating contribution in the sphere-photon interaction term such that, overall, the resonant frequency will be slightly red-shifted from $\frac{\Omega_P}{\sqrt{3}}$, as was more clear in the minimal coupling picture. Note that this Hamiltonian could have obtained by adding the following total time derivative

$$\frac{\mathrm{d}}{\mathrm{d}t}\left[\frac{4\rho R_s^2}{\sqrt{3}c} z_s \int \mathrm{d}\omega\, j_1\left(\frac{\omega R_s}{c} A(\omega)\right)\right] \tag{5.58}$$

to the Lagrangian in eq. (5.44). Alternatively, it could also have been implemented through a unitary partial PZW transformation

$$T_s = \exp\left\{-\frac{i}{\hbar}\int \mathrm{d}^3 r\, \mathbf{P}_s \cdot \mathbf{A}_\perp\right\}, \tag{5.59}$$

where the sphere's polarization is defined as $\dot{\mathbf{P}}_s = \mathbf{j}_s = -\rho \dot{z}_s \hat{\mathbf{z}}$. This polarization corresponds to a particular choice of $\mathbf{P}_s^\perp$, which, in the case considered here, allows us to find a very simple expression for $\mathbf{P}_s = -\rho z_s \hat{\mathbf{z}} + O(z_s^2)$, with the higher order terms arising from the temporal variation of the scalar field ρ itself. These corrections can be safely neglected in the small oscillation regime considered here.

The Hamiltonian in eq. (5.56) does not contain cross-couplings of field variables anymore. Still, to apply the Fano diagonalization procedure, another intermediate canonical transformation proves useful:

$$p_s' \to p = \frac{1}{\sqrt{m_s}} p_s', \qquad z_s \to z = \sqrt{m_s} z_s, \quad \text{and} \tag{5.60a}$$

$$\Pi'(\omega) \to X(\omega) = -\frac{1}{\sqrt{\varepsilon_0}\omega}\Pi'(\omega) \qquad A(\omega) \to P(\omega) = \sqrt{\varepsilon_0}\omega A(\omega). \tag{5.60b}$$

We have rescaled all the variables to remove the explicit "mass" factors from the Hamiltonian, and also swapped the roles of field coordinates and momenta. The minus sign is there to preserve the symplectic structure of Hamiltonian dynamics, that is, the form of Hamilton's equations. The oscillator Hamiltonian in its final form before the diagonalization is

$$H_{\mathrm{osc}} = \frac{1}{2}\left\{p^2 + \Omega_P^2 z^2 + \int \mathrm{d}\omega \left[P^2(\omega) + \omega^2 X^2(\omega)\right]\right\} + z\int \mathrm{d}\omega\, \gamma(\omega) X(\omega), \tag{5.61}$$

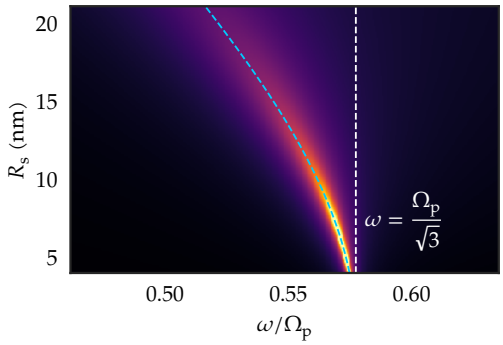

Figure 5.6: First Fano coefficient $c_1(\omega)$, as a function of frequency and the sphere's radius R_s. The metal conduction electron density is $\rho = 60\ e \cdot \mathrm{nm}^{-3}$, similar to that of silver. The vertical dashed line indicates the quasistatic value of the dipolar resonant frequency, and the dashed blue line follows eq. (5.68).

1

where the coupling is encoded in

$$\gamma(\omega) = 2\Omega_P \sqrt{\frac{R_s}{\pi c}}\, \omega j_1\left(\frac{\omega R_s}{c}\right). \tag{5.62}$$

Fano diagonalization We define here the polaritonic coordinates and momenta:

$$\Sigma(\omega) = c_1(\omega) z + \int \mathrm{d}\omega'\, c_2(\omega,\omega') X(\omega') \quad \text{and} \tag{5.63a}$$

$$\Xi(\omega) = c_1(\omega) p + \int \mathrm{d}\omega'\, c_2(\omega,\omega') P(\omega'), \tag{5.63b}$$

respectively. The goal of the diagonalization is to find the $c_1(\omega)$ and $c_2(\omega,\omega')$ coefficients, which determine the orthogonal transformation that diagonalizes H_{osc}. To that end, we use the harmonic oscillator equation of motion, $[H_{\mathrm{osc}}, \Xi(\omega)] = i\hbar\omega^2\Sigma(\omega)$, which implies that

$$\begin{cases} c_1(\omega)\left(\omega^2 - \Omega_P^2\right) = \int \mathrm{d}\omega'\, c_2(\omega,\omega')\gamma(\omega'), \\ c_2(\omega,\omega')\left(\omega^2 - \omega'^2\right) = \gamma(\omega') c_1(\omega). \end{cases} \tag{5.64}$$

A formal solution to these relations is

$$c_2(\omega,\omega') = \left[P\frac{1}{\omega^2-\omega'^2} + \frac{\omega^2 - \Omega_P^2 - F(\omega)}{\gamma^2(\omega)}\delta(\omega-\omega')\right]\gamma(\omega')c_1(\omega), \tag{5.65}$$

as can be checked by direct substitution. We have defined the shift function

$$F(\omega) = P\int \mathrm{d}\omega'\, \frac{\gamma^2(\omega')}{\omega^2-\omega'^2} = 2\Omega_P^2 \frac{\omega R_s}{c} j_1\left(\frac{\omega R_s}{c}\right) y_1\left(\frac{\omega R_s}{c}\right), \tag{5.66}$$

which is responsible for placing the plasmonic resonance close to $\frac{\Omega_\mathrm{P}}{\sqrt{3}}$ in this multipolar coupling framework, as $\lim_{x\to 0} x j_1(x) y_1(x) = \frac{-1}{3}$. Here, the analytical result includes j_1 and y_1, the first spherical Bessel functions, of the first and second kind, respectively, and has been obtained using the Fourier relations derived in appendix A.2. The final eigenmodes have to be determined through the orthonormalization condition on the coefficients implemented by imposing $[\Sigma(\omega), \Xi(\omega')] = i\hbar\delta(\omega - \omega')$. After some manipulations, written in appendix F.2, we reach

$$c_1(\omega) = \frac{\gamma(\omega)}{\sqrt{\left(\omega^2 - \Omega_\mathrm{P}^2 - F(\omega)\right)^2 + \left(\frac{\pi}{2\omega}\right)^2 \gamma^4(\omega)}}, \tag{5.67}$$

which concludes the Fano diagonalization. As fig. 5.6 reveals, the Fano coefficient c_1 is dominated by a resonance close to $\frac{\Omega_\mathrm{P}}{\sqrt{3}}$, whose precise value depends on the radius roughly as

$$\Omega_\mathrm{r} \approx \frac{\Omega_\mathrm{P}}{\sqrt{3}} \left[\sqrt{1 + \frac{4}{15}\left(\frac{\Omega_\mathrm{P} R_\mathrm{s}}{c}\right)^2} \right]^{-1}. \tag{5.68}$$

This expression has a considerable degree of accuracy, as indicated by the dashed blue line in the figure, and is derived in appendix F.3. Far from the resonance, $c_1(\omega)$ decays as

$$c_1(\omega) \approx \frac{\gamma(\omega)}{\omega^2 - \Omega_\mathrm{P}^2 - F(\omega)}, \tag{5.69}$$

and the other coefficient is dominated by the second term in the square brackets, such that

$$c_2(\omega, \omega') \approx \delta(\omega - \omega').$$

This goes back to confirm the comments made at the end of section 5.2.1 regarding $M_{\lambda\eta}$.

For our next purposes, we actually need to invert the relation between the eigenmodes and the original oscillators. Since the coefficients $c_1(\omega)$ and $c_2(\omega, \omega')$ form an orthogonal transformation, inversion is equivalent to transposition. Thus, with eq. (5.60), we find

$$p'_\mathrm{s} = \sqrt{m_\mathrm{s}} \int \mathrm{d}\omega\, c_1(\omega) \Xi(\omega), \tag{5.70a}$$

$$z_\mathrm{s} = \frac{1}{\sqrt{m_\mathrm{s}}} \int \mathrm{d}\omega\, c_1(\omega) \Sigma(\omega), \tag{5.70b}$$

$$\Pi'(\omega') = -\sqrt{\varepsilon_0}\omega' \int \mathrm{d}\omega\, c_2(\omega, \omega') \Sigma(\omega) \quad \text{and} \tag{5.70c}$$

$$A(\omega') = \frac{1}{\sqrt{\varepsilon_0}\omega'} \int \mathrm{d}\omega \, c_2(\omega, \omega')\Xi(\omega). \tag{5.70d}$$

5.3.3 Emitter-polariton interactions

After the diagonalization, we are ready to write the emitter's interactions in terms of the polaritonic eigenmodes just obtained. In the course of the diagonalization preparation, we have switched to a partial multipolar coupling picture that only affects the sphere-field interaction, while the emitter remains minimally coupled. Thus, we must deal with two terms, the $\mathbf{p}_i \cdot \mathbf{A}^{\perp}(\mathbf{r}_i)$ and the $q_i\phi(\mathbf{r}_i)$ interactions.

For the first one, we again separate the tm, $l = 1$, $m = 0$ modes from the rest. Adapting eqs. (5.17), (5.18) and (5.20) to (5.22) and using eq. (5.70d), we arrive at

$$\begin{aligned} H_{\mathrm{e-f}} \approx \hbar \sum_t i\sigma_t {\sum_{p,lm}}' \int \mathrm{d}\omega \, \frac{\omega_t}{\omega} g_{lm}^{(p),0}(\omega) \Big(\mathbf{d}_t \cdot \hat{\mathbf{u}}_{lm}^{(p)}(\omega)\Big) \Big[\big(a_{lm}^{(p)}(\omega)\big)^{\dagger} + a_{lm}^{(p)}(\omega) \Big] \\ + \mathrm{H.c.} \\ - \hbar \sum_t \sigma_t \int \mathrm{d}\omega \, \frac{\omega_t}{\omega} g_{\mathrm{p}}^{\perp}(\omega) (\mathbf{d}_t \cdot \hat{\mathbf{u}}(\omega)) \big[b^{\dagger}(\omega) - b(\omega) \big] + \mathrm{H.c.}, \end{aligned} \tag{5.71}$$

in the long-wavelength approximation. Here, $\hat{\mathbf{u}}_{lm}^{(p)}(\omega)$ and $\hat{\mathbf{u}}(\omega)$ are unit vectors along the direction of $\boldsymbol{\psi}_{lm}^{(p)}(\omega, \mathbf{r}_{\mathrm{e}})$ and

$$\int \mathrm{d}\omega' \, \frac{c_2(\omega, \omega')\boldsymbol{\psi}_{10}^{(\mathrm{tm})}(\omega', \mathbf{r}_{\mathrm{e}})}{\omega'}, \tag{5.72}$$

respectively. As the notation suggests, $a_{lm}^{(p)}(\omega)$ is the free-space photon annihilation operator corresponding to a particular spherical-wave mode, while $b(\omega)$ annihilates polaritonic excitations. The free-space and polaritonic coupling strength functions are given by

$$g_{lm}^{(p),0}(\omega) = \sqrt{\frac{\omega}{2\hbar\varepsilon_0}} \big| \boldsymbol{\psi}_{lm}^{(p)}(\omega, \mathbf{r}_{\mathrm{e}}) \big| \quad \text{and} \tag{5.73a}$$

$$g_{\mathrm{p}}^{\perp}(\omega) = \sqrt{\frac{\omega}{2\hbar\varepsilon_0}} \Big| \int \mathrm{d}\omega' \, c_2(\omega, \omega') \boldsymbol{\psi}_{10}^{(\mathrm{tm})}(\omega', \mathbf{r}_{\mathrm{e}}) \frac{\omega}{\omega'} \Big|, \tag{5.73b}$$

in complete agreement with the more general version in eq. (E.7). Assuming, for simplicity, that the emitter's relevant transition dipole moment points along the z axis, and recalling that it is also placed on the z axis, we see that it can only couple to "tm" modes due to the definition of the spherical waves in

eq. (5.49), as the "te" ones have no radial component. For concreteness, the radial component of the "tm" waves is

$$\hat{\mathbf{r}} \cdot \boldsymbol{\psi}_{lm}^{(\mathrm{tm})}(\omega, \mathbf{r}) = \frac{1}{|\mathbf{r}|}\sqrt{\frac{2l(l+1)}{\pi c}} j_l\Big(\frac{\omega|\mathbf{r}|}{c}\Big) Y_{lm}(\vartheta, \varphi), \tag{5.74}$$

and, along the z axis it is the only non-vanishing component. We may now use the expressions given in appendix A.2 to carry out the integration and find a closed analytical expression for the polaritonic transverse coupling:

$$g_{\mathrm{P}}^{\perp}(\omega) = \frac{1}{|\mathbf{r}_{\mathrm{e}}|}\sqrt{\frac{3\omega^3}{2\pi^2\hbar\varepsilon_0 c}} c_1(\omega)\Bigg\{\frac{(\omega^2 - \Omega_{\mathrm{P}}^2 - F(\omega)) j_1\Big(\frac{\omega R_{\mathrm{s}}}{c}\Big)}{\omega\gamma(\omega)} + \Omega_{\mathrm{P}}\frac{\sqrt{\pi c R_{\mathrm{s}}^3}}{|\mathbf{r}_{\mathrm{e}}|^2\omega^2}\Bigg[\frac{1}{3} + \frac{\omega|\mathbf{r}_{\mathrm{e}}|^2 j_1\Big(\frac{\omega R_{\mathrm{s}}}{c}\Big) y_1\Big(\frac{\omega|\mathbf{r}_{\mathrm{e}}|}{c}\Big)}{cR_{\mathrm{s}}}\Bigg]\Bigg\}. \tag{5.75}$$

All things considered, $g_{\mathrm{P}}^{\perp}(\omega)$ takes on a relatively simple form. Additionally, we can define partial transverse spectral densities:

$$J_{lm}^{(p),0}(\omega) = \Big(g_{lm}^{(p),0}(\omega)\Big)^2 \quad \text{and} \quad J_{\mathrm{P}}^{\perp}(\omega) = \Big(g_{\mathrm{P}}^{\perp}(\omega)\Big)^2. \tag{5.76}$$

The free-space modes can be combined into one single "bright" mode at each frequency with the same procedure used at the end of section 2.1.3. Since $Y_{lm}(\vartheta = 0, \varphi) = \sqrt{\frac{2l+1}{4\pi}}\delta_{m0}$, we can rewrite the uncoupled free-space part of eq. (5.71) as

$$-\hbar\sum_t \sigma_t \int \mathrm{d}\omega\, \frac{\omega_t}{\omega}\sqrt{J'^0(\omega)}(\mathbf{d}_t \cdot \hat{\mathbf{z}})\Big[(a'(\omega))^\dagger - a'(\omega)\Big] + \mathrm{H.c.}, \tag{5.77a}$$

where

$$a'(\omega) = i\frac{\sum_{l>1}\sqrt{l(l+1)(2l+1)}\, j_l\Big(\frac{\omega|\mathbf{r}_{\mathrm{e}}|}{c}\Big) a_{l0}^{(\mathrm{tm})}(\omega)}{f(\omega)}, \tag{5.77b}$$

$$f(\omega) = \sqrt{\sum_{l>1} l(l+1)(2l+1) j_l^2\Big(\frac{\omega|\mathbf{r}_{\mathrm{e}}|}{c}\Big)} \tag{5.77c}$$

$$= \sqrt{\frac{2}{3}\Big(\frac{\omega|\mathbf{r}_{\mathrm{e}}|}{c}\Big)^2 - 6 j_1^2\Big(\frac{\omega|\mathbf{r}_{\mathrm{e}}|}{c}\Big)} \quad \text{and}$$

$$J'^0(\omega) = {\sum_{p,lm}}' J_{lm}^{(p),0}(\omega) = J^{\perp,0}(\omega)\Bigg[1 - \frac{3c j_1\Big(\frac{\omega|\mathbf{r}_{\mathrm{e}}|}{c}\Big)}{\omega|\mathbf{r}_{\mathrm{e}}|}\Bigg]. \tag{5.77d}$$

The prime on the last summation symbol again denotes the absence of the

"tm", $l = 1$, $m = 0$ modes, which are accounted for separately through the polaritonic $b(\omega)$ operators. A simple check reveals the limits $\frac{J'^0(\omega)}{\omega^3} \to 0$ when $\omega \ll c/|\mathbf{r}_e|$, and $J'^0(\omega) \to J^{\perp,0}(\omega)$ when $\omega \gg c/|\mathbf{r}_e|$, which reflects that the "tm", $l = 1$, $m = 0$ modes dominate the emitter-photon interaction at low frequencies and become insignificant in the opposite limit. Of course, the $a'(\omega)$ and $b(\omega)$ can also be combined into a single set of "emitter-centered" modes, with a total transverse spectral density equal to

$$J^{\perp}(\omega) = J'^0(\omega) + J_{\mathrm{P}}^{\perp}(\omega). \tag{5.78}$$

According to appendix E, we remark that $J^{\perp}(\omega)$ automatically satisfies the EM sum rule in eq. (5.26b).

Next, we consider the Coulomb interaction between the emitter and the charges within the nanosphere. In the long-wavelength approximation, we have

$$H_{\mathrm{e-s}} \approx -\sum_t \sigma_t (\mathbf{d}_t \cdot \hat{\mathbf{z}}) \big(\hat{\mathbf{z}} \cdot \mathbf{E}^{\parallel}(\mathbf{r}_e)\big) + \mathrm{H.c.} \tag{5.79}$$

Because the electronic sphere oscillations are much smaller than R_s and $|\mathbf{r}_e|$, we can simply replace the electric field outside the sphere by the electric field associated to a dipole moment equal to $\boldsymbol{\mu} = -\rho \frac{4\pi R_s^3}{3} z_s \hat{\mathbf{z}}$:

$$\mathbf{E}_s^{\parallel}(\mathbf{r}) \approx \frac{3(\boldsymbol{\mu} \cdot \hat{\mathbf{r}})\hat{\mathbf{r}} - \boldsymbol{\mu}}{4\pi\varepsilon_0 |\mathbf{r}|^3} \propto z_s. \tag{5.80}$$

Using eq. (5.70b), we obtain

$$H_{\mathrm{e-s}} \approx \hbar \sum_t \sigma_t \int \mathrm{d}\omega \, (\mathbf{d}_t \cdot \hat{\mathbf{z}}) g^{\parallel}(\omega) \big(b^{\dagger}(\omega) + b(\omega)\big) + \mathrm{H.c.}, \tag{5.81}$$

where

$$g^{\parallel}(\omega) = \frac{2\rho R_s^3}{3\varepsilon_0 \sqrt{2 m_s \hbar \omega} |\mathbf{r}_e|^3} c_1(\omega) \tag{5.82}$$

and the corresponding longitudinal spectral density is

$$J_{\mathrm{P}}^{\parallel}(\omega) = \big(g^{\parallel}(\omega)\big)^2 = \frac{\Omega_{\mathrm{P}}^2 R_s^3}{36\pi\hbar\varepsilon_0 \omega |\mathbf{r}_e|^6} c_1^2(\omega). \tag{5.83}$$

Note that $J_{\mathrm{P}}^{\parallel}(\omega)$ cannot be straightforwardly combined with $J_{\mathrm{P}}^{\perp}(\omega)$ because, although they both represent the coupling between the emitter and the same polaritonic modes $b(\omega)$, the transverse one takes the sum of ladder operators, the longitudinal interaction contains the difference. In any case, the formulation of the simple model provided thus far allows us to recover analytical,

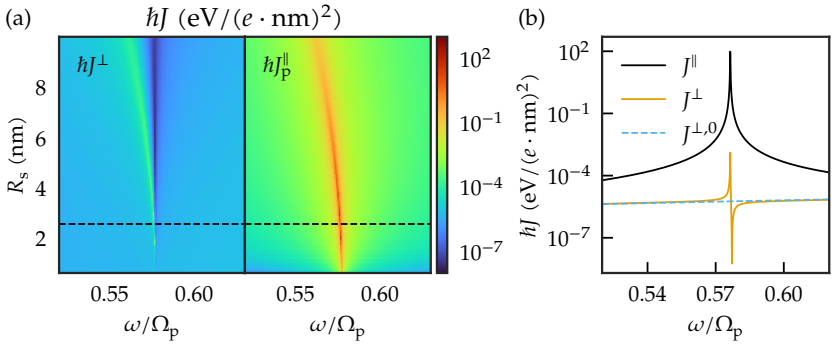

Figure 5.7: Spectral densities of the model for an emitter placed along the z axis at $|\mathbf{r}_{\mathrm{e}}| = R_{\mathrm{s}} + 1$ nm. (a) Map showing the dependence of $J^{\perp}$ (left) and $J^{\parallel}_{\mathrm{p}}$ (right) on the frequency and sphere's radius, as defined through eq. (5.78) and eq. (5.83), respectively. (b) Cut along the horizontal dashed line of panel (a). The dashed blue line represents the full free-space spectral density.

though not precisely simple, expressions for two independent spectral densities, one for the direct emitter-sphere Coulomb interaction, and another for the emitter-photon interaction. To continue our analysis, we show the dependence of these spectral densities on R_{s} and ω in fig. 5.7a, for an emitter placed at $|\mathbf{r}_{\mathrm{e}}| = R_{\mathrm{s}} + 1$ nm along the z axis. To allow for an even more direct comparison, we plot them at a fixed value of $R_{\mathrm{s}} \simeq 2.39$ nm in fig. 5.7b. Several features of fig. 5.7 stand out. First, $J^{\parallel}_{\mathrm{p}}$ is essentially a narrow peak that shows a similar red-shift with increasing radius as the one observed in the Fano coefficient (see fig. 5.6). Recall that our model of the plasmonic nanosphere was consistent with a loss-less Drude permittivity. Therefore, the finite width in figs. 5.7a and 5.7b has to do with the photon field that the negative sphere "drags" with itself, and becomes EM radiation. As for the transverse interaction, $J^{\perp}$ displays a peak too, several orders of magnitude smaller than $J^{\parallel}_{\mathrm{p}}$, followed by an equally narrow dip. Due to the presence of the free-space modes with $l > 1$, the dip does not reach 0 as could be expected from a typical Fano line shape. Besides, the dashed blue line in fig. 5.7b indicates the free-space spectral density, $J^{\perp,0}$, and it is clear that $J^{\perp}$ is essentially equal to it save for the narrow region close to the sphere's resonance. Hence, the USC regime is definitely out of reach for $J^{\perp}$, that is, for the emitter-photon interaction. Instead, it must originate from the direct Coulomb interaction between the emitter and the structure.

We can make the last statement more precise by defining the degree of

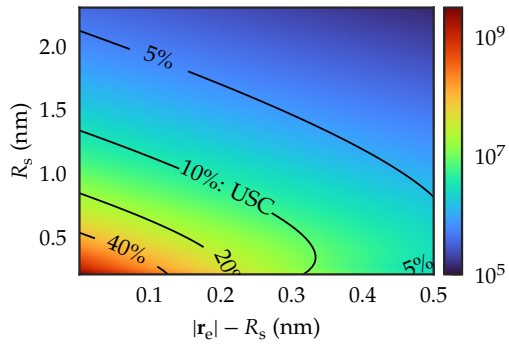

Figure 5.8: Longitudinality ℓ, defined in eq. (5.84). The contour lines are determined by the USC parameter η_{USC} for a reasonable emitter dipole moment value $|\mathbf{d}| = 10$ D, and the 10% line indicates the convential onset of the USC regime.

1

"longitudinality" as the following ratio

$$\ell = \frac{\left\langle J_{\mathrm{P}}^{\parallel} \right\rangle_{\mathrm{resonance}}}{\left\langle J^{\perp} \right\rangle_{\mathrm{resonance}}}. \tag{5.84}$$

Here, $\langle \dots \rangle_{\mathrm{resonance}}$ denotes an average taken over a narrow frequency interval fully containing the resonance. For concreteness, we have chosen the range $(0.57\Omega_{\mathrm{P}}, 0.58\Omega_{\mathrm{P}})$. The longitudinality is represented in fig. 5.8 as a function of R_{s} and $|\mathbf{r}_{\mathrm{e}}| - R_{\mathrm{s}}$. In addition, contour lines indicate the value of η_{USC} due to the longitudinal spectral density, for a transition dipole moment equal to $|\mathbf{d}| = 10$ D. To calculate it, we have fitted $J_{\mathrm{P}}^{\parallel}$ to a Lorentzian line shape with parameters g_{r}, ω_{r} and κ_{r},

$$J_{\mathrm{L}}(\omega) = \frac{g_{\mathrm{r}}^2}{\pi} \frac{\kappa_{\mathrm{r}}/2}{(\omega - \omega_{\mathrm{r}})^2 + (\kappa_{\mathrm{r}}/2)^2} \tag{5.85}$$

in the same interval considered for the average. Then, the USC ratio due to the longitudinal interaction is simply

$$\eta_{\mathrm{USC}} = \frac{|\mathbf{d}| g_{\mathrm{r}}}{\omega_{\mathrm{r}}}. \tag{5.86}$$

The figure shows that the degree of longitudinality ℓ takes extremely large values, from 10^5 to over 10^9. Most notably, it correlates positively with the values of η_{USC}; hence, the USC regime can only be reached through the longitudinal interaction between the emitter and the plasmonic nanosphere. Admittedly, the spatial arrangement and nanoparticle's size explored in fig. 5.8 are at the limit of experimental sensitivity. Still, fig. 5.8 has been prepared for illustrative purposes only, and we do not intend to claim that this configuration is ideal to reach the USC regime experimentally.

5.3.4 Sanity check

It is good practice to check one's results by comparing with other established methods. In the case at hand, the most direct comparison would be provided by using MQED. To that end, we take the long-wavelength, multipolar coupling Hamiltonian without magnetic effects in eq. (2.102). Explicitly, we have

$$\begin{aligned} H = &\sum_i \frac{\mathbf{p}_i^2}{2m_i} + \sum_{ij} \frac{q_i q_j}{8\pi\varepsilon_0 |\mathbf{r}_i - \mathbf{r}_j|} + \frac{1}{2\varepsilon_0} \int \mathrm{d}^3 r \, \left(\mathbf{P}_\mathrm{e}^\perp\right)^2 \\ &+ \sum_{\lambda=\mathrm{e,m}} \int \mathrm{d}^3 r \int \mathrm{d}\omega \, \hbar\omega \, \mathbf{f}_\lambda^\dagger(\mathbf{r},\omega) \cdot \mathbf{f}_\lambda(\mathbf{r},\omega) \\ &- \mathbf{d} \cdot \sum_{\lambda=\mathrm{e,m}} \int \mathrm{d}^3 r \int \mathrm{d}\omega \, \mathbf{G}_\lambda(\mathbf{r}_\mathrm{e},\mathbf{r},\omega) \cdot \mathbf{f}_\lambda(\mathbf{r},\omega) + \mathrm{H.c.}, \end{aligned} \tag{5.87}$$

where we have the PSE term and the interaction is written in terms of the polaritonic operators $\mathbf{f}_\lambda(\mathbf{r},\omega)$ that constitute the basis of MQED. Through the emitter-centered approach summarized in [180], assuming that the relevant transition dipole moment points along the z axis, we reduce the Hamiltonian above to

$$\begin{aligned} H = &\sum_i \frac{\mathbf{p}_i^2}{2m_i} + \sum_{ij} \frac{q_i q_j}{8\pi\varepsilon_0 |\mathbf{r}_i - \mathbf{r}_j|} + \frac{1}{2\varepsilon_0} \int \mathrm{d}^3 r \, \left(\mathbf{P}_\mathrm{e}^\perp\right)^2 \\ &+ \int \mathrm{d}\omega \, \hbar\omega \, C^\dagger(\omega) C(\omega) - \hbar(\mathbf{d}\cdot\hat{\mathbf{z}}) \int \mathrm{d}\omega \, \sqrt{J_\mathrm{MQED}(\omega)} \big(C^\dagger(\omega) + C(\omega)\big). \end{aligned}$$

Here, we have defined

$$C(\omega) = \frac{1}{\sqrt{J_\mathrm{MQED}(\omega)}} \sum_\lambda \int \mathrm{d}^3 r \, \hat{\mathbf{z}} \cdot \mathbf{G}_\lambda(\mathbf{r}_\mathrm{e},\mathbf{r},\omega) \cdot \mathbf{f}_\lambda(\mathbf{r},\omega) \quad \text{and} \tag{5.88a}$$

$$J_\mathrm{MQED}(\omega) = \frac{\omega^2}{\pi\hbar\varepsilon_0 c^2} \hat{\mathbf{z}} \cdot \mathrm{Im}\, \mathbf{G}(\mathbf{r}_\mathrm{e},\mathbf{r}_\mathrm{e},\omega) \cdot \hat{\mathbf{z}}, \tag{5.88b}$$

and we have removed the "dark" combinations of the $\mathbf{f}_\lambda(\mathbf{r},\omega)$ that are completely decoupled from the emitter.

In the MQED way, we have the full interaction of the emitter with the medium-assisted fields encoded in a single spectral density, $J_\mathrm{MQED}(\omega)$. This is at odds with the calculations presented before, as there were two different spectral densities, one for each physical interaction, which could not be directly combined. We have greatly benefited from having separate spectral densities for the purposes of illustrating the argument. However, the most direct comparison with MQED requires a single spectral density. We can remedy the problem by switching our calculations to a multicenter, multipolar

coupling picture. Then, we have only one emitter interaction term:

$$H_{\text{int}} = \frac{1}{\varepsilon_0}\int \mathrm{d}^3 r\, \mathbf{P}_{\text{e}}^{\perp}\cdot\mathbf{\Pi}^{\perp} \tag{5.89}$$

and $\mathbf{\Pi}^{\perp}$ can be written in terms of the polaritonic eigenmodes. Fortunately, the diagonalization procedure done earlier can be applied here with no changes required. The reason is that the structure-field interaction was, and still is, in the multipolar coupling picture, as mentioned right above eq. (5.55). The only difference, then, will be the physical significance of the eigenmodes, but the analytical mathematical expressions are the same. Therefore, with eq. (5.70c), we arrive at

$$\begin{aligned} H_{\text{int}} \approx i\hbar(\mathbf{d}\cdot\hat{\mathbf{z}})\sum_{p,lm}{}' \int \mathrm{d}\omega\, g_{lm}^{(p),0}(\omega)\Big[\big(a_{lm}^{(p)}(\omega)\big)^{\dagger} - a_{lm}^{(p)}(\omega)\Big] + \text{H.c.} \\ - \hbar(\mathbf{d}\cdot\hat{\mathbf{z}})\int \mathrm{d}\omega\, g_{\text{p}}(\omega)\big[b^{\dagger}(\omega) + b(\omega)\big] + \text{H.c.}, \end{aligned} \tag{5.90}$$

with the coupling strengths defined as

$$g_{lm}^{(p),0} = \sqrt{\frac{\omega}{2\hbar\varepsilon_0}}\big(\hat{\mathbf{z}}\cdot\boldsymbol{\psi}_{lm}^{(p)}(\mathbf{r}_{\text{e}})\big)\delta_{p,\text{tm}}\delta_{m0} \tag{5.91a}$$

$$g_{\text{p}}(\omega) = \sqrt{\frac{\omega}{2\hbar\varepsilon_0}}\int \mathrm{d}\omega'\, c_2(\omega,\omega')\hat{\mathbf{z}}\cdot\boldsymbol{\psi}_{10}^{(\text{tm})}(\omega',\mathbf{r}_{\text{e}})\frac{\omega'}{\omega}. \tag{5.91b}$$

The integral in $g_{\text{p}}(\omega)$ is different from the one in eq. (5.73b). Luckily, it is still similar enough that an analytical solution exists:

$$\begin{aligned} g_{\text{p}}(\omega) = \frac{1}{|\mathbf{r}_{\text{e}}|}\sqrt{\frac{3\omega^3}{2\pi^2\hbar\varepsilon_0 c}}c_1(\omega)\Bigg\{\frac{(\omega^2-\Omega_{\text{P}}^2-F(\omega))j_1\big(\frac{\omega R_{\text{s}}}{c}\big)}{\omega\gamma(\omega)} \\ + \Omega_{\text{P}}\frac{\sqrt{\pi c R_{\text{s}}^3}}{|\mathbf{r}_{\text{e}}|^2\omega^2}\left[\frac{\omega|\mathbf{r}_{\text{e}}|^2 j_1\big(\frac{\omega R_{\text{s}}}{c}\big)y_1\big(\frac{\omega|\mathbf{r}_{\text{e}}|}{c}\big)}{cR_{\text{s}}}\right]\Bigg\}. \end{aligned} \tag{5.92}$$

As intimidating as this expression can seem, a nice observation is that it is identical to eq. (5.75), although without the $\frac{1}{3}$ in the square brackets. Since $g_{\text{p}}(\omega)$ physically contains the Coulomb interaction, the $\frac{1}{3}$ must correspond to a negative Coulomb interaction that subtracts it from $g_{\text{p}}^{\perp}(\omega)$. Indeed, collecting all the factors that go with the $\frac{1}{3}$, we recover eq. (5.82) exactly.

Since all the mode operators involved in eq. (5.90) are orthogonal, we can

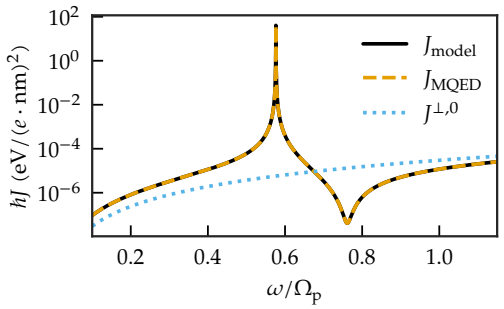

Figure 5.9: Comparison of the spectral densities derived from MQED, eq. (5.88b), and from the model in the multicenter, multipolar coupling picture, eq. (5.93). For the figure, the nanoparticle's radius is $R_s = 2.55$ nm. As in the previous plots, we have set $|\mathbf{r}_e| = R_s + 1$ nm.

1

now combine the spectral densities seamlessly into

$$J_{model} = \left(g_p(\omega)\right)^2 + {\sum_{p,lm}}' \left(g_{lm}^{(p),0}(\omega)\right)^2. \tag{5.93}$$

We now finish this comparison with a MQED result by plotting in fig. 5.9 both J_{MQED} and J_{model}. For the sake of the comparison, the scattering part of J_{MQED} has been obtained by retaining only the dipolar term in a multipolar expansion, since our model can only account for plasmonic excitations of this kind.

Both curves are dominated by a narrow peak corresponding to the dipolar plasmonic resonance, followed by a dip. Since we have not included material losses in the model, the dip is a direct consequence of the Fano diagonalization procedure for a single state (mode) coupled to a single continuum of states (modes), which always yields a point of perfect destructive interference. Still, the model's spectral density does not fully vanish at the dip, because it contains the free-space part of the modes that remain uncoupled from the sphere too, as per eq. (5.93). The perfect agreement between the curves displayed in the figure provides, a posteriori, further confirmation of the model's accuracy, particularly in the limit of small nanoparticles. For nanoparticle radii up to 50 nm, our analytical calculations still manage to quantitatively reproduce the main features of J_{MQED}. Beyond that, the dipolar resonance shifts to very low frequencies and significantly decreases in magnitude, and the free-space spectral density washes out everything in the range close to $\frac{\Omega_p}{\sqrt{3}}$. Physically, however, at those large radii and small emitter-nanosphere separations, higher multipoles become relevant, and a large pseudomode peak is developed at a finite frequency. Nevertheless, while these effects are not at all captured by the model discussed here, it still describes the response of small nanospheres perfectly well, as we intended from the outset.

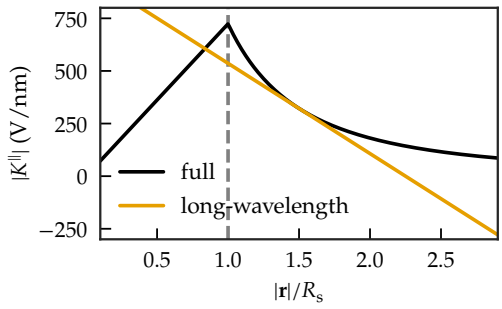

Figure 5.10: Linear coefficient in the series expansion of ϕ in terms of z_s. The vertical dashed line indicates the sphere's radius. The black curve takes into account the non-linear dependence of ϕ on $\mathbf{r}$, and hence the non-constant $\mathbf{E}_s^{\parallel}$, while the orange straight line corresponds to the constant $\mathbf{E}_s^{\parallel}$ imposed by the long-wavelength approximation in ab-initio simulations.

1

5.3.5 Polarization self-energy

Before ending the chapter, we can use the model to illustrate the actual relevance of the PSE due to the transverse fields. As we have seen in section 5.2.4, the full PSE is, in the long-wavelength approximation,

$$H_{\mathrm{DSE}} = \sum_{p,lm} \int \mathrm{d}\omega \, \frac{\left(g_{lm}^{(p),0}(\omega)\right)^2}{\omega} (\mathbf{d}\cdot\hat{\mathbf{z}})^2, \tag{5.94}$$

adapted to the model's particular notation. The full DSE, as has been argued at several points in the thesis (see section 2.4.1), softens the degree of divergence of the free-space Lamb shift, and allows for the recovery of Bethe's logarithmic formula. Still, if the USC regime is reached with the polaritonic modes within some frequency range, then those modes have to be treated explicitly, not just perturbatively, and likewise for the photonic modes significantly included in the polaritonic modes. It can, then, be argued that the part of the DSE associated to those modes should also be kept explicitly, as some people have done [178]. Our claim, according to the general argument in section 5.2, is that even if treated explicitly, that part of the DSE is still negligible.

Because of the symmetry of the model, only "tm", $l = 1$ and $m = 0$ modes behave different from the fully free-space scenario, due to their interaction with the nanosphere. Therefore, only these modes need to be considered for the explicit DSE contribution. However, since the diagonalization coefficient $c_2(\omega, \omega')$ converges to $\delta(\omega - \omega')$ far from the resonance, we only really need to include modes up to some "transparency" frequency Ω_T. Given that fig. 5.9 reveals that the sphere's spectral density converges to the free-space limit at frequencies close to Ω_P, we can take this value as Ω_T for illustration purposes. Taking eqs. (5.73a) and (5.74) into account, the explicit part of the DSE be-

comes

$$H_{\mathrm{DSE}} = (\mathbf{d}\cdot\hat{\mathbf{z}})^2 \sum_{p,lm} \int_0^{\Omega_{\mathrm{P}}} \mathrm{d}\omega \, \frac{3j_1^2\left(\frac{\omega|\mathbf{r}_{\mathrm{e}}|}{c}\right)}{2\hbar\varepsilon_0\pi^2 c|\mathbf{r}_{\mathrm{e}}|^2} \approx (\mathbf{d}\cdot\hat{\mathbf{z}})^2 \frac{\Omega_{\mathrm{P}}^3}{18\varepsilon_0\pi^2 c^3}$$
$$\approx 10^{-5}\ \mathrm{eV}/(e\cdot\mathrm{nm})^2 \times (\mathbf{d}\cdot\hat{\mathbf{z}})^2, \tag{5.95}$$

where the first approximation relies on $|\mathbf{r}_{\mathrm{e}}| \ll c/\Omega_{\mathrm{P}} \approx 20$ nm, for $\rho = 60\, e\cdot\mathrm{nm}^{-3}$, true in the cases under consideration to reach the USC regime. The numerical evaluation reveals that the part of the DSE that should be included in the Hamiltonian is very small indeed, contrary to what has been argued in other works.

Let us finish by addressing the absence of molecular bound states noted in [178]. As mentioned in section 5.2.4, since the DSE cannot "fix" it due to its smallness, there must be another resolution: it must be due to the effect of the long-wavelength approximation in ab-initio simulations, as it imposes a constant electric field over the computational box. We illustrate this point here by showing the full spatial dependence of ϕ, the sphere's Coulomb potential. In the small oscillation limit,

$$\phi(\mathbf{r}) = K^{\parallel}(\mathbf{r}) z_{\mathrm{s}} = z_{\mathrm{s}} \begin{cases} \dfrac{-\rho\hat{\mathbf{z}}\cdot\mathbf{r}}{3\varepsilon_0} & \text{if } |\mathbf{r}| \le R_{\mathrm{s}} \\ \dfrac{-\rho\hat{\mathbf{z}}\cdot\mathbf{r}}{3\varepsilon_0}\dfrac{R_{\mathrm{s}}^3}{|\mathbf{r}|^3} & \text{if } |\mathbf{r}| > R_{\mathrm{s}} \end{cases}. \tag{5.96}$$

We plot $K^{\parallel}$ for positions $\mathbf{r}$ along the z axis in fig. 5.10, where it is evident that a linear approximation of the potential, that is, a constant $\mathbf{E}_{\mathrm{s}}^{\parallel}$ will inevitably and unrealistically dismember the emitter.

5.4 Conclusions

Throughout the chapter, we have found ourselves highlighting various different, though complementary, issues. In the first section, we have seen how the Jaynes-Cummings Hamiltonian fails to capture the hallmark effects of the USC regime. Thus, one is forced to abandon the RWA and keep the full Rabi Hamiltonian, removing the simplifying assumptions that led to the Jaynes-Cummings model. Then, we have used the Rabi model to illustrate the phenomenology typically associated with the USC regime. However, the Rabi versus Jaynes-Cummings dichotomy sets up the deeper meaning and message of the chapter: simple toy models are fine until they are not anymore, and finding out how to correct them is generally not trivial. The only approach

that is sure to work is to take a few steps back and try to rederive the simple model from a more complete description. In section 5.1.2, we take the initial illustration further, by showing that the same simple model (specifically, the Rabi model) can account for completely different physical systems, which severely affects the meaning and value of the model's parameters. With it, we also pave the way to the main goal of the chapter, developed in the following sections, namely, establishing whether the USC regime can be reached at the few-emitter limit through photons or through the Coulomb interaction between the emitter and the nanocavity.

After enough context has been provided, we derive a fundamental bound on the degree to which photons can be confined by any cavity made of a realistic material. To obtain it, we consider the most favorable conditions; we imagine a cavity that confines photons perfectly up to a certain frequency, beyond which the material has to become transparent, and concentrates the coupling into a single transverse cavity mode. The remarkable result is that, even with those concessions in favor of photons, the total coupling strength can only reach an appreciable fraction of the bare frequencies if the transparency frequency is on the MeV scale. Since any cavity material becomes transparent at much lower frequencies (orders of magnitude lower, in fact), the USC is out of reach for the interaction between a few small emitters and photons. Another illuminating consequence of the bound is found by going back to the simplified single-mode models. By properly identifying the nature and origin of the PSE, we conclude that its effect must be negligible, as the USC regime is not achieved through photons.

We finish the chapter with an analytical example that illustrates the arguments and conclusions presented before. The example consists of a simplified description of a plasmonic nanosphere as two overlapping, homogeneously charged spheres. While this may sound like a very crude approximation, it is, actually, extremely accurate to describe the dipolar resonance of a small plasmonic sphere, as shown in fig. 5.9. By simplifying the model as much as possible, but not in excess, we correctly retain the relevant physics and obtain analytical expressions that mirror the arguments of section 5.2. Importantly, we see that the longitudinal interactions are, as claimed, the ones carrying the weight of the interaction. In any case, these calculations, together with the prior general arguments, should serve as a cautionary tale for anyone who finds themselves potentially extending a well-known model into a regime in which it has not been explicitly shown to work.

Chapter Six | Final conclusions

> Some of it wasn't very nice, but most of it was beautiful.
>
> *Dorothy Gale, The Wizard of Oz*

English

If we had to single out one aspect of light-matter interactions highlighted by this thesis, it would probably be the sheer breadth of the field. Indeed, we have explored quite different faces of the interaction between light and matter at the nanoscale. For instance, while chapters 3 and 4 deal with the description of phenomena in the weak coupling regime, chapter 5 changes the focus completely and is devoted to fundamental questions regarding the ultrastrong coupling regime. With this last chapter, we collect the main conclusions and outlook messages in each domain.

Weak coupling regime In chapter 3, we tackle the issue of dissipation induced on complex systems by general Markovian environments. While a Lindblad master equation (LME) can be derived for simple systems and environments with relative ease, when the simplifying assumptions are lifted, reaching the coveted LME is no longer a straightforward matter. To obtain such a master equation, under the sole premise that the environment has to be Markovian, we take a couple of steps back and revisit the framework of open quantum systems. There, the Bloch-Redfield equation (BRE) is the effective Markovian equation of motion that appears naturally after a perturbative treatment.

The BRE is an accurate master equation, very capable to describe dissipative phenomena. The problem with it is that, as a dynamical map, it is generally neither completely positive nor simply positive. Non-positivity means

that the populations' evolution predicted by the BRE can develop negative values, even if the density matrix starts out positive. Non-complete positivity means that, if the system is considered together with another one, the combined density matrix can develop negative populations, even if the additional system has no non-trivial dynamics. Besides, the BRE just looks more complicated than the standard LME that most studies employ. These issues have led to a general feeling of uneasiness around the BRE in many communities, which has fueled efforts to find ways to distill the LME that most closely follows the BRE. There are two practical advantages to this approach: first, by passing through a BRE, the parameters of the resulting LME are directly related to the underlying model of the environment, which automatically incorporates an ample variety of dissipative channels that are hard to envision otherwise. The second advantage, or goal perhaps, is that the final master equation is about as accurate as the BRE. One may wonder whether the similar accuracy still makes it worth the effort to transform the BRE into a LME. We argue that it does, because (i) it simplifies its structure and the interpretation of each term, (ii) it achieves complete positivity, an important and sought-out property in the field of open quantum systems, and (iii) it has computational benefits such as enabling quantum Monte Carlo simulations.

In the chapter, we revisit the traditional way to arrive at a LME, which is a procedure known as the secular approximation. The issue with it is that several physical effects are outright missed by it, which can be very relevant in emitters with realistic energy level structures. A goal of the community of open quantum systems is to find alternative procedures to reach a LME. In particular, we consider one approach that has been proposed recently [266], which we refer to as the geometric approach, as it involves taking suitable geometric means of the parameters in the BRE. Our contribution has been to identify and fix some lingering issues. Namely, the geometric LME, when generalized to deal with sufficiently complex environments, can display a non-Hermitian, environment-induced energy shift, and negative dissipative rates. Both these issues are critical, but our analysis shows that their fix required relatively minimal modifications. The Hermiticity of the energy shift was rescued by replacing the geometric mean with an arithmetic one. As for the negative dissipative rates, we performed extensive statistical studies to realize and confirm that the geometric procedure on its own, while not ensuring their absence, does in fact greatly suppress them. Thus, our final contribution to the field is a method to reach a LME from the BRE, inspired in the one in [266], which is more robust and has a greater degree of generality. As we have mentioned, the only real assumption is that the environment is Markovian.

We build on this methodological success in chapter 4 to describe the interaction between an atom and the vacuum fields supported by a nanoparticle. Physically, the common expectation is that the nanoparticle will induce small energy shifts and dissipation. The energy shifts depend on the relative position between the atom and the nanoparticle, and are generally known as Casimir-Polder potentials. They are a prime example of the dispersion forces that govern the nanoscale world of atoms and nanoparticles, responsible for adsorption to surfaces. The dissipative rates also vary with the relative location, and the common intuition is that they would tend to increase as the separation becomes smaller, an intuition backed by the well-known Purcell enhancement effect [15]. The customary account of these effects would be naturally captured by a secularized LME, which begs the question of the relation between chapter 4 and the ideas discussed in chapter 3. The issue with that kind of treatment is that the effects that the secular approximation misses can be relevant in this context, and quite so in fact.

To illustrate the shortcomings of the secular approximation, we focus on the dynamics of a fine-structure multiplet of the hydrogen atom, when it is placed in the vicinity of a spheroidal, AlN nanoparticle. The closeness in energy of the states under consideration implies that, rather than mere energy shifts, an environment-induced internal atomic interaction between different fine-structure states also appears, which are absent from the secularized master equation. In principle, these couplings are always there, and are of the same order as the regular Casimir-Polder shifts; the reason for their relevance is the small energy gap between the states that we consider. Indeed, the fine structure of the studied $n = 7$ multiplet is of the order of 10^{-6} eV, and the Casimir-Polder shifts reach a comparable energy scale when the atom-nanoparticle separation is about 50 nm. The environment-induced couplings prove to be quite consequential, as the effective energy spectrum of the atom develops marked avoided crossings and the eigenstates become complex mixtures of the original fine-structure eigenstates. For similar reasons, instead of mere decay rates associated to the hydrogenic states, a more accurate depiction of the dissipation includes off-diagonal rates that, in turn, yield complicated decay channels involving many fine-structure states at once.

Properly accounting for these effects requires the use of the ideas developed in the previous chapter, although the energy structure and the symmetry of the spatial arrangement considered grant us the possibility to perform additional simplifications. After these are carried out, it suffices to diagonalize an effective, non-Hermitian 7×7 Hamiltonian in order to show the great impact of the off-diagonal couplings and dissipative rates in the selected sys-

tem. For the particular configuration chosen in the chapter, perhaps the most striking feature directly caused by the off-diagonal terms is a reversal of the expected Purcell enhancement. As explained there, the nanoparticle-modified eigenstates and dissipative channels align in such a way that the dissipative rate of one of the eigenstates starts decreasing as the atom approaches the nanoparticle. Such effects, which would be completely missing from less refined methods, open the door to new potential knobs for the manipulation of quantum states, that may lead to unforeseen applications in, e.g., the field of quantum information science.

Ultrastrong coupling regime In the second part of the results presented in the thesis, chapter 5 deals with a foundational question concerning the ultrastrong coupling (USC) regime. More explicitly, it is about identifying the physical effect that lies at the origin of ultrastrong light-matter interactions. When it comes to reaching the USC regime, there are two main factors to consider: the matter coupling operator, e.g., the dipole moment, and the degree of field enhancement within the spatial region containing the matter. A common route to USC physics is to increase the matter operator through collective phenomena that require a macroscopic number of individual emitters in the cavity. In our work, we focus on the other extreme, where only a few small emitters are considered. The strategy is, in such cases, to boost the field enhancement by confining light to subwavelength volumes. In optics, nanocavities formed by plasmonic nanoparticles are promising candidates to reach the USC reegime, as are THz resonators in the far infrared. An important consequence of subwavelength confinement is that the role of transverse and longitudinal fields, that is, charge-photon and Coulomb charge-charge interactions, respectively, is reversed. The closer proximity of the emitter to the material structure of the cavity significantly enhances the Coulomb interactions, whereas the transverse, propagating fields are barely different from the free-space limit in comparison. In the field of nanophotonics, this is the justificaction for the well-known quasistatic approximation.

In chapter 5, we shed light on the concrete role of longitudinal and transverse fields. To that end, we first derive a fundamental limit to the degree of enhancement of the emitter-photon coupling strength achievable through any cavity made out of a realistic material, regardless of the geometry. With this bound, the coupling strength cannot be a sizeable fraction of the bare excitation frequencies unless the dipole moment of the matter part describes collective excitations, or the cavity perfectly concentrates the coupling strength of photons up to energies on the order of 2 MeV. The first scenario is auto-

matically discarded, because we focus on the few-emitter limit of USC. As for the second, it would require a material that can perfectly reflect photons from the whole spectrum up to gamma rays. Since such materials do not exist in the real world, thus possibility is too eliminated. Hence, the ultrastrong ratio η_{USC} cannot be larger than 0.1, unless Coulomb (longitudinal) interactions are considered explicitly; moreover, according to our analysis, η_{USC} can only take values comparable to 0.1 through the Coulomb interaction between the emitter and the cavity.

The difference in the physical origin of USC is not just a matter of nitpicking. Indeed, even if the emitter interaction terms with photons and the cavity's charges can be cast in a mathematically similar form with some assumptions, the meaning and value of the parameters are quite different. For example, the contentious polarization self-energy term that appears in the multipolar coupling Hamiltonian can be related to the emitter-photon coupling strength. Accordingly, some authors have claimed that it must play a key role in the USC regime. However, when the USC regime is reached through Coulomb interactions, the polarization self-energy is no longer related to the interactions that lead to such large coupling regimes. Thus, it stops being reasonable to ascribe important effects to it, different from the ones it already has in the absence of a cavity.

To finish, we bring the general ideas of the chapter to a more tangible level by explicitly solving the paradigmatic example of an emitter interacting with a plasmonic nanosphere. In order to obtain analytical insights, we simplify the description of the nanosphere in such a way that all the relevant and illustrative effects are still included. Then, the full problem is solved by obtaining closed expressions for the transverse (emitter-photon) and longitudinal (emitter-sphere) coupling strengths, when written in terms of the polaritonic eigenmodes of the sphere-photon system. Our calculations unequivocally show that the Coulomb interaction between the emitter and the sphere is the one that can give rise to USC, while the transverse interaction with photons has no hope of reaching it. With this example, we illustrate the other main point of the chapter, namely, that appropriate simplifications can make for a great theoretical tool, as long as they are truly appropriate. In that sense, hastily applying a simple model can imply the risk of inadvertedly extending it beyond its actual range of validity. While our model of the plasmonic sphere is a very crude one, we make sure a posteriori that it indeed captures the physics correctly. Otherwise, we keep the full electromagnetic complexity and only consider particular configurations to reach the final analytical expressions.

General remarks It would be disingenuous to say that the study of light, matter and their interactions started recently. Still, despite its age, the field of light-matter interactions is very much alive and well. Not only has it shaped our current knowledge of physics, but it is also a seemingly unending source of research avenues to this day. Since its early moments, the expanding body of light-matter literature became naturally organized in several major branches. As these areas kept growing, parts of them diffused into the neighboring topics, blurring the frontiers; however, sometimes, the speed and impact at which different areas merge suggests almost ballistic behavior, rather than diffusive. The intertwining of research topics is an extremely fertile ground to explore and test new ideas. In this ever-expanding field, it is part of the theoretician's job to stay alert and avoid the trap of directly applying a well-known model to a new experimental situation without first ensuring that it is valid. As someone once said, physics is a science, but approximation is an art form. The research results described in this thesis are, in different ways, examples of the kinds of effects and insights that can be completely missed by a less careful approach.

Castellano

Si tuviésemos que remarcar un aspecto de las interacciones entre la luz y la materia destacados por esta tesis, probablemente sería la enorme amplitud del campo. En efecto, hemos explorado caras notablemente distintas de la interacción entre la luz y la materia en la nanoescala. Sin ir más lejos, mientras que los capítulos 3 y 4 lidian con la descripción de fenómenos propios del régimen de acoplamiento débil, el capítulo 5 cambia el foco de atención completamente y está dedicado a cuestiones fundamentales sobre el régimen de acoplamiento ultrafuerte. Con este último capítulo reunimos las principales conclusiones y perspectivas en cada dominio.

Régimen de acoplamiento débil En el capítulo 3, abordamos la cuestión de la disipación inducida por entornos Markovianos generales en sistemas complejos. Mientras que para sistemas y entornos simples se puede derivar una ecuación maestra de Lindblad (LME), cuando las simplificaciones dejan de ser apropiadas, alcanzar la deseada ecuación de Lindblad se convierte en un asunto complicado. Para obtener una ecuación maestra de ese tipo, suponiendo únicamente que el entorno es Markoviano, tenemos que dar un paso atrás y revisar el formalismo the sistemas cuánticos abiertos. En este, la ecuación maestra efectiva que aparece de forma natural tras un tratamiento perturbativo es la ecuación de Bloch-Redfield (BRE).

La BRE puede describir con precisión fenómenos disipativos. El problema de esta ecuación es que, como mapa dinámico, generalmente no es ni completamente positiva, ni simplemente positiva. La no-positividad significa que, en la evolución predicha por la BRE, las poblaciones pueden desarrollar valores negativos, incluso si la matriz de densidad comienza siendo positiva. La falta de positividad completa implica que, si el sistema se considera junto con otro, la matriz de densidad combinada puede desarrollar también poblaciones negativas, incluso si el sistema adicional carece de dinámica no trivial. Además, la BRE tiene un aspecto más complicado que las LME empleadas en la mayoría de estudios. Estos aspectos negativos han dado pie a un sentimiento generalizado de desconfianza sobre la BRE en muchos ámbitos, lo que ha motivado esfuerzos para encontrar maneras de extraer la LME que más se aproxime a la BRE. Podemos destacar dos ventajas prácticas a esta manera de proceder. Primero, al pasar por una BRE, los parámetros de la LME resultante quedan directamente ligados al modelo subyacente del entorno, incorporando de forma automática una amplia variedad de canales disipativos que, de otro modo, serían difíciles de prever. La segunda ventaja, o quizá objetivo, es que la ecuación maestra final es parecida a la BRE en términos de precisión. Dada la similitud en la precisión, cabría preguntarse si realmente vale la pena transformar la BRE en una LME. Aquí argumentamos que sí, porque (i) la estructura e interpretación de cada término resulta ser más sencilla, (ii) se logra la positividad completa, una importante y deseable propiedad en el campo de los sistemas cuánticos abiertos, y (iii) presenta beneficios computacionales al posibilitar, por ejemplo, simulaciones cuánticas de Monte Carlo.

En dicho capítulo, revisamos la derivación tradicional de la LME a partir de la BRE, que consiste en un procedimiento conocido como la aproximación secular. El problema de esta aproximación es que se pierden definitivamente varios efectos físicos, algunos de los cuales pueden ser muy relevantes para emisores con estructuras de niveles energéticos realistas. Un objetivo de la comunidad de sistemas cuánticos abiertos es encontrar métodos alternativos para obtener una LME. En particular, consideramos uno propuesto recientemente [266] que designamos como procedimiento geométrico, ya que requiere de la evaluación adecuada de medias geométricas de los parámetros de la BRE. Nuestra contribución ha sido la identificación de algunos problemas que afectan al método geométrico, y su posterior solución. En concreto, cuando la LME geométrica se generaliza para tratar entornos suficientemente complejos, puede presentar un desplazamiento de niveles no Hermítico, así como constantes de decaimiento negativas. Ambas dificultades son críticas, pero nuestro análisis demuestra que se pueden solventar con cambios relativamente poco

invasivos. La Hermiticidad del desplazamiento de energías, por su parte, se respeta a base de reemplazar las medias geométricas por medias aritméticas. En cuanto a los decaimientos negativos, a partir de simulaciones iniciales nos percatamos de que el método geométrico por sí solo, si bien no asegura la positividad, sí que suprime los valores negativos significativamente. Esta observación fue confirmada mediante estudios estadísticos exhaustivos. Así, nuestra contribución final al campo consiste en un método para alcanzar una LME desde la BRE que está inspirado en el de [266], aunque es más robusto y tiene mayor grado de generalidad. Como hemos mencionado, la única suposición necesaria es que el entorno ha de ser suficientemente Markoviano.

En el capítulo 4, nos apoyamos sobre este éxito metodológico para describir la interacción entre un átomo y el campo de vacío modificados por una nanopartícula. Físicamente, la expectativa es que la nanopartícula induzca correcciones energéticas pequeñas y disipación. Las correcciones energéticas dependen de la posición relativa entre el átomo y la nanopartícula, y se conocen comúnmente como potenciales de Casimir-Polder. Son un buen ejemplo de las fuerzas de dispersión que gobiernan el mundo nanoscópico de los átomos y las nanopartículas, responsables de la adsorción en superficies. Los ritmos de decaimiento también varían con la posición relativa, y la intuición común es que tienden a aumentar a medida que la separación disminuye. Dicha expectativa está reforzada por el bien conocido efecto Purcell [15]. La descripción habitual de estos effectos queda perfectamente capturada en la LME secularizada, lo que sugiere que las ideas del capítulo 3 podrían no ser relevantes en este. Sin embargo, los capítulos 3 y 4 están íntimamente relacionados porque existen efectos adicionales, descartados por la aproximación secular, que pueden ser relevantes en el contexto de átomos y nanopartículas, y, de hecho, lo son en el capítulo 4.

Para ilustrar los defectos de la aproximación secular, nos centramos en la dinámica de un multiplete de estructura fina del átomo de hidrógeno cuando se coloca en la vecindad de una nanopartícula esferoidal de AlN. La cercanía en energía de los estados involucrados implica que no solo aparecen correcciones de las energías, los potenciales de Casimir-Polder, sino que también aparecen acoplamientos entre distintos estados de la estructura fina. La LME secularizada no contiene tales términos. En principio, los acoplamientos sí están presentes, y son del mismo orden que los potenciales de Casimir-Polder. La razón de su importancia es la pequeña diferencia de energía entre los estados considerados. Efectivamente, la estructura fina del multiplete estudiado, $n = 7$, es del orden de 10^{-6} eV, y los potenciales de Casimir-Polder alcanzan una escala de energías comparable cuando la separación entre el átomo

y la nanopartícula es del orden de 50 nm. Los acoplamientos inducidos por el entorno acaban teniendo importantes consecuencias, dado que el espectro de energías efectivo del átomo desarrolla marcados "cruces evitados" y los autoestados se convierten en mezclas complejas de los estados de estructura fina originales. Por motivos similares, en lugar de simples constantes de decaimiento asociadas a los estados propios del hidrógeno, una descripción más completa de la disipación incluye términos no diagonales que generan complejos canales de decaimiento que involucran numerosos estados de estructura fina a la vez.

El tratamiento adecuado de estos efectos requiere del uso de las ideas desarrolladas en el capítulo previo, aunque la estructura energética y la simetría de la composición espacial estudiada nos brindan la posibilidad de llevar a cabo approximaciones adicionales. Tras realizarlas, basta con diagonalizar un Hamiltoniano efectivo no Hermítico 7×7 para mostrar el gran impacto de los acoplamientos no diagonales en el sistema elegido. Para la configuración particular seleccionada, quizá la característica más llamativa directamente causada por los términos no diagonales es la inversión de la expectativa referente al comportamiento del efecto Purcell al variar la distancia entre el átomo y la nanopartícula. Como se explica en el capítulo, los autoestados y canales disipativos se alinean de tal manera que una de las constantes disipativas comienza a disminuir a medida que el átomo se aproxima a la nanopartícula. Tales efectos, completamente ausentes en métodos menos refinados, abren la puerta a nuevas formas de manipular estados cuánticos que pueden llevar al desarrollo de aplicaciones inesperadas en, por ejemplo, el campo de la información cuántica.

Régimen de acoplamiento ultrafuerte En la segunda parte de los resultados presentados en esta tesis, el capítulo 5 lidia con una pregunta fundacional sobre el régimen de acoplamiento ultrafuerte (USC). Explícitamente, se identifica el efecto físico subyacente al origen del régimen de USC en la interacción entre luz y materia. Cuando se trata de alcanzar el régimen de USC, hay que considerar dos factores principales: el operador de acoplamiento de la materia, por ejemplo, el momento dipolar, y el grado de amplificación del campo en la región espacial que contiene a la materia. Una posibilidad empleada comúnmente consiste en incrementar el operador de la materia a través de fenómenos colectivos que precisan de una cantidad macroscópica de emisores individuales en la cavidad. En nuestro trabajo, nos centramos en el extremo opuesto, en el que solo se incluyen unos pocos emisores pequeños. En esos casos, la estrategia se basa en incrementar la amplificación del campo mediante el con-

finamiento de la luz a volúmenes inferiores a la longitud de onda de la luz. En óptica, las nanocavidades formadas por nanopartículas plasmónicas son candidatas prometedoras para alcanzar el régimen de USC, así como lo son los resonadores en THz en el infrarrojo lejano. Una consequencia importante del confinamiento inferior a la longitud de onda es que el rol de los campos transversales y longitudinales, esto es, los que median las interacciones carga-fotón y carga-carga respectivamente, se invierte. La proximidad espacial del emisor a la estructura material de la cavidad amplifica las interacciones carga-carga de Coulomb, mientras que, por el contrario, los campos transversales propagantes apenas se diferencian del límite del campo en ausencia de estructura material. En el campo de la nanofotónica, esta es la justificación de la bien conocida aproximación cuasiestática.

En el capítulo 5, clarificamos el papel concreto que juegan los campos transversales y longitudinales. Para ello, primero derivamos un límite fundamental relativo al grado de amplificación de la interacción entre emisores y fotones que se puede conseguir mediante cualquier tipo de cavidad construida con un material realista, independientemente de su geometría. Debido a este límite, el acoplamiento entre emisores y fotones solo podría alcanzar fracciones significativas de las frecuencias naturales de excitación si, o bien el momento dipolar describiese excitaciones colectivas, o bien la cavidad concentrase perfectamente el acoplamiento a los fotones con energías del orden de 2 MeV. El primer escenario queda automáticamente descartado, ya que aquí nos centramos en el límite de pocos emisores. En cuanto al segundo, requeriría un material que, como mínimo, pudiera reflejar perfectamente fotones del espectro electromagnético entero hasta rayos gamma. Puesto que no existen tales materiales, esta posibilidad queda también eliminada. Por tanto, el coeficiente de acoplamiento ultrafuerte η_{USC} no puede ser mayor que 0.1, a no ser que la interacción de Coulomb (longitudinal) sea incluida explícitamente. Es más, de acuerdo con nuestro análisis, η_{USC} solo puede alcanzar valores del orden de 0.1 a través de la interacción de Coulomb entre el emisor y la cavidad.

La diferencia en el orígen físico del régimen de USC no se trata de un mero ejercicio académico. De hecho, aunque en algunos casos los términos de interacción del emisor con fotones y con las cargas que forman la cavidad se pueden expresar matemáticamente de manera similar, el significado y valor de los parámetros es ciertamente distinto. Por ejemplo, el polémico término de autoenergía de polarización que aparece en el Hamiltoniano con interacción multipolar puede relacionarse con el acoplamiento entre el emisor y los fotones. Por ello, algunos autores han afirmado que debe jugar un papel relevante en el régimen de USC. Sin embargo, cuando el régimen de USC se alcanza me-

diante la interacción de Coulomb, el término de autoenergía de polarización ya no está relacionado con el acoplamiento que da lugar a física en el régimen de USC. Así, deja de ser razonable asociarle efectos importantes distintos a los que ya tiene en ausencia de una cavidad.

Para acabar, ilustramos las ideas del capítulo con un ejemplo concreto. Con tal objetivo, resolvemos explícitamente el caso paradigmático de un emisor interactuando con una nanoesfera plasmónica. Para extraer información de manera analítica, simplificamos la descripción de la nanoesfera procurando incluir todos los efectos relevantes. De esta manera, podemos resolver el problema completo obteniendo expresiones cerradas para los acoplamientos correspondientes a las interacciones transversales (emisor-fotón) y longitudinales (emisor-esfera), al escribirlos en términos de los modos normales polaritónicos. Nuestros cálculos muestran, sin lugar a dudas, que la interacción de Coulomb entre el emisor y la esfera es la única que puede dar lugar al régimen de USC, mientras que la interacción transveral con fotones no puede alcanzarlo. Con este ejemplo también ilustramos el otro punto principal del capítulo, es decir, que las simplificaciones adecuadas pueden ser una gran herramienta teórica, siempre y cuando sean realmente adecuadas. En ese sentido, al aplicar apresuradamente un modelo demasiado sencillo se corre el riesgo inadvertido de extenderlo más allá de su rango real de validez. Aunque nuestro modelo de la esfera plasmónica no es excesivamente refinado, nos aseguramos a posteriori de que realmente captura la física correctamente. Por lo demás, mantenemos la complejidad electromagnética completa y tan solo consideramos configuraciones particulares para alcanzar las expresiones analíticas finales.

Comentarios generales El estudio de la luz, la materia y sus interacciones es una pieza central del conocimiento desde hace siglos que ha dado forma a gran parte de nuestra manera actual de entender y hacer física. Aun así, pese a su larga trayectoria, el campo de interacciones entre luz y materia continúa siendo robusto y dinámico, y supone una fuente de temas de investigación virtualmente inagotable. Desde su comienzo, la investigación en interacciones luz-materia quedó paulatinamiente organizada en varias ramas principales. Con el tiempo, dichas ramas continuaron creciendo hasta solapar con las adyacentes, desdibujando las fronteras. En ocasiones, el impacto de un área sobre otra cuando se entremezclan puede ser transformador, disruptivo y profundo. Generalmente, de hecho, el entrelazamiento de temas de investigación es un terreno sumamente fértil para explorar y probar nuevas ideas. En un campo en continua expansión como el de las interacciones entre luz y materia, es responsabilidad del sector teórico permanecer alerta para evitar la trampa de aplicar

directamente modelos bien conocidos en una situaciones experimentales nuevas, sin antes asegurar su validez. Como alguien dijo una vez, la física es una ciencia, pero aproximar es un arte. Los resultados de la investigación descritos en esta tesis son, en distintas formas, ejemplos de los tipos de efectos y comprensión que pueden quedar sepultados por un tratamiento descuidado.

Appendices

> For particulars, as every one knows, make for virtue and happiness; generalities are intellectually necessary evils.
>
> *Aldous Huxley, Brave new world*

Summary In the appendices that follow, we discuss details that have been skipped in the previous chapters. First, appendix A contains a summary of useful mathematical relations, derivations, analytical integrals, operator identities and the proof of a proposition concerning the positive semidefiniteness of a particular kind of matrix. We continue in appendix B with the numerical verification of the methods developed in chapter 4, namely, the Lindblad equation and the effective non-Hermitian Hamiltonian. After that, appendix C includes a short discussion of some relevant properties of the EM Green tensor and the calculations pertaining to the gauge invariance discussion in MQED of section 2.2.4. Next, we collect the details of the PZW transformation in appendix D, as well as minor modifications thereof. These are then extensively used in appendix E to derive EM sum rules concerning the spectral density, and to prove an expression for the PSE. Last, appendix F completes the calculations required for the analytical model used in chapter 5.

Appendix

A Useful mathematical relations

The present appendix provides a collection of the basic mathematical tools employed throughout the thesis. We also point to their most important applications, which are scattered in the main text's chapters and in the next appendices.

A.1 Short bestiary of important functions

We collect here the definitions for some relevant functions that appear in the preceding chapters:

Generalized Laguerre function These are the solutions to the associated Laguerre differential equations:

$$L_\lambda^\mu(x) = \sum_{k=0}^{\lambda} \frac{(-1)^k}{k!} \binom{\mu+\lambda}{\lambda+k} x^k \tag{A.1}$$

where $\lambda = n - l - 1$ and $\mu = 2l + 1$. Note that there exist different conventions in the literature for these functions (see [226]).

Associated Legendre polynomials These polynomials solve the general Legendre equation, and are defined by

$$P_\lambda^\mu(x) = \frac{(-1)^\mu}{2^\lambda \lambda!} \left(1 - x^2\right)^{\mu/2} \frac{\mathrm{d}^{\lambda+\mu}}{\mathrm{d}x^{\lambda+\mu}} \left(x^2 - 1\right)^\lambda \tag{A.2}$$

where λ and μ are integers and $|\mu| \leq \lambda$.

Spherical harmonics The solutions to the radial part of the Schrödinger equation with a central potential are

$$Y_\lambda^\mu(\vartheta,\varphi) = -\sqrt{\frac{(\lambda-\mu)!}{(\lambda+\mu)!}\frac{(2\lambda+1)}{4\pi}}P_\lambda^\mu(\cos\vartheta)e^{im\varphi}. \tag{A.3}$$

Their real versions are given by

$$Y_{\lambda\mu} = \begin{cases} \sqrt{2}(-1)^\mu \operatorname{Im} Y_\lambda^{-\mu} & \text{if } \mu<0, \\ Y_\lambda^0 & \text{if } \mu=0, \quad \text{and} \\ \sqrt{2}(-1)^\mu \operatorname{Re} Y_\lambda^\mu & \text{if } \mu>0. \end{cases} \tag{A.4}$$

Spherical Bessel functions In spherical coordinates, the solutions to the radial part of the Helmholtz equation follow the general expressions:

$$j_\mu = (-x)^\mu\left(\frac{1}{x}\frac{\mathrm{d}}{\mathrm{d}x}\right)^\mu\frac{\sin x}{x} \quad \text{and} \tag{A.5}$$

$$y_\mu = -(-x)^\mu\left(\frac{1}{x}\frac{\mathrm{d}}{\mathrm{d}x}\right)^\mu\frac{\cos x}{x}. \tag{A.6}$$

Dirac delta distribution The Dirac delta hardly needs any introduction, but it has some properties that are worth writing down:

$$\int \mathrm{d}x\, f(x)\partial_x\delta(x-x') = -\partial_x f(x'). \tag{A.7a}$$

With the chain rule:

$$\left.\begin{aligned}\partial_x\delta(x+\sigma x') &= \partial_{x+\sigma x'}\delta(x+\sigma x') \\ \partial_{x'}\delta(x+\sigma x') &= \sigma\partial_{x+\sigma x'}\delta(x+\sigma x')\end{aligned}\right\} \implies \partial_{x'}\delta(x+\sigma x') = \sigma\partial_x\delta(x+\sigma x') \tag{A.7b}$$

Another relation involving a Dirac delta that will come up in the Fano diagonalization of section 5.3 is

$$P\frac{1}{(x-y)(x'-y)} = \frac{1}{x-x'}P\left[\frac{1}{x'-y}-\frac{1}{x-y}\right] + \pi^2\delta(x-y)\delta(x'-y). \tag{A.7c}$$

A.2 Fourier transform relations

The mathematical tools of Fourier analysis are heavily featured in certain parts of the thesis. Here, we revisit them and point to the location in the text where

they are important. Most notably, the integrals involved in the analytic model of chapter 5 make extensive use of Fourier relations.

Basic definition For a function $f(x)$, we define its Fourier transform as

$$\tilde{f}(k) \equiv \mathcal{F}[f(x)](k) = \frac{1}{\sqrt{2\pi}} \int_{-\infty}^{\infty} \mathrm{d}x\, f(x) e^{-ikx}, \tag{A.8}$$

and the inverse relation is

$$\mathcal{F}^{-1}\left[\tilde{f}(k)\right](x) = \frac{1}{\sqrt{2\pi}} \int_{-\infty}^{\infty} \mathrm{d}k\, \tilde{f}(k) e^{ikx}. \tag{A.9}$$

Basic properties From the definitions, it is direct that

$$\mathcal{F}[f(x - x_0)](k) = e^{-ikx_0} \mathcal{F}[f(x)](k), \tag{A.10}$$

$$\mathcal{F}[f(ax)](k) = \frac{1}{|a|} \mathcal{F}[f(x)]\left(\frac{k}{a}\right), \quad \text{and} \tag{A.11}$$

$$\mathcal{F}[f(x)g(x)](k) = \frac{1}{\sqrt{2\pi}} \left(\mathcal{F}[f(x)] * \mathcal{F}[g(x)]\right)(k), \tag{A.12}$$

where $*$ denotes the convolution operation, namely,

$$[f * g](x) = \int_{-\infty}^{\infty} \mathrm{d}x'\, f(x') g(x - x'). \tag{A.13}$$

Basic transforms The basic Fourier transforms required in our calculations are

$$\mathcal{F}[\theta(t)](\omega) = \frac{1}{\sqrt{2\pi}} \left[-iP\frac{1}{\omega} + \pi\delta(\omega) \right], \tag{A.14}$$

$$\mathcal{F}\left[x^{-1}\right](k) = -i\sqrt{\frac{\pi}{2}} \mathrm{sign}(k), \tag{A.15}$$

$$\mathcal{F}[\delta(x)] = \frac{1}{\sqrt{2\pi}} \quad \text{and} \tag{A.16}$$

$$\mathcal{F}[j_1(x)](k) = \begin{cases} i\sqrt{\frac{\pi}{2}} k & \text{if } |k| < 1, \\ 0 & \text{otherwise.} \end{cases} \tag{A.17}$$

Correlation functions In chapter 2, a relation between λ_{rt} and γ_{rt} has been written. We derive it here with the expressions above:

$$\frac{\gamma(\omega)}{2} + i\lambda(\omega) = \int_0^{\infty} \mathrm{d}\tau\, c(\tau) e^{i\omega\tau} = \sqrt{2\pi}\mathcal{F}[c(\tau)\theta(\tau)](-\omega)$$

$$= \big(\mathcal{F}[c(\tau)] * \mathcal{F}[\theta(\tau)]\big)(-\omega)$$
$$= \frac{1}{\sqrt{2\pi}} \int \mathrm{d}\omega' \left[-iP\frac{1}{-\omega-\omega'} + \pi\delta(-\omega-\omega')\right]\mathcal{F}[c(\tau)](\omega'),$$

which implies that

$$\gamma(\omega) = \sqrt{2\pi}\mathcal{F}[c(\tau)](-\omega) \quad \text{and} \tag{A.18}$$
$$\lambda(\omega) = \frac{1}{\sqrt{2\pi}} P \int \mathrm{d}\omega' \, \frac{\mathcal{F}[c(\tau)](-\omega')}{\omega-\omega'} = \frac{1}{2\pi} P \int \mathrm{d}\omega' \, \frac{\gamma(\omega')}{\omega-\omega'} \tag{A.19}$$

Further transforms The basic transforms and properties above allow us to find

$$\mathcal{F}[j_1(x)j_1(yx)](k) = \frac{1}{\sqrt{2\pi}}\big(\mathcal{F}[j_1(x)] * \mathcal{F}[j_1(yx)]\big)(k)$$
$$= -\sqrt{\frac{\pi}{8}}\frac{1}{y^2}\begin{cases} \int_{-1}^{1} \mathrm{d}k' \, k'(k-k') & \text{if } 0 < k < y-1 \\ \int_{-1}^{k-y} \mathrm{d}k' \, k'(k-k') & \text{if } y-1 \le k < y+1 \\ 0 & \text{if } k \ge y+1 \end{cases}$$
$$= \sqrt{\frac{\pi}{8}}\frac{1}{y^2}\begin{cases} \frac{2}{3} & \text{if } 0 < k < y-1 \\ \frac{k^3 - 3(y^2+1)k + 2(y^3+1)}{6} & \text{if } y-1 \le k < y+1 \\ 0 & \text{if } k \ge y+1, \end{cases}$$

where $y \ge 1$. By virtue of the integrand's symmetry, we may extend the result to negative k as

$$\mathcal{F}[j_1(x)j_1(yx)](k) \tag{A.20}$$
$$= \sqrt{\frac{\pi}{8}}\frac{1}{y^2}\begin{cases} \frac{2}{3} & \text{if } |k| < y-1, \\ \frac{|k|^3 - 3(y^2+1)|k| + 2(y^3+1)}{6} & \text{if } y-1 \le |k| < y+1 \\ 0 & \text{otherwise.} \end{cases} \tag{A.21}$$

Setting $k = 0$ and $y = 1$, we arrive at

$$\frac{1}{\sqrt{2\pi}} \int_{-\infty}^{\infty} \mathrm{d}x \, j_1^2(x) = \sqrt{\frac{2}{\pi}} \int_0^{\infty} \mathrm{d}x \, j_1^2(x) = \frac{1}{3}\sqrt{\frac{\pi}{2}}, \tag{A.22}$$

which comes in handy to compute the polarization self-energy of the analytic model of a plasmonic sphere in eq. (5.57).

Another transform that is convenient to obtain is

$$\begin{aligned}\mathcal{F}\Big[\left(x^2-x_0^2\right)^{-1}\Big](k) &= \frac{1}{2x_0}\mathcal{F}\Big[(x-x_0)^{-1}-(x+x_0)^{-1}\Big](k)\\ &= \frac{e^{-ikx_0}-e^{ikx_0}}{2x_0}\mathcal{F}\big[x^{-1}\big](k) = -\sqrt{\frac{\pi}{2}}\frac{\sin(|k|x_0)}{x_0}.\end{aligned} \tag{A.23}$$

More complicated transforms At this point, we can combine the results thus far to evaluate two more complicated integrals. First,

$$\begin{aligned}\mathcal{F}\big[x^{-2}j_1^2(x)\big](k) &= \frac{1}{\sqrt{2\pi}}\int \mathrm{d}k'\ \mathcal{F}\big[j_1^2(x)\big](k')\mathcal{F}\big[x^{-2}\big](k-k')\\ &= \frac{1}{\sqrt{2\pi}}\frac{\pi}{4}\int_{-2}^{2}\mathrm{d}k'\ \frac{|k'|^3-6|k'|+4}{6}|k-k'|\\ &= \frac{\pi}{24\sqrt{2\pi}}\left(\frac{k^5}{10}-2k^3+4k^2-\frac{16}{5}\right),\end{aligned}$$

for $0 < k < 2$, and zero for $k > 0$. There, the Fourier transform of x^{-2} is obtained as the $x_0 \to 0$ limit of eq. (A.23). Taking the form of the integrand into consideration, the extension to negative values is

$$\mathcal{F}\big[x^{-2}j_1^2(x)\big](k) = \begin{cases}\dfrac{\pi}{24\sqrt{2\pi}}\left(\dfrac{|k|^5}{10}-2|k|^3+4k^2-\dfrac{16}{5}\right) & \text{if } |k|<2,\\ 0 & \text{otherwise.}\end{cases} \tag{A.24}$$

The resulting expression is useful to evaluate the equation of motion for the analytical model of the plasmonic nanosphere of chapter 5. Those calculations are shown in appendix F.3.

The second integral of interest is a more complicated generalization. For that reason, we only evaluate it explicitly at $k = 0$:

$$\begin{aligned}&\mathcal{F}\left[\frac{j_1(x)j_1(yx)}{x^2-x_0^2}\right](k=0)\\ &\quad= \frac{1}{\sqrt{2\pi}}\int \mathrm{d}k'\ \mathcal{F}[j_1(x)j_1(yx)](k')\mathcal{F}\Big[\left(x^2-x_0^2\right)^{-1}\Big](-k') \qquad (A.25)\\ &\quad= \sqrt{\frac{2}{\pi}}\int_0^\infty \mathrm{d}k'\ [j_1(x)j_1(yx)](k')\mathcal{F}\Big[\left(x^2-x_0^2\right)^{-1}\Big](k')\\ &\quad= -\sqrt{\frac{\pi}{2}}\frac{1}{12y^2x_0}\left\{\int_0^{y-1}\mathrm{d}k'\ 4\sin(k'x_0)\right.\end{aligned}$$

$$+\int_{y-1}^{y+1} \mathrm{d}k' \left[k'^3 - 3(y^2+1)k' + 2(y^3+1)\right]\sin(k'x_0)\Bigg\}$$
$$= -\sqrt{\frac{\pi}{2}}\frac{1}{y^2x_0^2}\left[\frac{1}{3} + y^2x_0 j_1(x_0)y_1(yx_0)\right]. \tag{A.26}$$

The last step entails a repeated and dull application of integration by parts, plus a reshuffling of terms, and has been skipped for the reader's sake. This particular integral is required to compute the Fano energy shift integral $F(\Omega)$ in eq. (5.66) and the emitter-polariton coupling strengths in the minimal and multipolar coupling schemes, $g_{\mathrm{p}}^{\perp}(\omega)$ and $g_{\mathrm{p}}(\omega)$ in eqs. (5.75) and (5.92).

A.3 Transverse and longitudinal vector fields

Here, we succinctly discuss the properties of transverse and longitudinal vector fields following references [194, 301]. Although the Helmholtz decomposition theorem is the mathematical backbone that justifies the whole section, we need not concern ourselves with its most general formulation. Instead, we confine our attention to its consequences on a much narrower situation. Let $\mathbf{F}$ be a twice differentiable vector field defined on $\mathbb{R}^3$ that vanishes faster than $1/|\mathbf{r}|$ as $|\mathbf{r}| \to \infty$. Then, the theorem states that there exist two unique fields $\mathbf{F}^{\perp}$ and $\mathbf{F}^{\parallel}$, respectively, such that

$$\nabla\cdot\mathbf{F}^{\perp} = 0, \quad \text{and} \quad \nabla\times\mathbf{F}^{\parallel} = \mathbf{0} \tag{A.27a}$$

and

$$\mathbf{F} = \mathbf{F}^{\perp} + \mathbf{F}^{\parallel}. \tag{A.27b}$$

Then, $\mathbf{F}^{\perp}$ and $\mathbf{F}^{\parallel}$ are the so-called transverse and longitudinal components. These names stem from the fact that, in reciprocal space,

$$\mathbf{k}\cdot\tilde{\mathbf{F}}^{\perp}(\mathbf{k}) = 0 \quad \text{and} \quad \mathbf{k}\times\tilde{\mathbf{F}}^{\parallel}(\mathbf{k}) = \mathbf{0}, \tag{A.28}$$

where $\tilde{\mathbf{F}}^{\perp}(\mathbf{k})$ and $\tilde{\mathbf{F}}^{\parallel}(\mathbf{k})$ are the Fourier expansion coefficients of $\mathbf{F}^{\perp}$ and $\mathbf{F}^{\parallel}$.

The introduction of the transverse and longitudinal components allows us to split the space of twice differentiable vector fields with the specified boundary condition into two orthogonal components. To each subspace, we can assign a projection delta operator $\delta^{\perp}$ and $\delta^{\parallel}$, where $\delta = \delta^{\perp} + \delta^{\parallel}$. In the real-space representation, the action of these δ operators on vector fields is given by a dot product over spatial indices and an integration over the spatial variable. Thus,

$$\mathbf{F}(\mathbf{r}) = \int \mathrm{d}^3 r' \; \delta(\mathbf{r}-\mathbf{r}') \cdot \mathbf{F}(\mathbf{r}), \tag{A.29a}$$

$$\mathbf{F}^{\perp}(\mathbf{r}) = \int \mathrm{d}^3 r' \; \delta^{\perp}(\mathbf{r}-\mathbf{r}') \cdot \mathbf{F}(\mathbf{r}), \tag{A.29b}$$

$$\mathbf{F}^{\parallel}(\mathbf{r}) = \int \mathrm{d}^3 r' \; \delta^{\parallel}(\mathbf{r}-\mathbf{r}') \cdot \mathbf{F}(\mathbf{r}). \tag{A.29c}$$

The real-space representation of these delta functions is

$$\delta(\mathbf{r}-\mathbf{r}') = -\frac{1}{4\pi}\nabla_{\mathbf{r}}^2\left(\frac{\mathbf{1}}{|\mathbf{r}-\mathbf{r}'|}\right) \tag{A.30a}$$

$$\begin{aligned}\delta^{\perp}(\mathbf{r}-\mathbf{r}') &= \frac{1}{4\pi}\nabla_{\mathbf{r}} \times \nabla_{\mathbf{r}} \times \left(\frac{\mathbf{1}}{|\mathbf{r}-\mathbf{r}'|}\right) \\ &= \frac{2}{3}\delta(\mathbf{r}-\mathbf{r}') - \frac{\mathbf{1}|\mathbf{r}-\mathbf{r}'|^2 - 3(\mathbf{r}-\mathbf{r}')\otimes(\mathbf{r}-\mathbf{r}')}{4\pi|\mathbf{r}-\mathbf{r}'|^5} \quad \text{and}\end{aligned} \tag{A.30b}$$

$$\begin{aligned}\delta^{\parallel}(\mathbf{r}-\mathbf{r}') &= -\frac{1}{4\pi}\nabla_{\mathbf{r}} \otimes \nabla_{\mathbf{r}}\left(\frac{\mathbf{1}}{|\mathbf{r}-\mathbf{r}'|}\right) \\ &= \frac{1}{3}\delta(\mathbf{r}-\mathbf{r}') + \frac{\mathbf{1}|\mathbf{r}-\mathbf{r}'|^2 - 3(\mathbf{r}-\mathbf{r}')\otimes(\mathbf{r}-\mathbf{r}')}{4\pi|\mathbf{r}-\mathbf{r}'|^5},\end{aligned} \tag{A.30c}$$

where we have used $\nabla^2\mathbf{F} = (\nabla\otimes\nabla)\cdot\mathbf{F} - \nabla\times\nabla\times\mathbf{F}$, and differentiated with care (see [301] and the references therein). Since they are essentially projection operators, they also satisfy

$$\int \mathrm{d}^3 s \; \delta^{\perp/\parallel}(\mathbf{r}-\mathbf{s}) \cdot \delta^{\perp/\parallel}(\mathbf{r}'-\mathbf{s}) = \delta^{\perp/\parallel}(\mathbf{r}-\mathbf{r}') \quad \text{and} \tag{A.31}$$

$$\int \mathrm{d}^3 s \; \delta^{\parallel/\perp}(\mathbf{r}-\mathbf{s}) \cdot \delta^{\perp/\parallel}(\mathbf{r}'-\mathbf{s}) = \mathbf{0}, \tag{A.32}$$

which allows us to write

$$\int \mathrm{d}^3 r \; \mathbf{F}\cdot\mathbf{T} = \int \mathrm{d}^3 r \; \mathbf{F}^{\parallel}\cdot\mathbf{T}^{\parallel} + \int \mathrm{d}^3 r \; \mathbf{F}^{\perp}\cdot\mathbf{T}^{\perp}, \tag{A.33}$$

for any two vector fields $\mathbf{F}$ and $\mathbf{T}$, as the crossed contributions vanish.

Finally, the concepts of transversality and longitudinality can be extended to dyadic tensors as well, as done extensively in section 2.2. Specifically, for the dyadic tensors like the EM Green tensor $\mathbf{G}$ we can have either transversality or longitudinality, from the left, from the right, or from both sides:

$$^{\perp/\parallel}\mathbf{G}(\mathbf{r},\mathbf{r}',\omega) = \int \mathrm{d}^3 s \, \mathrm{d}^3 s' \; \delta^{\perp/\parallel}(\mathbf{r}-\mathbf{s}) \cdot \mathbf{G}(\mathbf{s},\mathbf{r}',\omega), \tag{A.34a}$$

$$\mathbf{G}^{\perp/\parallel}(\mathbf{r},\mathbf{r}',\omega) = \int \mathrm{d}^3 s \, \mathrm{d}^3 s' \; \mathbf{G}(\mathbf{r},\mathbf{s},\omega) \cdot \delta^{\perp/\parallel}(\mathbf{s}-\mathbf{r}'), \quad \text{and} \tag{A.34b}$$

$$^{\perp/\parallel}\mathbf{G}^{\perp/\parallel}(\mathbf{r},\mathbf{r}',\omega) = \int \mathrm{d}^3 s \, \mathrm{d}^3 s' \; \delta^{\perp/\parallel}(\mathbf{r}-\mathbf{s}) \cdot \mathbf{G}(\mathbf{s},\mathbf{s}',\omega) \cdot \delta^{\perp/\parallel}(\mathbf{s}'-\mathbf{r}'). \tag{A.34c}$$

A.3.1 Orthonormal bases for transverse fields

Before finishing with our account of transverse and longitudinal fields, we give here the expressions for two useful bases of transverse vector fields that are used in chapter 2 and chapter 5:

Real plane waves Transverse fields can be expanded in terms of the following set of orthogonal functions

$$\boldsymbol{\psi}^{\mathrm{c}}_{p}(\mathbf{k},\mathbf{r}) = \frac{\sqrt{2}\cos(\mathbf{k}\cdot\mathbf{r})}{(2\pi)^{3/2}}\boldsymbol{\epsilon}_{p}(\mathbf{k}) \quad \text{and} \quad \boldsymbol{\psi}^{\mathrm{s}}_{p}(\mathbf{k},\mathbf{r}) = \frac{\sqrt{2}\sin(\mathbf{k}\cdot\mathbf{r})}{(2\pi)^{3/2}}\boldsymbol{\epsilon}_{p}(\mathbf{k}). \tag{A.35}$$

Here, the superindices "c" and "s" indicate which trigonometric function is used, $\mathbf{k}$ belongs to a reciprocal half space, and $\boldsymbol{\epsilon}_{p}(\mathbf{k})$ are polarization unit-vectors perpendicular to $\mathbf{k}$ and to each other, labeled with $p = 1, 2$. The normalization ensures that

$$\int \mathrm{d}^3 r\; \boldsymbol{\psi}^{f}_{p}(\mathbf{k},\mathbf{r}) \cdot \boldsymbol{\psi}^{f'}_{p'}(\mathbf{k}',\mathbf{r}) = \delta_{ff'}\delta_{pp'}\delta^{(3)}(\mathbf{k}-\mathbf{k}'), \tag{A.36}$$

as can be checked with eq. (A.16). For completeness, the more common complex version of these plane waves is

$$\boldsymbol{\psi}_{p}(\mathbf{k},\mathbf{r}) = \frac{e^{i(\mathbf{k}\cdot\mathbf{r})}}{(2\pi)^{3/2}}\boldsymbol{\epsilon}_{p}(\mathbf{k}), \tag{A.37}$$

where $\mathbf{k}$ now belongs to the full reciprocal space to compensate for the fact that only one family of functions is required.

Real spherical waves Another basis that plays a key role in chapter 5 is that of spherical waves:

$$\boldsymbol{\psi}^{(\mathrm{te})}_{lm}(\omega,\mathbf{r}) = \frac{\omega}{c}\sqrt{\frac{2}{l(l+1)\pi c}}\, j_l\!\left(\frac{\omega|\mathbf{r}|}{c}\right)\left[\hat{\boldsymbol{\vartheta}}\frac{\partial_\varphi}{\sin\vartheta} - \hat{\boldsymbol{\varphi}}\partial_\vartheta\right]Y_{lm}(\vartheta,\varphi) \quad \text{and} \tag{A.38a}$$

$$\begin{aligned}\boldsymbol{\psi}^{(\mathrm{tm})}_{lm}(\omega,\mathbf{r}) = \frac{c}{\omega}\nabla\times\boldsymbol{\psi}^{(\mathrm{te})}_{lm}(\omega,\mathbf{r}) &= \hat{\mathbf{r}}\frac{1}{|\mathbf{r}|}\sqrt{\frac{2l(l+1)}{\pi c}}\, j_l\!\left(\frac{\omega|\mathbf{r}|}{c}\right)Y_{lm}(\vartheta,\varphi) \\ &+ \frac{1}{|\mathbf{r}|}\sqrt{\frac{2}{l(l+1)\pi c}}\,\partial_{|\mathbf{r}|}\Big[|\mathbf{r}|j_l\!\left(\frac{\omega|\mathbf{r}|}{c}\right)\Big]\left[\hat{\boldsymbol{\vartheta}}\partial_\vartheta + \hat{\boldsymbol{\varphi}}\frac{\partial_\varphi}{\sin\vartheta}\right]Y_{lm}(\vartheta,\varphi),\end{aligned} \tag{A.38b}$$

where $l \geq 1$, $|m| \leq l$ and $\omega > 0$. Again, we work with real functions by choosing the real spherical harmonics over their more common complex counter-

parts, Y_l^m, defined in appendix A.1.

A.3.2 Example

An illustrative observation is that even if the support of $\mathbf{F}$ is finite, meaning that it only takes non-zero values within a finite region of space, the support of $\mathbf{F}^\perp$ and $\mathbf{F}^\parallel$ will generally be unbounded. For concreteness, let us consider the current density due to the motion of the negatively charged sphere of section 5.3:

$$\mathbf{j}_\mathrm{s}(\mathbf{r}) \approx -\rho(\mathbf{r})\dot{z}_\mathrm{s}\hat{\mathbf{z}}, \tag{A.39}$$

where $\rho(\mathbf{r}) = \rho\theta(R_\mathrm{s} - |\mathbf{r} - z_\mathrm{s}\hat{\mathbf{r}}|) \approx \rho\theta(R_\mathrm{s} - |\mathbf{r}|)$. Note that the charge density written in section 5.3 includes the explicit oscillation of the negative sphere, which is neglected in the subsequent calculations, while we neglect it from the beginning here. Thus, the current density has its support confined to a sphere of radius R_s. We next explore its ensuing transverse and longitudinal parts. First, with the results of section F.1.2, we can expand the transverse part of $\mathbf{j}_\mathrm{s}$ in the spherical wave basis to find

$$\mathbf{j}_\mathrm{s}^\perp(\mathbf{r}) = \int \mathrm{d}\omega\, \frac{-4\rho\dot{z}_\mathrm{s}R_\mathrm{s}^2}{\sqrt{3}c} j_1\!\left(\frac{\omega R_\mathrm{s}}{c}\right)\boldsymbol{\psi}_{10}^{(\mathrm{tm})}(\omega, \mathbf{r}). \tag{A.40}$$

The integral above is hard to do analytically, although a combination of the methods developed in appendix A.2 shoud allow it. In any case, we avoid such endeavor and will merely evaluate it numerically.

On the other hand, upon manipulating Maxwell' equations we may write

$$\frac{1}{c^2}\ddot{\mathbf{E}}^\perp - \nabla^2\mathbf{E}^\perp = -\mu_0\partial_t\mathbf{j}_\mathrm{s} - \frac{1}{c^2}\ddot{\mathbf{E}}^\parallel \implies \partial_t\mathbf{j}_\mathrm{s}^\parallel = -\varepsilon_0\ddot{\mathbf{E}}^\parallel. \tag{A.41}$$

The longitudinal field due to the nanosphere, $\mathbf{E}^\parallel$ is, to the level approximation required here,

$$\mathbf{E}^\parallel(\mathbf{r}) = \begin{cases} \dfrac{-\rho z_\mathrm{s}R_\mathrm{s}^3}{3\varepsilon_0|\mathbf{r}|^3}\left[3\cos\vartheta\sin\vartheta\hat{\mathbf{x}} + \left(3\cos^2\vartheta - 1\right)\hat{\mathbf{z}}\right] & \text{if } |\mathbf{r}| > R_\mathrm{s}, \\ \dfrac{\rho z_\mathrm{s}}{3\varepsilon_0}\hat{\mathbf{z}} & \text{if } |\mathbf{r}| \le R_\mathrm{s}. \end{cases} \tag{A.42}$$

Therefore,

$$\mathbf{j}_\mathrm{s}^\parallel(\mathbf{r}) = \begin{cases} \dfrac{\rho\dot{z}_\mathrm{s}R_\mathrm{s}^3}{3|\mathbf{r}|^3}\left[3\cos\vartheta\sin\vartheta\hat{\mathbf{x}} + \left(3\cos^2\vartheta - 1\right)\hat{\mathbf{z}}\right] & \text{if } |\mathbf{r}| > R_\mathrm{s}, \\ \dfrac{-\rho\dot{z}_\mathrm{s}}{3}\hat{\mathbf{z}} & \text{if } |\mathbf{r}| \le R_\mathrm{s}, \end{cases} \tag{A.43}$$

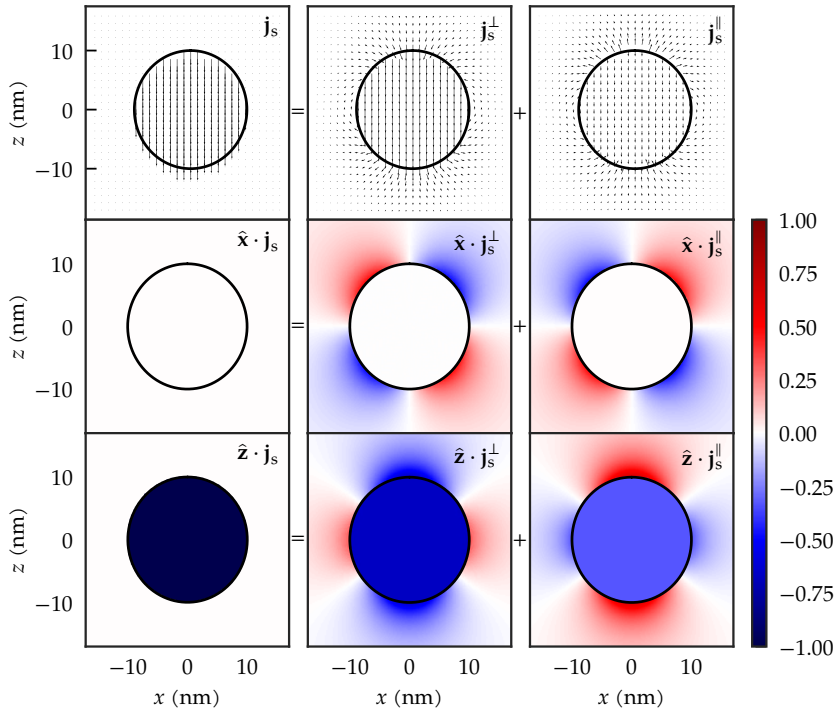

Figure A.1: Cut along the $x-z$ plane of the current density associated to the motion of the negatively charged sphere of the analytical calculations in section 5.3. Left, center and right columns: total, transverse and longitudinal currents. Top, middle and bottom rows: full vector field, x component and z component.

that is, constant in the interior of the sphere, and a dipolar pattern outside. Because $\mathbf{j}_s = \mathbf{j}_s^\perp + \mathbf{j}_s^\parallel$, we can use the information on $\mathbf{j}_s^\parallel$ to say more about the transverse part:

$$\mathbf{j}_s^\perp(\mathbf{r}) = \begin{cases} \dfrac{-\rho \dot{z}_s R_s^3}{3|\mathbf{r}|^3}\left[3\cos\vartheta\sin\vartheta\hat{\mathbf{x}} + \left(3\cos^2\vartheta - 1\right)\hat{\mathbf{z}}\right] & \text{if } |\mathbf{r}| > R_s, \\ \dfrac{-2\rho\dot{z}_s}{3}\hat{\mathbf{z}} & \text{if } |\mathbf{r}| \leq R_s. \end{cases} \tag{A.44}$$

We have thus been able to skip the analytical calculation of eq. (A.40).

In order to more graphically understand the above expressions, we plot the current in fig. A.1 along the $x-z$ plane. The top panels contain the full vector fields, while the next rows represent the x and z components. Vertically, the columns correspond, from left to right, to $\mathbf{j}_s$, $\mathbf{j}_s^\perp$ and $\mathbf{j}_s^\parallel$. It is necessary to clarify that $\mathbf{j}^\perp$ has been directly computed with eq. (A.40). With fig. A.2 we show that, indeed, the numerical evaluation of eq. (A.40) converges to the

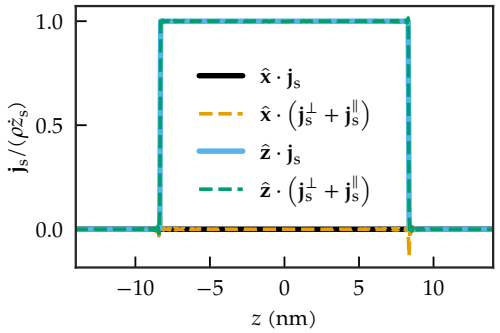

Figure A.2: Cut along the $x = 0$ nm line showing the components of eq. (A.40). Continuous lines represent the x and z components of $\mathbf{j}_s$, while dashed lines correspond to the sum of $\mathbf{j}_s^{\perp}$ and $\mathbf{j}_s^{\parallel}$, with the transverse part obtained numerically through eq. (A.40).

1

analytical result. Because we expand here a discontinuous function in terms of orthogonal functions, the spherical-wave functions, fig. A.2 displays the well-known Gibbs phenomenon at the discontinuities, to the extent that the plotting mesh allows.

As fig. A.1 clearly shows, $\mathbf{j}_s^{\perp}$ and $\mathbf{j}_s^{\parallel}$ are not limited to the spherical region within which $\mathbf{j}_s$ is non-zero. This fact has important consequences; for instance, it can be used to recover the finite propagation speed of EM fields, even when the $\mathbf{E}^{\parallel}$ is a manifestly instantaneous function of the charges [205]. Indeed, considering this precise example of a localized source current $\mathbf{j}_s$, we can look at the transverse fields in eq. (A.41):

$$\frac{1}{c^2}\ddot{\mathbf{E}}^{\perp} - \nabla^2\mathbf{E}^{\perp} = -\mu_0\partial_t\mathbf{j}_s^{\perp}. \tag{A.45}$$

Accordingly, $\mathbf{E}^{\perp}$ satisfies a wave equation with a finite propagation speed equal to c. However, its source, $\mathbf{j}_s^{\perp}$, is no longer a localized one. Instead it extends beyond the range of $\mathbf{j}_s$, and is linked to the instantaneous longitudinal field through its relation with $\mathbf{j}_s^{\parallel} \sim \dot{\mathbf{E}}^{\parallel}$.

A.4 Operator identities

In order to evaluate numerous expressions related to unitary transformations, we will use Campbell's identity [302]

$$e^X Y e^{-X} = Y + [X,Y] + \frac{1}{2!}[X,[X,Y]] + \frac{1}{3!}[X,[X,[X,Y]]] + \cdots \tag{A.46}$$

Particularly relevant will be the situation where $[X,[X,Y]] = 0$. We study here in detail two model transformations.

Transformation 1 Let x and p be a position variable and its canonically conjugate momentum, that is, $[p, x] = -i\hbar$. We choose $X = f(x)$ and $Y = p$, such that f is a smooth function. Then,

$$e^{f(x)} p e^{-f(x)} = p + [f(x), p] + \frac{1}{2}[f(x), [f(x), p]] + \cdots \tag{A.47a}$$

with $[f(x), p] = i\hbar \partial_x f(x)$. Since $[f(x), \partial_x f(x)] = 0$, only the first two terms are non-vanishing, and the final result is

$$e^{f(x)} p e^{-f(x)} = p + i\hbar \partial_x f(x). \tag{A.47b}$$

Transformation 2 Let a_μ and $a_\mu^\dagger$ be a collection of ladder opperators labeled with an abstract label μ in the spirit of section 2.1.3. Consider now the combination $X = \sum_\mu \left(\alpha_\mu a_\mu - \alpha_\mu^* a_\mu^\dagger \right)$, where α_μ are complex coefficients, and $Y = a_{\mu'}$. The relevant commutator that we have to calculate is

$$\left[\sum_\mu \alpha_\mu a_\mu - \alpha_\mu^* a_\mu^\dagger, a_{\mu'} \right] = \alpha_{\mu'}^*. \tag{A.48a}$$

Since the result is a mere scalar, the nested commutators vanish such that the final expression is

$$e^{\sum_\mu \left(\alpha_\mu a_\mu - \alpha_\mu^* a_\mu^\dagger \right)} a_{\mu'} e^{-\sum_\mu \left(\alpha_\mu a_\mu - \alpha_\mu^* a_\mu^\dagger \right)} = a_{\mu'} + \alpha_{\mu'}^*, \tag{A.48b}$$

which is just a concrete realization of a displacement operator.

A.5 About the non-positive definiteness of certain kinds of matrices

It is claimed in section 3.4.2 that the arithmetic mean replacement would not yield a positive semidefinite Kossakowski matrix. The following proposition shows this claim to be the case in general.

Proposition 1. *Let* $\mathbf{A}$ *be a real* $n \times n$ *matrix with elements* $A_{ij} = \frac{a_{ii} + a_{jj}}{2}$ *and* $a_{ii} \geq 0$ *for all* $i = 1, \ldots, n$. *Then,* $\mathbf{A}$ *is diagonalizable and has eigenvalues* $\lambda_0 = 0$, *with multiplicity* $n - 2$, *and*

$$\lambda_\pm = \sum_i \frac{a_{ii}}{2} \pm \frac{1}{2} \sqrt{n \sum_i a_{ii}^2}, \tag{A.49}$$

where $\lambda_- < 0$.

Proof. The fact that it is diagonalizable follows from **A** being real and symmetric. Let us next tackle the existence and multiplicity of $\lambda_0 = 0$. To that end, we note that **A** can be seen as a collection of n row vectors $\mathbf{a}_i^{\mathsf{t}} = (A_{11}, A_{12}, \dots, A_{1n})$. If we combine the first and second row vectors, $i = 1$ and $i = 2$, we have

$$\mathbf{a}_1 - \mathbf{a}_2 = \frac{a_{11} - a_{22}}{2}(1, 1, \dots, 1), \tag{A.50}$$

and similar relations hold for $i = 2$ and $i = 3$, $i = 3$ and $i = 4$, and all consecutive pairs. This means that the plane π_{12} spanned by $\mathbf{a}_1^{\mathsf{t}}$ and $\mathbf{a}_2^{\mathsf{t}}$ contains $(1, 1, \dots, 1)$, and so does the plane π_{23} spanned by $\mathbf{a}_2^{\mathsf{t}}$ and $\mathbf{a}_3^{\mathsf{t}}$. Therefore, $\pi_{12} = \pi_{23}$, as they share two vectors by construction. We may apply the same reasoning recursively to all rows to realize that $\operatorname{span}\{\mathbf{a}_i^{\mathsf{t}} \mid i = 1, \dots, n\} = \pi_{12}$. Consequently, there are only two linearly independent row vectors in **A**, and the equation $\mathbf{A}\mathbf{x} = \mathbf{0}$ has, thus, $n - 2$ independent solutions, given by the subspace orthogonal to the plane π. Equivalently, the eigenvalue $\lambda_0 = 0$ has multiplicity $n - 2$.

With this first result, we can write the characteristic polynomial of **A** as

$$p_{\mathbf{A}}(\lambda) = (-\lambda)^{n-2}\left(\lambda^2 - \alpha\lambda + \gamma\right). \tag{A.51}$$

From Leibniz's formula for the determinant,

$$\det \mathbf{A} = \sum_{i_1, \dots, i_n} \varepsilon_{i_1, \dots, i_n} A_{1 i_1} \cdots A_{n i_n}, \tag{A.52}$$

it is straightforward that $\alpha = \sum_i a_{ii}$. The other coefficient $\gamma \equiv \gamma_n + \gamma_{n-2}$ requires a bit more work. We need to consider two cases:

1. n diagonal elements: Because $i_k = k$, the Levi-Civita symbol yields a $+1$, and the full product is $A_{11}A_{22} \cdots A_{nn}$. We have to select a pair of indices $i \neq j$, take a_{ii} and a_{jj} from them and $-\lambda$ from the rest, and sum over all possible pairs, without double counting:

$$\gamma_n = \sum_{i<j} a_{ii} a_{jj}. \tag{A.53a}$$

2. $n - 2$ diagonal elements: We now have to choose a pair of indices and swap them: $i_k = l$ and $i_l = k$, with $l \neq k$. Thus, the Levi-Civita symbol is -1. In doing so, we take two matrix elements from outside the diagonal in the product $A_{11} \cdots A_{lk} \cdots A_{kl} \cdots A_{nn}$. Summing over all pairs of indices

that can be swapped, we have

$$\gamma_{n-2} = -\sum_{k<l}\left(\frac{a_{ll}+a_{kk}}{2}\right)^2 = -\frac{n-1}{4}\sum_i a_{ii}^2 - \sum_{i<j}\frac{a_{ii}a_{jj}}{2}. \tag{A.53b}$$

Hence,

$$\gamma = \gamma_n + \gamma_{n-2} = -\sum_{k<l}\left(\frac{a_{ll}+a_{kk}}{2}\right)^2 = -\frac{n-1}{4}\sum_i a_{ii}^2 + \sum_{i<j}\frac{a_{ii}a_{jj}}{2}, \tag{A.53c}$$

and the two non-vanishing eigenvalues are

$$\lambda_\pm = \frac{\alpha}{2} \pm \frac{1}{2}\sqrt{\alpha^2 - 4\gamma^2} = \sum_i \frac{a_{ii}}{2} \pm \frac{1}{2}\sqrt{n\sum_i a_{ii}^2}. \tag{A.54}$$

In particular, λ_- is negative because

$$\begin{aligned}\sum_{i<j}(a_{ii}-a_{jj})^2 =& (n-1)\sum_i a_{ii}^2 - \sum_{i<j} 2a_{ii}a_{jj} > 0 \\ \implies & n\sum_i a_{ii}^2 > \sum_i a_{ii}^2 + \sum_{i<j} 2a_{ii}a_{jj} = \left(\sum_i a_{ii}\right)^2\end{aligned} \tag{A.55}$$

□

Appendix B | Numerical verification of the methods in chapter 4

Here, we perform simulations to validate the methods developed in chapter 4, namely, the LME in eq. (4.15) and the effective Hamiltonian in eq. (4.25). To that end, we apply both methods to a system where an exact solution is possible, and compare both methods with the exact dynamics.

B.1 Simulations

We study the populations of the $n = 3$ multiplet in the hydrogen atom coupled to an EM environment characterized by a Lorentzian spectral density, whose spectral functions are given in eqs. (3.6b) and (3.6c). For simplicity, we assume that the atom and the EM environment interact only through the z components. The parameters are taken to be $\hbar g_{\mathrm{r}} = 4 \cdot 10^{-4}$ eV$/(ea_0)$, $\hbar\kappa_{\mathrm{r}} = 2 \cdot 10^{-3}$ eV and $\hbar\omega_{\mathrm{r}} = 1.95$ eV, and these values are used to represent the spectral functions in fig. B.1. As was mentioned in sections 2.4.4 and 3.4.2, a single Lorentzian resonance is equivalent to a single, lossy bosonic mode with which the atom interacts [201, 253], with the exact atom-mode dynamics being described by the LME in eq. (2.181) [303]. Hence, we can compare the approximate solutions obtained with our approaches, eq. (4.15) and eq. (4.25), to the exact dynamics given by eq. (2.181).

In the simulations for the numerical verification, we include the first 4 Bohr

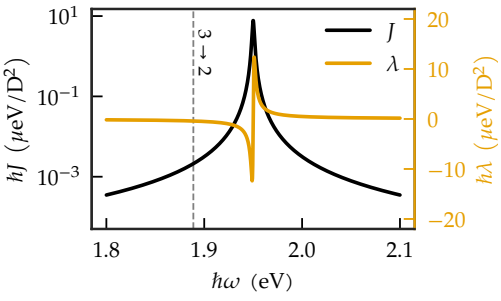

Figure B.1: Spectral functions of the single-mode environment that allow for an exact solution. The black line corresponds to the spectral density, $J = 2\pi\gamma$, while the orange line is the energy shift function λ.

1

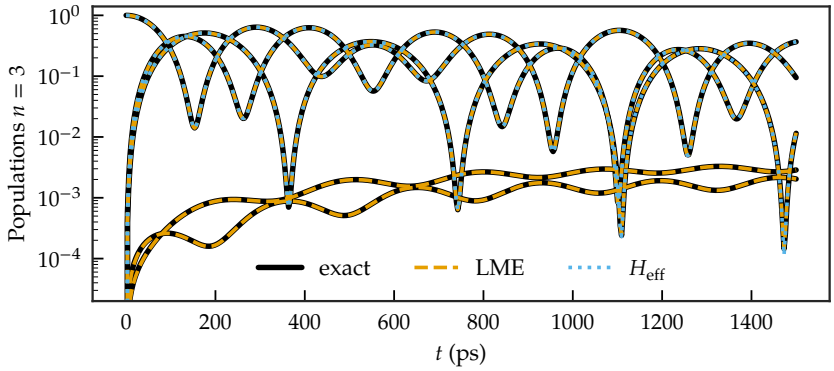

Figure B.2: Time evolution of the atomic populations. Continuous black lines: numerical solution to the exact dynamics from eq. (2.181). Dashed orange lines: geometric LME from eq. (4.15). Blue dotted lines: effective non-Hermitian Hamiltonian from eq. (4.25). Adapted from [267].

levels of the hydrogen atom (60 states) to ensure the convergence of the results and take $|\psi(0)\rangle = \big|n = 3, l = 0, j = 1/2, m_j = 1/2\big\rangle$ as the initial state, with zero excitations in the bosonic mode for the exact method. In fig. B.2, we present the population of the $|3, l, j, 1/2\rangle$ states only, as those are the ones of interest in the effective Hamiltonian description. According to the effective Hamiltonian, only the $|3, 0, 1/2, 1/2\rangle$, $|3, 2, 3/2, 1/2\rangle$ and $|3, 2, 5/2, 1/2\rangle$ states should become populated (common m_j and parity). Indeed, the populations that correspond to these states are the three largest populations in the figure. The agreement with the exact result for these lines is perfect, validating both the final LME in eq. (4.15) and the effective non-Hermitian Hamiltonian in eq. (4.25). The marked oscillations present in the evolution are due to the off-diagonal elements in the effective Hamiltonian, which a full secularization would have missed completely. Therefore, this numerical test already show the relevance of the off-diagonal terms in the CP Hamiltonian, as analyzed in more depth in section 4.3. The two additional lines present in the geometric LME and the exact solutions are the populations of the $|3, 1, 1/2, 1/2\rangle$ and $|3, 1, 3/2, 1/2\rangle$ states. These opposite-parity states become populated through the refilling term, discarded in the effective Hamiltonian description. Their populations, although small, are still unrealistically large in these simulations because they are proportional to $J(\omega = \Delta_{\text{fs}}/\hbar) \approx J(\omega = 0)$. Since we take J to be a Lorentzian function, it does not converge to zero as $\omega \to 0$. Realistic spectral densities, such as the one calculated for the AlN ellipsoidal nanoparticle, do converge to zero in that limit and, in turn, the states with opposite parity remain unpopulated to a much larger degree.

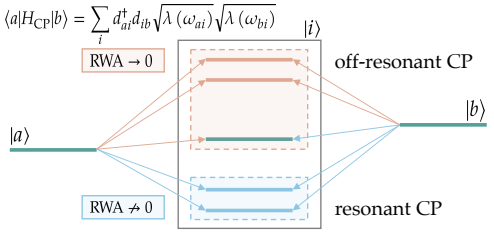

Figure B.3: Schematic illustration of the resonant (blue arrows) and off-resonant (orange arrows) contributions to the CP coupling between states $|a\rangle$ and $|b\rangle$ due to the intermediate states $|i\rangle$.

As for numerical advantages, the geometric LME is superior to the exact result because it involves no additional bosonic mode, which implies that the total Hilbert space that must be propagated with it is at least half in size of that of the exact method. Meanwhile, the effective Hamiltonian only requires keeping track of three states, and all other states are effectively included in the sums over "intermediate" states that yield the CP shift and the dissipative part. Furthermore, not only is the simulated part of the system much smaller, but also the included timescales are much more concentrated in the effective Hamiltonian method. The others explicitly include both fine-structure corrections, i.e., the scale we care about, and the gross structure of the Bohr levels, which yields a more numerically demanding task in the cases of the exact and the geometric LME approaches.

We finish this section with one last appropriate numerical confirmation, namely, that the counter-rotating terms in the atom-environment interaction are important. In the geometric LME prescription derived in [266], the starting point is the BRE reached after applying the RWA approximation. As a consequence, after carrying out the whole derivation in analogy with section 2.4.3, the $\Lambda_{ij}(\delta)$ functions defined in eq. (4.2d) are only evaluated in $\delta \geq 0$. The geometric LME directly inherits this additional restriction and, therefore, only the so-called resonant part of the CP shift appears, schematically depicted in fig. B.3. Thus, the CP shift Hamiltonian is not properly described without the counter-rotating interaction terms, as we would miss the effect of the $n = 4$ atomic level completely and some $n = 3$ intra-level contributions. In the discussion presented in chapter 3 and here, we have made sure to avoid the RWA for this precise reason. We present in fig. B.4 an illustration of the relevance of the counter-rotating terms. There, the precise frequency and shape of the oscillations is severely modified depending on whether the counter-rotating terms are neglected or kept.

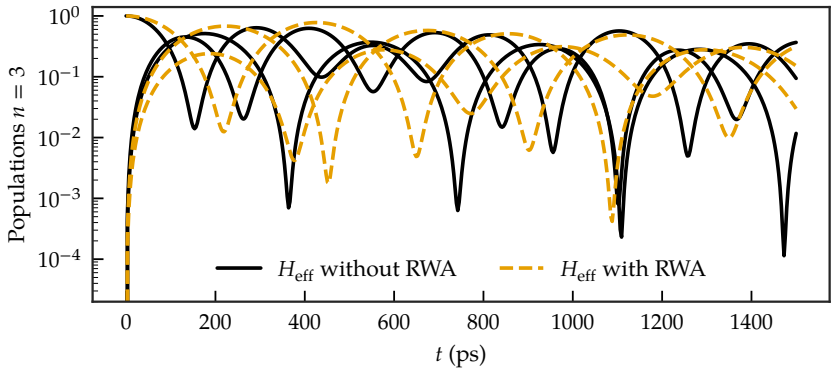

Figure B.4: Time evolution of the atomic populations obtained with the effective, non-Hermitian Hamiltonian of eq. (4.25). Continuous black lines: including counter-rotating terms. Dashed orange lines: applying the RWA to the atom-environment interaction. Adapted from [267].

Appendix C | Details of macroscopic QED

We begin this appendix by revisiting a few properties of the Green tensor, which plays a foundational role in MQED. Then, we carry out certain preliminary calculations and use them to complement the statements in section 2.2.4.

C.1 Electromagnetic Green tensor

Free-space The following expression corresponds to the free-space Green tensor [204]

$$\mathbf{G}^0(\mathbf{r},\mathbf{r}+\boldsymbol{\rho},\omega) = -\frac{c^2}{3\omega^2}\delta(\boldsymbol{\rho}) - \frac{c^2 e^{i\omega|\boldsymbol{\rho}|/c}}{4\pi\omega^2|\boldsymbol{\rho}|^3}\left\{\left[1 - i\frac{\omega|\boldsymbol{\rho}|}{c} - \left(\frac{\omega|\boldsymbol{\rho}|}{\omega}\right)^2\right]\mathbf{1} - \left[3 - 3i\frac{\omega|\boldsymbol{\rho}|}{c} - \left(\frac{\omega|\boldsymbol{\rho}|}{\omega}\right)^2\right]\frac{\boldsymbol{\rho}\otimes\boldsymbol{\rho}}{|\boldsymbol{\rho}|^2}\right\}. \tag{C.1}$$

Particularly helpful is the expression

$$\lim_{\boldsymbol{\rho}\to\mathbf{0}} \mathrm{Im}\,\mathbf{G}^0(\mathbf{r},\mathbf{r}+\boldsymbol{\rho},\omega) = \lim_{\boldsymbol{\rho}\to\mathbf{0}} \mathrm{Im}\,{}^{\perp}\mathbf{G}^0(\mathbf{r},\mathbf{r}+\boldsymbol{\rho},\omega) = \frac{\omega}{6\pi c}\mathbf{1}, \tag{C.2}$$

which determines the free-space spectral density.

Integral relations For our upcoming calculations, a couple of integral relations will be of service, which are obtained through simple contour integration techniques. First,

$$\begin{aligned} I_1 &= \int_0^\infty \mathrm{d}\omega\, \frac{\omega}{c^2}\mathrm{Im}\,{}^{\perp}\mathbf{G}(\mathbf{r},\mathbf{r}',\omega) = \frac{1}{2i}\int_0^\infty \mathrm{d}\omega\, \frac{\omega}{c^2}\left({}^{\perp}\mathbf{G}(\mathbf{r},\mathbf{r}',\omega) - {}^{\perp}\mathbf{G}(\mathbf{r},\mathbf{r}',-\omega)\right) \\ &= \frac{1}{2i}\int_{-\infty}^\infty \mathrm{d}\omega\, \frac{\omega}{c^2}{}^{\perp}\mathbf{G}(\mathbf{r},\mathbf{r}',\omega) = \frac{-1}{2}\lim_{|\omega|\to\infty}\int_0^\pi \mathrm{d}\alpha\, \frac{\omega^2}{c^2}{}^{\perp}\mathbf{G}(\mathbf{r},\mathbf{r}',\omega) \\ &= \frac{\pi}{2}\delta^{\perp}(\mathbf{r}-\mathbf{r}'), \end{aligned} \tag{C.3}$$

where we have utilized the Schwartz reflection principle, that is, $\mathbf{G}(\mathbf{r},\mathbf{r}',\omega) = \mathbf{G}^*(\mathbf{r},\mathbf{r}',-\omega^*)$, and

$$\lim_{|\omega|\to\infty} \frac{\omega^2}{c^2}\mathbf{G}(\mathbf{r},\mathbf{r}',\omega) = -\delta(\mathbf{r}-\mathbf{r}'), \tag{C.4}$$

which follows from eq. (2.76). The second relation is

$$\begin{aligned} I_2 &= \int_0^\infty \mathrm{d}\omega\, \frac{\omega}{c^2}\mathrm{Im}\,{}^{\parallel}\mathbf{G}(\mathbf{r},\mathbf{r}',\omega) = \frac{1}{2i}P\int_{-\infty}^{\infty}\mathrm{d}\omega\,\frac{\omega}{c^2}{}^{\parallel}\mathbf{G}(\mathbf{r},\mathbf{r}',\omega) \\ &= \frac{\pi}{2}\left[\delta^{\parallel}(\mathbf{r}-\mathbf{r}') + \left(\frac{\omega^2}{c^2}{}^{\parallel}\mathbf{G}(\mathbf{r},\mathbf{r}',\omega)\right)\Big|_{\omega=0}\right]. \end{aligned} \tag{C.5}$$

In this case, we have used eq. (C.4) and the presence of a simple pole at $\omega = 0$ in $\omega\mathbf{G}(\mathbf{r},\mathbf{r}',\omega)$. Physically, this pole can be related to the electrostatic electric field due to a point-dipole, $\mathbf{E}(\mathbf{r},\omega) \propto \omega^2\mathbf{G}(\mathbf{r},\mathbf{r}_\mathrm{d},\omega)\cdot\mathbf{d}$. In the limit $\omega\to 0$, the electric field must recover a finite time-independent value. Hence,

$$\lim_{\omega\to 0}\omega^2{}^{\parallel}\mathbf{G}(\mathbf{r},\mathbf{r}_\mathrm{d},\omega) \neq \mathbf{0}. \tag{C.6}$$

The third relation of this kind is

$$I_3 = \int_0^\infty \mathrm{d}\omega\,\frac{\omega}{c^2}\mathrm{Im}\,{}^{\perp}\mathbf{G}^{\parallel}(\mathbf{r},\mathbf{r}',\omega) = \frac{1}{2i}\int_{-\infty}^{\infty}\mathrm{d}\omega\,\frac{\omega}{c^2}{}^{\perp}\mathbf{G}^{\parallel}(\mathbf{r},\mathbf{r}',\omega) = \mathbf{0}. \tag{C.7}$$

C.2 Incomplete MQED gauge in section 2.2.4

We write out in full glory the explicit calculations required to transform the physical operators according to the unitary operator defined in eq. (2.103).

1. Transformation of $\mathbf{p}_i$. This one follows from a simple application of the general transformation in eq. (A.47b):

$$\mathbf{p}_i' = \mathbf{p}_i - q_i\nabla_{\mathbf{r}_i}\chi(\mathbf{r}_i). \tag{C.8}$$

2. Transformation of $\mathbf{f}_\lambda(\mathbf{r}',\omega)$. We now resort to eq. (A.48b) and replace the abstract index μ with $\mathbf{r}',\omega,\lambda$ and a spatial index k. With that, α_μ becomes

$$\alpha_\mu \to \frac{1}{\hbar\omega}\int \mathrm{d}^3r\,\mathbf{P}_\mathrm{at}(\mathbf{r})\cdot{}^{\parallel}\mathbf{G}_\lambda(\mathbf{r},\mathbf{r}',\omega)\cdot\hat{\mathbf{u}}_k, \tag{C.9}$$

where $\hat{\mathbf{u}}_k$ is a unit vector along the Cartesian index k, and we obtain

$$\mathbf{f}_\lambda'(\mathbf{r}',\omega) = \mathbf{f}_\lambda(\mathbf{r}',\omega) + \frac{1}{\hbar\omega}\int \mathrm{d}^3r\,\left({}^{\parallel}\mathbf{G}_\lambda^*(\mathbf{r},\mathbf{r}',\omega)\right)^{\mathrm{t}}\cdot\mathbf{P}_\mathrm{at}(\mathbf{r}). \tag{C.10}$$

3. Transformation of $\mathbf{A}^{\perp}$. From the previous result, we have

$$\begin{aligned}
\left(\mathbf{A}^{\perp}(\mathbf{r})\right)' &= \sum_{\lambda}\int \mathrm{d}^3r' \int \mathrm{d}\omega\, \frac{1}{i\omega}{}^{\perp}\mathbf{G}_{\lambda}(\mathbf{r},\mathbf{r}',\omega)\cdot\mathbf{f}'_{\lambda}(\mathbf{r}',\omega) + \text{H.c.} \\
&= \mathbf{A}^{\perp}(\mathbf{r}) \\
&\quad + \sum_{\lambda}\int \mathrm{d}\omega \int \mathrm{d}^3r'\, \mathrm{d}^3s\, \frac{{}^{\perp}\mathbf{G}_{\lambda}(\mathbf{r},\mathbf{r}',\omega)\cdot\left({}^{\parallel}\mathbf{G}_{\lambda}(\mathbf{s},\mathbf{r}',\omega)\right)^{*\mathrm{t}}\cdot\mathbf{P}_{\mathrm{at}}(\mathbf{s})}{i\hbar\omega^2} + \text{H.c.} \\
&= \mathbf{A}^{\perp}(\mathbf{r}) + \int \mathrm{d}^3s \int \mathrm{d}\omega\, \frac{1}{i\pi\varepsilon_0 c^2}\mathrm{Im}\,{}^{\perp}\mathbf{G}^{\parallel}(\mathbf{r},\mathbf{s},\omega)\cdot\mathbf{P}_{\mathrm{at}}(\mathbf{s}) + \text{H.c.} \\
&= \mathbf{A}^{\perp}(\mathbf{r}), \qquad \text{(C.11)}
\end{aligned}$$

where we have used eq. (2.86) and, in the last step, the second term vanishes because

$$\int \mathrm{d}^3s \int \mathrm{d}\omega\, \frac{1}{i\pi\varepsilon_0 c^2}\mathrm{Im}{}^{\perp}\mathbf{G}^{\parallel}(\mathbf{r},\mathbf{s},\omega)\cdot\mathbf{P}_{\mathrm{at}}(\mathbf{s}) \qquad \text{(C.12)}$$

is anti-Hermitian.

4. Transformation of $\mathbf{E}^{\parallel}$. The last quantity that we have to transform is the longitudinal electric field operator:

$$\begin{aligned}
\left(\mathbf{E}^{\parallel}(\mathbf{r})\right)' &= \int \mathrm{d}^3r' \int \mathrm{d}\omega\, {}^{\parallel}\mathbf{G}_{\lambda}(\mathbf{r},\mathbf{r}',\omega)\cdot\mathbf{f}'_{\lambda}(\mathbf{r}',\omega) + \text{H.c.} \\
&= \mathbf{E}^{\parallel}(\mathbf{r}) \\
&\quad + \sum_{\lambda}\int \mathrm{d}\omega \int \mathrm{d}^3r'\, \mathrm{d}^3s\, \frac{{}^{\parallel}\mathbf{G}_{\lambda}(\mathbf{r},\mathbf{r}',\omega)\cdot\left({}^{\parallel}\mathbf{G}_{\lambda}(\mathbf{s},\mathbf{r}',\omega)\right)^{*\mathrm{t}}\cdot\mathbf{P}_{\mathrm{at}}(\mathbf{s})}{\hbar\omega} + \text{H.c.} \\
&= \mathbf{E}^{\parallel}(\mathbf{r}) + \frac{2}{\pi\varepsilon_0}\int \mathrm{d}^3s \int \mathrm{d}\omega\, \frac{\omega}{c^2}\mathrm{Im}\,{}^{\parallel}\mathbf{G}^{\parallel}(\mathbf{r},\mathbf{s},\omega)\cdot\mathbf{P}_{\mathrm{at}}(\mathbf{s}) \\
&= \mathbf{E}^{\parallel}(\mathbf{r}) + \frac{2}{\pi\varepsilon_0}\int \mathrm{d}^3s\, \frac{\pi}{2}\left[\delta^{\parallel}(\mathbf{r}-\mathbf{s}) + \left(\frac{\omega^2}{c^2}{}^{\parallel}\mathbf{G}^{\parallel}(\mathbf{r},\mathbf{s},\omega)\right)\Big|_{\omega=0}\right]\cdot\mathbf{P}_{\mathrm{at}}(\mathbf{s}) \\
&= \mathbf{E}^{\parallel}(\mathbf{r}) + \frac{1}{\varepsilon_0}\mathbf{P}^{\parallel}_{\mathrm{at}}(\mathbf{s}) + \frac{1}{\varepsilon_0}\int \mathrm{d}^3s\, \left(\frac{\omega^2}{c^2}{}^{\parallel}\mathbf{G}^{\parallel}(\mathbf{r},\mathbf{s},\omega)\right)\Big|_{\omega=0}\cdot\mathbf{P}_{\mathrm{at}}(\mathbf{s}). \qquad \text{(C.13)}
\end{aligned}$$

Again, we have used eq. (2.86) to reach the third line, and then eq. (C.5) to obtain the final expression.

Appendix D | Power-Zienau-Woolley transformation

We provide here the detailed calculations relative to the PZW transformation performed in section 2.1.2 to reach the multipolar coupling scheme from the minimal coupling Hamiltonian in the Coulomb gauge. Then, we discuss in some depth the modified versions of the PZW that are succinctly described at the end of section 2.1.2, and examine the relation between the PZW transformation usually performed in the context of MQED and these modified versions.

D.1 Calculation details

The standard PZW transformation takes us from the minimal coupling Hamiltonian and is implemented by

$$T = \exp\left\{-\frac{i}{\hbar}\int \mathrm{d}^3 r\, \mathbf{P}\cdot\mathbf{A}^{\perp}\right\} = \exp\left\{-\frac{i}{\hbar}\int \mathrm{d}^3 r\, \mathbf{P}^{\perp}\cdot\mathbf{A}^{\perp}\right\}, \tag{D.1a}$$

where

$$\mathbf{A}^{\perp}(\mathbf{r}) = \sum_{\lambda}\sqrt{\frac{\hbar}{2\varepsilon_0\omega_\lambda}}\boldsymbol{\psi}_\lambda(\mathbf{r})\left(a_\lambda^\dagger + a_\lambda\right), \tag{D.1b}$$

$$\mathbf{P}(\mathbf{r}) = \sum_i q_i \mathbf{r}_i \int_0^1 \mathrm{d}\sigma\, \delta^{(3)}(\mathbf{r}-\sigma\mathbf{r}_i) \quad \text{and} \tag{D.1c}$$

$$\mathbf{P}^{\perp}(\mathbf{r}) = \sum_\lambda P_\lambda \boldsymbol{\psi}_\lambda(\mathbf{r}) = \sum_\lambda\left[\sum_j q_j \int_0^1 \mathrm{d}\sigma\, \mathbf{r}_j \boldsymbol{\psi}_\lambda\left(\sigma\mathbf{r}_j\right)\right]\boldsymbol{\psi}_\lambda(\mathbf{r}). \tag{D.1d}$$

For notational convenience, we have chosen the point around which the polarization is calculated to be the origin, to avoid keeping track of the $\mathbf{r}_O$ in eq. (2.37). We remark here that $\mathbf{P}$ is a polarization field including every charge in the system. Then, using eq. (A.47b), the momentum transforms as

$$T\mathbf{p}_i T^\dagger = \mathbf{p}_i + \nabla_{\mathbf{r}_i}\int \mathrm{d}^3 r\, \mathbf{P}\cdot\mathbf{A}^{\perp}$$

$$
\begin{aligned}
&= \mathbf{p}_i + \sum_j q_j \int_0^1 \mathrm{d}\sigma \int \mathrm{d}^3 r \, \nabla_{\mathbf{r}_i} \left[\mathbf{r}_j \cdot \mathbf{A}^\perp(\mathbf{r}) \delta^{(3)}\left(\mathbf{r} - \sigma \mathbf{r}_j\right) \right] \\
&= \mathbf{p}_i + \sum_j q_j \int_0^1 \mathrm{d}\sigma \int \mathrm{d}^3 r \left[\delta_{ij} \mathbf{A}^\perp(\mathbf{r}) \delta^{(3)}\left(\mathbf{r} - \sigma \mathbf{r}_j\right) \right. \\
&\qquad\qquad \left. + \left(\mathbf{r}_j \cdot \mathbf{A}^\perp(\mathbf{r})\right) \nabla_{\mathbf{r}_i} \delta^{(3)}\left(\mathbf{r} - \sigma \mathbf{r}_j\right) \right] \\
&= \mathbf{p}_i + q_i \int_0^1 \mathrm{d}\sigma \, \mathbf{A}^\perp(\sigma \mathbf{r}_i) + R_{\mathbf{p}_i}
\end{aligned}
$$

where

$$
\begin{aligned}
R_{\mathbf{p}_i} &= \sum_j q_j \int_0^1 \mathrm{d}\sigma \int \mathrm{d}^3 r \left(\mathbf{r}_j \cdot \mathbf{A}^\perp(\mathbf{r})\right) \nabla_{\mathbf{r}_i} \delta^{(3)}\left(\mathbf{r} - \sigma \mathbf{r}_j\right) \\
&= \sum_j q_j \int_0^1 \mathrm{d}\sigma \int \mathrm{d}^3 r \left[\mathbf{r}_j \times \nabla_{\mathbf{r}_i} \delta^{(3)}\left(\mathbf{r} - \sigma \mathbf{r}_j\right) \times \mathbf{A}^\perp(\mathbf{r}) \right. \\
&\qquad\qquad \left. + \left(\mathbf{r}_j \cdot \nabla_{\mathbf{r}_i} \delta^{(3)}\left(\mathbf{r} - \sigma \mathbf{r}_j\right)\right) \mathbf{A}^\perp(\mathbf{r}) \right] \\
&= -q_i \int_0^1 \mathrm{d}\sigma \int \mathrm{d}^3 r \, \sigma \left[\mathbf{r}_i \times \nabla_{\mathbf{r}} \delta^{(3)}(\mathbf{r} - \sigma \mathbf{r}_i) \times \mathbf{A}^\perp(\mathbf{r}) \right. \\
&\qquad\qquad \left. + \left(\mathbf{r}_i \cdot \nabla_{\mathbf{r}} \delta^{(3)}(\mathbf{r} - \sigma \mathbf{r}_i)\right) \mathbf{A}^\perp(\mathbf{r}) \right] \\
&= q_i \int_0^1 \mathrm{d}\sigma \int \mathrm{d}^3 r \, \sigma \left[\mathbf{r}_i \times \nabla_{\mathbf{r}} \times \mathbf{A}^\perp(\mathbf{r}) + (\mathbf{r}_i \cdot \nabla_{\mathbf{r}}) \mathbf{A}^\perp(\mathbf{r}) \right] \delta^{(3)}(\mathbf{r} - \sigma \mathbf{r}_i) \\
&= -q_i \int_0^1 \mathrm{d}\sigma \, \sigma \left[\mathbf{B}(\sigma \mathbf{r}_i) \times \mathbf{r}_i - (\mathbf{r}_i \cdot \nabla_{\mathbf{r}}) \mathbf{A}^\perp(\mathbf{r}) \big|_{\mathbf{r} = \sigma \mathbf{r}_i} \right] \\
&= -q_i \int_0^1 \mathrm{d}\sigma \, \sigma \left[\mathbf{B}(\sigma \mathbf{r}_i) \times \mathbf{r}_i - \partial_\sigma \mathbf{A}^\perp(\sigma \mathbf{r}_i) \right] \\
&= -q_i \int_0^1 \mathrm{d}\sigma \left[\sigma \mathbf{B}(\sigma \mathbf{r}_i) \times \mathbf{r}_i + \mathbf{A}^\perp(\sigma \mathbf{r}_i) \right] + q_i \mathbf{A}^\perp(\mathbf{r}_i)
\end{aligned}
$$

and, hence,

$$
T \mathbf{p}_i T^\dagger = \mathbf{p}_i + q_i \mathbf{A}^\perp(\mathbf{r}_i) - q_i \int_0^1 \mathrm{d}\sigma \, \sigma \mathbf{B}(\sigma \mathbf{r}_i) \times \mathbf{r}_i . \tag{D.2}
$$

In order to reach the last expression of $\mathbf{R}_{\mathbf{p}_i}$, we have used $(\mathbf{a} \cdot \mathbf{b})\mathbf{c} = \mathbf{a} \times \mathbf{c} \times \mathbf{b} + (\mathbf{a} \cdot \mathbf{c})\mathbf{b}$, followed by judicious application of eq. (A.7b) and eq. (A.7a). The last step merely amounts to integration by parts. For the field momentum, we find

$$
T a_{\lambda'} T^\dagger = a_{\lambda'} + i \sqrt{\frac{1}{2\varepsilon_0 \hbar \omega_{\lambda'}}} \sum_j q_j \int_0^1 \mathrm{d}\sigma \, \mathbf{r}_j \cdot \boldsymbol{\psi}_{\lambda'}\left(\sigma \mathbf{r}_j\right) = a_{\lambda'} + i \sqrt{\frac{1}{2\varepsilon_0 \hbar \omega_{\lambda'}}} P_{\lambda'} \tag{D.3}
$$

by simply identifying the coefficients α_λ in eq. (A.48b). From this transformation rule and the canonical field momentum's expansion shown in eq. (2.45),

we have

$$T\boldsymbol{\Pi}^{\perp}T^{\dagger} = \sum_{\lambda} T\Pi_{\lambda}T^{\dagger}\boldsymbol{\psi}_{\lambda} = \sum_{\lambda}(\Pi_{\lambda} + P_{\lambda})\boldsymbol{\psi}_{\lambda} = \boldsymbol{\Pi}^{\perp} + \mathbf{P}. \tag{D.4}$$

Since T is a function of $\mathbf{r}_i$ and $\mathbf{A}^{\perp}$, the canonical coordinates remain unchanged after the PZW transformation. Finally, the full minimal coupling Hamiltonian becomes

$$\begin{aligned}
THT^{\dagger} &= \sum_i \frac{\left(T\mathbf{p}_i T^{\dagger} - q_i \mathbf{A}^{\perp}(\mathbf{r}_i)\right)^2}{2m_i} + \sum_{i\neq j}\frac{q_i q_j}{8\pi\varepsilon_0|\mathbf{r}_i - \mathbf{r}_j|} \\
&\quad + \int \mathrm{d}^3 r \left[\frac{\left(T\boldsymbol{\Pi}^{\perp}T^{\dagger}\right)^2}{2\varepsilon_0} + \frac{\varepsilon_0 c^2}{2}\left(\nabla\times\mathbf{A}^{\perp}\right)^2\right] \\
&= \sum_i \frac{\left(\mathbf{p}_i - q_i\int_0^1 \mathrm{d}\sigma\, \sigma\mathbf{B}[\mathbf{r}_{\mathrm{O}} + \sigma(\mathbf{r}_i - \mathbf{r}_{\mathrm{O}})]\times(\mathbf{r}_i - \mathbf{r}_{\mathrm{O}})\right)^2}{2m_i} \\
&\quad + \sum_{i\neq j}\frac{q_i q_j}{8\pi\varepsilon_0|\mathbf{r}_i - \mathbf{r}_j|} + \frac{1}{2\varepsilon_0}\int \mathrm{d}^3 r\,\left(\mathbf{P}^{\perp}\right)^2 \\
&\quad + \int \mathrm{d}^3 r\left[\frac{\left(\boldsymbol{\Pi}^{\perp}\right)^2}{2\varepsilon_0} + \frac{\varepsilon_0 c^2}{2}\mathbf{B}^2\right] + \frac{1}{\varepsilon_0}\int \mathrm{d}^3 r\,\mathbf{P}^{\perp}\cdot\boldsymbol{\Pi}^{\perp},
\end{aligned} \tag{D.5}$$

Besides the calculation details, we emphasize here once last time that the new canonical momenta are still represented by $\mathbf{p}_i$ and $\boldsymbol{\Pi}^{\perp}$, although their physical meaning is different compared with the minimal coupling picture.

D.2 Further PZW transformations

In the previous section, we have performed the "full" PZW transformation, meaning that all charges are included in the polarization $\mathbf{P}$. Oftentimes, however, it is convenient to group the charges in two sets, and only one them is included in the polarization field, giving rise to a partial PZW transformation in which some charges are minimally coupled and others are multipolarly coupled. Furthermore, it is not necessary that all charges included in the polarization share a common center. If, indeed, there are several charge centers and the subsets of charges associated to each center do not overlap, then the multicenter PZW transformation eliminates the direct Coulomb interaction between them, as shown in eq. (2.41).

Let us bring the discussion down to a more concrete level. In the interest of chapter 5, we are going to explicitly consider our charges grouped in two sets:

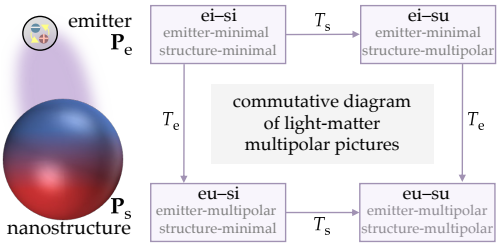

Figure D.1: Sketch of the relation between the partial multipolar pictures discussed in this appendix. Here, T_i is a unitary operator implementing either partial PZW transformation: the one relative to the emitter (structure) when $i = \mathrm{e}$ (s). The labels atop the boxes introduce the picture's shortened notation.

an emitter (C_e) and some nanostructure (C_s). Accordingly, we discuss four cases according to which coupling picture is used for each, schematically depicted in fig. D.1. Our starting point is the minimal coupling Hamiltonian in eq. (2.13). For compactness, we refer to it as ei–si to emphasize that the interaction of the field with both the Emitter and Structure are in mInimal coupling. Next, we can apply a partial PZW transformation T_i, whose polarization field $\mathbf{P}_i$ can correspond to either the emitter ($i = \mathrm{e}$) or the structure ($i = \mathrm{s}$):

$$T_i = \exp\left\{-\frac{i}{\hbar}\int \mathrm{d}^3 r\, \mathbf{P}_i \cdot \mathbf{A}^\perp\right\}. \tag{D.6}$$

If T_e is applied, we reach the eu–si, as the field-Emitter interaction is in mUltipolar coupling, while the field-Structure interaction is in mInimal coupling. On the contrary, T_s brings us to ei–su. Last, the successive application of T_e and T_s, regardless of the order, takes us from ei–si to eu–su, a picture where both emitter and structure interact with the field through multipolar coupling. Note that this merely corresponds to a multicenter PZW transformation with two charge centers. In the following, we write the Hamiltonian in each picture, and explain any lingering details.

eu–si The ensuing Hamiltonian is

$$\begin{aligned} H = &\sum_{i\in C_\mathrm{e}} \frac{\mathbf{p}_i^2}{2m_i} + \sum_{i\neq j\in C_\mathrm{e}} \frac{q_i q_j}{8\pi\varepsilon_0 |\mathbf{r}_i - \mathbf{r}_j|} + \frac{1}{2\varepsilon_0}\int \mathrm{d}^3 r\, \left(\mathbf{P}_\mathrm{e}^\perp\right)^2 \\ &+ \sum_{i\in C_\mathrm{s}} \frac{\left(\mathbf{p}_i - q_i \mathbf{A}^\perp(\mathbf{r}_i)\right)^2}{2m_i} + \sum_{i\neq j\in C_\mathrm{s}} \frac{q_i q_j}{8\pi\varepsilon_0 |\mathbf{r}_i - \mathbf{r}_j|} - \int \mathrm{d}^3 r\, \mathbf{P}_\mathrm{e}^\parallel \cdot \mathbf{E}_\mathrm{s}^\parallel \\ &+ \int \mathrm{d}^3 r \left[\frac{\left(\mathbf{\Pi}^\perp\right)^2}{2\varepsilon_0} + \frac{\varepsilon_0 c^2}{2}\left(\nabla \times \mathbf{A}^\perp\right)^2\right] + \frac{1}{\varepsilon_0}\int \mathrm{d}^3 r\, \mathbf{P}^\perp \cdot \mathbf{\Pi}^\perp, \end{aligned} \tag{D.7}$$

where magnetic effects in the emitter-field interaction have been neglected. The canonical field momentum $\mathbf{\Pi}^\perp$ physically represents $-\varepsilon_0\mathbf{E}^\perp - \mathbf{P}_\mathrm{e}^\perp$.

EI–SU After acting with T_s, we arrive at

$$\begin{aligned} H = &+ \sum_{i\in C_\mathrm{e}} \frac{\left(\mathbf{p}_i - q_i\mathbf{A}^\perp(\mathbf{r}_i)\right)^2}{2m_i} + \sum_{i\neq j\in C_\mathrm{e}} \frac{q_i q_j}{8\pi\varepsilon_0\left|\mathbf{r}_i - \mathbf{r}_j\right|} \\ &\sum_{i\in C_\mathrm{s}} \frac{\mathbf{p}_i^2}{2m_i} + \sum_{i\neq j\in C_\mathrm{s}} \frac{q_i q_j}{8\pi\varepsilon_0\left|\mathbf{r}_i - \mathbf{r}_j\right|} + \frac{1}{2\varepsilon_0}\int \mathrm{d}^3r\, \left(\mathbf{P}_\mathrm{s}^\perp\right)^2 - \int \mathrm{d}^3r\, \mathbf{P}_\mathrm{e}^\parallel \cdot \mathbf{E}_\mathrm{s}^\parallel \\ &+ \int \mathrm{d}^3r \left[\frac{\left(\mathbf{\Pi}^\perp\right)^2}{2\varepsilon_0} + \frac{\varepsilon_0 c^2}{2}\left(\nabla\times\mathbf{A}^\perp\right)^2\right] + \frac{1}{\varepsilon_0}\int \mathrm{d}^3r\, \mathbf{P}_\mathrm{s}^\perp \cdot \mathbf{\Pi}^\perp, \end{aligned} \tag{D.8}$$

and magnetic effects in the emitter-field interaction have again been neglected. As expected, the canonical field momentum $\mathbf{\Pi}^\perp$ corresponds to $-\varepsilon_0\mathbf{E}^\perp - \mathbf{P}_\mathrm{s}^\perp$. This picture is particularly relevant for section 5.3.1, as the arguments therein are done in it.

EU–SU After acting with T_s, we arrive at

$$\begin{aligned} H = &+ \sum_{i\in C_\mathrm{e}} \frac{\mathbf{p}_i^2}{2m_i} + \sum_{i\neq j\in C_\mathrm{e}} \frac{q_i q_j}{8\pi\varepsilon_0\left|\mathbf{r}_i - \mathbf{r}_j\right|} + \frac{1}{2\varepsilon_0}\int \mathrm{d}^3r\, \left(\mathbf{P}_\mathrm{e}^\perp\right)^2 \\ &\sum_{i\in C_\mathrm{s}} \frac{\mathbf{p}_i^2}{2m_i} + \sum_{i\neq j\in C_\mathrm{s}} \frac{q_i q_j}{8\pi\varepsilon_0\left|\mathbf{r}_i - \mathbf{r}_j\right|} + \frac{1}{2\varepsilon_0}\int \mathrm{d}^3r\, \left(\mathbf{P}_\mathrm{s}^\perp\right)^2 \\ &+ \int \mathrm{d}^3r \left[\frac{\left(\mathbf{\Pi}^\perp\right)^2}{2\varepsilon_0} + \frac{\varepsilon_0 c^2}{2}\left(\nabla\times\mathbf{A}^\perp\right)^2\right] + \frac{1}{\varepsilon_0}\int \mathrm{d}^3r\, \left(\mathbf{P}_\mathrm{e} + \mathbf{P}_\mathrm{s}^\perp\right) \cdot \mathbf{\Pi}^\perp. \end{aligned} \tag{D.9}$$

At this point, the fate of magnetic effects should be hardly surprising, and, likewise, the canonical field momentum $\mathbf{\Pi}^\perp$ corresponds to $-\varepsilon_0\mathbf{E}^\perp - \mathbf{P}_\mathrm{e}^\perp - \mathbf{P}_\mathrm{s}^\perp$. This picture is also important for section 5.3.4.

We finish this section on the details of the PZW transformation with some final remarks concerning its use in the context of MQED. In that case, the unitary operator is given by eq. (2.98) [204], which means that it reaches a partial multipolar picture, according to our description above. Besides that, the actual calculations are very similar to those in appendix D.1, with a single complication. Because the relative coordinates are used, one has to carry the non-standard commutation relation in eq. (2.94c) throughout the whole calculation and final expressions. This requires some more patience, but with the template of the calculations done at the beginning of the section, it is relatively

direct.

Appendix E | Electromagnetic sum rules and polarization self-energy

In this appendix, we derive several electromagnetic sum rules for the QED scenario of an emitter and a nanostructure, such as the one used in chapter 5, eq. (5.26b) [299]. Furthermore, we analyze the relation of these sum rules with the particular coupling picture used to derive it. In particular, we consider the four pictures described in appendix D, namely, EI–SI, EU–SI, EI–SU and EU–SU, and we will see how some sum rules are easier to deduce in one picture or another. Finally, we justify eq. (5.38), which appears in section 5.2.4 and section 5.3.5, by building on the sum rules.

E.1 Sum rules and pictures

The general idea is to describe the nanostructure as a collection of polarization harmonic oscillators, and diagonalize the structure-field oscillator Hamiltonian. From the polaritonic eigenmodes, we find the emitter-polariton couplings, the transverse spectral density $J^{\perp}$ and its associated sum rules. We repeat this procedure in each of the pictures described in the previous appendix. Note that we drop here the $\sim$ notation to denote "multipolar coupling" quantities, as the wider variety of pictures here makes it rather impractical to generalize.

E.1.1 EI–SU

We begin with the EI–SU partial multipolar coupling picture because, as we will see in the following, the sum rule in eq. (5.26b) comes out rather straightforwardly in it. The structure is modeled through a collection of harmonic polarization oscillators with coordinates X_α, canonical momenta P_α and frequencies ω_α. After a mode expansion of eq. (D.8) (see section 2.1.3), the

structure-field part of the Hamiltonian to be diagonalized is

$$\begin{aligned} H_{\mathrm{osc}} &= H_{\mathrm{s}} + H_{\mathrm{f}} + H_{\mathrm{s-f}} \\ &= \sum_{\alpha\alpha'}\left[\frac{\delta_{\alpha\alpha'}}{2}P_\alpha P_{\alpha'} + \frac{\omega_\alpha^2\delta_{\alpha\alpha'} + c_{\alpha\alpha'}}{2}X_\alpha X_{\alpha'}\right] \\ &\quad + \sum_{\lambda\lambda'}\left[\frac{\delta_{\lambda\lambda'}}{2\varepsilon_0}\Pi_\lambda\Pi_{\lambda'} + \frac{\varepsilon_0\omega_\lambda^2\delta_{\lambda\lambda'}}{2}A_\lambda A_{\lambda'}\right] \\ &\quad + \sum_{\alpha\lambda} C_{\alpha\lambda}X_\alpha\Pi_\lambda, \end{aligned} \tag{E.1}$$

Note that we describe the polarization oscillators as a system of coupled harmonic oscillators for generality, although they can always be diagonalized independently of the photonic oscillators.

where $c_{\alpha\alpha'}$ is a non-diagonal matrix accounting for possible couplings between the polarization oscillators. As for $C_{\alpha\lambda}$, it describes the couplings between the polarization field and the free-space photonic modes. In order to find the eigenmodes, we can proceed in two steps: first, we canonically rescale and swap our canonical field variables from $\{A_\lambda, \Pi_\lambda\}$ to

$$\left\{\frac{-\Pi_\lambda}{\sqrt{\varepsilon_0}\omega_\lambda}, \sqrt{\varepsilon_0}\omega_\lambda A_\lambda\right\} \equiv \{\tilde{X}_\lambda, \tilde{P}_\lambda\}. \tag{E.2}$$

Then, we express the oscillator Hamiltonian in terms of these new variables:

$$\begin{aligned} H_{\mathrm{osc}} &= H_{\mathrm{s}} + H_{\mathrm{f}} + H_{\mathrm{s-f}} \\ &= \sum_{\alpha\alpha'}\left[\frac{\delta_{\alpha\alpha'}}{2}P_\alpha P_{\alpha'} + \frac{\omega_\alpha^2\delta_{\alpha\alpha'} + c_{\alpha\alpha'}}{2}X_\alpha X_{\alpha'}\right] \\ &\quad + \sum_{\lambda\lambda'}\left[\frac{\delta_{\lambda\lambda'}}{2}\tilde{P}_\lambda\tilde{P}_{\lambda'} + \frac{\omega_\lambda^2\delta_{\lambda\lambda}}{2}\tilde{X}_\lambda\tilde{X}_{\lambda'}\right] \\ &\quad - \sum_{\alpha\lambda'}\sqrt{\varepsilon_0}\omega_\lambda C_{\alpha\lambda}X_\alpha\tilde{X}_\lambda. \end{aligned} \tag{E.3a}$$

Thanks to the first transformation, the light and matter oscillators are coupled through their coordinates, which reduces the problem of finding the eigenmodes to diagonalizing a symmetric quadratic form K, given by

$$K_{\alpha\alpha'} = \frac{\omega_\alpha^2}{2}\delta_{\alpha\alpha'} + \frac{c_{\alpha\alpha'}}{2}(1 - \delta_{\alpha\alpha'}) \tag{E.3b}$$

in the polarization sector,

$$K_{\lambda\lambda'} = \frac{\omega_\lambda^2}{2}\delta_{\lambda\lambda'} \tag{E.3c}$$

in the photonic sector, and

$$K_{\alpha\lambda} = K_{\lambda\alpha} = -\frac{\sqrt{\epsilon_0}\omega_\lambda}{2}C_{\alpha\lambda} \tag{E.3d}$$

for the couplings. Such a quadratic form can be diagonalized with an orthogonal transformation O, where $O^{\mathrm{t}} = O^{-1}$, such that $OKO^{\mathrm{t}} = D$. Thus, we can write the polaritonic coordinates and momenta as

$$\Sigma_\eta = \sum_\alpha O_{\eta\alpha} X_\alpha + \sum_\lambda O_{\eta\lambda} \frac{-\Pi_\lambda}{\sqrt{\varepsilon_0}\omega_\lambda} \quad \text{and} \tag{E.4a}$$

$$\Xi_\eta = \sum_\alpha O_{\eta\alpha} P_\alpha + \sum_\lambda O_{\eta\lambda} \big(\sqrt{\varepsilon_0}\omega_\lambda A_\lambda\big), \tag{E.4b}$$

respectively, where we have already undone the transformation from eq. (E.2). For the interaction between the emitter and the polaritonic modes, we must invert the above relations:

$$P_\alpha = \sum_\eta O_{\eta\alpha} \Xi_\eta, \qquad \Pi_\lambda = -\sqrt{\varepsilon_0}\omega_\lambda \sum_\eta O_{\eta\lambda} \Sigma_\eta, \tag{E.5a}$$

$$X_\alpha = \sum_\eta O_{\eta\alpha} \Sigma_\eta \quad \text{and} \quad A_\lambda = \frac{1}{\sqrt{\varepsilon_0}\omega_\lambda} \sum_\eta O_{\eta\lambda} \Xi_\eta. \tag{E.5b}$$

Once the light-matter eigenmodes have been found, we need to express these coordinates and momenta in terms of photonic and polaritonic ladder operators, $a_\lambda^{(\dagger)}$ and $b_\lambda^{(\dagger)}$, with expressions analogous to those of eq. (2.45). Then, the $\mathbf{p}_i \cdot \mathbf{A}^\perp(\mathbf{r}_i)$ term becomes, in the long-wavelength approximation,

$$\begin{aligned}
\sum_i \frac{q_i}{m_i} \mathbf{p}_i \cdot \mathbf{A}^\perp(\mathbf{r}_i) &\approx \sum_{t\lambda} i\sigma_t \omega_t (\mathbf{d}_t \cdot \boldsymbol{\psi}_\lambda(\mathbf{r}_\mathrm{e})) A_\lambda + \mathrm{H.c.} \\
&= \hbar \sum_{t\lambda} i\sigma_t \frac{\omega_t}{\omega_\lambda} g_{t,\lambda}^{\perp,0} \big(a_\lambda^\dagger + a_\lambda\big) + \mathrm{H.c.} \\
&= \sum_{t\eta} i\sigma_t \frac{\omega_t}{\omega_\eta} \sum_\lambda (\mathbf{d}_t \cdot \boldsymbol{\psi}_\lambda(\mathbf{r}_\mathrm{e})) \frac{\omega_\eta}{\sqrt{\varepsilon_0}\omega_\lambda} O_{\eta\lambda} \Xi_\eta + \mathrm{H.c.} \\
&= -\hbar \sum_{t\eta} \sigma_t \frac{\omega_t}{\omega_\eta} g_{t,\eta} \big(b_\eta^\dagger - b_\eta\big) + \mathrm{H.c.}
\end{aligned} \tag{E.6}$$

where we have expanded the emitter operator in terms of its transitions σ_t, and the coupling strengths are

$$g_{t,\lambda}^{\perp,0} = \sqrt{\frac{\omega_\lambda}{2\hbar\varepsilon_0}} (\mathbf{d}_t \cdot \boldsymbol{\psi}_\lambda(\mathbf{r}_\mathrm{e})) \quad \text{and} \tag{E.7a}$$

$$g_{t,\lambda}^{\perp} = \sqrt{\frac{\omega_\eta}{2\hbar\varepsilon_0}} \sum_\lambda \frac{\omega_\eta}{\omega_\lambda} (\mathbf{d}_t \cdot \boldsymbol{\psi}_\lambda(\mathbf{r}_\mathrm{e})) O_{\eta\lambda}. \tag{E.7b}$$

The corresponding spectral densities are

$$J^{\perp,0}_{t,\mu} = \sum_{\lambda} \frac{\omega_\lambda}{2\hbar\varepsilon_0} |\mathbf{d}_t \cdot \boldsymbol{\psi}_\lambda(\mathbf{r}_\mathrm{e})|^2 \delta\big(\omega_\lambda - \omega_\mu\big) \quad \text{and} \tag{E.8a}$$

$$J^{\perp}_{t,\mu} = \sum_{\eta} \frac{\omega_\eta}{2\hbar\varepsilon_0} \sum_{\lambda\lambda'} \frac{\omega_\eta^2 O_{\eta\lambda} O_{\eta\lambda'}}{\omega_\lambda \omega_{\lambda'}} (\mathbf{d}_t \cdot \boldsymbol{\psi}_\lambda(\mathbf{r}_\mathrm{e}))(\mathbf{d}_t^* \cdot \boldsymbol{\psi}_{\lambda'}(\mathbf{r}_\mathrm{e}))\delta\big(\omega_\eta - \omega_\mu\big). \tag{E.8b}$$

Note that, for compactness, we have included here the dipole moment in the definition of the couplings and spectral densities, as opposed to the convention in the rest of the thesis, but it has no further consequences.

There are two sum rules that can be straightforwardly derived from the above spectral densities. For the first one, we use the orthogonality of O, that is, $\sum_\eta O_{\eta\lambda} O_{\eta\lambda'} = \delta_{\lambda\lambda'}$, which implies that

$$\begin{aligned}
\sum_{\mu} \frac{J^{\perp}_{t,\mu}}{\omega_\mu^3} &= \sum_{\eta} \sum_{\lambda\lambda'} O_{\eta\lambda} O_{\eta\lambda'} \frac{(\mathbf{d}_t \cdot \boldsymbol{\psi}_\lambda(\mathbf{r}_\mathrm{e}))(\mathbf{d}_t^* \cdot \boldsymbol{\psi}_{\lambda'}(\mathbf{r}_\mathrm{e}))}{2\hbar\varepsilon_0 \omega_\lambda \omega_{\lambda'}} \\
&= \sum_{\lambda} \frac{\omega_\lambda}{2\hbar\varepsilon_0} \frac{|\mathbf{d}_t \cdot \boldsymbol{\psi}_\lambda(\mathbf{r}_\mathrm{e})|^2}{\omega_\lambda^3} = \sum_{\mu} \sum_{\lambda} \frac{\omega_\lambda}{2\hbar\varepsilon_0} \frac{|\mathbf{d}_t \cdot \boldsymbol{\psi}_\lambda(\mathbf{r}_\mathrm{e})|^2}{\omega_\mu^3} \delta\big(\omega_\lambda - \omega_\mu\big) \\
&= \sum_{\mu} \frac{J^{\perp,0}_{t,\mu}}{\omega_\mu^3}.
\end{aligned} \tag{E.9}$$

By noting that $J^{\perp,0}_{t,\mu} \propto \omega_\mu^3$, as is clear in eq. (2.66), we directly recover eq. (5.26b). As for the second, we use that, from the definition of the orthogonal transformation, $\sum_\eta O_{\eta\lambda} \omega_\eta^2 O_{\eta\lambda'} = \omega_\lambda^2 \delta_{\lambda\lambda'}$. Thus,

$$\begin{aligned}
\sum_{\mu} \frac{J^{\perp}_{t,\mu}}{\omega_\mu} &= \sum_{\eta} \sum_{\lambda\lambda'} \omega_\eta^2 O_{\eta\lambda} O_{\eta\lambda'} \frac{(\mathbf{d}_t \cdot \boldsymbol{\psi}_\lambda(\mathbf{r}_\mathrm{e}))(\mathbf{d}_t \cdot \boldsymbol{\psi}_{\lambda'}(\mathbf{r}_\mathrm{e}))^*}{2\hbar\varepsilon_0 \omega_\lambda \omega_{\lambda'}} \\
&= \sum_{\lambda} \omega_\lambda^2 \frac{|\mathbf{d}_t \cdot \boldsymbol{\psi}_\lambda(\mathbf{r}_\mathrm{e})|^2}{2\hbar\varepsilon_0} = \sum_{\mu} \sum_{\lambda} \frac{\omega_\lambda}{2\hbar\varepsilon_0} \frac{|\mathbf{d}_t \cdot \boldsymbol{\psi}_\lambda(\mathbf{r}_\mathrm{e})|^2}{\omega_\mu} \delta\big(\omega_\lambda - \omega_\mu\big) \\
&= \sum_{\mu} \frac{J^{\perp,0}_{t,\mu}}{\omega_\mu}.
\end{aligned} \tag{E.10}$$

A final interesting observation, already hinted at in the beginning of the section, is that we have chosen to work in the EI–SU picture because, in it, the properties of O, from which the sum rules follow, are the simplest. In fact, the above sum rules cannot be derived with the analogous procedure in the other pictures. Still, $J^{\perp}_{t,\eta}$ is a well-defined quantity that follows eqs. (E.9) and (E.10), regardless of how direct these are to derive in the other pictures.

E.1.2 eu–su

In this picture, both the emitter-field and structure-field interactions are written in multipolar coupling. Furthermore, because it results from a multicenter PZW transformation, there is no explicit Coulomb interaction between the emitter and the structure. This means that the emitter-polariton spectral density in the eu–su picture does not merely correspond to $J^{\perp}_{t,\eta}$, but to a full $J_{t,\eta}$ that implicitly includes the Coulomb interaction (see section 5.3.4). Under these circumstances, the structure-field diagonalization from section E.1.1 is still valid, even if the operators represent different physical quantities, strictly speaking. More explicitly, the mathematical shape of the quadratic form to be diagonalized is identical to the one introduced in eq. (E.3a), and, therefore, so are the orthogonal matrix O and the inversion relations in eq. (E.5). From eq. (D.9), the emitter-field interaction is

$$\begin{aligned}
\frac{1}{\varepsilon_0}\int \mathrm{d}^3 r\, \mathbf{P}_\mathrm{e}\cdot\boldsymbol{\Pi}^{\perp} &\approx \frac{1}{\varepsilon_0}\sum_{t\lambda}\sigma_t(\mathbf{d}_t\cdot\boldsymbol{\psi}_\lambda(\mathbf{r}_\mathrm{e}))\Pi_\lambda + \mathrm{H.c.}\\
&= i\hbar\sum_{t\lambda}\sigma_t g^{\perp,0}_{t,\lambda}\big(a^\dagger_\lambda - a_\lambda\big) + \mathrm{H.c.}\\
&= -\frac{1}{\sqrt{\varepsilon_0}}\sum_{t\eta}\sigma_t\sum_{\lambda}\omega_\lambda(\mathbf{d}_t\cdot\boldsymbol{\psi}_\lambda(\mathbf{r}_\mathrm{e}))O_{\eta\lambda}\Sigma_\eta + \mathrm{H.c.}\\
&= -\frac{1}{\sqrt{\varepsilon_0}}\sum_{t\eta}\sigma_t g_{t,\eta}\Big(b^\dagger_\eta + b_\eta\Big) + \mathrm{H.c.},
\end{aligned} \tag{E.11}$$

where

$$g^{\perp,0}_{t,\lambda} = \sqrt{\frac{\omega_\lambda}{2\hbar\varepsilon_0}}(\mathbf{d}_t\cdot\boldsymbol{\psi}_\lambda(\mathbf{r}_\mathrm{e})) \quad \text{and} \tag{E.12a}$$

$$g_{t,\eta} = \sqrt{\frac{\omega_\eta}{2\hbar\varepsilon_0}}\sum_{\lambda}\frac{\omega_\lambda}{\omega_\eta}(\mathbf{d}_t\cdot\boldsymbol{\psi}_\lambda(\mathbf{r}_\mathrm{e}))O_{\eta\lambda}. \tag{E.12b}$$

Note that $g_{t,\eta}$ does not have a $\perp$ symbol on it, and has a different factor of $\frac{\omega_\eta}{\omega_\lambda}$ compared to $g^{\perp}_{t,\eta}$ in eq. (E.7). The associated spectral densities are

$$J^{\perp,0}_{t,\mu} = \sum_{\lambda}\frac{\omega_\lambda}{2\hbar\varepsilon_0}|\mathbf{d}_t\cdot\boldsymbol{\psi}_\lambda(\mathbf{r}_\mathrm{e})|^2\delta\big(\omega_\lambda-\omega_\mu\big) \quad \text{and} \tag{E.12c}$$

$$J_{t,\mu} = \sum_{\eta}\frac{\omega_\eta}{2\hbar\varepsilon_0}\sum_{\lambda\lambda'}\frac{\omega_\lambda\omega_{\lambda'}O_{\eta\lambda}O_{\eta\lambda'}}{\omega_\eta^2}(\mathbf{d}_t\cdot\boldsymbol{\psi}_\lambda(\mathbf{r}_\mathrm{e}))(\mathbf{d}_t\cdot\boldsymbol{\psi}_{\lambda'}(\mathbf{r}_\mathrm{e}))^*\delta\big(\omega_\eta-\omega_\mu\big). \tag{E.12d}$$

Again, this "full" spectral density satisfies two sum rules directly analo-

gous to those discussed in the previous case, that is, which follow from the same properties of O. However, none of them turn out to be the sum rule in eq. (5.26b). Through analogous manipulations as the ones before, we arrive at

$$\sum_{\mu} \omega_{\mu} J_{t,\mu} = \sum_{\mu} \omega_{\mu} J^{\perp,0}_{t,\mu}, \tag{E.13}$$

from the orthogonality of O, and at

$$\sum_{\mu} \omega^3_{\mu} J_{t,\mu} = \sum_{\mu} \omega^3_{\mu} J^{\perp,0}_{t,\mu}, \tag{E.14}$$

from $\sum_{\eta} O_{\eta\lambda} \omega^2_{\eta} O_{\eta\lambda'} = \omega^2_{\lambda} \delta_{\lambda\lambda'}$.

E.1.3 EI–SI

The sum rules derived in the preceding sections trace back to the properties of the orthogonal diagonalization matrix O. In the next two sections, the structure-field Hamiltonian is expressed in the minimal coupling scheme, which essentially modifies the quadratic form to be diagonalized. With a mode expansion of the minimal coupling Hamiltonian, we reach the following oscillator Hamiltonian:

$$\begin{aligned} H_{\mathrm{osc}} &= H_{\mathrm{s}} + H_{\mathrm{f}} + H_{\mathrm{s-f}} \\ &= \sum_{\alpha\alpha} \left[\frac{\delta_{\alpha\alpha'}}{2} P_{\alpha} P_{\alpha'} + \frac{\omega^2_{\alpha} \delta_{\alpha\alpha'} + c'_{\alpha\alpha'}}{2} X_{\alpha} X_{\alpha'} \right] \\ &\quad + \sum_{\lambda\lambda'} \left[\frac{\delta_{\lambda\lambda'}}{2\varepsilon_0} \Pi_{\lambda} \Pi_{\lambda'} + \frac{\varepsilon_0 \left(\omega^2_{\lambda} \delta_{\lambda\lambda'} + c^{(A^2)}_{\lambda\lambda'} \right)}{2} A_{\lambda} A_{\lambda'} \right] \\ &\quad + \sum_{\alpha\lambda} C'_{\alpha\lambda} P_{\alpha} A_{\lambda'}. \end{aligned} \tag{E.15}$$

Here, we consider possible interactions between polarization oscillators with $c'_{\alpha\alpha'}$, generally different from those in eq. (E.1). Additionally, the off-diagonal coefficients $c^{(A^2)}_{\lambda\lambda'}$ represent the diamagnetic term.

Again, to find the eigenmodes of the system, we may first perform a canonical transformation that takes us from $\{P_{\alpha}, X_{\alpha}, \Pi_{\lambda}, A_{\lambda}\}$ to

$$\left\{ \Omega_{\alpha} \sum_{\alpha'} R_{\alpha'\alpha} X_{\alpha'}, \frac{-1}{\Omega_{\alpha}} \sum_{\alpha'} R_{\alpha'\alpha} P_{\alpha'}, \frac{\Pi_{\lambda}}{\sqrt{\varepsilon_0}}, \sqrt{\varepsilon_0} A_{\lambda} \right\} \equiv \{ P'_{\alpha}, X'_{\alpha}, \tilde{P}_{\lambda}, \tilde{X}_{\lambda} \}. \tag{E.16}$$

On the photonic sector, the transformation amounts to a mere rescaling. On the polarization sector, however, we diagonalize the oscillators through an orthogonal matrix R, which satisfies

$$\sum_{\alpha_1\alpha_2} R_{\alpha\alpha_1}\Omega_{\alpha_1}^2\delta_{\alpha_1\alpha_2}R_{\alpha'\alpha_2} = \omega_\alpha^2\delta_{\alpha\alpha'} + c'_{\alpha\alpha'} \tag{E.17}$$

and then swap positions and momenta, and rescale by the eigenfrequencies Ω_α. With this transformation, we simplify the final diagonalization step as much as possible, and reduce it to a similar procedure to the one in section E.1.2. Expressing eq. (E.18a) in terms of the new variables, we arrive at

$$\begin{aligned} H_{\text{osc}} &= H_{\text{s}} + H_{\text{f}} + H_{\text{s-f}} \\ &= \sum_{\alpha\alpha'}\left[\frac{\delta_{\alpha\alpha'}}{2}P'_\alpha P'_{\alpha'} + \frac{\Omega_\alpha^2\delta_{\alpha\alpha'}}{2}X'_\alpha X'_{\alpha'}\right] \\ &\quad + \sum_{\lambda\lambda'}\left[\frac{\delta_{\lambda\lambda'}}{2}\tilde{P}_\lambda\tilde{P}_{\lambda'} + \frac{\omega_\lambda^2\delta_{\lambda\lambda'} + c_{\lambda\lambda'}^{(A^2)}}{2}\tilde{X}_\lambda\tilde{X}_{\lambda'}\right] \\ &\quad - \sum_{\alpha\lambda}\left[\sum_{\alpha'}\frac{C'_{\alpha'\lambda}R_{\alpha'\alpha}}{\sqrt{\varepsilon_0}\Omega_\alpha}\right]X'_\alpha\tilde{X}_\lambda. \end{aligned} \tag{E.18a}$$

Just like before, finding the eigenmodes amounts to diagonalizing a real and symmetric quadratic form K' given by

$$K'_{\alpha\alpha'} = \frac{1}{2}\Omega_\alpha^2\delta_{\alpha\alpha'} \tag{E.18b}$$

in the polarization sector. As for the photon sector, we have

$$K'_{\lambda\lambda'} = \frac{\omega_\lambda^2\delta_{\lambda\lambda'} + c_{\lambda\lambda'}^{(A^2)}}{2}, \tag{E.18c}$$

and

$$K'_{\alpha\lambda} = \frac{1}{2}\sum_{\alpha'}\frac{C'_{\alpha'\lambda}R_{\alpha'\alpha}}{\sqrt{\varepsilon_0}\Omega_\alpha} \tag{E.18d}$$

couples light and matter. The quadratic form K' can be diagonalized with an orthogonal transformation O', with $O'^{-1} = O'^{\text{t}}$, such that $O'K'O'^{\text{t}} = D$. The diagonal matrix D carries no prime, because it must be the same in eq. (E.3a) and in eq. (E.18a): the Hamiltonians are unitarily related, and thus share their energy spectrum.

Next, the polaritonic coordinates and momenta are

$$\Sigma_\eta = \sum_\alpha O'_{\eta\alpha} X'_\alpha + \sum_\lambda O'_{\eta\lambda} \sqrt{\varepsilon_0} A_\lambda \quad \text{and} \tag{E.19a}$$

$$\Xi_\eta = \sum_\alpha O'_{\eta\alpha} P'_\alpha + \sum_\lambda O'_{\eta\lambda} \frac{\Pi_\lambda}{\sqrt{\varepsilon_0}}, \tag{E.19b}$$

respectively, where we have not undone the polarization oscillator diagonalization implemented by R, as it is not needed for what follows. We may invert these relations to find

$$X'_\alpha = \sum_\eta O'_{\eta\alpha} \Sigma_\eta, \qquad \sqrt{\varepsilon_0} A_\lambda = \sum_\eta O'_{\eta\lambda} \Sigma_\eta, \tag{E.20a}$$

$$P'_\alpha = \sum_\eta O'_{\eta\alpha} \Xi_\eta \quad \text{and} \quad \frac{\Pi_\lambda}{\sqrt{\varepsilon_0}} = \sum_\eta O'_{\eta\lambda} \Xi_\eta. \tag{E.20b}$$

Incidentally, it is straightforward to see that the matrix $M_{\lambda\eta}$ in eq. (5.24) is related to the orthogonal matrix through

$$M_{\lambda\eta} = \sqrt{\frac{\omega_\lambda}{\omega_\eta}} O'_{\eta\lambda}. \tag{E.21}$$

Now, we look at the emitter's interaction with the field, which is expressed in minimal coupling as:

$$\begin{aligned}
\sum_i \frac{q_i}{m_i} \mathbf{p}_i \cdot \mathbf{A}^\perp(\mathbf{r}_i) &\approx \sum_{t\lambda} i\sigma_t \omega_t (\mathbf{d}_t \cdot \boldsymbol{\psi}_\lambda(\mathbf{r}_\mathrm{e})) A_\lambda + \mathrm{H.c.} \\
&= \hbar \sum_{t\lambda} i\sigma_t \frac{\omega_t}{\omega_\lambda} g^{\perp,0}_{t,\lambda} \left(a^\dagger_\lambda + a_\lambda\right) + \mathrm{H.c.} \\
&= \sum_{t\eta} i\sigma_t \frac{\omega_t}{\omega_\eta} \sum_\lambda (\mathbf{d}_t \cdot \boldsymbol{\psi}_\lambda(\mathbf{r}_\mathrm{e})) \frac{\omega_\eta}{\sqrt{\varepsilon_0}} O'_{\eta\lambda} \Sigma_\eta + \mathrm{H.c.} \\
&= \hbar \sum_{t\eta} i\sigma_t \frac{\omega_t}{\omega_\eta} g^\perp_{t,\eta} \left(b^\dagger_\eta + b_\eta\right) + \mathrm{H.c.},
\end{aligned} \tag{E.22}$$

with

$$g^{\perp,0}_{t,\lambda} = \sqrt{\frac{\omega_\lambda}{2\hbar\varepsilon_0}} (\mathbf{d}_t \cdot \boldsymbol{\psi}_\lambda(\mathbf{r}_\mathrm{e})) \quad \text{and} \tag{E.23a}$$

$$g^\perp_{t,\eta} = \sqrt{\frac{\omega_\eta}{2\hbar\varepsilon_0}} \sum_\lambda (\mathbf{d}_t \cdot \boldsymbol{\psi}_\lambda(\mathbf{r}_\mathrm{e})) O'_{\eta\lambda}, \tag{E.23b}$$

and the corresponding spectral densities are

$$J^{\perp,0}_{t,\mu} = \sum_{\lambda} \frac{\omega_\lambda}{2\hbar\varepsilon_0} |\mathbf{d}_t \cdot \boldsymbol{\psi}_\lambda(\mathbf{r}_\mathrm{e})|^2 \delta\big(\omega_\lambda - \omega_\mu\big) \quad \text{and} \tag{E.23c}$$

$$J^{\perp}_{t,\mu} = \sum_{\eta} \frac{\omega_\eta}{2\hbar\varepsilon_0} \sum_{\lambda\lambda'} O'_{\eta\lambda} O'_{\eta\lambda'} (\mathbf{d}_t \cdot \boldsymbol{\psi}_\lambda(\mathbf{r}_\mathrm{e}))(\mathbf{d}_t \cdot \boldsymbol{\psi}_{\lambda'}(\mathbf{r}_\mathrm{e}))^* \delta\big(\omega_\eta - \omega_\mu\big). \tag{E.23d}$$

Because the transverse spectral density is a well-defined quantity, $J^{\perp}_{t,\mu}$ must be equal to the one in eq. (E.8b), even if their expressions seem different. These apparently contradictory facts are reconciled by realizing that $O \neq O'$. From the orthogonality of O', we straightforwardly recover the following sum rule:

$$\sum_{\mu} \frac{J^{\perp}_{t,\mu}}{\omega_\mu} = \sum_{\mu} \frac{J^{\perp,0}_{t,\mu}}{\omega_\mu}, \tag{E.24}$$

which coincides with the one as in eq. (E.10). Additionally, $J^{\perp}_{t,\mu}$ must still satisfy the sum rule in eq. (5.26b), or eq. (E.9). Nevertheless, it is not as simple to relate it directly to the properties of O'.

E.1.4 eu–si

In the last picture, the structure-field Hamiltonian and its associated quadratic form, are identical to eq. (E.18a). Therefore, the ensuing diagonalization and orthogonal matrix O' remain unchanged. The emitter-field interaction is

$$\begin{aligned}
\frac{1}{\varepsilon_0} \int \mathrm{d}^3 r \, \mathbf{P}_\mathrm{e} \cdot \boldsymbol{\Pi}^{\perp} &\approx \frac{1}{\varepsilon_0} \sum_{t\lambda} \sigma_t (\mathbf{d}_t \cdot \boldsymbol{\psi}_\lambda(\mathbf{r}_\mathrm{e})) \Pi_\lambda + \mathrm{H.c.} \\
&= i\hbar \sum_{t\lambda} \sigma_t g^{\perp,0}_{t,\lambda} \big(a^\dagger_\lambda - a_\lambda\big) + \mathrm{H.c.} \\
&= \frac{1}{\sqrt{\varepsilon_0}} \sum_{t\eta} \sigma_t \sum_{\lambda} (\mathbf{d}_t \cdot \boldsymbol{\psi}_\lambda(\mathbf{r}_\mathrm{e})) O'_{\eta\lambda} \Xi_\eta + \mathrm{H.c.} \\
&= i\hbar \sum_{t\eta} \sigma_t g^{\perp}_{t,\eta} \big(b^\dagger_\eta - b_\eta\big) + \mathrm{H.c.}
\end{aligned} \tag{E.25}$$

The coupling functions, given by

$$g^{\perp,0}_{t,\lambda} = \sqrt{\frac{\omega_\lambda}{2\hbar\varepsilon_0}} (\mathbf{d}_t \cdot \boldsymbol{\psi}_\lambda(\mathbf{r}_\mathrm{e})) \quad \text{and} \tag{E.26a}$$

$$g^{\perp}_{t,\lambda} = \sqrt{\frac{\omega_\eta}{2\hbar\varepsilon_0}} \sum_{\lambda} (\mathbf{d}_t \cdot \boldsymbol{\psi}_\lambda(\mathbf{r}_\mathrm{e})) O'_{\eta\lambda}, \tag{E.26b}$$

are identical to eq. (E.23). Accordingly, every conclusion reached in the previous section holds with no further contemplations required.

E.2 Polarization self-energy

In section 5.2.4, we have shown that the PSE can be expressed as a sum over the emitter-field coupling strength in the multipolar coupling scheme, that is,

$$H_{\mathrm{PSE}} = \frac{1}{2\varepsilon_0}\int \mathrm{d}^3 r \left(\mathbf{P}_{\mathrm{e}}^{\perp}\right)^2 \approx \hbar \sum_{\lambda} \frac{\left(g_{\lambda}^{\perp,0}\right)^2}{\omega_{\lambda}} \left(\mathbf{d}\cdot\hat{\mathbf{u}}_{\lambda}\right)^2 = H_{\mathrm{DSE}}. \tag{E.27}$$

Here, $\hat{\mathbf{u}}_{\lambda}$ is a polarization unit vector of the mode function $\boldsymbol{\psi}_{\lambda}(\mathbf{r}_{\mathrm{e}})$, and

$$g_{\lambda}^{\perp,0} = \sqrt{\frac{\omega_{\lambda}}{2\hbar\varepsilon_0}} |\boldsymbol{\psi}_{\lambda}(\mathbf{r}_{\mathrm{e}})| \tag{E.28}$$

is the coupling strength between the emitter and the "multipolar-coupling photons", which, physically, are not just photons, as the canonical field momentum in the EU–SI picture is $\boldsymbol{\Pi}^{\perp} = -\varepsilon_0 \mathbf{E}^{\perp} - \mathbf{P}_{\mathrm{e}}^{\perp}$. In any case, the nanostructure surrounding the emitter is not included in these excitations. However, as done multiple times in chapter 5, it is typically more convenient to work with the hybrid structure-field excitations, to which the emitter is then coupled with $g_{\eta}^{\perp}$. The question addressed here is whether one can write

$$H_{\mathrm{DSE}} = \hbar \sum_{\eta} \frac{\left(g_{\eta}^{\perp}\right)^2}{\omega_{\eta}} \left(\mathbf{d}\cdot\hat{\mathbf{u}}_{\eta}\right)^2. \tag{E.29}$$

The answer, as it often happens in life, is that it depends. Fortunately, all the leg work done in the preceding sections of this appendix will come in handy, as we can use the expressions for the coupling strengths in each possible picture with an emitter PSE term: EU–SI and EU–SU.

EU–SI In this picture (see section E.1.4),

$$g_{\eta}^{\perp} = \sqrt{\frac{\omega_{\eta}}{2\hbar\varepsilon_0}} \left| \sum_{\lambda} O'_{\eta\lambda} \boldsymbol{\psi}_{\lambda}(\mathbf{r}_{\mathrm{e}}) \right|, \tag{E.30}$$

where we have removed the $\mathbf{d}_t \cdot \hat{\mathbf{u}}_\eta$ factor to match the definitions in chapter 5, with $\hat{\mathbf{u}}_\eta$ a unit vector along the direction of

$$\sum_\lambda O'_{\eta\lambda} \boldsymbol{\psi}_\lambda(\mathbf{r}_\mathrm{e}). \tag{E.31}$$

Because O' is an orthogonal matrix, we have

$$\begin{aligned} H_\mathrm{DSE} &\stackrel{?}{=} \hbar \sum_\eta \frac{\left(g_\eta^\perp\right)^2}{\omega_\eta} \left(\mathbf{d} \cdot \hat{\mathbf{u}}_\eta\right)^2 = \hbar \sum_\eta \frac{\left(\mathbf{d} \cdot \sum_\lambda O'_{\eta\lambda} \boldsymbol{\psi}_\lambda(\mathbf{r}_\mathrm{e})\right)^2}{\omega_\eta} \frac{\omega_\eta}{2\hbar\varepsilon_0} \\ &= \hbar \sum_{\lambda\lambda'} \frac{(\mathbf{d} \cdot \boldsymbol{\psi}_\lambda(\mathbf{r}_\mathrm{e}))(\mathbf{d} \cdot \boldsymbol{\psi}_{\lambda'}(\mathbf{r}_\mathrm{e}))}{2\hbar\varepsilon_0} \sum_\eta O_{\eta\lambda} O_{\eta\lambda'} \\ &= \hbar \sum_\lambda \frac{\omega_\lambda |\boldsymbol{\psi}_\lambda(\mathbf{r}_\mathrm{e})|^2}{2\hbar\varepsilon_0\omega_\lambda} (\mathbf{d} \cdot \hat{\mathbf{u}}_\lambda) = \hbar \sum_\lambda \frac{\left(g_\lambda^{\perp,0}\right)^2}{\omega_\lambda} (\mathbf{d} \cdot \hat{\mathbf{u}}_\lambda)^2 \stackrel{!}{=} H_\mathrm{DSE}. \end{aligned} \tag{E.32}$$

With the above manipulations, we have shown that the PSE is related to the emitter-field coupling strength in the partial multipolar coupling picture, as was required for the argument concerning the PSE in section 5.2.4.

There is another possible way to prove the relation, which will be useful in the following. We must first realize that, in going from EI–SI to EU–SI, the oscillator Hamiltonian in eq. (E.18a) becomes

$$T_\mathrm{e} H_\mathrm{osc} T_\mathrm{e}^\dagger = H_\mathrm{osc} + \frac{1}{\varepsilon_0} \int \mathrm{d}^3 r \, \mathbf{P}_\mathrm{e}^\perp \cdot \boldsymbol{\Pi}^\perp + \frac{1}{2\varepsilon_0} \int \mathrm{d}^3 r \, \left(\mathbf{P}_\mathrm{e}^\perp\right)^2. \tag{E.33}$$

In other words, the multipolar emitter-field interaction and PSE appear from the transformation of the oscillator Hamiltonian, and are identified as the linear and quadratic terms in $\mathbf{P}_\mathrm{e}^\perp$. By expressing T_e and H_osc in terms of the structure-field eigenmodes b_η from the start, we automatically reach the emitter-field and PSE, both in terms of $g_\eta^\perp$, and it is evident that eq. (E.29) must hold. In any case, we will next show that some care has to be taken with these kinds of relations, as it is different in the EU–SU.

EU–SU From appendix D, we know that the EU–SU picture is reached from the EI–SU with T_e. The initial oscillator Hamiltonian is

$$\begin{aligned} H_\mathrm{osc} = &\sum_{i \in C_\mathrm{s}} \frac{\mathbf{p}_i^2}{2m_i} + \sum_{i \neq j \in C_\mathrm{s}} \frac{q_i q_j}{8\pi\varepsilon_0 |\mathbf{r}_i - \mathbf{r}_j|} + \frac{1}{\varepsilon_0} \int \mathrm{d}^3 r \, \left(\mathbf{P}_\mathrm{s}^\perp\right)^2 \\ &+ \int \mathrm{d}^3 r \left[\frac{\left(\boldsymbol{\Pi}^\perp\right)^2}{2\varepsilon_0} + \frac{\varepsilon_0 c^2}{2} \left(\nabla \times \mathbf{A}^\perp\right)^2 \right] + \frac{1}{\varepsilon_0} \int \mathrm{d}^3 r \, \mathbf{P}_\mathrm{s}^\perp \cdot \boldsymbol{\Pi}^\perp. \end{aligned} \tag{E.34}$$

Now, applying T_e yields

$$T_\mathrm{e} H_\mathrm{osc} T_\mathrm{e}^\dagger = H_\mathrm{osc} + \frac{1}{\varepsilon_0}\int \mathrm{d}^3 r\, \mathbf{P}_\mathrm{e}^\perp \cdot \mathbf{\Pi}^\perp + \frac{1}{\varepsilon_0}\int \mathrm{d}^3 r\, \mathbf{P}_\mathrm{e}^\perp \cdot \mathbf{P}_\mathrm{s}^\perp + \frac{1}{2\varepsilon_0}\int \mathrm{d}^3 r\, \left(\mathbf{P}_\mathrm{e}^\perp\right)^2. \tag{E.35}$$

The term with the integral of $\mathbf{P}_\mathrm{e}^\perp \cdot \mathbf{P}_\mathrm{s}^\perp$ comes from the transformation of the structure-field interaction, which now depends on $\mathbf{\Pi}^\perp$ rather than on $\mathbf{A}^\perp$. Unlike $\mathbf{A}^\perp$, it turns out that $\mathbf{\Pi}^\perp$ does not commute with T_e. If we were to express the equation above through the polaritonic eigenmodes, we would reach one linear and one quadratic term in $\mathbf{P}_\mathrm{e}^\perp$. The quadratic one still corresponds to the PSE; however, the linear one is not merely the emitter-field interaction: it also contains the $\mathbf{P}_\mathrm{e}^\perp \cdot \mathbf{P}_\mathrm{s}^\perp$ term. More specifically, the full linear and quadratic terms do fulfill the DSE relation, since

$$\frac{1}{\varepsilon_0}\int \mathrm{d}^3 r\, \mathbf{P}_\mathrm{e}^\perp \cdot \left(\mathbf{\Pi}^\perp + \mathbf{P}_\mathrm{s}^\perp\right) \approx \hbar \sum_\eta \left(\mathbf{d}\cdot\hat{\mathbf{u}}_\eta\right) g_\eta^\perp \left(b_\eta^\dagger + b_\eta\right), \tag{E.36}$$

and the PSE is

$$H_\mathrm{DSE} = \hbar \sum_\eta \frac{\left(g_\eta^\perp\right)^2}{\omega_\eta}\left(\mathbf{d}\cdot\hat{\mathbf{u}}_\eta\right)^2. \tag{E.37}$$

However, the emitter-field interaction is not determined by $g_\eta^\perp$, but by a different coupling g_η:

$$\frac{1}{\varepsilon_0}\int \mathrm{d}^3 r\, \mathbf{P}_\mathrm{e}^\perp \cdot \mathbf{\Pi}^\perp \approx \hbar \sum_\eta \left(\mathbf{d}\cdot\hat{\mathbf{u}}_\eta\right) g_\eta \left(b_\eta^\dagger + b_\eta\right), \tag{E.38}$$

as we saw in section E.1.2. This coupling function physically includes the Coulomb interaction, which is why we remove the $\perp$ superscript. Indeed, the $\mathbf{P}_\mathrm{e}^\perp \cdot \mathbf{P}_\mathrm{s}^\perp$ interaction exactly cancels the explicit Coulomb interaction term. Explicitly, if there is no overlap between the emitter and structure polarization fields, we can write

$$\frac{1}{\varepsilon_0}\int \mathrm{d}^3 r\, \mathbf{P}_\mathrm{e}^\perp \cdot \mathbf{P}_\mathrm{s}^\perp = -\frac{1}{\varepsilon_0}\int \mathrm{d}^3 r\, \mathbf{P}_\mathrm{e}^\parallel \cdot \mathbf{P}_\mathrm{s}^\parallel = \int \mathrm{d}^3 r\, \mathbf{P}_\mathrm{e}^\parallel \cdot \mathbf{E}_\mathrm{s}^\parallel. \tag{E.39}$$

In short, the appearance of an extra $\mathbf{P}_\mathrm{e}^\perp \cdot \mathbf{P}_\mathrm{s}^\perp$ term compared to eq. (E.33) is indicative of the shift of the Coulomb interaction from being an independent term in the Hamiltonian to being included in g_η.

Appendix F | Analytical calculations for the model in chapter 5

Here, we provide the details of the analytical calculations involved in section 5.3. First, we perform the necessary integrals over the volume of the electronic sphere. Next, we go over some aspects of the Fano diagonalization procedure. Finally, we use Maxwell's equations to find the effective equation of motion of the electronic sphere and obtain the photon-induced red-shift.

F.1 Integrals over slightly displaced spherical volumes

F.1.1 Coulomb interaction between the charged spheres

We have to integrate the electrostatic potential due to the ionic sphere ϕ_+ over the volume of the electronic sphere. The off-set of their centers complicates matters, but an exact analytical expression can still be obtained. We split the electronic sphere's volume in three parts: the regions I and II are in the overlap between the spheres, and are defined by $z_s - R_s \leq z \leq z_s/2$ (I), $z_s/2 < z \leq R_s$ (II), while the non-overlapping part is region III (see fig. F.1). For convenience, we use cilyndrical coordinates in regions I and II, where the integration over

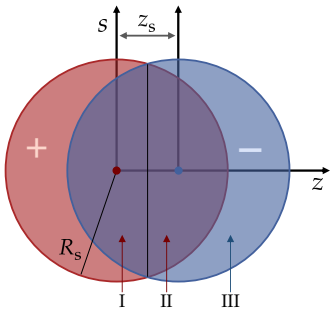

Figure F.1: Graphical representation of the integration regions (I and II in the overlapping region, and III out of the ionic sphere) for the Coulomb interaction between the electronic and ionic spheres.

the azimuthal angle yields a 2π factor. Then, we have

$$\begin{aligned}\int_{\mathrm{I/II}} \mathrm{d}^3 r\, \rho\phi_+ &= \frac{\pi\rho^2}{3\varepsilon_0} \int_{\mathrm{I/II}} \mathrm{d}z \int_0^{S_{\mathrm{I/II}}(z)} \mathrm{d}s\, s\big(3R_\mathrm{s}^2 - s^2 - z^2\big) \\ &= \frac{\pi\rho^2}{12\varepsilon_0} \int_{\mathrm{I/II}} \mathrm{d}z \left[\big(6R_\mathrm{s}^2 - 2z^2\big) S_{\mathrm{I/II}}^2(z) - S_{\mathrm{I/II}}^4(z)\right], \end{aligned} \tag{F.1}$$

where $S_\mathrm{I}(z) = \sqrt{R_\mathrm{s}^2 + (z - z_\mathrm{s})^2}$ and $S_\mathrm{II}(z) = \sqrt{R_\mathrm{s}^2 + z^2}$. The integrands over z of regions I and II are then simply polynomic functions. After lengthy manipulations, we obtain

$$\int_{\mathrm{I+II}} \mathrm{d}^3 r\, \rho\phi_+ = \frac{\pi\rho^2}{3\varepsilon_0}\left[\frac{8R_\mathrm{s}^5}{5} - R_\mathrm{s}^4 z_\mathrm{s} - \frac{R_\mathrm{s}^3 z_\mathrm{s}^2}{3} + \frac{R_\mathrm{s}^2 z_\mathrm{s}^3}{4} - \frac{z_\mathrm{s}^5}{120}\right]. \tag{F.2}$$

We change to spherical coordinates for region III. Again, the azimuthal angle's integral provides a 2π factor. The integral limits over the polar angle ϑ are 0 and ϑ_0, where $\cos\vartheta_0 = \frac{z_\mathrm{s}}{2R_\mathrm{s}}$, and the radial integration limits are R_s and $D(\cos\vartheta) = z_\mathrm{s}\cos\vartheta + \sqrt{z_\mathrm{s}^2\cos^2\vartheta + R_\mathrm{s}^2 - z_\mathrm{s}^2}$. Thus,

$$\begin{aligned}\int_{\mathrm{III}} \mathrm{d}^3 r\, \rho\phi_+ &= \frac{2\pi\rho^2 R_\mathrm{s}^3}{3\varepsilon_0} \int_0^{\vartheta_0} \mathrm{d}\vartheta \int_{R_\mathrm{s}}^{D(\cos\vartheta)} \mathrm{d}r\, r^2 \frac{1}{r} \\ &= \frac{\pi\rho^2 R_\mathrm{s}^3}{3\varepsilon_0} \int_{\frac{z_\mathrm{s}}{2R_\mathrm{s}}}^1 \mathrm{d}x \left[D^2(x) - R_\mathrm{s}^2\right] = \frac{\pi\rho^2}{3\varepsilon_0}\left[R_\mathrm{s}^4 z_\mathrm{s} - \frac{R_\mathrm{s}^3 z_\mathrm{s}^2}{3}\right] \end{aligned} \tag{F.3}$$

where $x = \cos\vartheta$, and the intermediate steps are immediate integrals. Then, the whole electrostatic interaction between the spheres is

$$\int \mathrm{d}^3 r\, \rho\phi_+ = \frac{\pi\rho^2}{3\varepsilon_0}\left[\frac{8R_\mathrm{s}^5}{5} - \frac{2R_\mathrm{s}^3 z_\mathrm{s}^2}{3} + \frac{R_\mathrm{s}^2 |z_\mathrm{s}|^3}{4} - \frac{|z_\mathrm{s}|^5}{120}\right]. \tag{F.4}$$

Finally, in the small oscillation limit, we can discard all terms but the constant and quadratic ones. The constant cancels the electrostatic self-energies of the spheres, and the quadratic term gives rise to a harmonic restoring force. Expressed in terms of the electronic sphere's mass and the plasma frequency $\Omega_\mathrm{P} = \sqrt{\frac{\rho e}{m_\mathrm{e}\varepsilon_0}}$, we recover

$$\int \mathrm{d}^3 r\, \rho\phi_+ = \frac{8\pi\rho^2 R_\mathrm{s}^5}{15\varepsilon_0} - \frac{m_\mathrm{s}}{2}\frac{\Omega_\mathrm{P}^2}{3} z_\mathrm{s}^2. \tag{F.5}$$

F.1.2 Minimal coupling interaction between the sphere and photons

The nanosphere-photon interaction is given by the generalization of $\mathbf{p}_i - q_i\mathbf{A}^{\perp}(\mathbf{r}_i)$ to an extended charge distribution that appears in eq. (5.47). To reach eq. (5.53), we expand the vector potential in the spherical-wave basis

$$\int \mathrm{d}^3r\, \rho\big(\hat{\mathbf{z}}\cdot\mathbf{A}^{\perp}\big) = \frac{4\rho R_{\mathrm{s}}^2}{\sqrt{3c}} \sum_{p,lm} \int \mathrm{d}\omega\, A_{lm}^{(p)}(\omega) \int \mathrm{d}^3r\, \rho\Big(\hat{\mathbf{z}}\cdot\boldsymbol{\psi}_{lm}^{(p)}(\omega)\Big), \tag{F.6}$$

Here, we perform the spatial integration for tm and te modes separately. As we will see shortly, the finite values of z_{s} can be neglected, which simplifies the charge density to $\rho(\mathbf{r}) = \rho\theta(|\mathbf{r}| - R_{\mathrm{s}})$. The price to pay is that terms $O(z_{\mathrm{s}})$ and beyond are discarded, which is, nevertheless, fine if the constant term is non-zero and the oscillations are small. With these considerations, let us evaluate the tm integral first:

$$\begin{aligned}
I_{lm}^{(\mathrm{tm})}(\omega) &= \int \mathrm{d}^3r\, \rho\Big(\hat{\mathbf{z}}\cdot\boldsymbol{\psi}_{lm}^{(\mathrm{tm})}(\omega)\Big) = \frac{c}{\omega}\int \mathrm{d}^3r\, \rho\Big(\hat{\mathbf{z}}\cdot\nabla\times\boldsymbol{\psi}_{lm}^{(\mathrm{te})}(\omega)\Big) \\
&= \frac{c}{\omega}\int \mathrm{d}^3r\, \Big[-\nabla\cdot\Big(\rho\hat{\mathbf{z}}\times\boldsymbol{\psi}_{lm}^{(\mathrm{te})}(\omega)\Big) + \boldsymbol{\psi}_{lm}^{(\mathrm{te})}(\omega)\cdot\nabla\times\Big(\rho\hat{\mathbf{z}}\Big)\Big] \\
&= \frac{c}{\omega}\int \mathrm{d}^3r\, \boldsymbol{\psi}_{lm}^{(\mathrm{te})}(\omega)\cdot\nabla\rho\times\hat{\mathbf{z}} \\
&= -\frac{\rho c}{\omega}\int_{\Omega}\mathrm{d}\Omega\int_0^{\infty}\mathrm{d}r\, r^2\delta(r-R_{\mathrm{s}})\boldsymbol{\psi}_{lm}^{(\mathrm{te})}(\omega)\cdot\hat{\mathbf{r}}\times\big(\hat{\mathbf{r}}\cos\vartheta - \hat{\boldsymbol{\vartheta}}\sin\vartheta\big) \\
&= \frac{\sqrt{2}\rho R_{\mathrm{s}}^2 j_l\Big(\frac{\omega R_{\mathrm{s}}}{c}\Big)}{\sqrt{l(l+1)\pi c}}\int_{\Omega}\mathrm{d}\Omega\,\sin\vartheta\Big[\hat{\boldsymbol{\vartheta}}\frac{\partial_\varphi}{\sin\vartheta} - \hat{\boldsymbol{\varphi}}\partial_\vartheta\Big]Y_{lm}(\vartheta,\varphi)\cdot\hat{\boldsymbol{\varphi}} \\
&= -\frac{\sqrt{2}\rho R_{\mathrm{s}}^2 j_l\Big(\frac{\omega R_{\mathrm{s}}}{c}\Big)}{\sqrt{l(l+1)\pi c}}\int_{\Omega}\mathrm{d}\Omega\sin\vartheta\,\partial_\vartheta Y_{lm}(\vartheta,\varphi) \\
&= \frac{\sqrt{8}\rho R_{\mathrm{s}}^2 j_l\Big(\frac{\omega R_{\mathrm{s}}}{c}\Big)}{\sqrt{l(l+1)\pi c}}\int\mathrm{d}\Omega\,\cos\vartheta\,Y_{lm}(\vartheta,\varphi) \\
&= \frac{4\sqrt{2}\rho R_{\mathrm{s}}^2 j_l\Big(\frac{\omega R_{\mathrm{s}}}{c}\Big)}{\sqrt{3l(l+1)c}}\int_{\Omega}\mathrm{d}\Omega\,Y_{10}(\vartheta,\varphi)Y_{lm}(\vartheta,\varphi) \\
&= \frac{4\rho R_{\mathrm{s}}^2}{\sqrt{3c}} j_1\Big(\frac{\omega R_{\mathrm{s}}}{c}\Big)\delta_{l1}\delta_{m0}.
\end{aligned}$$

In the above lengthy manipulations, we have started with the relation between tm and te mode functions, to benefit from the simpler expression of the te ones. Then, we have used integration by parts on the curl. Then, the divergence vanishes directly because $\rho = 0$ at $|\mathbf{r}| > R_{\mathrm{s}}$. As for the curl, it can be

written in terms of the charge density's gradient, which yields a $-\delta(r-R_s)\hat{\mathbf{r}}$. We next express $\hat{\mathbf{z}}$ in spherical coordinates through $\hat{\mathbf{z}} = \hat{\mathbf{r}}\cos\vartheta - \hat{\boldsymbol{\vartheta}}\sin\vartheta$, and take the vector product $\hat{\mathbf{r}}\times\hat{\boldsymbol{\vartheta}} = \hat{\boldsymbol{\varphi}}$. The radial integration is trivial, recalling the definition of $\boldsymbol{\psi}^{(\mathrm{te})}_{lm}$ from eq. (5.49). The remaining angular integral can be evaluated through integration by parts, and then using the orthonormality of the spherical harmonics. Thus, only the $l=1, m=0$ element is non-zero. If we had not neglected the displacement, there would be further contributions of $O(z_s)$, but those are negligible in the small oscillation limit.

Let us finish by evaluating the $\lambda = \mathrm{te}$ terms:

$$\begin{aligned} I^{(\mathrm{te})}_{lm}(\omega) &= \int \mathrm{d}^3 r\, \rho\big(\hat{\mathbf{z}}\cdot\boldsymbol{\psi}^{(\mathrm{te})}_{lm}(\omega)\big) \\ &= \rho\int \mathrm{d}^3 r\, \frac{\omega}{c}\sqrt{\frac{2}{l(l+1)\pi c}} j_l\Big(\frac{\omega|\mathbf{r}|}{c}\Big)\hat{\mathbf{z}}\cdot\Big[\hat{\boldsymbol{\vartheta}}\frac{\partial_\varphi}{\sin\vartheta} - \hat{\boldsymbol{\varphi}}\partial_\vartheta\Big]Y_{lm}(\vartheta,\varphi) \\ &= \frac{-\rho\omega\sqrt{2}}{\sqrt{l(l+1)\pi c^3}}\int_\Omega \mathrm{d}\Omega\, \partial_\varphi Y_{lm}(\vartheta,\varphi)\int_0^{R_s}\mathrm{d}r\, r^2 j_l\Big(\frac{\omega r}{c}\Big) = 0. \end{aligned}$$

In the last line, we have used

$$\partial_\varphi Y_{lm} = \partial_\varphi\big(\alpha Y^m_l + \beta Y^{-m}_l\big) = im\big(\alpha Y^m_l - \beta Y^{-m}_l\big),$$

where Y^m_l are the usual complex harmonic oscillator, together with $\int \mathrm{d}\Omega\, Y^m_l \propto \delta_{m0}$, to find that the whole integral cancels. Consequently, in the limit of small oscillations, the sphere only couples to tm, $l=1$ and $m=0$ modes.

F.2 Details of the Fano diagonalization

The integrals involved in the Fano diagonalization itself, and in the reexpression of the interactions in terms of the polaritonic eigenmodes can all be related to the formulas in appendix A.2. Here, we find the explicit expression of $c_1(\omega)$ given in eq. (5.67), which comes from imposing $[\Sigma(\omega),\Xi(\omega')] = i\hbar\delta(\omega-\omega')$. This relation is equivalent to

$$\begin{aligned} \delta(\omega-\omega') &= c_1(\omega)c_1(\omega') + \int \mathrm{d}\Omega\, c_2(\omega,\Omega)c_2(\omega',\Omega) \\ &= c_1(\omega)c_1(\omega')\{A(\omega)\delta(\omega-\omega') + B(\omega,\omega')\} \end{aligned} \tag{F.7}$$

where we have used the defitions of $c_2(\omega,\omega')$, eq. (5.65), and $F(\omega)$, eq. (5.66), together with the partial fraction decomposition formula in eq. (A.7c), and

$$A(\omega) = \frac{\left(\omega^2 - \Omega_\mathrm{P}^2 - F(\omega)\right)^2}{\gamma^2(\omega)} + \frac{\pi^2}{4\omega^2}\gamma^2(\omega), \tag{F.8a}$$

$$B(\omega,\omega') = \frac{F(\omega) - F(\omega')}{\omega^2 - \omega'^2} + \frac{1}{\omega - \omega'} P \int \mathrm{d}\Omega \, \frac{\gamma^2(\Omega)}{(\omega+\Omega)(\omega'+\Omega)} \left[\frac{1}{\omega' - \Omega} - \frac{1}{\omega - \Omega}\right] \tag{F.8b}$$

It turns out that $B(\omega,\omega')$ vanishes, since

$$\begin{aligned}
-\frac{F(\omega) - F(\omega')}{\omega^2 - \omega'^2} &\overset{?}{=} \frac{1}{\omega - \omega'} P \int \mathrm{d}\Omega \, \frac{\gamma^2(\Omega)}{(\omega+\Omega)(\omega'+\Omega)} \left[\frac{1}{\omega' - \Omega} - \frac{1}{\omega - \Omega}\right] \\
&= \frac{1}{\omega^2 - \omega'^2} P \int \mathrm{d}\Omega \, \frac{\gamma^2(\Omega)}{(\omega+\Omega)(\omega'+\Omega)} \left[\frac{\omega+\omega'}{\omega' - \Omega} - \frac{\omega+\omega'}{\omega - \Omega}\right] \\
&= \frac{1}{\omega^2 - \omega'^2} P \int \mathrm{d}\Omega \left[\frac{\gamma^2(\Omega)}{\omega'^2 - \Omega^2} + \frac{\gamma^2(\Omega)}{(\omega'+\Omega)(\omega+\Omega)} \right. \\
&\qquad \left. - \frac{\gamma^2(\Omega)}{\omega^2 + \Omega^2} - \frac{\gamma^2(\Omega)}{(\omega'+\Omega)(\omega+\Omega)}\right] \\
&\overset{!}{=} \frac{F(\omega') - F(\omega)}{\omega^2 - \omega'^2},
\end{aligned} \tag{F.9}$$

and, accordingly,

$$\delta(\omega - \omega') = c_1(\omega) c_1(\omega') \left[\frac{\left(\omega^2 - \Omega_\mathrm{P}^2 - F(\omega)\right)^2}{\gamma^2(\omega)} + \frac{\pi^2}{4\omega^2}\gamma^2(\omega)\right] \delta(\omega - \omega'). \tag{F.10}$$

Therefore,

$$c_1^2(\omega) = \frac{\gamma^2(\omega)}{\left(\omega^2 - \Omega_\mathrm{P}^2 - F(\omega)\right)^2 + \frac{\pi^2}{4\omega^2}\gamma^4(\omega)}. \tag{F.11}$$

By taking the square root we arrive at eq. (5.67), which corresponds to one particular choice of the coefficient's phase.

F.3 Photon-induced shift

Finally, we derive the effective classical equation of motion of the electronic sphere from Maxwell's equations, eq. (2.1), and the Lorentz force equation, eq. (2.4). We start by deriving the equation of motion for the field variables and the sphere, and then find a solution. Through the combination of the

curl of Faraday's law, eq. (2.1c), with the time derivative of Ampere's law eq. (2.1d), we arrive at

$$\frac{1}{c^2}\ddot{\mathbf{E}}^{\perp} - \nabla^2\mathbf{E}^{\perp} = -\mu_0\partial_t\mathbf{j}_{\mathrm{s}}^{\perp}. \tag{F.12}$$

We next perform a mode expansion of the fields with the spherical-wave basis introduced in section A.3.1:

$$\mathbf{E}^{\perp}(\mathbf{r}) = \sum_{p,lm}\int \mathrm{d}\omega\, E_{lm}^{(p)}(\omega)\boldsymbol{\psi}_{lm}^{(p)}(\omega,\mathbf{r}) \quad \text{and} \tag{F.13a}$$

$$\mathbf{j}_{\mathrm{s}}^{\perp}(\mathbf{r}) = \int \mathrm{d}\omega\, \frac{-4\rho\dot{z}_{\mathrm{s}}R_{\mathrm{s}}^2}{\sqrt{3c}} j_1\!\left(\frac{\omega R_{\mathrm{s}}}{c}\right)\boldsymbol{\psi}_{10}^{(\mathrm{tm})}(\omega,\mathbf{r}), \tag{F.13b}$$

where the current's expansion has been retrieved from section A.3.2. Then, the current acts as a source for the tm, $l = 1$, $m = 0$ modes only, and, for those modes, eq. (F.12) becomes

$$\ddot{E}_{10}^{(\mathrm{tm})}(\omega) + \omega^2 E_{10}^{(\mathrm{tm})}(\omega) = \frac{4\rho R_{\mathrm{s}}^2}{\varepsilon_0\sqrt{3c}} j_1\!\left(\frac{\omega R_{\mathrm{s}}}{c}\right)\ddot{z}_{\mathrm{s}}. \tag{F.14}$$

The electronic sphere obeys Newton's second law of motion, where the force is due to the Coulomb field of the ionic sphere and the transverse EM field. The first term is obtained from the derivative of the potential in eq. (5.48)

$$\mathbf{F}_{\mathbf{E}^{\parallel}} = -m_{\mathrm{s}}\frac{\Omega_{\mathrm{P}}^2}{3} z_{\mathrm{s}}\hat{\mathbf{z}}, \tag{F.15a}$$

The force coming from $\mathbf{E}^{\perp}$ and $\mathbf{B}^{\perp}$ is harder to evaluate in general; however, there are a few simplifying notions. First, we remark that the symmetry of the configuration implies that the net force must be aligned with the z axis. Consequently, the force due to $\mathbf{E}^{\perp}$ is

$$\begin{aligned}\mathbf{F}_{\mathbf{E}^{\perp}} &= \hat{\mathbf{z}}\int \mathrm{d}^3r\, \rho(\mathbf{r})\hat{\mathbf{z}}\cdot\mathbf{E}^{\perp}(\mathbf{r}) = \sum_{p,lm}\int \mathrm{d}\omega\, E_{lm}^{(p)}(\omega)\int \mathrm{d}^3r\, \rho(\mathbf{r})\hat{\mathbf{z}}\cdot\boldsymbol{\psi}_{lm}^{(p)}(\omega,\mathbf{r}) \\ &= -\int \mathrm{d}\omega\, \frac{4\rho R_{\mathrm{s}}^2}{\sqrt{3c}} j_1\!\left(\frac{\omega R_{\mathrm{s}}}{c}\right)E_{10}^{(\mathrm{tm})}(\omega)\hat{\mathbf{z}}\end{aligned} \tag{F.15b}$$

which can be easily related to the expansion of $\mathbf{j}_{\mathrm{s}}^{\perp}$. As for the magnetic field,

$$\mathbf{F}_{\mathbf{B}^{\perp}} = \hat{\mathbf{z}}\int \mathrm{d}^3r\, \hat{\mathbf{z}}\cdot\mathbf{j}_{\mathrm{s}}(\mathbf{r})\times\mathbf{B}^{\perp}(\mathbf{r}) = \mathbf{0}, \tag{F.15c}$$

because the vector product ensures that the force is perpendicular to the z axis, and must vanish for symmetry reasons. Therefore,

$$\ddot{z}_\mathrm{s} + \frac{\Omega_\mathrm{P}^2}{3} z_\mathrm{s} = -\int \mathrm{d}\omega \, \frac{4\rho R_\mathrm{s}^2}{m_\mathrm{s}\sqrt{3c}} j_1\!\left(\frac{\omega R_\mathrm{s}}{c}\right) E_{10}^{(\mathrm{tm})}(\omega) \tag{F.16}$$

After reaching the coupled system of equations formed by eqs. (F.14) and (F.16), we proceed to solve them. To begin with, we define

$$g(\omega) = \frac{4\rho R_\mathrm{s}^2}{\sqrt{3c}} j_1\!\left(\frac{\omega R_\mathrm{s}}{c}\right) \tag{F.17}$$

for convenience. Then,

$$E_{10}^{(\mathrm{tm})}(\omega) = \frac{g(\omega)}{\omega^2 \varepsilon_0}\left\{\ddot{z}_\mathrm{s} - \int_0^t \mathrm{d}\tau \, \cos[\omega(t-\tau)]\dddot{z}_\mathrm{s}(\tau)\right\} \tag{F.18}$$

is a solution of eq. (F.14), with $E_{10}^{(\mathrm{tm})}(\omega, t=0) = \frac{g(\omega)}{\varepsilon_0\omega^2}\ddot{z}_\mathrm{s}$ and $\dot{E}_{10}^{(\mathrm{tm})}(\omega, t=0) = 0$, as can be checked with direct substitution. We plug eq. (F.18) in eq. (F.16), and obtain

$$\ddot{z}_\mathrm{s} + \frac{\Omega_\mathrm{P}^2}{3} z_\mathrm{s} = -\int \mathrm{d}\omega \, \frac{g^2(\omega)}{\omega^2 \varepsilon_0 m_\mathrm{s}}\left\{\ddot{z}_\mathrm{s} - \int_0^t \mathrm{d}\tau \, \cos[\omega(t-\tau)]\dddot{z}_\mathrm{s}(\tau)\right\}. \tag{F.19}$$

With eq. (A.24), the first term on the right-hand side becomes

$$-\frac{4}{15}\left(\frac{\Omega_\mathrm{P} R_\mathrm{s}}{c}\right)^2 \ddot{z}_\mathrm{s} \tag{F.20}$$

which reveals the frequency's dependence on the radius written in eq. (5.68):

$$\left[1 + \frac{4}{15}\left(\frac{\Omega_\mathrm{P} R_\mathrm{s}}{c}\right)^2\right]\ddot{z}_\mathrm{s} + \frac{\Omega_\mathrm{P}^2}{3} z_\mathrm{s} = \cdots \implies \ddot{z}_\mathrm{s} + \frac{\Omega_\mathrm{P}^2}{3}\left[1 + \frac{4}{15}\left(\frac{\Omega_\mathrm{P} R_\mathrm{s}}{c}\right)^2\right]^{-1} z_\mathrm{s} = \cdots \tag{F.21}$$

As for the missing term, we may write it as

$$\frac{8\rho^2 R_\mathrm{s}^6 \sqrt{2\pi}}{3c^3 \varepsilon_0 m_\mathrm{s}} \int_0^{\min(2, ct/R_\mathrm{s})} \mathrm{d}k \; \mathcal{F}\left[x^{-2} j_1^2(x)\right](k) \dddot{z}_\mathrm{s}\!\left(t - \frac{kR_\mathrm{s}}{c}\right) \simeq \frac{2\Omega_\mathrm{P}^2 R_\mathrm{s}^3}{9c^3} \dddot{z}_\mathrm{s}(t) \tag{F.22}$$

where $k = c(t-\tau)/R_\mathrm{s}$, and we have used eq. (A.24) again. In the last approximate equality, we have assumed $t > 2R_\mathrm{s}/c$, and then performed a Markov

approximation. The final equation of motion for the electronic sphere is

$$\left[1+\frac{4}{15}\left(\frac{\Omega_{\mathrm{P}}R_{\mathrm{s}}}{c}\right)^2\right]\ddot{z}_{\mathrm{s}}+\frac{\Omega_{\mathrm{P}}^2}{3}z_{\mathrm{s}}-\frac{2\Omega_{\mathrm{P}}^2R_{\mathrm{s}}^3}{9c^3}\dddot{z}_{\mathrm{s}}(t)=0, \tag{F.23}$$

and we can interpret each term in an intuitive way: the first square bracket corresponds to a sort of *electromagnetic inertia*, because the sphere *drags* the EM field in its motion. The second term is the Coulomb force that the ions exert over the electrons, and the last term, proportional to the *jerk*, represents the dissipation rate due to the so-called *radiation-reaction force*. This kind of equation of motion was considered in the Abraham-Lorentz model of the electron [304–306].

Bibliography

[1] J. C. Maxwell, XXV. On physical lines of force, London Edinburgh Dublin Philos. Mag. & J. Sci. **21**, 161–175 (1861) (p. 2).

[2] A. Einstein, Zur Elektrodynamik bewegter Körper, Ann. Phys. **322**, 891–921 (1905) (p. 2).

[3] M. Planck, Über das Gesetz der Energieverteilung im Normalspectrum, Ann. Phys. **309**, 553–563 (1901) (p. 2).

[4] A. Einstein, Über einen die Erzeugung und Verwandlung des Lichtes betreffenden heuristischen Gesichtspunkt, Ann. Phys. **322**, 132–148 (1905) (p. 2).

[5] N. Bohr, I. On the constitution of atoms and molecules, London Edinburgh Dublin Phil. Mag. & J. Sci. **26**, 1–25 (1913) (p. 2).

[6] P. A. M. Dirac, Quantum theory of emission and absorption of radiation, Proc. Roy. Soc. Lond. A **114**, 243 (1927) (p. 2).

[7] P. Jordan, Zur Quantenmechanik der Gasentartung, Z. Phys. **44**, 473–480 (1927) (p. 2).

[8] W. Heisenberg and W. Pauli, Zur Quantendynamik der Wellenfelder, Z. Phys. **56**, 1–61 (1929) (p. 2).

[9] W. Heisenberg and W. Pauli, Zur Quantentheorie der Wellenfelder. II, Z. Phys. **59**, 168–190 (1930) (p. 2).

[10] *The Nobel Prize in Physics*, Nobel Foundation, 1965 (p. 3).

[11] S. S. Schweber, *QED and the men who made it: Dyson, Feynman, Schwinger, and Tomonaga* (Princeton University Press, 1994) (pp. 3, 65, 67).

[12] D. Craig and T. Thirunamachandran, *Molecular Quantum Electrodynamics: An Introduction to Radiation-molecule Interactions*, Theoretical Chemistry: A Series of Monographs 8 (Academic Press, 1984) (pp. 3, 17).

[13] P. W. Milonni, *The Quantum Vacuum: An Introduction to Quantum Electrodynamics* (Academic Press, 1994) (pp. 3, 65–67, 156).

[14] C. Cohen-Tannoudji, J. Dupont-Roc, and G. Grynberg, *Photons and Atoms: Introduction to Quantum Electrodynamics* (Wiley, 2007) (pp. 3, 17, 23, 27, 30–32, 56, 147).

[15] E. M. Purcell, "Spontaneous emission probabilities at radio frequencies", in Proceedings of the American Physical Society, Vol. 69 (1946) (pp. 4, 138, 181, 186).

[16] H. B. G. Casimir and D. Polder, The influence of retardation on the London-van der Waals forces, Phys. Rev. **73**, 360–372 (1948) (pp. 4, 67).

[17] W. E. Lamb and R. C. Retherford, Fine structure of the Hydrogen atom by a microwave method, Phys. Rev. **72**, 241–243 (1947) (pp. 4, 65).

[18] K. H. Drexhage, "IV Interaction of light with monomolecular dye layers", in *Progress in optics*, Vol. 12, edited by E. Wolf (Elsevier, 1974), pp. 163–232 (p. 4).

[19] D. Kleppner, Inhibited spontaneous emission, Phys. Rev. Lett. **47**, 233–236 (1981) (p. 4).

[20] P. Goy et al., Observation of cavity-enhanced single-atom spontaneous emission, Phys. Rev. Lett. **50**, 1903–1906 (1983) (p. 4).

[21] W. Jhe et al., Suppression of spontaneous decay at optical frequencies: test of vacuum-field anisotropy in confined space, Phys. Rev. Lett. **58**, 666–669 (1987) (p. 4).

[22] D. J. Heinzen et al., Enhanced and inhibited visible spontaneous emission by atoms in a confocal resonator, Phys. Rev. Lett. **58**, 1320–1323 (1987) (p. 4).

[23] G. Björk et al., Modification of spontaneous emission rate in planar dielectric microcavity structures, Phys. Rev. A **44**, 669–681 (1991) (p. 4).

[24] D. J. Heinzen and M. S. Feld, Vacuum radiative level shift and spontaneous emission linewidth of an atom in an optical resonator, Phys. Rev. Lett. **59**, 2623–2626 (1987) (p. 4).

[25] E. A. Hinds and V. Sandoghdar, Cavity QED level shifts of simple atoms, Phys. Rev. A **43**, 398–403 (1991) (p. 4).

[26] V. Sandoghdar et al., Direct measurement of the van der Waals interaction between an atom and its images in a micron-sized cavity, Phys. Rev. Lett. **68**, 3432–3435 (1992) (p. 4).

[27] V. Sandoghdar et al., Spectroscopy of atoms confined to the single node of a standing wave in a parallel-plate cavity, Phys. Rev. A **53**, 1919–1922 (1996) (p. 4).

[28] M. Marrocco et al., Quantum electrodynamic shifts of Rydberg energy levels between parallel metal plates, Phys. Rev. Lett. **81**, 5784–5787 (1998) (p. 4).

[29] G. Binnig, C. F. Quate, and C. Gerber, Atomic force microscope, Phys. Rev. Lett. **56**, 930–933 (1986) (p. 4).

[30] D. Meschede, H. Walther, and G. Müller, One-atom maser, Phys. Rev. Lett. **54**, 551–554 (1985) (p. 5).

[31] G. Rempe, H. Walther, and N. Klein, Observation of quantum collapse and revival in a one-atom maser, Phys. Rev. Lett. **58**, 353–356 (1987) (pp. 5, 8).

[32] M. Weidinger et al., Trapping states in the micromaser, Phys. Rev. Lett. **82**, 3795–3798 (1999) (p. 5).

[33] R. J. Thompson, G. Rempe, and H. J. Kimble, Observation of normal-mode splitting for an atom in an optical cavity, Phys. Rev. Lett. **68**, 1132–1135 (1992) (p. 5).

[34] A. Boca et al., Observation of the vacuum Rabi spectrum for one trapped atom, Phys. Rev. Lett. **93**, 233603 (2004) (p. 5).

[35] P. Maunz et al., Normal-mode spectroscopy of a single-bound-atom–cavity system, Phys. Rev. Lett. **94**, 033002 (2005) (p. 5).

[36] M. Brune et al., Quantum Rabi oscillation: a direct test of field quantization in a cavity, Phys. Rev. Lett. **76**, 1800–1803 (1996) (p. 5).

[37] C. J. Hood et al., Real-time cavity QED with single atoms, Phys. Rev. Lett. **80**, 4157–4160 (1998) (p. 5).

[38] P. Münstermann et al., Dynamics of single-atom motion observed in a high-finesse cavity, Phys. Rev. Lett. **82**, 3791–3794 (1999) (p. 5).

[39] J. Ye, D. W. Vernooy, and H. J. Kimble, Trapping of single atoms in cavity QED, Phys. Rev. Lett. **83**, 4987–4990 (1999) (p. 5).

[40] J. McKeever et al., State-insensitive cooling and trapping of single atoms in an optical cavity, Phys. Rev. Lett. **90**, 133602 (2003) (p. 5).

[41] K. M. Birnbaum et al., Photon blockade in an optical cavity with one trapped atom, Nature, 87–90 (2005) (p. 5).

[42] D. Press et al., Photon antibunching from a single quantum-dot microcavity system in the strong coupling regime, Phys. Rev. Lett. **98**, 117402 (2007) (p. 5).

[43] R. Bhuyan et al., The rise and current status of polaritonic photochemistry and photophysics, Chem. Rev. **123**, 10877–10919 (2023) (pp. 5, 11).

[44] F. Schlawin, D. M. Kennes, and M. A. Sentef, Cavity quantum materials, Appl. Phys. Rev. **9**, 011312 (2022) (p. 5).

[45] A. Imamoğlu et al., Nonequilibrium condensates and lasers without inversion: exciton-polariton lasers, Phys. Rev. A **53**, 4250–4253 (1996) (p. 5).

[46] P. Grangier, G. Reymond, and N. Schlosser, Implementations of quantum computing using cavity quantum electrodynamics schemes, Fortschr. Phys. **48**, 859–874 (2000) (p. 5).

[47] A. F. Kockum et al., Ultrastrong coupling between light and matter, Nat. Rev. Phys. **1**, 19–40 (2019) (p. 5).

[48] P. Forn-Díaz et al., Ultrastrong coupling regimes of light-matter interaction, Rev. Mod. Phys. **91**, 025005 (2019) (p. 5).

[49] J. H. Shirley, Solution of the Schrödinger equation with a Hamiltonian periodic in time, Phys. Rev. **138**, B979–B987 (1965) (p. 6).

[50] C. Cohen-Tannoudji, J. Dupont-Roc, and C. Fabre, A quantum calculation of the higher order terms in the Bloch-Siegert shift, J. Phys. B: At. Mol. Opt. Phys. **6**, L214 (1973) (p. 6).

[51] F. De Zela, E. Solano, and A. Gago, Micromaser without the rotating-wave approximation: The Bloch-Siegert shift and related effects, Optics Communications **142**, 106–118 (1997) (p. 6).

[52] C. Ciuti, G. Bastard, and I. Carusotto, Quantum vacuum properties of the intersubband cavity polariton field, Phys. Rev. B **72**, 115303 (2005) (pp. 6, 140, 154).

[53] A. A. Anappara et al., Giant intersubband polariton splitting in InAs/AlSb microcavities, Solid State Commun. **142**, 311–313 (2007) (pp. 6, 154).

[54] A. A. Anappara et al., Signatures of the ultrastrong light-matter coupling regime, Phys. Rev. B **79**, 201303 (2009) (pp. 6, 154).

[55] S. D. Liberato, C. Ciuti, and I. Carusotto, Quantum vacuum radiation spectra from a semiconductor microcavity with a time-modulated vacuum Rabi frequency, Phys. Rev. Lett. **98**, 103602 (2007) (pp. 6, 141).

[56] Y. Todorov et al., Ultrastrong light-matter coupling regime with polariton dots, Phys. Rev. Lett. **105**, 196402 (2010) (pp. 6, 154).

[57] D. Ballester et al., Quantum simulation of the ultrastrong-coupling dynamics in circuit quantum electrodynamics, Phys. Rev. X **2**, 021007 (2012) (p. 6).

[58] T. Schwartz et al., Reversible switching of ultrastrong light-molecule coupling, Phys. Rev. Lett. **106**, 196405 (2011) (pp. 6, 154).

[59] J. George et al., Multiple rabi splittings under ultrastrong vibrational coupling, Phys. Rev. Lett. **117**, 153601 (2016) (p. 6).

[60] J. Galego, F. J. Garcia-Vidal, and J. Feist, Cavity-induced modifications of molecular structure in the strong-coupling regime, Phys. Rev. X **5**, 041022 (2015) (p. 6).

[61] F. Herrera and F. C. Spano, Cavity-controlled chemistry in molecular ensembles, Phys. Rev. Lett. **116**, 238301 (2016) (p. 6).

[62] L. A. Martínez-Martínez et al., Can ultrastrong coupling change ground-state chemical reactions?, ACS Photonics **5**, 167–176 (2018) (p. 6).

[63] F. J. Garcia-Vidal, C. Ciuti, and T. W. Ebbesen, Manipulating matter by strong coupling to vacuum fields, Science **373**, eabd0336 (2021) (p. 6).

[64] A. Blais et al., Cavity quantum electrodynamics for superconducting electrical circuits: an architecture for quantum computation, Phys. Rev. A **69**, 062320 (2004) (p. 6).

[65] A. Wallraff et al., Strong coupling of a single photon to a superconducting qubit using circuit quantum electrodynamics, Nature **431**, 162–167 (2004) (p. 6).

[66] R. J. Schoelkopf and S. M. Girvin, Wiring up quantum systems, Nature **451**, 664–669 (2008) (p. 6).

[67] M. Devoret, S. Girvin, and R. Schoelkopf, Circuit-QED: how strong can the coupling between a Josephson junction atom and a transmission line resonator be?, Ann. Phys. **519**, 767–779 (2007) (p. 6).

[68] J. Bourassa et al., Ultrastrong coupling regime of cavity QED with phase-biased flux qubits, Phys. Rev. A **80**, 032109 (2009) (p. 6).

[69] T. Niemczyk et al., Circuit quantum electrodynamics in the ultrastrong-coupling regime, Nat. Phys. **6**, 772–776 (2010) (p. 6).

[70] P. Forn-Díaz et al., Observation of the Bloch-Siegert shift in a qubit-oscillator system in the ultrastrong coupling regime, Phys. Rev. Lett. **105**, 237001 (2010) (pp. 6, 142).

[71] G. Scalari et al., Ultrastrong coupling of the cyclotron transition of a 2D electron gas to a THz metamaterial, Science **335**, 1323–1326 (2012) (pp. 6, 146).

[72] J. Casanova et al., Deep strong coupling regime of the Jaynes-Cummings model, Phys. Rev. Lett. **105**, 263603 (2010) (p. 6).

[73] F. Yoshihara et al., Superconducting qubit–oscillator circuit beyond the ultrastrong coupling regime, Nat. Phys. **13**, 44–47 (2017) (p. 6).

[74] R. H. Brown and R. Q. Twiss, Correlation between photons in two coherent beams of light, Nature **177**, 27–29 (1956) (p. 7).

[75] E. M. Purcell, The question of correlation between photons in coherent light rays, Nature **178**, 1449–1450 (1956) (p. 7).

[76] L. Mandel and E. Wolf, *Optical coherence and quantum optics* (Cambridge University Press, 1995) (p. 7).

[77] R. J. Glauber, Photon correlations, Phys. Rev. Lett. **10**, 84–86 (1963) (pp. 7, 8).

[78] R. J. Glauber, The quantum theory of optical coherence, Phys. Rev. **130**, 2529–2539 (1963) (p. 7).

[79] R. J. Glauber, Coherent and incoherent states of the radiation field, Phys. Rev. **131**, 2766–2788 (1963) (p. 7).

[80] E. C. G. Sudarshan, Equivalence of semiclassical and quantum mechanical descriptions of statistical light beams, Phys. Rev. Lett. **10**, 277–279 (1963) (p. 7).

[81] H. J. Kimble, M. Dagenais, and L. Mandel, Photon antibunching in resonance fluorescence, Phys. Rev. Lett. **39**, 691–695 (1977) (p. 8).

[82] J. H. Eberly, N. B. Narozhny, and J. J. Sanchez-Mondragon, Periodic spontaneous collapse and revival in a simple quantum model, Phys. Rev. Lett. **44**, 1323–1326 (1980) (p. 8).

[83] D. C. Burnham and D. L. Weinberg, Observation of simultaneity in parametric production of optical photon pairs, Phys. Rev. Lett. **25**, 84–87 (1970) (p. 8).

[84] C. K. Hong and L. Mandel, Experimental realization of a localized one-photon state, Phys. Rev. Lett. **56**, 58–60 (1986) (p. 8).

[85] C. K. Hong, Z. Y. Ou, and L. Mandel, Measurement of subpicosecond time intervals between two photons by interference, Phys. Rev. Lett. **59**, 2044–2046 (1987) (p. 8).

[86] R. Loudon and P. Knight, Squeezed light, J. Mod. Opt. **34**, 709–759 (1987) (p. 8).

[87] P. G. Kwiat et al., New high-intensity source of polarization-entangled photon pairs, Phys. Rev. Lett. **75**, 4337–4341 (1995) (p. 8).

[88] A. Aspect, P. Grangier, and G. Roger, Experimental realization of Einstein-Podolsky-Rosen-Bohm Gedankenexperiment: a new violation of Bell's inequalities, Phys. Rev. Lett. **49**, 91–94 (1982) (p. 8).

[89] M. Reck et al., Experimental realization of any discrete unitary operator, Phys. Rev. Lett. **73**, 58–61 (1994) (p. 8).

[90] A. K. Ekert, Quantum cryptography based on Bell's theorem, Phys. Rev. Lett. **67**, 661–663 (1991) (p. 8).

[91] C. H. Bennett et al., Teleporting an unknown quantum state via dual classical and einstein-podolsky-rosen channels, Phys. Rev. Lett. **70**, 1895–1899 (1993) (p. 8).

[92] P. Townsend, J. Rarity, and P. Tapster, Single photon interference in 10 km long optical fibre interferometer, Electron. Lett. **29**, 634–635 (1993) (p. 8).

[93] A. Muller, H. Zbinden, and N. Gisin, Underwater quantum coding, Nature **378**, 449–449 (1995) (p. 8).

[94] E. Knill, R. Laflamme, and G. J. Milburn, A scheme for efficient quantum computation with linear optics, Nature **409**, 46–52 (2001) (p. 8).

[95] J. Aasi et al., Enhanced sensitivity of the LIGO gravitational wave detector by using squeezed states of light, Nat. Photonics **7**, 613–619 (2013) (pp. 8, 11, 12).

[96] B. P. Abbott et al. (LIGO Scientific Collaboration and Virgo Collaboration), Observation of gravitational waves from a binary black hole merger, Phys. Rev. Lett. **116**, 061102 (2016) (pp. 8, 11).

[97] D. E. Chang, V. Vuletić, and M. D. Lukin, Quantum nonlinear optics — photon by photon, Nat. Photonics **8**, 685–694 (2014) (p. 8).

[98] R. P. Feynman, Simulating physics with computers, Int. J. Theor. Phys. **21**, 467–488 (1982) (p. 9).

[99] R. P. Feynman, "Quantum mechanical computers", in Conference on lasers and electro-optics (1984) (p. 9).

[100] A. Montanaro, Quantum algorithms: an overview, npj Quantum Inf **2**, 1–8 (2016) (p. 9).

[101] B. Fauseweh, Quantum many-body simulations on digital quantum computers: State-of-the-art and future challenges, Nat. Commun. **15**, 2123 (2024) (p. 9).

[102] P. W. Shor, Polynomial-time algorithms for prime factorization and discrete logarithms on a quantum computer, SIAM J. Comput. **26**, 1484–1509 (1997) (p. 9).

[103] L. Henriet et al., Quantum computing with neutral atoms, Quantum **4**, 327 (2020) (p. 9).

[104] C. S. Adams, J. D. Pritchard, and J. P. Shaffer, Rydberg atom quantum technologies, J. Phys. B: At. Mol. Opt. Phys. **53**, 012002 (2019) (p. 9).

[105] C. D. Bruzewicz et al., Trapped-ion quantum computing: progress and challenges, Appl. Phys. Rev. **6**, 021314 (2019) (p. 9).

[106] C. E. Bradley et al., A ten-qubit solid-state spin register with quantum memory up to one minute, Phys. Rev. X **9**, 031045 (2019) (p. 9).

[107] G. Burkard et al., Semiconductor spin qubits, Rev. Mod. Phys. **95**, 025003 (2023) (p. 9).

[108] P. Krantz et al., A quantum engineer's guide to superconducting qubits, Appl. Phys. Rev. **6**, 021318 (2019) (p. 9).

[109] M. Kjaergaard et al., Superconducting qubits: current state of play, Annu. Rev. Condens. Matter Phys. **11**, 369–395 (2020) (p. 9).

[110] G. Kurizki et al., Quantum technologies with hybrid systems, Proc. Natl. Acad. Sci. **112**, 3866–3873 (2015) (p. 9).

[111] C. Stehle et al., Plasmonically tailored micropotentials for ultracold atoms, Nat. Photonics **5**, 494–498 (2011) (p. 9).

[112] J. D. Thompson et al., Coupling a single trapped atom to a nanoscale optical cavity, Science **340**, 1202–1205 (2013) (pp. 9, 132).

[113] S. Ebadi et al., Quantum phases of matter on a 256-atom programmable quantum simulator, Nature **595**, 227–232 (2021) (p. 9).

[114] T. Botzem et al., Tuning methods for semiconductor spin qubits, Phys. Rev. Appl. **10**, 054026 (2018) (p. 9).

[115] F. Flamini, N. Spagnolo, and F. Sciarrino, Photonic quantum information processing: a review, Rep. Prog. Phys. **82**, 016001 (2018) (p. 9).

[116] J. L. O'Brien, A. Furusawa, and J. Vučković, Photonic quantum technologies, Nat. Photonics **3**, 687–695 (2009) (pp. 9, 10).

[117] D. Hangleiter, J. Carolan, and K. P. Y. Thébault, *Analogue quantum simulation: a new instrument for scientific understanding* (Springer International Publishing, 2022) (p. 10).

[118] M. Lewenstein et al., Ultracold atomic gases in optical lattices: mimicking condensed matter physics and beyond, Adv. Phys. **56**, 243–379 (2007) (p. 10).

[119] L. K. Joshi et al., Probing many-body quantum chaos with quantum simulators, Phys. Rev. X **12**, 011018 (2022) (p. 10).

[120] J. Eisert, M. Friesdorf, and C. Gogolin, Quantum many-body systems out of equilibrium, Nat. Phys. **11**, 124–130 (2015) (p. 10).

[121] J. Argüello-Luengo et al., Analogue quantum chemistry simulation, Nature **574**, 215–218 (2019) (p. 10).

[122] A. Aspuru-Guzik and P. Walther, Photonic quantum simulators, Nat. Phys. **8**, 285–291 (2012) (p. 10).

[123] J. Wang et al., Integrated photonic quantum technologies, Nat. Photonics **14**, 273–284 (2020) (p. 10).

[124] M. Barbieri, Optical quantum metrology, PRX Quantum **3**, 010202 (2022) (p. 10).

[125] L. Ruppert and R. Filip, Light-matter quantum interferometry with homodyne detection, Opt. Express **25**, 15456–15467 (2017) (p. 10).

[126] L. Ruppert, A. Rakhubovsky, and R. Filip, High-precision multiparameter estimation of mechanical force by quantum optomechanics, Sci. Rep. **12**, 16022 (2022) (p. 10).

[127] S. Barzanjeh et al., Optomechanics for quantum technologies, Nat. Phys. **18**, 15–24 (2022) (p. 10).

[128] M. Kamble, J. Wang, and G. S. Agarwal, Quantum metrology of absorption and gain parameters using two-mode bright squeezed light, Phys. Rev. A **109**, 053715 (2024) (p. 10).

[129] C. H. Bennett and G. Brassard, The dawn of a new era for quantum cryptography: the experimental prototype is working!, SIGACT News **20**, 78–80 (1989) (p. 10).

[130] J. Kołodyński et al., Device-independent quantum key distribution with single-photon sources, Quantum **4**, 260 (2020) (p. 10).

[131] M. Zahidy et al., Quantum key distribution using deterministic single-photon sources over a field-installed fibre link, npj Quantum Inf **10**, 1–6 (2024) (p. 10).

[132] G. Romero et al., Ultrafast quantum gates in circuit QED, Phys. Rev. Lett. **108**, 120501 (2012) (p. 10).

[133] S. Felicetti et al., Photon transfer in ultrastrongly coupled three-cavity arrays, Phys. Rev. A **89**, 013853 (2014) (p. 10).

[134] T. H. Kyaw et al., Creation of quantum error correcting codes in the ultrastrong coupling regime, Phys. Rev. B **91**, 064503 (2015) (p. 10).

[135] X. Xiong et al., Ultrastrong coupling in single plexcitonic nanocubes, Nanophotonics **9**, 257–266 (2020) (p. 10).

[136] M. Arndt et al., Wave–particle duality of C60 molecules, Nature **401**, 680–682 (1999) (p. 11).

[137] M. Arndt and K. Hornberger, Testing the limits of quantum mechanical superpositions, Nat. Phys. **10**, 271–277 (2014) (p. 11).

[138] O. Romero-Isart et al., Large quantum superpositions and interference of massive nanometer-sized objects, Phys. Rev. Lett. **107**, 020405 (2011) (p. 11).

[139] M. Roda-Llordes et al., Macroscopic quantum superpositions via dynamics in a wide double-well potential, Phys. Rev. Lett. **132**, 023601 (2024) (p. 11).

[140] N. C. Zambon et al., Motional entanglement of remote optically levitated nanoparticles, (2024) (p. 11).

[141] M. Bild et al., Schrödinger cat states of a 16-microgram mechanical oscillator, Science **380**, 274–278 (2023) (p. 11).

[142] J. A. Hutchison et al., Modifying chemical landscapes by coupling to vacuum fields, Angew. Chem. Int. Ed. **51**, 1592–1596 (2012) (p. 11).

[143] J. del Pino, J. Feist, and F. J. Garcia-Vidal, Quantum theory of collective strong coupling of molecular vibrations with a microcavity mode, New J. Phys. **17**, 053040 (2015) (p. 11).

[144] R. F. Ribeiro et al., Polariton chemistry: controlling molecular dynamics with optical cavities, Chem. Sci. **9**, 6325–6339 (2018) (p. 11).

[145] J. Galego Pascual, *Polaritonic chemistry: manipulating molecular structure through strong light–matter coupling*, Springer Theses (Springer International Publishing, 2020) (p. 11).

[146] K. Nagarajan, A. Thomas, and T. W. Ebbesen, Chemistry under vibrational strong coupling, J. Am. Chem. Soc. **143**, 16877–16889 (2021) (p. 11).

[147] J. Fregoni and S. Corni, "Chapter 7 - polaritonic chemistry", in *Theoretical and computational photochemistry*, edited by C. García-Iriepa and M. Marazzi (Elsevier, 2023), pp. 191–211 (p. 11).

[148] L. Rocca and G. C, Polariton lasing, Nat. Photon. **4**, 343–345 (2010) (p. 11).

[149] J. Kasprzak et al., Bose–Einstein condensation of exciton polaritons, Nature **443**, 409–414 (2006) (p. 11).

[150] J. Keeling and S. Kéna-Cohen, Bose-Einstein condensation of exciton-polaritons in organic microcavities, Annu. Rev. Phys. Chem. **71**, 435–459 (2020) (p. 11).

[151] J. Tang et al., Room temperature exciton–polariton Bose–Einstein condensation in organic single-crystal microribbon cavities, Nat. Commun. **12**, 3265 (2021) (p. 11).

[152] T. J. Kippenberg and K. J. Vahala, Cavity optomechanics: back-action at the mesoscale, Science **321**, 1172–1176 (2008) (p. 11).

[153] M. Aspelmeyer, T. J. Kippenberg, and F. Marquardt, Cavity optomechanics, Rev. Mod. Phys. **86**, 1391–1452 (2014) (p. 11).

[154] D. F. Walls, Squeezed states of light, Nature **306**, 141–146 (1983) (p. 12).

[155] S. Bose, K. Jacobs, and P. L. Knight, Preparation of nonclassical states in cavities with a moving mirror, Phys. Rev. A **56**, 4175–4186 (1997) (p. 12).

[156] W. Marshall et al., Towards quantum superpositions of a mirror, Phys. Rev. Lett. **91**, 130401 (2003) (p. 12).

[157] A. Mari and J. Eisert, Gently modulating optomechanical systems, Phys. Rev. Lett. **103**, 213603 (2009) (p. 12).

[158] E. E. Wollman et al., Quantum squeezing of motion in a mechanical resonator, Science **349**, 952–955 (2015) (p. 12).

[159] P. Rabl, Photon blockade effect in optomechanical systems, Phys. Rev. Lett. **107**, 063601 (2011) (p. 12).

[160] L. Bakemeier, A. Alvermann, and H. Fehske, Route to chaos in optomechanics, Phys. Rev. Lett. **114**, 013601 (2015) (p. 12).

[161] G.-L. Zhu et al., Cavity optomechanical chaos, Fundam. Res. **3**, 63–74 (2023) (p. 12).

[162] J.-M. Pirkkalainen et al., Cavity optomechanics mediated by a quantum two-level system, Nat. Commun. **6**, 6981 (2015) (p. 12).

[163] R. Esteban, J. J. Baumberg, and J. Aizpurua, Molecular optomechanics approach to surface-enhanced Raman scattering, Acc. Chem. Res. **55**, 1889–1899 (2022) (p. 12).

[164] M. Á. Martínez-García and D. Martín-Cano, Coherent electron-vibron interactions in surface-enhanced Raman scattering (SERS), Phys. Rev. Lett. **132**, 093601 (2024) (p. 12).

[165] F. Beaudoin, J. M. Gambetta, and A. Blais, Dissipation and ultrastrong coupling in circuit QED, Phys. Rev. A **84**, 043832 (2011) (pp. 12, 84, 141, 142).

[166] A. Settineri et al., Dissipation and thermal noise in hybrid quantum systems in the ultrastrong-coupling regime, Phys. Rev. A **98**, 053834 (2018) (pp. 12, 84, 141).

[167] M. Lednev, F. J. García-Vidal, and J. Feist, Lindblad master equation capable of describing hybrid quantum systems in the ultrastrong coupling regime, Phys. Rev. Lett. **132**, 106902 (2024) (pp. 12, 85, 104, 141).

[168] A. Stokes and A. Nazir, Gauge ambiguities imply Jaynes-Cummings physics remains valid in ultrastrong coupling QED, Nat. Commun. **10**, 499 (2019) (pp. 12, 138, 145).

[169] O. Di Stefano et al., Resolution of gauge ambiguities in ultrastrong-coupling cavity quantum electrodynamics, Nat. Phys. **15**, 803–808 (2019) (pp. 12, 145).

[170] D. M. Rouse et al., Avoiding gauge ambiguities in cavity quantum electrodynamics, Sci. Rep. **11**, 4281 (2021) (pp. 12, 145).

[171] C. Gustin, S. Franke, and S. Hughes, Gauge-invariant theory of truncated quantum light-matter interactions in arbitrary media, Phys. Rev. A **107**, 013722 (2023) (p. 12).

[172] E. Rousseau and D. Felbacq, The quantum-optics Hamiltonian in the multipolar gauge, Sci. Rep. **7**, 11115 (2017) (p. 12).

[173] A. Vukics, G. Kónya, and P. Domokos, The gauge-invariant Lagrangian, the Power–Zienau–Woolley picture, and the choices of field momenta in nonrelativistic quantum electrodynamics, Sci Rep **11**, 16337 (2021) (pp. 12, 22, 32).

[174] A. Stokes and A. Nazir, Identification of Poincaré-gauge and multipolar nonrelativistic theories of QED, Phys. Rev. A **104**, 032227 (2021) (p. 12).

[175] F. Benz et al., Single-molecule optomechanics in "picocavities", Science **354**, 726–729 (2016) (pp. 12, 146).

[176] M. Kuisma et al., Ultrastrong coupling of a single molecule to a plasmonic nanocavity: a first-principles study, ACS Photonics **9**, 1065–1077 (2022) (pp. 12, 146).

[177] V. Rokaj et al., Light–matter interaction in the long-wavelength limit: no ground-state without dipole self-energy, J. Phys. B: At. Mol. Opt. Phys. **51**, 034005 (2018) (pp. 12, 32, 159).

[178] C. Schäfer et al., Relevance of the quadratic diamagnetic and self-polarization terms in cavity quantum electrodynamics, ACS Photonics **7**, 975–990 (2020) (pp. 12, 32, 146, 157–159, 176, 177).

[179] U. Muniain et al., Description of ultrastrong light–matter interaction through coupled harmonic oscillator models and their connection with cavity-qed hamiltonians, Nanophotonics, doi:10.1515/nanoph-2024-0528 (2025) (pp. 12, 146).

[180] J. Feist, A. I. Fernández-Domínguez, and F. J. García-Vidal, Macroscopic QED for quantum nanophotonics: emitter-centered modes as a minimal basis for multiemitter problems, Nanophotonics **10**, 477–489 (2021) (pp. 12, 32, 37, 38, 40, 96, 173).

[181] J. Galego et al., Cavity casimir-polder forces and their effects in ground-state chemical reactivity, Phys. Rev. X **9**, 021057 (2019) (pp. 12, 32, 146).

[182] J. Schwinger et al., *Classical Electrodynamics* (Perseus Books Reading, 1998) (p. 21).

[183] M. Born, W. Heisenberg, and P. Jordan, Zur quantenmechanik. II. Z. Phys. **35**, 557–615 (1926) (p. 28).

[184] P. A. M. Dirac and R. H. Fowler, The physical interpretation of the quantum dynamics, Proc. R. Soc. Lond. A **113**, 621–641 (1927) (p. 28).

[185] P. Jordan, Über kanonische Transformationen in der Quantenmechanik, Z. Phys. **37**, 383–386 (1926) (pp. 28, 29).

[186] F. London, Über die Jacobischen Transformationen der Quantenmechanik, Z. Phys. **37**, 915–925 (1926) (p. 28).

[187] P. A. Mello and M. Moshinsky, Nonlinear canonical transformations and their representations in quantum mechanics, J. Math. Phys. **16**, 2017–2028 (1975) (p. 28).

[188] A. Duncan and M. Janssen, From canonical transformations to transformation theory, 1926-1927: the road to Jordan's Neue Begründung, Stud. Hist. Philos. Sci. B **40**, On The History Of The Quantum, 352–362 (2009) (p. 28).

[189] A. Anderson, Quantum canonical transformations and integrability. Beyond unitary transformations, Phys. Lett. B **319**, 157–162 (1993) (p. 28).

[190] E. A. Power and S. Zienau, Coulomb gauge in non-relativistic quantum electro-dynamics and the shape of spectral lines, Phil. Trans. R. Soc. Lond. A Math. Phys. Sci. **251**, 427–454 (1959) (p. 30).

[191] R. G. Woolley, Molecular quantum electrodynamics, Proc. R. Soc. Lond. A **321**, 557–572 (1971) (p. 30).

[192] A. Vukics, T. Grießer, and P. Domokos, Elimination of the A-square problem from cavity QED, Phys. Rev. Lett. **112**, 073601 (2014) (pp. 31, 145).

[193] A. Vukics, T. Grießer, and P. Domokos, Fundamental limitation of ultrastrong coupling between light and atoms, Phys. Rev. A **92**, 043835 (2015) (p. 31).

[194] D. Steck, *Quantum and atom optics*, version 0.14, Available at `http://steck.us/teaching`, 2007 (pp. 33, 198).

[195] S. Y. Buhmann and D.-G. Welsch, Casimir-Polder forces on excited atoms in the strong atom-field coupling regime, Phys. Rev. A **77**, 012110 (2008) (pp. 37, 136).

[196] T. Hümmer et al., Weak and strong coupling regimes in plasmonic QED, Phys. Rev. B **87**, 115419 (2013) (p. 37).

[197] B. Rousseaux et al., Adiabatic passage mediated by plasmons: a route towards a decoherence-free quantum plasmonic platform, Phys. Rev. B **93**, 045422 (2016) (p. 37).

[198] D. Dzsotjan et al., Mode-selective quantization and multimodal effective models for spherically layered systems, Phys. Rev. A **94**, 023818 (2016) (p. 37).

[199] A. Castellini et al., Quantum plasmonics with multi-emitters: application to stimulated Raman adiabatic passage, Eur. Phys. J. D **72**, 223 (2018) (p. 37).

[200] H. Varguet et al., Non-hermitian hamiltonian description for quantum plasmonics: from dissipative dressed atom picture to fano states, J. Phys. B: At. Mol. Opt. Phys. **52**, 055404 (2019) (p. 37).

[201] I. Medina et al., Few-mode field quantization of arbitrary electromagnetic spectral densities, Phys. Rev. Lett. **126**, 093601 (2021) (pp. 40, 84, 104, 207).

[202] S. Y. Buhmann and D.-G. Welsch, Dispersion forces in macroscopic quantum electrodynamics, Progress in Quantum Electronics **31**, 51–130 (2007) (pp. 40, 49).

[203] S. Scheel and S. Y. Buhmann, Macroscopic Quantum Electrodynamics Concepts and applications, Acta Physica Slovaca **58**, 675–809 (2008) (p. 40).

[204] S. Y. Buhmann, *Dispersion Forces I: Macroscopic Quantum Electrodynamics and Ground-State Casimir, Casimir–Polder and van der Waals Forces*, Vol. 1, Springer Tracts in Modern Physics (Springer-Verlag, Berlin Heidelberg, 2012) (pp. 40, 43, 45, 50, 55–57, 67, 121, 156, 211, 219).

[205] J. D. Jackson, *Classical Electrodynamics*, 2nd ed. (John Wiley & Sons, 1975) (pp. 42, 203).

[206] H. T. Dung et al., Electromagnetic-field quantization and spontaneous decay in left-handed media, Phys. Rev. A **68**, 043816 (2003) (pp. 44, 45).

[207] J. M. Jauch and K. M. Watson, Phenomenological quantum electrodynamics, Phys. Rev. **74**, 950–957 (1948) (p. 44).

[208] M. Hillery and L. D. Mlodinow, Quantization of electrodynamics in nonlinear dielectric media, Phys. Rev. A **30**, 1860–1865 (1984) (p. 44).

[209] R. J. Glauber and M. Lewenstein, Quantum optics of dielectric media, Phys. Rev. A **43**, 467–491 (1991) (p. 44).

[210] B. Huttner and S. M. Barnett, Quantization of the electromagnetic field in dielectrics, Phys. Rev. A **46**, 4306–4322 (1992) (pp. 44, 45).

[211] R. Matloob et al., Electromagnetic field quantization in absorbing dielectrics, Phys. Rev. A **52**, 4823–4838 (1995) (p. 45).

[212] T. Gruner and D.-G. Welsch, Green-function approach to the radiation-field quantization for homogeneous and inhomogeneous Kramers-Kronig dielectrics, Phys. Rev. A **53**, 1818–1829 (1996) (p. 45).

[213] H. T. Dung, L. Knöll, and D.-G. Welsch, Three-dimensional quantization of the electromagnetic field in dispersive and absorbing inhomogeneous dielectrics, Phys. Rev. A **57**, 3931–3942 (1998) (p. 45).

[214] S. Scheel, L. Knöll, and D.-G. Welsch, QED commutation relations for inhomogeneous Kramers-Kronig dielectrics, Phys. Rev. A **58**, 700–706 (1998) (p. 45).

[215] A. Tip et al., Equivalence of the Langevin and auxiliary-field quantization methods for absorbing dielectrics, Phys. Rev. A **63**, 043806 (2001) (p. 45).

[216] S. Y. Buhmann, D. T. Butcher, and S. Scheel, Macroscopic quantum electrodynamics in nonlocal and nonreciprocal media, New J. Phys. **14**, 083034 (2012) (p. 45).

[217] T. G. Philbin, Canonical quantization of macroscopic electromagnetism, New J. Phys. **12**, 123008 (2010) (pp. 47, 49).

[218] V. Dorier et al., Canonical quantization for quantum plasmonics with finite nanostructures, Phys. Rev. A **100**, 042111 (2019) (p. 49).

[219] V. Dorier, S. Guérin, and H.-R. Jauslin, Critical review of quantum plasmonic models for finite-size media, Nanophotonics **9**, 3899–3907 (2020) (p. 49).

[220] G. Semin, H.-R. Jauslin, and S. Guérin, Canonical quantum plasmonics for finite nanostructures: exact solution in one dimension, Phys. Rev. A **110**, 043514 (2024) (p. 49).

[221] H. Friedrich, ed., *Theoretical Atomic Physics*, SpringerLink Bücher (Springer Berlin Heidelberg, Berlin, Heidelberg, 2006) (p. 49).

[222] R. Zietal and C. Eberlein, Gauge transformation in macroscopic quantum electrodynamics near polarizable surfaces, Phys. Rev. D **100**, 065002 (2019) (p. 52).

[223] C. Gustin, S. Franke, and S. Hughes, Gauge-invariant theory of truncated quantum light-matter interactions in arbitrary media, Phys. Rev. A **107**, 013722 (2023) (p. 52).

[224] C.-H. Chang et al., Constructing "designer atoms" via resonant graphene-induced Lamb shifts, ACS Photonics **4**, 3098–3105 (2017) (pp. 52, 55, 136).

[225] S. Y. Buhmann, *Dispersion Forces II: Many-Body Effects, Excited Atoms, Finite Temperature and Quantum Friction*, Vol. 2, Springer Tracts in Modern Physics (Springer-Verlag, Berlin Heidelberg, 2012) (pp. 55, 56).

[226] H. A. Bethe and E. E. Salpeter, *Quantum mechanics of one- and two-electron atoms* (Dover Publications, 1957) (pp. 58, 60, 62–64, 67, 116, 193).

[227] C. Cohen-Tannoudji, B. Diu, and F. Laloe, *Quantum mechanics: Vol. 1* (Wiley, New York, 1977) (p. 58).

[228] A. Messiah, *Quantum mechanics*, Dover books on physics (Dover Publications, 1999) (p. 58).

[229] W. Gordon, Zur Berechnung der Matrizen beim Wasserstoffatom, Ann. Phys. **394**, 1031–1056 (1929) (p. 60).

[230] P. A. M. Dirac, The quantum theory of the electron, Proc. R. Soc. Lond. A **117**, 610–624 (1928) (p. 61).

[231] P. A. M. Dirac, *The principles of quantum mechanics*, 3rd ed. (Oxford, 1947) (p. 61).

[232] W. A. Barker and F. N. Glover, Reduction of relativistic two-particle wave equations to approximate forms. III, Phys. Rev. **99**, 317–324 (1955) (p. 63).

[233] M. I. Eides, H. Grotch, and V. A. Shelyuto, Theory of light Hydrogen-like atoms, Phys. Rep. **342**, 63–261 (2001) (p. 63).

[234] S. Navas et al. (Particle Data Group), Review of particle physics, Phys. Rev. D **110**, 030001 (2024) (p. 64).

[235] J. R. Oppenheimer, Note on the theory of the interaction of field and matter, Phys. Rev. **35**, 461–477 (1930) (p. 65).

[236] W. V. Houston, A new method of analysis of the structure of H_α and D_α, Phys. Rev. **51**, 446–449 (1937) (p. 65).

[237] R. C. Williams, The fine structures of Hα and Dα under varying discharge conditions, Phys. Rev. **54**, 558–567 (1938) (p. 65).

[238] S. Pasternack, Note on the fine structure of Hα and Dα, Phys. Rev. **54**, 1113–1113 (1938) (p. 65).

[239] H. A. Bethe, The electromagnetic shift of energy levels, Phys. Rev. **72**, 339–341 (1947) (pp. 65, 156).

[240] A. Salam et al., *From a life of physics* (WORLD SCIENTIFIC, 1989) (p. 66).

[241] J. B. French and V. F. Weisskopf, The electromagnetic shift of energy levels, Phys. Rev. **75**, 1240–1248 (1949) (p. 67).

[242] R. L. Jaffe, Casimir effect and the quantum vacuum, Phys. Rev. D **72**, 021301 (2005) (p. 67).

[243] H. Nikolić, Proof that Casimir force does not originate from vacuum energy, Phys. Lett. B **761**, 197–202 (2016) (p. 67).

[244] A. Kossakowski, On quantum statistical mechanics of non-Hamiltonian systems, Rep. Math. Phys. **3**, 247–274 (1972) (p. 69).

[245] G. Lindblad, On the generators of quantum dynamical semigroups, Commun. Math. Phys. **48**, 119–130 (1976) (p. 70).

[246] D. Manzano, A short introduction to the Lindblad master equation, AIP Adv. **10**, 025106 (2020) (p. 70).

[247] R. Ingarden and A. Kossakowski, On the connection of nonequilibrium information thermodynamics with non-Hamiltonian quantum mechanics of open systems, Ann. Phys. **89**, 451–485 (1975) (p. 70).

[248] V. Gorini, A. Kossakowski, and E. C. G. Sudarshan, Completely positive dynamical semigroups of N-level systems, J. Math. Phys. **17**, 821–825 (1976) (p. 70).

[249] H. Breuer and F. Petruccione, *The theory of open quantum systems* (Oxford University Press, 2002) (pp. 74, 79, 81).

[250] J. Jeske et al., Bloch-Redfield equations for modeling light-harvesting complexes, J. Chem. Phys. **142**, 064104 (2015) (pp. 79, 90, 95).

[251] R. Hartmann and W. T. Strunz, Accuracy assessment of perturbative master equations: embracing nonpositivity, Phys. Rev. A **101**, 012103 (2020) (pp. 79, 90).

[252] Á. Rivas and S. Huelga, *Open quantum systems: an introduction* (Springer Berlin, Heidelberg, 2011) (p. 79).

[253] A. Imamoğlu, Stochastic wave-function approach to non-Markovian systems, Phys. Rev. A **50**, 3650–3653 (1994) (pp. 83, 207).

[254] A. Ridolfo et al., Photon blockade in the ultrastrong coupling regime, Phys. Rev. Lett. **109**, 193602 (2012) (p. 84).

[255] M. Sánchez-Barquilla et al., Few-mode field quantization for multiple emitters, Nanophotonics **11**, 4363–4374 (2022) (pp. 85, 104).

[256] C. J. S. Martínez, J. Feist, and F. J. García-Vidal, A mixed perturbative-nonperturbative treatment for strong light-matter interactions, Nanophotonics **13**, 2669–2678 (2024) (pp. 85, 104).

[257] D. Fernández de la Pradilla, E. Moreno, and J. Feist, Recovering an accurate Lindblad equation from the Bloch-Redfield equation for general open quantum systems, Phys. Rev. A **109**, 062225 (2024) (pp. 87, 89, 90, 99, 102, 107, 109, 110).

[258] T. Becker, C. Netzer, and A. Eckardt, Quantum trajectories for time-local non-Lindblad master equations, Phys. Rev. Lett. **131**, 160401 (2023) (p. 91).

[259] G. Schaller and T. Brandes, Preservation of positivity by dynamical coarse graining, Phys. Rev. A **78**, 022106 (2008) (pp. 95, 110).

[260] P. R. Eastham et al., Bath-induced coherence and the secular approximation, Phys. Rev. A **94**, 012110 (2016) (p. 95).

[261] D. Farina and V. Giovannetti, Open-quantum-system dynamics: recovering positivity of the Redfield equation via the partial secular approximation, Phys. Rev. A **100**, 012107 (2019) (pp. 95, 110).

[262] F. Nathan and M. S. Rudner, Universal Lindblad equation for open quantum systems, Phys. Rev. B **102**, 115109 (2020) (pp. 95, 110).

[263] E. Mozgunov and D. Lidar, Completely positive master equation for arbitrary driving and small level spacing, Quantum **4**, 227 (2020) (pp. 95, 110).

[264] P. P. Potts, A. A. S. Kalaee, and A. Wacker, A thermodynamically consistent Markovian master equation beyond the secular approximation, New J. Phys. **23**, 123013 (2021) (pp. 95, 110).

[265] A. D'Abbruzzo, V. Cavina, and V. Giovannetti, A time-dependent regularization of the Redfield equation, SciPost Phys. **15**, 117 (2023) (pp. 95, 110).

[266] G. McCauley et al., Accurate Lindblad-form master equation for weakly damped quantum systems across all regimes, npj Quantum Information **6**, 1–14 (2020) (pp. 95, 96, 99, 102, 104, 109, 110, 119, 120, 124, 135, 180, 185, 186, 209).

[267] D. Fernández de la Pradilla, E. Moreno, and J. Feist, Vacuum-field-induced state mixing, SciPost Phys. **15**, 252 (2023) (pp. 104, 113, 115, 118, 130, 131, 208, 210).

[268] N. J. Higham, Computing a nearest symmetric positive semidefinite matrix, Linear Algebra and its Applications **103**, 103–118 (1988) (p. 105).

[269] S. Foteinopoulou et al., Phonon-polaritonics: enabling powerful capabilities for infrared photonics, Nanophotonics **8**, 2129–2175 (2019) (p. 117).

[270] S. Adachi, *Optical Properties of Crystalline and Amorphous Semiconductors* (Springer US, 1999) (p. 117).

[271] C. R. Gubbin, S. De Liberato, and T. G. Folland, Surface phonon polaritons for infrared optoelectronics, J. Appl. Phys. **131**, 030901 (2022) (p. 117).

[272] M. T. H. Reid and S. G. Johnson, Efficient computation of power, force, and torque in BEM scattering calculations, IEEE Transactions on Antennas and Propagation **63**, 3588–3598 (2015) (pp. 118, 128).

[273] SCUFF-EM, GitHub, `http://github.com/homerreid/scuff-EM` (pp. 118, 128).

[274] P. M. Visser and G. Nienhuis, Solution of quantum master equations in terms of a non-Hermitian Hamiltonian, Phys. Rev. A **52**, 4727 (1995) (p. 126).

[275] B. Kramer and A. MacKinnon, Localization: theory and experiment, Rep. Prog. Phys. **56**, 1469–1564 (1993) (pp. 132, 136).

[276] J. Block and S. Scheel, Casimir-Polder-induced Rydberg macrodimers, Phys. Rev. A **100**, 062508 (2019) (p. 136).

[277] T. G. Walker and M. Saffman, Consequences of Zeeman degeneracy for the van der Waals blockade between rydberg atoms, Phys. Rev. A **77**, 032723 (2008) (p. 136).

[278] S. Ribeiro et al., Casimir-Polder interaction from exact diagonalization and surface-induced state mixing, EPL **110**, 51003 (2015) (p. 136).

[279] S. Y. Buhmann et al., Casimir-Polder forces: A nonperturbative approach, Phys. Rev. A **70**, 052117 (2004) (p. 136).

[280] M. Donaire et al., Casimir-Polder–induced Rabi oscillations, Europhys. Lett. **109**, 24003 (2015) (p. 136).

[281] G. Günter et al., Sub-cycle switch-on of ultrastrong light–matter interaction, Nature **458**, 178–181 (2009) (p. 141).

[282] L. Garziano et al., Switching on and off of ultrastrong light-matter interaction: photon statistics of quantum vacuum radiation, Phys. Rev. A **88**, 063829 (2013) (p. 141).

[283] M. Cirio et al., Ground state electroluminescence, Phys. Rev. Lett. **116**, 113601 (2016) (p. 141).

[284] J. Hausinger and M. Grifoni, Dissipative dynamics of a biased qubit coupled to a harmonic oscillator: analytical results beyond the rotating wave approximation, New J. Phys. **10**, 115015 (2008) (p. 142).

[285] D. De Bernardis et al., Breakdown of gauge invariance in ultrastrong-coupling cavity QED, Phys. Rev. A **98**, 053819 (2018) (pp. 143, 145).

[286] J. Keeling, *Light-matter interactions and quantum optics*, Available at `https://www.st-andrews.ac.uk/~jmjk/keeling/teaching/quantum-optics.pdf` (p. 145).

[287] K. Hepp and E. H. Lieb, On the superradiant phase transition for molecules in a quantized radiation field: the Dicke maser model, Ann. Phys. **76**, 360–404 (1973) (p. 145).

[288] Y. K. Wang and F. T. Hioe, Phase transition in the Dicke model of superradiance, Phys. Rev. A **7**, 831–836 (1973) (p. 145).

[289] K. Rzażewski, K. Wódkiewicz, and W. Żakowicz, Phase transitions, two-level atoms, and the A^2 term, Phys. Rev. Lett. **35**, 432–434 (1975) (p. 145).

[290] J. Keeling, Coulomb interactions, gauge invariance, and phase transitions of the Dicke model, J. Phys. Condens. Matter **19**, 295213 (2007) (p. 145).

[291] P. Nataf and C. Ciuti, No-go theorem for superradiant quantum phase transitions in cavity QED and counter-example in circuit QED, Nat. Commun. **1**, 72 (2010) (pp. 145, 146).

[292] A. Vukics and P. Domokos, Adequacy of the Dicke model in cavity QED: a counter-no-go statement, Phys. Rev. A **86**, 053807 (2012) (p. 145).

[293] T. Grießer, A. Vukics, and P. Domokos, Depolarization shift of the superradiant phase transition, Phys. Rev. A **94**, 033815 (2016) (p. 145).

[294] D. De Bernardis, T. Jaako, and P. Rabl, Cavity quantum electrodynamics in the nonperturbative regime, Phys. Rev. A **97**, 043820 (2018) (p. 145).

[295] H. Groß et al., Near-field strong coupling of single quantum dots, Sci. Adv. **4**, eaar4906 (2018) (p. 146).

[296] C. Fábri et al., Impact of Cavity on Molecular Ionization Spectra, J. Phys. Chem. Lett. **15**, 4655–4661 (2024) (p. 146).

[297] G. L. Paravicini-Bagliani et al., Magneto-transport controlled by Landau polariton states, Nat. Phys. **15**, 186–190 (2019) (p. 146).

[298] T. Tufarelli et al., Signatures of the A^2 term in ultrastrongly coupled oscillators, Phys. Rev. A **91**, 063840 (2015) (p. 146).

[299] S. M. Barnett and R. Loudon, Sum rule for modified spontaneous emission rates, Phys. Rev. Lett. **77**, 2444–2446 (1996) (pp. 152, 221).

[300] U. Fano, Effects of configuration interaction on intensities and phase shifts, Phys. Rev. **124**, 1866–1878 (1961) (p. 162).

[301] A. M. Stewart, Longitudinal and transverse components of a vector field, Sri Lankan J. Phys. **12**, 33–42 (2012) (pp. 198, 199).

[302] B. C. Hall, *Lie Groups, Lie Algebras, and Representations: An Elementary Introduction*, Vol. 222, Graduate Texts in Mathematics (Springer International Publishing, Cham, 2015) (p. 203).

[303] D. Tamascelli et al., Nonperturbative treatment of non-Markovian dynamics of open quantum systems, Phys. Rev. Lett. **120**, 030402 (2018) (p. 207).

[304] H. Spohn, *Dynamics of charged particles and their radiation field* (Cambridge University Press, 2004) (p. 240).

[305] A. Yaghjian, *Relativistic dynamics of a charged sphere* (Springer New York, 2006) (p. 240).

[306] F. Rohrlich, *Classical charged particles*, 3rd (World Scientific, 2007) (p. 240).

List of Figures

From weak to ultrastrong coupling in light-matter interactions

Throughout history, the study of light, matter and their interactions has guided our understanding of reality, and yet it is now as active as it has ever been. In fact, we are not limited to learning about light-matter interactions as they come in nature, but we can actually engineer them with cavities nowadays. In this thesis, we explore fundamental aspects relative to the interaction of a quantum emitter with light in the presence of a cavity, in the weak and ultrastrong coupling regimes. The first part focuses on analyzing the phenomenology of the weak coupling regime, and developing methods that capture all the relevant effects. In the second part, we address foundational questions about the ultrastrong coupling regime in light-matter interactions. Specifically, we discuss the roles of transverse and longitudinal fields in reaching the ultrastrong coupling regime with the emitter. In both parts, our results highlight the general importance of taking a step back to improve one's perspective before moving forwards.